UNIVERSITÀ DEGLI STUDI DELLA CALABRIA
Facoltà di Scienze Matematiche Fisiche e Naturali
Dipartimento di Chimica

Dottorato di ricerca in Metodologie Chimiche Inorganiche
XXIII ciclo

AREA 03 –Scienze Chimiche, SSD-CHIM03/Chimica generale ed inorganica

Studio Teorico dell'attivazione di legami C-H e C-C mediante cationi di attinidi in fase gassosa

Supervisore
Dott.ssa Maria del Carmen Michelini

Coordinatore
Ch.mo Prof. Nino Russo

Candidata
Emanuela Di Santo
Emanuela Disanto

A.A. 2009-2010

Abstract

Density functional theory calculations were performed to study the ability of thorium (Th^+, Th^{2+}) and uranium (U^+, U^{2+}) cations to activate the C-H and C-C bonds of methane, ethane and propane in the gas-phase.

The potential energy surfaces were explored taking into consideration different spin states. A close description of the reaction pathways leading to different reaction products is presented, and the obtained results are compared with experimental data.
Th^+ activates the C-H bonds of methane and ethane, in contrast, U^+ is inert in both reactions. Th^{2+} reacts with all three alkanes, whereas U^{2+} reacts with C_2H_6 and C_3H_8, with product distributions different than those of Th^{2+}.

The computed potential energy profiles, which all proceed by insertion, were used to evaluate the relationship between the energetics of the bare $Th^{+\,(2+)}$ and $U^{+\,(2+)}$ ions and the energies for C-H and C-C bond activation. It was found that the computed energetics for insertion are entirely consistent with the empirical model which relates insertion efficiency to the energy needed to promote the $An^{+\,(2+)}$ ion from its ground state to a prepared divalent state with two non 5f valence electrons suitable for bond formation in {C-$An^{+\,(2+)}$-H} and {C-$An^{+\,(2+)}$-C} activated intermediates.

Elenco delle pubblicazioni

I. *Methane C-H bond activation by gas-Phase* Th^+ *and* U^+*: reaction mechanisms and bonding analysis*.
Emanuela Di Santo, Maria del Carmen Michelini, Nino Russo
Organometallics **2009,** 28, 3716-3726.

II. *Activation of ethane C-H and C-C bonds by gas-phase* Th^+ *and* U^+*: a theoretical study*.
Emanuela Di Santo, Maria del Carmen Michelini, Nino Russo
J.Phys.Chem. A **2009**, 113, 14699-14705.

III. *Gas phase reactions of the bare* Th^{2+} *and* U^{2+} *ions with small alkanes,* CH_4*,* C_2H_6*, and* C_3H_8*: an experimental and theoretical study of elementary organoactinide chemistry*.
Emanuela Di Santo, Marta Santos, Maria del Carmen Michelini, Joaquim Marçalo, Nino Russo, John K. Gibson, 2010
Submitted.

Indice

Introduction

In this thesis, we are going to illustrate the outcomes of theoretical investigations at Density Functional Theory (DFT) level aimed to study the reactivity of actinide cations with small alkanes in the gas phase. One of the fundamental goals of this work was to get insight into the mechanistic details of the C-H and C-C bonds activation process, and the role played by the 5f electrons.

In **Chapter 1** are illustrated the main characteristics of the actinide cations. Whereas the lanthanides are all rather similar in their condensed phase chemistries, substantial differences in this chemistry are found between the homologous actinide and lanthanide elements, as well as between the members of the actinide series. The early actinides (through Pu) are particularly differentiated from the homologous early lanthanides in two major regards. Firstly, the actinides exhibit a variety of oxidation states, from a maximum state for Ac of +3 up to +7, for Np. A second major difference between the actinides and lanthanides is that the 5f electrons of the early actinides are more available for the direct participation in bonding, in sharp contrast to the localized nature of the 4f electrons of all of the lanthanides. Beyond Pu, the 5f orbitals are increasingly localized and generally do not participate in bonding.

A primary motivation for studying gas-phase actinide ion chemistry is to better understand the unique character of the electronic structures and energetics of the actinides, and particularly both the direct and indirect roles of the 5f electrons. Most of the distinctive chemistry of the actinides can be traced either directly or indirectly to the changing character of the 5f electrons. The electronic structure and energetics of the actinides are more affected by relativistic effects than lighter elements due to the high nuclear charge. Relativistic effects are central in understanding the unique chemical behavior of the actinides and specifically the energetics of electronic configurations. Essentially, the 5f electrons are relatively high in energy and spatially extended for the early actinides, resulting in high oxidation states and/or the possible direct participation of the 5f electrons in bonding. As the nuclear charge increases, the 5f electrons become increasingly stabilized and spatially contracted (localized) relative to the valence 6d and 7s electrons.

During the last decade a great body of studies has been performed on the reactivity of actinide cations with small molecules in the gas phase. This research has been mainly carried out using mass spectroscopic techniques, which are able to provide thermochemical data as well as some insight into the reaction mechanisms.

The main goal of this work was to perform a detailed theoretical study of the gas phase reaction mechanisms of the interaction of four different actinide cations (Th^+, Th^{2+}, U^+ and U^{2+}) with CH_4, C_2H_6, and C_3H_8. The chosen cations are characterized by ground state electronic configurations that contain an increasing number of 5f electrons, ranging from zero in Th^+ to four in U^{2+}. The systematic analysis of the reaction mechanisms and energetics involved in their reactivity with small alkanes has permitted us to get insight into the role played by the 5f electrons in the bond activation process.

Chapter 2 illustrates the computational approach selected to study the reaction mechanisms. We have used two different approaches of DFT to analyze the reactions under study.

The reaction mechanisms for the activation of the C-H and C-C bonds of CH_4, C_2H_6 and C_3H_8 by $Th^{+(2+)}$ and $U^{+(2+)}$ are described in **Chapter 3.** We discuss the similarities and differences found between the different cations, and the efficiency of the different theoretical approaches to model the reaction processes, by direct comparison with experimental data. A central goal of this work was to determine if DFT can reliably model the reaction mechanisms of actinide ions with small molecules in the gas-phase.

1

La chimica dei cationi degli attinidi in fase gassosa

Introduzione

Il numero di studi, sia teorici che sperimentali, condotti sulla reattività in fase gassosa di ioni metallici è andato gradualmente aumentando nel corso degli ultimi tre decenni. Nei primi anni, gli studi si sono concentrati sui metalli alcalini[1-3] per poi estendersi sugli elementi di transizione e, in particolare sui metalli del blocco *d*.[4-13]

Un grande impulso a questo campo di ricerca si è avuto alla fine degli anni ’70 dagli studi sperimentali sull’attivazione dei legami C-C e C-H in fase gassosa mediata da ioni di metalli di transizione.[4,5] Nelle ultime due decadi lo sforzo è stato concentrato sullo studio delle reazioni di attivazione di piccole molecole organiche, in particolare di idrocarburi, da parte di ioni dei metalli di transizione. L’obiettivo principale di questi lavori era quello di cercare di comprendere il ruolo del metallo centrale sull’evoluzione delle reazioni stesse.[6-13]

ll numero di lavori sulla reattività degli elementi del blocco f in fase gassosa, è aumentato in anni più recenti. La maggior parte di questi studi hanno avuto per oggetto il ruolo degli elettroni 4f dei lantanidi che risulta alquanto differenti rispetto a quello degli elettroni d più esterni degli elementi di transizione.[14-26] Gli elettroni 4f, infatti, non partecipano all’attivazione di legami chimici, e per avere un’inserzione effettiva nei legami è necessario che la configurazione elettronica del metallo sia tale da avere almeno due elettroni di valenza non 4f (5d,6s). In particolare, l’efficienza di attivazione di legami C-C o C-H di idrocarburi, in fase gassosa, da parte di cationi monopositivi dei lantanidi (Ln^+), è correlabile con l’energia di promozione ($\Delta E\ [Ln^+]$) dallo stato elettronico fondamentale (GS, *Ground State*) allo stato eccitato a più bassa energia con configurazione $[Xe]4f^{n-2}5d^16s^1$. Per esempio, la configurazione del GS del Gd^+ ($4f^75d^16s^1$) è adatta all’inserzione rispetto all’Eu^+ che, invece ha bisogno di un’energia di promozione di 3.8 eV ($4f^76s^1 \rightarrow 4f^65d^16s^{1)}$.[27] Questo dato è relazionabile all’osservazione che il Gd^+ è più efficiente nell’attivare il butene, mentre l’Eu^+ è quasi inerte nell’attivare questo reagente. Una relazione analoga è stata proposta nel caso degli ioni attinidi (An^+) poiché è stato osservato che l’efficienza dei processi di attivazione di idrocarburi può essere correlata all’energia di promozione dal GS al primo stato eccitato con configurazione elettronica con due elettroni di valenza non 5f.[28]

Tuttavia, le proprietà chimico-fisiche fra le due serie, 4f e 5 f, sono sostanzialmente differenti, e, mentre la chimica dei lantanidi è piuttosto simile in fase gassosa ed in fase condensata, le differenze sono rilevanti per gli attinidi, soprattutto per i primi membri della serie.[29-31] Infatti, la chimica dei lantanidi è dominata dallo stato di ossidazione +3, mentre gli attinidi, ed in particolar modo i primi membri della serie, possiedono solitamente numeri di ossidazione più alti (da +3 a +7).

Lo studio questi sistemi in fase gassosa, sia dal punto di vista teorico che sperimentale, dà la possibilità di analizzare le proprietà chimico-fisiche di tali sistemi in assenza di fattori perturbativi quali la solvatazione o la presenza di nodi adiacenti nel reticolo cristallino permettendo di correlare le capacità catalitiche degli ioni metallici con la loro struttura elettronica.

1.1 Gli attinidi e i suoi cationi

Con il termine Attinidi si indicano i quindici elementi compresi fra l'attinio e il laurenzio (fig. 1.1).

Prima del 1940 erano noti solo gli attinidi naturali: *torio, protoattinio, e uranio*, gli altri sono stati prodotti artificialmente dopo questa data.

Attinidi	Simbolo	numero atomico	Configurazione elettronica del GS
Attinio	Ac	89	$6d^1 7s^2$
Torio	Th	90	$6d^2 7s^2$
Protoattinio	Pa	91	$5f^2 6d^1 7s^2$
Uranio	U	92	$5f^3 6d^1 7s^2$
Nettunio	Np	93	$5f^4 6d^1 7s^2$
Plutonio	Pu	94	$5f^6 7s^2$
Americio	Am	95	$5f^7 7s^2$
Curio	Cm	96	$5f^7 6d^1 7s^2$
Berkelio	Bk	97	$5f^9 7s^2$
Californio	Cf	98	$5f^{10} 7s^2$
Einsteinio	Es	99	$5f^{11} 7s^2$
Fermio	Fm	100	$5f^{12} 7s^2$
Mendelevio	Md	101	$5f^{13} 7s^2$
Nobelio	No	102	$5f^{14} 7s^2$
Laurenzio	Lr	103	$5f^{14} 6d^1 7s^2$

Fig 1.1 Attinidi e loro configurazione elettronica dello stato fondamentale

Lo studio teorico di questi sistemi comporta numerose difficoltà dovute sia agli effetti relativistici, che sono alla base del comportamento chimico-fisico degli elementi pesanti, che all'elevato numero di elettroni nel guscio di valenza.

Come accennato in precedenza, la struttura elettronica degli elementi della serie 5f differisce notevolmente da quella dei lantanidi nei quali gli elettroni 4f essendo schermati da parte degli elettroni 5s e 5p e di conseguenza mostrano capacità di attivazione di legami minore. Per i primi quattro elementi della serie degli attinidi (Th, Pa, U, Np) la differenza di energia fra gli orbitali 5 f e 6d7s è piccola, e di conseguenza gli elettroni possono occupare i livelli 5f o 6d e 7s o entrambi. Con l'aumentare del numero atomico lungo la serie degli attinidi, gli orbitali 5f diventano più energeticamente stabili e più contratti spazialmente rispetto agli elettroni di valenza 6d e 7s, quindi mostrano un comportamento più simile ai lantanidi.

Gli orbitali 5f dei primi elementi della serie possiedono, dunque, energie relativamente alte e sono spazialmente più diffusi, essendo quindi più disponibili per la formazione di legami. Inoltre, questo spiega i più alti stati di ossidazione dei primi membri, in confronto con gli elementi più a destra della serie e ai lantanidi.[30] Come si può vedere dalla figura 1.2, gli stati di ossidazione più comuni per il Th, Pa e U, sono +4, +5 e +6, rispettivamente. Lo stato di ossidazione +6 è lo stato di ossidazione più comune per l'uranio. Esso si riscondra, per esempio, nel UF_6 e nel diossicatione UO_2^{2+} che è stabile ed esiste sia in soluzione che allo stato cristallino. Per gli ultimi elementi della serie, da Am a Lr, lo stato di ossidazione più stabile è il +3.

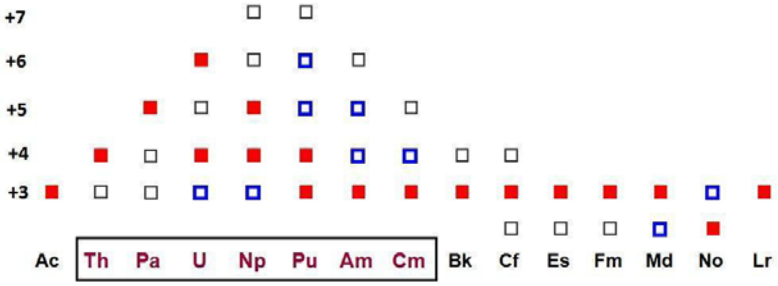

Fig 1.2 Stati di ossidazione assunti dagli attinidi nei differenti composti. Gli stati di ossidazione più comuni sono rappresentati dai quadrati rossi, e quelli meno comuni dai quadrati azzurri e vuoti, in ordine decrescente d'importanza.

Gli studi sperimentali riguardanti le reazioni dei cationi degli attinidi, e in particolare dei cationi An^+ e An^{2+}, con idrocarburi e diversi reagenti ossidanti in fase gassosa sono stati fondamentali per approfondire la conoscenza del comportamento chimico degli attinidi.[28,32-53]

Sulla base delle configurazione elettroniche dei cationi An^+ monopositivi, e con l'obiettivo di analizzare le caratteristiche di reattività di questi cationi, spesso si considera una suddivisione approssimativa degli attinidi, simile a quella fatta in base al loro comportamento in condizioni normali di pressione e temperatura: *blocco d* (Ac-Th) che non possiedono elettroni di tipo *f* nello stato fondamentale; *blocco f* – di legame (Pa-Pu); *blocco f-localizzati* (Am-Lr).

La figura 1.3 riassume le principali informazioni sulle strutture elettroniche ed energetiche dei monocationi degli attinidi.[28] L'energia di promozione corrisponde alla transizione tra il livello J più basso del termine dello stato fondamentale, al livello J più basso del termine dello stato eccitato. Sulla base della correlazione precedentemente riscontrata fra le energie di promozioni dallo stato elettronico fondamentale a stati eccitati "divalenti" nel caso dei cationi monopositivi dei lantanidi, e l'efficienza di attivazione di idrocarburi, si potrebbe prevedere una rapporto simili nel caso degli ioni An^+. Tuttavia, la possibile partecipazione diretta degli elettroni 5f nel legame potrebbe permettere a certe reazioni di procedere senza bisogno di promozione a stati eccitati contenenti elettroni di tipo 6d. Diversi studi sperimentali sulla reattività di cationi An^+ sono stati intrapresi con l'obiettivo di trovare conferma a questa ipotesi.[41]

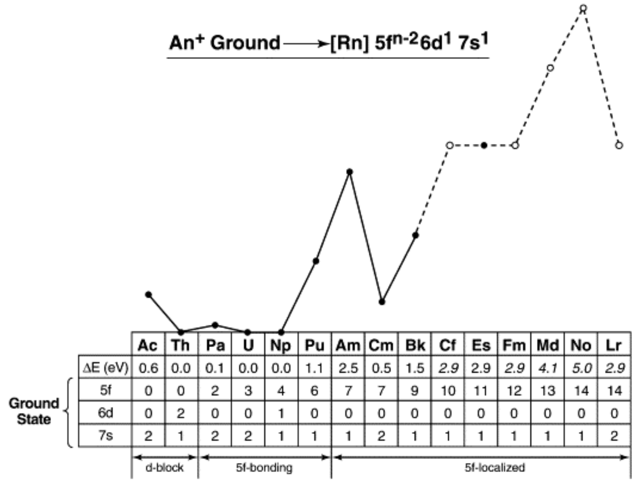

		Ac	Th	Pa	U	Np	Pu	Am	Cm	Bk	Cf	Es	Fm	Md	No	Lr
	ΔE (eV)	0.6	0.0	0.1	0.0	0.0	1.1	2.5	0.5	1.5	*2.9*	2.9	*2.9*	*4.1*	*5.0*	*2.9*
Ground State	5f	0	0	2	3	4	6	7	7	9	10	11	12	13	14	14
	6d	0	2	0	0	1	0	0	0	0	0	0	0	0	0	0
	7s	2	1	2	2	1	1	1	2	1	1	1	1	1	1	2

Fig 1.3: Monocationi degli attinidi: strutture elettroniche ed energetiche. L'energie di promozioni (Δ*E)* dal ground state al primo stato eccitato sono calcolate da Blaise and Wyart[54] tranne per Md^+, No^+ and Lr^+ calcolate da Brewer.[55] Il valore dei gap è rappresentata da cerchi pieni con linee connesse, mentre le stime corrispondono ai cerchi vuoti e linee tratteggiate.Rif[28]

Quest’argomento risulta di fondamentale importanza per la comprensione della chimica degli ioni attinidi in fase gassosa, ed è stato uno degli interessi iniziali di questa tesi di dottorato.[56,57]

La reattività dei cationi An^{2+} è stata molto meno studiata in confronto con quella dei cationi An^{+}.[37,44,54,58] Fino ad ora non è stata chiaramente stabilita una correlazione diretta fra la reattività osservata e le strutture elettroniche ed energie di promozione dei cationi dipositivi, come invece proposta per i cationi An^{+}. Tutti i cationi An^{2+}, con l’unica eccezione del catione Th^{2+}, hanno energie di promozione dallo stato fondamentale ad stati eccitati “divalenti” che sono piuttosto alte, oscillando da i 2.4 eV nel caso del U^{2+} a 8.7 eV nel caso del Am^{2+}. Con l’obiettivo di approfondire quest’ argomento nel lavoro di tesi di dottorato si è proceduto ad analizzare in modo sistematico, il processo di attivazione dei legami C-H e C-C del metano, etano e propano, da parte dei cationi Th^{2+} e U^{2+}.[58]

1.2 Effetti relativistici

Le più importanti caratteristiche della struttura elettronica degli Attinidi sono la conseguenza di forti effetti relativistici. La teoria della relatività speciale di Einstein indica che non è possibile accelerare una particella a velocità simile o superiori a quella della luce, *c*. La massa *m* di una particella di massa a riposo m_0, che si muove a una velocità ν è data dalla equazione

$$m = \frac{m_0}{\sqrt{1-\left(\frac{v}{c}\right)^2}} \qquad (1.1)$$

La velocità radiale media, $< \nu_{rad} >$, in unità atomiche, degli elettroni nel guscio 1s di un atomo è approssimativamente uguale al numero atomico, Z. Per l’uranio (Z = 92) ad esempio, il rapporto fra la velocità radiale media di un elettrone in un orbitale 1s e la velocità della luce, $< \nu_{rad} >/c$, è approssimativamente 0.67. Di conseguenza, l’incremento di massa relativistica media di un elettrone 1s nell’atomo di uranio sarà dato dalla equazione

$$m = \frac{m_0}{\sqrt{1-(0.67)^2}} \approx 1.35 m_0 \qquad (1.2)$$

Considerando l'espressione del radio di Bohr, la quale indica una dipendenza inversamente proporzionale alla massa, si può concludere che l'incremento di massa produrrà una marcata contrazione radiale di tale orbitali, ed una concomitante stabilizzazione energetica.

L'effetto del termine massa-velocità è immediato sugli elettroni di tipo *s* e *p*, in quanto più vicini al nucleo. La contrazione di tali orbitali si estende anche agli orbitali *s* e *p* dei livelli energetici più esterni, a causa delle relazioni d'ortogonalità esistente fra di loro. Contrariamente, il potenziale effettivo risentito dagli elettroni *d* e *f*, che non si avvicinano mai al nucleo, sarà più efficacemente schermato dagli elettroni *s* e *p* e causerà la loro destabilizzazione energetica ed espansione radiale.

La *correzione massa-velocità,* corrisponde alla correzione dell'energia cinetica degli elettroni derivante dalla variazione della loro massa con la velocità. Così come la massa di un elettrone è correlata con l'energia cinetica e quindi con la sua distanza dal nucleo, allo stesso modo gli effetti massa-velocità causano un aumento dell'energia cinetica che comporta una distanza nucleo-elettrone più corta, soprattutto per gli orbitali più interni. Questo vuol dire che l'hamiltoniano non relativistico sottostima le energie cinetiche. Gli effetti relativistici che sono indipendenti dallo spin sono chiamati *effetti cinematici* per distinguerli dagli effetti relativistici dipendente dallo spin, in particolare, l'accoppiamento spin-orbita.

L'accoppiamento spin-orbita descrive l'interazione tra il momento angolare orbitale e il momento di spin degli elettroni di un atomo. Ci sono due approssimazioni limite per descrivere l'accoppiamento tra diversi momenti angolari all'interno dell'atomo, tutte e due basate sulla addizione dei vettori che descrivono il momento orbitalico e il momento di spin. Una di queste approssimazioni, l'*accoppiamento LS* o di *Russell-Saunders* è più adatto a situazioni in cui l'interazione spin-orbita è debole in confronto con l'energia di repulsione interelettronica, e quindi, prevale negli elementi a basso numero atomico Z. L'altro approccio, detto *accoppiamento j-j,* è applicabile a situazioni in cui le interazioni spin-orbita sono forti in confronto con le interazioni elettrostatiche fra gli elettroni.

L'accoppiamento di Russell-Saunders descrive l'interazione tra il momento angolare orbitale totale L ($L = l_1 + l_2 + ... + l_N$) e lo spin totale S ($S = s_1 + s_2 + ... + s_N$) basato sul modello vettoriale dell'atomo. L'interazione tra *L* ed *S* definisce il momento angolare totale *J* ($J = L + S$) di un sistema elettronico.

Nello schema di *accoppiamento j-j* ciascun momento angolare orbitale l_i e ciascun momento angolare di spin s_i di ciascun elettrone sono accoppiati per dare un momento angolare totale j_i ($j_i = l_i + s_i$) individuale dell'elettrone considerato. La somma dei momenti angolari totali di tutti gli elettroni fornisce il momento angolare totale dell'intero sistema elettronico $\left(J_N = \sum_{i=1}^{N} j_i \right)$.

Le strutture elettroniche dei cationi dei lantanidi, ed in particolare gli ioni Ln^{3+}, sono ben descritte dall'accoppiamento di Russell-Saunders. In contrasto, l'accoppiamento spin-orbita degli ioni attinidi ed suoi composti, sono molti più grandi di quelli dei lantanidi, al punto che l'approssimazione di Russell-Saunders è molto meno valida. Purtroppo, nemmeno l'accoppiamento puro *j-j* funziona bene nel caso degli attinidi, dovuto, in parte, al fatto che l'accoppiamento spin-orbita non domina sulle repulsioni interelettroniche, ma anche dovuto al fatto che gli orbitali 5f, in particolar modo nel caso dei primi membri della serie degli attinidi sono molto più sensibili all'intorno chimico, in confronto agli orbitali 4f dei lantanidi. I fattori che determinano la grandezza dell'accoppiamento spin-orbita nel caso di atomi multielettronici sono complessi, ma in generale, aumentano con l'aumento della carica nucleare, e, per lo stesso numero quantico principale, diminuiscono nell'ordine p > d > f. Gli elettroni con numero quantico secondario $l > 0$ subiscono il ben noto splitting dei livelli energetici a causa dell'effetto spin-orbita, che si riflette nella cosiddetta "struttura fine" degli spettri atomici. Le interazioni spin-orbita alterano le proprietà spettroscopiche di molecole contenenti elementi pesanti. In alcuni casi, infatti, le interazioni spin-orbita non solo splittano gli stati eccitati, ma mescolano i differenti stati eccitati.

1.3 Studi sperimentali sulla reattività dei cationi degli attinidi in fase gassosa

A causa dell'incapacità di gestire in sicurezza lavorativa gli attinidi altamente radiottativi, i primi lavori sperimentali hanno riguardato principalmente i cationi degli elementi Th e U, e solo più recentemente, gli altri membri della serie.

Nel 1977 Armentrout e collaboratori,[32] hanno analizzato la reazione di U^+ con CD_4 utilizzando metodologie di "fascio di ioni guidato". [32,33] I suoi risultati sono riprodotti nella figura 1.2, e, come si può osservare la reazione procede, in modo endotermico, verso la produzione di UD^+. Questi studi iniziali hanno fornito informazioni termodinamiche fondamentali, ma non hanno fornito nessuna informazione riguardante il meccanismo di reazione o il ruolo svolto dagli elettroni 5f nel processo di attivazione del legame.

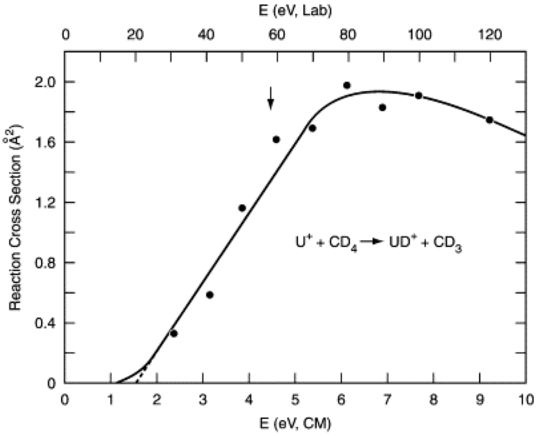

Fig 1.2 Relazione tra energie e sezioni d'urto ottenuti da uno studio di "un fascio di ioni guidato" per la reazione di U^+ con CD_4.Rif[32]

.

Successivamente, e grazie allo sviluppo della tecnica FTICR–MS (*Fourier Transform– Ion Cyclotron Resonance – Mass Spectrometry*), lo studio di reazioni in fasse gassosa di cationi degli attinidi si è ampliato, considerando diversi substrati organici,[34-36] fra cui, alcani (metano, etano, propano, n-butano) e alcheni (etene, propene, 1-butene, ecc.). La FTICR–MS è una tecnica di spettrometria di massa ad alta risoluzione che permette ottenere informazione di tipo cinetico. Le costanti di velocità (k) sono determinate osservando il decadimento dell'intensità dello ione reagente in funzione del tempo. Tali costanti (k) sono solitamente confrontate con le costanti di velocità di collisione (k_{COL}) ed il rapporto tra k/k_{COL} definisce l'efficienza di reazione.

Il primo studio sulla reazione del Th^+ con idrocarburi[36] ha messo in rilievo la forte reattività e l'efficienza di questo catione, il quale, in contrasto con il catione U^+,[35] riesce ad attivare il forte legame C-H del metano. Questa maggiore reattività del Th^+ rispetto all'U^+, confermata anche in alcune reazioni con areni,[37] è stata attribuita alla particolare configurazione elettronica dello stato fondamentale del Th^+ che contiene due elettroni di valenza non f ([Rn] $6d^2$ 7s).

Gli studi di reattività in fase gassosa si sono successivamente estesi allo studio di diversi cationi degli elementi transuranici, e i corrispettivi ossidi, utilizzando la tecnica

LAPRD (*Laser Ablation with Prompt Reaction and Detection)*. I primi studi si sono concentrati sulle reazioni di questi cationi con diversi idrocarburi.[38-40] L'analisi dei risultati ottenuti ha permesso di stabilire un ordine di reattività fra i diversi cationi An^+:

$$Th^+ \geq Pa^+ \geq U^+ \approx Np^+ > Cm^+ \geq Pu^+ > Bk^+ > Am^+ \approx Cf^+ \geq Es^+$$

Questi studi sperimentali hanno quindi portato a confermare l'ipotesi secondo la quale, analogamente a quanto accade nel caso dei cationi Ln^+, la reattività degli ioni An^+ verso gli idrocarburi è correlata inversamente con l'energia necessaria per promuovere lo ione dalla stato fondamentale allo stato eccitato con configurazione elettronica "divalente" (con due elettroni spaiati non-5f, del tipo $[Rn]5f^{n-2}\,6d\,7s$). Nella figura 1.3 viene mostrato un grafico delle variazioni di energie di promozioni lungo la serie degli attinidi (cationi An^+) dallo stato fondamentale ai due stati eccitati avente configurazioni elettroniche contenente due elettroni non-5f, cioè, $[Rn]5f^{n-2}6d7s$ e $[Rn]5f^{n-2}6d^2$, rispettivamente. Questo grafico evidenzia la correlazione inversa fra reattività dei cationi e l'energia di promozione a uno stato eccitato adatto all' inserzione.

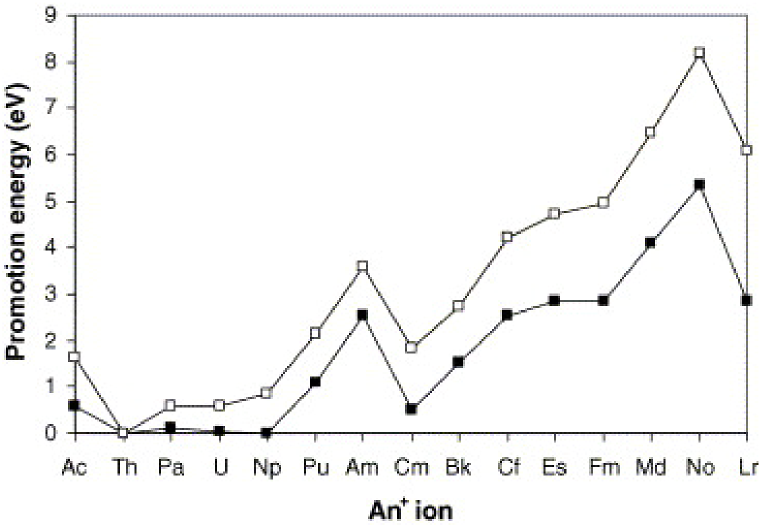

Fig1.3 Energie di promozioni di ioni An^+ dallo stato fondamentale agli stati eccitati avente configurazione con due elettroni non f $[Rn]5f^{n-2}6d7s$ (quadrati pieni) and $[Rn]5f^{n-2}6d^2$ (quadrati vuoti).[54-55]Gli stati fondamentali sono: Ac^+, $[Rn]7s^2$; Th^+, $[Rn]6d^27s$; Pa^+, $[Rn]5f^27s^2$; U^+, $[Rn]5f^37s^2$; Np^+, $[Rn]5f^46d7s$; Pu^+, $[Rn]5f^67s$; Am^+, $[Rn]5f^77s$; Cm^+, $[Rn]5f^77s^2$; Bk^+, $[Rn]5f^97s$; Cf^+, $[Rn]5f^{10}7s$; Es^+, $[Rn]5f^{11}7s$; Fm^+, $[Rn]5f^{12}7s$; Md^+, $[Rn]5f^{13}7s$; No^+, $[Rn]5f^{14}7s$; Lr^+, $[Rn]5f^{14}7s^2$.Rif[41]

Questo tipo di sistematizzazione basato sull'energia di promozione può fornire una guida per predire la chimica degli ioni attinidi e il comportamento di tali elementi in fase condensata.[41]

Un'altra tecnica utilizzata nello studio della reattività degli ioni attinidi è stata la QIT/MS (*quadrupole ion trap mass spectrometry*), spettrometria di massa a trappola ionica quadrupolare. Anche questa metodica fornisce informazioni di tipo cinetico e, rispetto alla tecnica LAPRD, ha come vantaggio la possibilità di isolare i prodotti primari ottenuti, esaminando le reazioni successive. Diverse reazioni che coinvolgono cationi degli attinidi sono state studiate utilizzando questa metodologia, fra cui, le reazioni dei cationi mono- e dipositivi dell'uranio con O_2 e H_2O.[44] Gli stessi cationi sonno stati analizzati nelle loro reazioni con 1,2,3,4,5-pentametilciclopentadine (HCp^*)[45] e esafluoruro di zolfo.[46]

Per approfondire gli studi inizialmente fatti mediante la tecnica LAPRD, sono stati riesaminate le reazioni dei cationi An^+ ed AnO^+ (An= Th, Pa,U, Np, Pu, Am), e i rispettivi cationi dipositivi, con diversi ossidanti (N_2O, C_2H_4O, H_2O, O_2, CO_2, NO, CH_2O), attraverso la FTICR-MS. I risultati hanno ulteriormente confermato l'esistenza di una correlazione tra l'efficienza della reazione e l'energia di promozione dallo stato fondamentale a quello eccitato per i cationi, la quale risulta più elevata nel caso dei cationi dipositivi.[47-51]

1.4 Studi teorici sulla reattività dei cationi degli attinidi in fase gassosa

Studi teorici riguardanti l'analisi dettagliata dei meccanismi di reazione dei cationi degli attinidi, e del ruolo svolto dagli elettroni 5f nel processo catalitico, sono relativamente scarsi in letteratura. Soltanto ultimi anni, sono stati riportati studi su meccanismi di attivazione da parte dei primi membri della serie degli attinidi, di legami semplici, quali O-H, N-O, N-N, ecc.[59-62] Le reazioni U^+, U^{2+} con H_2O sono state studiate usando differenti approcci della teoria del funzionale di densità.[59] Entrambi i cationi attivano il legame O-H dell'acqua con la conseguente eliminazione di H_2. I meccanismi di reazione per l'interazione dei cationi U^+ e U^{2+} con N_2O sono stati analizzati in dettaglio, ed è stato riportato che entrambi i cationi attivano esotermicamente i legami N-N e N-O del N_2O.[60] In tutti i casi, i meccanismi di reazione coinvolgono incroci fra superfici a diverso spin elettronico.

Le reazioni in fase gassosa dei cationi mono e dipositivi del Th con H_2O sono state studiate in dettaglio utilizzando diverse approssimazioni teoriche, quale DFT, CCSD(T) (C*oupled-cluster with Singlets, Double and perturbative Triple excitations*)[61] e attraverso dinamica molecolare ab-initio.[62] Entrambi i cationi reagiscono esotermicamente con H_2O per produrre i corrispondenti ossidi ed idrogeno.

L'efficienza di reazione dei cationi dei primi membri della serie degli attinidi (Ac^+-Pu^+)[63] nell'attivazione del legame C-H del metano è stata recentemente analizzata utilizzando diversi approcci della DFT. In questo lavoro non sono stati riportati i meccanismi di reazione per eliminazione di H_2, e lo studio ha riguardato solamente il processo d'inserzione del catione nel legame C-H determinando la struttura e l'energetica del primo intermedio di inserzione (H-An^+-CH_3). La reattività dei cationi Th^+, Th^{2+}, e dell'atomo neutro, Th, con metano è stata recentemente riesaminata da De Almeida e collaboratori.[64] I risultati teorici riportati per le reazioni dei cationi Th^+ e Th^{2+} sono d'accordo con i risultati ottenuti in questo lavoro di tesi dottorale.

1.5 Obiettivi della tesi

La ricerca è stata rivolta allo studio teorico dei meccanismi di reazione coinvolti nei processi di attivazione dei legami C-H e C-C mediante cationi degli elementi della serie degli attinidi. In particolare, si sono studiate reazioni di attivazione di alcani a catena corta (metano, etano e propano) mediate dai cationi mono- e dipositivi dei primi membri della serie degli attinidi (Th^+, Th^{2+}, U^+ e U^{2+}). I cationi sono stati scelti sulla base della loro diversa configurazioni elettroniche nello stato fondamentale; (Th^+= [Rn] $6d^2$ 7s; Th^{2+}= [Rn] 5f 6d ; U^+= [Rn] $5f^3$ $7s^2$; U^{2+}= [Rn] $5f^4$).

Gli obiettivi principali dello studio di queste reazioni sono stati:

1) ottenere una conoscenza dettagliata dei processi di attivazione dei legami C-H e C-C in fase gassosa, mediati da centri metallici contenenti elettroni di tipo 5f e analizzare la loro influenza nel processo catalitico;

2) valutare l' affidabilità della teoria del funzionale della densità nello studio di sistemi contenenti elementi appartenenti alla serie degli attinidi, mediante il confronto con i dati sperimentali;

Tenendo conto delle difficoltà che ostacolano gli studi sperimentali di questi elementi la nostra ricerca teorica può aiutare ad approfondire la conoscenza della chimica degli attinidi.

Bibliografia

1. S.K. Searle’s, P. Earle *Can. J. Chem.*, **47**, 2619 (1969).
2. I. Didi, P. Kabale *J. Phys. Che.*, **74**, 1466 (1970).
3. R.H. Stanley, J.L. Beauchamp, *J. Am. Chem. Soc.*, **97**, 5920 (1975).
4. J. Allison, D.P. Ridge *J. Am. Chem. Soc.*, **99**, 35 (1977).
5. J. Allison, R.B. Freas, D.P. Ridge *J. Am. Chem. Soc.*, **101**, 1332 (1979).
6. P.B. Armentrout, D.H. Russell (Ed.), New York, **1**, (1989).
7. K. Eller, H. Schwarz, *Chem. Rev.*, **91**, 1121 (1991).
8. J. C. Weisshaar, *Acc. Chem. Res.*, **26**, 213 (1993).
9. B. S. Freiser, *Acc. Chem. Res*,. **27**, 353 (1994).
10. K. Seemeyer, D. Schröder, M. Kempf, O. Lettau, J. Müller and H. Schwarz *Organometallics*, **14**, 4465 (1995).
11. B.S. Freiser *J. Mass Spectrom.*, **31**, 703 (1996).
12. P.A.M. Van Koppen, P.R. Kemper, M.T. Bowers, B.S. Freiser (Ed.), Kluwer, Dordrecht, **157** (1996).
13. K.J. Fisher, I.G. Dance and G.D. Willett *Rapid Commun. Mass Spectrom.*, **10**, 106 (1996).
14. G. T. Seaborg, *Radiochim. Acta*, **61**, 115 (1993).
15. J.L. Thomas, R.G. Hayes, *J. Organometall. Chem.*, **23**, 487 (1970).
16. Y. Huang, M.B. Wise, D.B. Jacobson, B.S. Freiser, *Organometallics*, **6**, 346 (1987).
17. J.B. Schilling, J.L. Beauchamp *J. Am. Chem. Soc.*, **110**, 15 (1988).
18. L.S. Sunderlin, P.B. Armentrout *J. Am. Chem. Soc.*, **111**, 3845 (1989).
19. Y.A. Ranasinghe, T.J. MacMahon, B.S. Freiser *J. Am. Chem. Soc.*, **114**, 9112 (1992).
20. Y.A. Ranasinghe, B.S. Freiser *Chem. Phys. Lett.*, **200**, 135 (1992).
21. W.W. Yin, A.G. Marshall, J. Marçalo, A. Pires de Matos *J. Am. Chem. Soc.*, **116**, 8666 (1994).
22. C. Heinemann, D. Schröder, H. Schwarz *Chem. Ber.*, **127**, 1807 (1994).
23. H.H. Cornehl, C. Heinemann, D. Schröder, H. Schwarz *Organometallics*, **14**, 992 (1995).
24. J. Marçalo, A. Pires de Matos, W.J. Evans *Organometallics*, **15**, 345 (1996).
25. J.K. Gibson, *Organometallics*, **16**, 4214 (1997).
26. J. Marçalo, A. Pires de Matos and W.J. Evans *Organometallics* **16**, 3845 (1997).
27. W. C. Martin, R.Zalubas, L. Hagan, NBS (NIST), Washington, DC, (1978).
28. J.K. Gibson, *Int. J. Mass Spectrom.* **214**, 1 (2002).
29. J.J. Katz, L.R. Morss, G.T. Seaborg, 2nd Edition, Chapman & Hall, London, 1121, (1986).
30. F.A. Cotton, G. Wilkinson, 5th Edition, Wiley, New York, 955 (1988).
31. M.V. Nevitt, M.B. Brodsky, in: J.J. Katz, G.T. Seaborg, L.R. Morss (Eds.), 2nd Edition, Chapman & Hall, London, 1388 (1986).
32. P. Armentrout, R. Hodges, J.L. Beauchamp *J. Am. Chem. Soc.*, **99**, 3162 (1977).
33. P.B. Armentrout, R.V. Hodges and J.L. Beauchamp *J. Chem. Phys.*, **66**, 4683 (1977).
34. Z. Liang, A.G. Marshall, A. Pires de Matos, J.C. Spirlet, in: L.R. Morss, J. Fuger (Eds.) Washington, DC, 247 (1992).
35. C. Heinemann, H.H. Cornehl, H. Schwarz, *J. Organometall. Chem.*, **501**, 201 (1995).
36. J. Marçalo, J.P. Leal, A. Pires de Matos, *Int. J. Mass Spectrom. Ion Processes*, **157/158**, 265 (1996).
37. J. Marçalo, J.P. Leal, A. Pires de Matos and A.G. Marshall, *Organometallics*, **16**, 4581 (1997).
38. J. K. Gibson *J. Am. Chem. Soc.*, **120**, 2633 (1998).
39. J. K. Gibson *J. Mass Spectrom.*, **34**, 1166 (1999).
40. J. K. Gibson, R.G. Haire, *Reson. Ion. Spectr. 2000*, **584**, 79 (2001).
41. J. K. Gibson, J. Marçalo, *Coord.Chem.Rev.*, **250**, 776 (2006).
42. J.K. Gibson, R.G. Haire, *Inorg. Chem.*, **41**, 5897 (2002).

43. J. K. Gibson, *Int. J. Mass Spectrom.,* **216**, 185 (2002).
44. G. P. Jackson, F. L. King, D. E. Goeringer, D. C.Duckworth, *J. Phys. Chem. A*, **106**, 7788 (2002).
45. G. P. Jackson, J. K. Gibson, D. C. Duckworth, *Int. J. Mass Spectrom.*, **220**, 419 (2002).
46. G. P. Jackson, J. K. Gibson, D. C. Duckworth, *J. Phys. Chem. A*, **108**, 1042 (2004).
47. M Santos, J.Marçalo, A. Pires de Matos, J. K. Gibson, R. G. Haire, *J. Phys. Chem. A*, **106**, 7190 (2002).
48. M.Santos, J.Marçalo, J. P. Leal, A. Pires de Matos, J. K. Gibson, R. G. Haire, *Int. J. Mass Spectrom.*, **228**, 457 (2003).
49. J. K. Gibson, R. G. Haire, M.Santos, J.Marçalo, A. Pires de Matos, *J. Phys. Chem. A*, **109**, 2768 (2005).
50. J. K. Gibson, R. G.Haire, J.Marçalo, M.Santos, A.Pires de Matos, J. P. Leal, *J. Nucl. Mater*, **344**, 24 (2005).
51. M. Santos, A.Pires de Matos, J. Marçalo, J. K.Gibson, R. G.Haire, R.Tyagi, R. M. Pitzer, *J. Phys. Chem. A*, **110**, 5751 (2006).
52. J. K. Gibson, R. G. Haire, J. Marçalo, M. Santos, A. Pires de Matos, M. K.Mrozik, R. M. Pitzer, B.E. Bursten, *Organometallics*, **26**, 3947 (2007).
53. J. Marçalo, J. K. Gibson, *J. Phys. Chem. A*, **113**, 12599 (2009).
54. J. Blaise, J.-F. Wyart, International Tables of Selected Constants, Energy Levels and Atomic Spectra of Actinides, Vol. 20, Tables of Constants and Numerical Data (Tables de Constantes et Données Numériques), Paris, (1992).
55. L. Brewer *J. Opt. Soc. Am.*, **61**, 1666 (1971).
56. E. Di Santo, M. C. Michelini, N. Russo, *Organometallics*, **28**, 3716 (2009).
57. E. Di Santo, M. C. Michelini, N. Russo, *J. Phys. Chem. A*, **113**, 14699 (2009).
58. E. Di Santo, M. Santos, M. C. Michelini, J. Marcalo, J. K. Gibson, N. Russo (2010), *submitted.*
59. M. C. Michelini, N. Russo, E. Sicilia, *Angew. Chem., Int. Ed*, **45**, 1095 (2006).
60. M. E. Alikhani, M. C. Michelini, N. Russo, B. Silvi, *J. Phys. Chem. A,* **112**, 12966 (2008).
61. G. Mazzone, M. C. Michelini, N. Russo, E. Sicilia, *Inorg. Chem.*, **47**, 2083 (2008).
62. J. Zhou, H. Bernhard Schlegel; *J. Phys. Chem. A*, **114**, 8613 (2010).
63. K. J. De Almeida, H. A. Duarte, *Organometallics*, **28**, 3203 (2009).
64. K. J. De Almeida, H. A. Duarte, *Organometallics*, **29**, 3735 (2010).

2

Approccio teorico

Introduzione

La chimica teorica è il campo in cui i metodi matematici sono combinati con le leggi fondamentali della fisica per studiare i problemi chimici. Il principale “ingrediente” della chimica teorica è la meccanica quantistica che descrive il comportamento della materia a livelli microscopici per i quali le leggi della meccanica classica non sono valide.

In meccanica quantistica, l’equazione generale è quella di Schrödinger dipendente dal tempo, dalla cui risoluzione è possibile, in linea di principio, ottenere tutte le proprietà del sistema, fra cui l’energia. Per la chimica dello stato fondamentale è sufficiente l’utilizzo della forma indipendente dal tempo dell’equazione di Schrödinger. Purtroppo l’equazione di Schrödinger è risolvibile in maniera esatta per l’atomo di idrogeno e per pochi altri sistemi a pochissimi corpi. Per trattare i sistemi multielettronici di interesse chimico è necessaria l’introduzione di alcune approssimazioni.

2.1 Metodi quantomeccanici

La prima approssimazione utilizzata e quella di *Born-Oppenheimer,*[1-2] per la quale, considerata la differenza in peso e velocità tra nuclei ed elettroni, è possibile disaccoppiare il moto dei nuclei da quello degli elettroni e considerare i nuclei fissi. Suddividendo il sistema molecolare in due sottosistemi (elettronico e nucleare), l’espressione dell’equazione di Schrödinger viene semplificata, in quanto è possibile trascurare l’energia cinetica dei nuclei e mantenere costante l’interazione nucleo-nucleo.

La ricerca di metodi teorici atti a fornire delle soluzioni approssimate dell’equazione di Schrödinger senza ricorrere a semplificazioni come nei metodi semiempirici, nei quali si introducono parametri ottenuti sperimentalmente, ha condotto alla messa a punto dei metodi Hartree-Fock (HF), post-HF e la teoria del funzionale della densità (DFT, *Density Functional Theory*). La teoria HF non tenendo in considerazione l’energia di correlazione da risultati quantitativi non del tutto affidabile. D’altra parte, i metodi post-HF garantiscono alti livelli di accuratezza ma il costo computazionale richiesto tende ad aumentare considerevolmente con l’aumento delle dimensioni dei sistemi, rendendoli utili per la trattazione solo di sistemi semplici. Per sistemi più complessi, la necessità di coniugare accuratezza dei risultati e costi computazionali contenuti si traduce nell'utilizzo della teoria del funzionale della densità.

2.2 La teoria del funzionale della densità

La teoria del funzionale della densità ha trovato un suo solido fondamento teorico nell'enunciazione dei due teoremi di *Hohenberg e Kohn.* Hohenberg e Kohn dimostrarono che la densità elettronica dello stato fondamentale non degenere di un sistema di elettroni permette di determinare univocamente tutte le proprietà dello stato fondamentale.[3] Quindi ogni grandezza fisica osservabile dello stato fondamentale, come ad esempio l'energia totale, può essere espressa come un funzionale della densità, $E[\rho]$. L'energia $E[\rho]$ è infatti un funzionale della densità elettronica $\rho(\mathbf{r})$, la quale è a sua volta una funzione delle coordinate spaziali (x, y, z). Inoltre per il funzionale $E[\rho]$ vale un principio di minimizzazione che si deduce direttamente dal principio di minima energia valido per il valore di aspettazione dell'hamiltoniano del sistema.

Il funzionale energia elettronica $E[\rho]$ viene generalmente suddiviso in diversi contributi che tengono conto separatamente dell'energia cinetica elettronica $T[\rho]$, dell'energia potenziale di interazione elettrone-elettrone $V_{ee}[\rho]$ e dell'energia potenziale di interazione elettrone-nucleo $V_{Ne}[\rho]$. I primi due contributi sono indipendenti dalle posizioni nucleari e possono quindi essere raggruppati insieme nel *funzionale universale* della densità $F[\rho]$:

$$E[\rho] = F[\rho] + V_{Ne}[\rho] \qquad 2.1$$

La determinazione esatta del funzionale $F[\rho]$ non è ad oggi possibile.

Riconosciuta la limitazione di questa equazione Kohn e Sham introdussero un set di orbitali (analogo agli orbitali di HF) utilizzando i quali l'energia cinetica può essere divisa in due parti, l'energia cinetica (T_S) di un sistema di N elettroni non-interagenti (con la stessa densità del sistema reale interagente) e una parte residua T_C (che è la parte mancante alla descrizione accurata del sistema reale interagente).[4] Anche l'energia di repulsione elettrone-elettrone $V_{ee}[\rho]$, può essere separata in due differenti contributi, l'interazione classica di Coulomb (J) ed una parte non-classica contenente lo scambio e la correlazione (E_{XC}). Viene così introdotto nell'equazione dell'energia totale del sistema il cosiddetto funzionale di scambio e correlazione $E_{XC}[\rho]$, dove viene incluso il contributo della parte residuale dell'energia cinetica ed i termini di scambio e correlazione:

$$E[\rho] = T_S[\rho] + J[\rho] + V_{Ne}[\rho] + E_{XC}[\rho] \qquad 2.2$$

I primi tre termini possono essere calcolati esplicitamente. Il termine di scambio e correlazione $E_{XC}[\rho]$ raggruppa tutti i contributi all'energia totale non conosciuti.

2.2.1 Approssimazioni per il Funzionale di Scambio e Correlazione

Un approccio per calcolare l'energia di scambio e correlazione è basato sull'assunzione che la densità varia solo localmente e lentamente e può, quindi, essere trattata come un gas elettronico omogeneo.[4] L'energia di scambio di un gas di elettroni con densità uniforme può essere calcolata esattamente, ed è su questa evidenza che fonda le sue basi l'Approssimazione della Densità di Spin Locale (LSDA, *Local Spin Density Approximation*). Sono stati sviluppati differenti funzionali per calcolare l'energia di correlazione di un gas di elettroni uniforme. Uno dei più popolari è certamente il funzionale di correlazione Vosko-Wilk-Nusair (VWN).[5]

Mentre l'assunzione della distribuzione omogenea di elettroni è adatta per alcuni sistemi, per molti sistemi di interesse chimico non è di particolare utilità poiché la distribuzione elettronica non è uniforme.

Un importante miglioramento in tal senso si è avuto con l'introduzione di un gradiente della densità elettronica. Nasce così l'approssimazione del Gradiente Generalizzato (GGA, *Generalized Gradient Approximation*), la quale non tiene soltanto conto della densità in un dato punto, ma anche della sua derivata. Kohn e Sham[4] proposero di considerare l'approssimazione *LDA* come il primo termine di una espansione in serie di Taylor per $E_{xc}[\rho]$ (intorno al valore ottenibile per una densità uniforme) e di aggiungere ad essa gli altri termini della serie. Questa nuova approssimazione, chiamata dell'espansione del gradiente (GEA, *Gradient Expansion Approximation*) non è di apprezzabile uso pratico ma fu fondamentale per dare l'input alla costruzione di numerosi tipi di funzionali per lo scambio e la correlazione tra cui il funzionale di Perdew e Wang PW86[6] utile per garantire la condizione di normalizzazione della funzione di scambio. Becke ha introdotto un funzionale corretto per il gradiente per l'energia di scambio denominato B88.[7] Tale funzionale contiene un parametro semi-empirico, che è stato fittato sullo scambio di Hartree-Fock dei sei atomi di gas nobili. Un popolare funzionale di correlazione corretto per il gradiente è stato sviluppato da Lee, Yang e Parr, dalle iniziali dei quali è stato coniato il nome di LYP.[8] La combinazione dei due funzionali dà vita ad un funzionale ampiamente utilizzato come il BLYP. Successivamente Becke sostenne che poteva essere realizzato un ulteriore sviluppo nello schema GGA se fosse stata inclusa nel funzionale una certa quantità dello scambio di Hartree-Fock esatto,[9] portando così alla definizione di funzionali ibridi, tra i quali il più popolare è certamente il B3LYP.

Il B3LYP è un funzionale ibrido che contiene i funzionali di scambio e correlazione B88, LYP e VWN,[5,8,9] insieme con il 20% dello scambio HF esatto:

$$E_{XC}^{B3LYP} = (1-a)E_X^{LSDA} + aE_X^{HF} + bE_X^{B88} + cE_c^{LYP} + (1-c)E_C^{VWN} \qquad 2.3$$

I coefficienti a=0.20, b=0.72 e c=0.81 sono stati presi dal funzionale ibrido B3PW91.[2,9] I loro valori sono stati ottimizzati per B3PW91 attraverso un fit lineare dei minimi quadrati per 116 energie determinate sperimentalmente (56 energie di atomizzazione, 42 potenziali di ionizzazione, 8 affinità protoniche e 10 energie atomiche totali).

Il suo successo è dovuto all'accuratezza dei risultati che fornisce in svariate applicazioni chimiche, anche nel caso di sistemi complessi da trattare quali ad esempio composti contenenti metalli pesanti.

In questo lavoro di tesi, il funzionale B3LYP è stato utilizzato in tutte le reazioni studiate (capitolo 3).

Il funzionale PW91, è invece un funzionale di scambio e correlazione GEA non ibrido, proposto da Perdew e Wang nel 1991.[10] E' stato costruito introducendo un taglio nello spazio a lungo raggio dell'espansione del gradiente di densità.

$$F_X(x) = \frac{bx^2 - (b-\beta)x^2 \exp\left[-cx^2\right] - 10^{-6}x^d}{1 + b\sinh^{-1}(x) - \dfrac{10^{-6}x^d}{A_x}} \qquad 2.4$$

$$b = 0.0042 \qquad \beta = 5(36\pi)^{-5/3}$$

$$c = 1.6455 \qquad A_x = -\frac{3}{2}\left(\frac{3}{4\pi}\right)^{1/3}$$

$$d = 4.00$$

Questo funzionale è stato utilizzato in alcune reazioni studiate (Capitolo 3: publicazione I e II).

2.3 Set di funzioni di base

In linea di principio il set di funzioni di base con cui descrivere gli orbitali è completamente arbitrario, purché sia finito. Il criterio variazionale stabilisce solo che più esso è grande, maggiore è la flessibilità variazionale e migliori sono i risultati. Poiché per tempi computazionali limitati il set di funzioni di base deve essere piuttosto piccolo, è, quindi, importante che le funzioni abbiano un senso fisico.

La formazione di legami chimici può essere interpretata come una alterazione delle distribuzioni elettroniche presenti negli atomi isolati. Pertanto, le nuove distribuzioni possono essere rappresentate come combinazioni lineari di orbitali atomici (LCAO, *Linear Combination of Atomic Orbitals*), in modo che le funzioni di base rappresentino abbastanza fedelmente orbitali atomici. L'utilizzo di orbitali atomici garantisce la "portabilità" delle funzioni, in quanto si può costruire un insieme di base per qualsiasi molecola usando una quantità limitata di set di base noti e classificati, corrispondenti all'identità degli atomi costituenti.

La minimizzazione del numero di funzioni di base (a parità di qualità dei risultati) non può essere l'unico criterio guida, bisogna considerare la semplicità e la velocità di calcolo. In base, soprattutto, a quest'ultima considerazione il set di base che spesso si sceglie di utilizzare è un set di funzioni gaussiane (GTO, *Gaussian Type Orbital*).

In realtà, le funzioni gaussiane non sono le funzioni ottimali per rappresentare gli orbitali atomici che risulterebbero da calcoli HF esatti, in quanto la dipendenza esponenziale è quadratica, per cui tali funzioni decrescono più rapidamente con l'aumentare della distanza. Le funzioni STO (*Slater Type Orbitals)*, riproducono in modo migliore la dipendenza esponenziale dalla distanza dai nuclei, simile a quello di semplici esponenziali idrogenoidi. Sono, inoltre, funzioni che con l'aumentare del numero di funzioni assicurano una convergenza rapida. Uno dei motivi per cui la maggior parte dei codici di calcolo utilizzano funzioni gaussiane è che queste funzioni possono essere integrate analiticamente, mentre le funzioni di tipo Slater devono essere integrate numericamente.

Per ridurre il numero di funzioni di base senza abbassare la qualità nella descrizione di quelle funzioni atomiche meno modificate dalla formazione dei legami chimici (orbitali atomici di core) ciascuna funzione è definita da una combinazione lineare di gaussiane. Le gaussiane importanti per la descrizione di orbitali interni, vicini ai nuclei, contribuiscono alla descrizione di orbitali di valenza e viceversa. Inoltre, poiché i coefficienti di combinazione degli orbitali del sistema molecolare non sono molto differenti da quelli dell'atomo isolato, i coefficienti vengono normalmente determinati da calcoli sugli atomi isolati.

I parametri che caratterizzano le funzioni di base, nonché il loro ottimale numero complessivo (nel senso di un compromesso fra praticabilità computazionale e qualità dei risultati), dipendono ovviamente in linea di principio dal particolare sistema fisico e potrebbero essere trattati come ulteriori parametri variazionali insieme ai coefficienti di combinazione; per ragioni di praticità si preferisce, però, determinare il set di base a priori secondo criteri consolidati.

2.4 Effetti Relativistici

Come accennato nel primo capitolo gli effetti relativistici giocano un ruolo importante nello studio degli elementi pesanti.

L'analogo relativistico dell'equazione di Schrödinger non relativistica è l'equazione di Dirac a quattro componenti.

$$H^{D}\psi = E\psi \qquad 2.5$$

dove H^D è l'hamiltoniano di Dirac per un atomo multi elettronico. Nella teoria non relativistica ogni orbitale molecolare è descritto come una funzione scalare associata ad spin up o down. Nella teoria molecolare relativistica gli orbitali sono rappresentati da quattro componenti spinori, le quali comprendono componenti elettroniche grandi (ϕ) e positroniche piccole (χ) ognuna con spin up e down:

$$\psi = \begin{pmatrix} \phi \\ \chi \end{pmatrix} \qquad 2.6$$

L'equazione di Dirac a quattro componenti può essere trasformata in una rappresentazione in cui le componente larghe e piccole sono disaccoppiate.

Le prime teorie basate sulla trasformazione sviluppata da Foldy e Wouthuysen[11] per l'eliminazione della componente piccole, hanno portato alla formulazione di operatori contenenti termini singolari, come l'operatore di Breit-Pauli, i quali rendono il loro utilizzo dubbioso, almeno nelle approssimazioni variazionali.

Nelle ultime decadi si sono sviluppate diverse trasformazioni regolari, fra cui la trasformazione di Douglas-Kroll[12] e la trasformazione ZORA[13] (*Zero order regular approximation*), che hanno reso possibile l'utilizzo delle approssimazioni a due componenti in calcoli di struttura elettronica molecolare.

La funzione d'onda può essere ulteriormente semplificata separando l'Hamiltoniano in una parte dipendente dallo spin e una parte indipendente dallo spin, e risolvendo la parte indipendente dallo spin prima di includere l'accoppiamento Spin-Orbita. Questo conduce ai metodi relativistici denominati *scalari* o solamente ad *un componente.*

In questo lavoro di tesi le correzioni relativistiche sono state introdotte a livello scalare, in due differenti modi. In un primo approccio, utilizzando l'approssimazione scalare ZORA, implementata nel codice di calcolo ADF (*Amsterdam Density Functional*);[14] in un secondo approccio, mediante l'utilizzo di pseudopotenziali di core relativistici, utilizzando il programma Gaussian03.[15]

2.4.1 Approssimazione regolare di ordine zero, ZORA

L'equazione ZORA ha una struttura simile a quella non relativistica, in cui l'hamiltoniano è il seguente

$$H_{ZORA} = \vec{\sigma} \cdot \vec{p} \, \frac{c^2}{2mc^2 - V} \, \vec{\sigma} \cdot \vec{p} + V$$

$$= \sum_i p_i \frac{c^2}{2mc^2 - V} p_i + \frac{mc^2}{\left(2mc^2 - V\right)} \vec{\sigma} \cdot \left(\nabla V \times \vec{p}\right) + V \qquad 2.7$$

dove $\vec{\sigma}$ = (σ_x, σ_y, σ_z) è il vettore formato dalle matrici di Pauli, $\vec{p}$ = -ih∇ è l'operatore momento, c la velocità della luce, ed m la massa dell'elettrone. Si noti che l'hamiltoniano può essere scritto come la somma di termini che hanno la simmetria usuale della molecola e un termine spin-orbita.

Gli elementi di matrice relativi alla parte di spin orbita possono essere separati in una parte spaziale (dipendente dal potenziale) e una di spin. Quando il termine spin-orbita è trascurato si parla di approssimazione scalare.

Come detto nella sezione precedente, si è utilizzato l’approssimazione ZORA implementata nel programma ADF. Il codice di calcolo ADF è basato su un’integrazione numerica[16-18], le cui funzioni di base sono di tipo Slater, e gli orbitali molecolari sono espressi come combinazione lineare di frammenti, i quali possono essere costituiti da singoli atomi o più atomi.

Nel codice ADF è possibile usare l’approccio “frozen core”: cioè, escludere dal calcolo variazionale gli elettroni che popolano il guscio più interno e utilizzare solo gli orbitali molecolari degli elettroni di valenza. Al fine di garantire l’ortogonalità tra gli orbitali “frozen core” $\{\varphi_i^C\}$ e le funzioni di base di valenza $\{\chi_\nu^V\}$ il set di base delle funzioni di valenza è scelto esplicitamente ortogonale a quello “frozen core”.

2.4.2 Potenziali effettivi di core relativistici

Nei sistemi di grandi dimensioni, contenenti metalli, è possibile applicare un’ulteriore approssimazione agli LCAO, tramite l’utilizzo di *pseudopotenziali o potenziali effettivi di core* (ECP, *Effective Core Potentials*). L’introduzione di uno pseudopotenziale ha principalmente lo scopo di abbassare sensibilmente il costo computazionale, in quanto corrisponde alla diminuzione del numero di elettroni che le funzioni LCAO devono rappresentare. Tale metodologia di calcolo è supportata da una delle assunzioni principali in chimica, la quale stabilisce che gli elettroni dei livelli energetici più interni siano relativamente inerti e non perturbati dall’intorno molecolare, in quanto molte delle proprietà chimiche più importanti degli atomi e delle molecole sono determinate dalle interazioni dei loro elettroni di valenza con gli elettroni di valenza di altri atomi o molecole. L’utilizzo di potenziali di core effettivi o pseudopotenziali in principio non influenza la qualità della riproduzione delle proprietà molecolari, a condizione che siano sufficientemente piccoli, ma permette, come detto, di ridurre i tempi e le risorse di calcolo.

Nel caso specifico in cui i sistemi da trattare coinvolgano metalli pesanti, per i quali è necessario tenere conto dell’influenza degli effetti relativistici, si introducono i cosiddetti *potenziali effettivi di core relativistici* (RECP, *Relativistic Effective Core Potentials*). Le correzioni relativistiche tendono ovviamente ad essere più significative nella regione che immediatamente circonda il nucleo poiché l’energia cinetica di questi elettroni è maggiore. Pertanto, è ragionevole assumere che gli elettroni più interni risentano in misura maggiore degli effetti della relatività rispetto a quelli più esterni che hanno una probabilità molto più bassa di trovarsi vicino al nucleo. Le interazioni degli elettroni di valenza con i nuclei e con gli altri elettroni dovrebbero essere sufficientemente ben descritte da un hamiltoniano non-relativistico. Anche se gli elettroni di valenza non risentono di effetti relativistici diretti significativi, i cambiamenti degli elettroni di core hanno conseguenze dirette sullo schermo nucleare e sull'ortogonalità. Poiché il comportamento degli elettroni di core non cambia in maniera significativa nel passaggio dall'ambiente atomico a quello molecolare, un metodo basato sull'utilizzo degli *ECP* che incorpora gli effetti relativistici risentiti dagli elettroni di core è di grande utilità pratica.

Diversi studi teorici hanno dimostrato che per sistemi contenti attinidi, i potenziali effettivi di core relativistici che rappresentano i 60 elettroni di core (SC-RECP *small core relativistic effective core potential*) costituiscono un buon bilancio fra le correzioni relativistiche, introdotte con gli RECP, ed il trattamento esplicito degli elettroni di valenza. In contrasto RECP rappresentanti i 78 elettroni di core (LC-RECP, *large core relativistic effective core potential*), danno di solito risultati meno soddisfacenti.[19-20]

Sulla base di questi risultati la scelta dello pseudopotenziale che meglio rappresentasse il comportamento dei 60 elettroni di core del Th e U è ricaduta sul potenziale effettivo di core relativistico di tipo Stuttgart/Dresden (SDD).[21] Questo RECP sostituisce i 60 elettroni di core corrispondente ai gusci 1-4, lasciando il trattamento esplicito dei gusci con n = 5 (5s, 5p, 5d, e 5f), oltre ai 6s, 6p, 6d e 7s.

Questo RECP è stato utilizzato in tutte le reazioni analizzate in questo lavoro di tesi (capitolo 3).

2.5 Analisi teorica dei meccanismi di reazione

La conoscenza dei meccanismi secondo i quali avviene una reazione chimica è, da sempre, di notevole interesse scientifico e rappresenta un traguardo importante sia per la chimica teorica che per quella sperimentale.

Lo studio di una reazione chimica può avvenire attraverso la costruzione di una superficie di energia che includa tutti i punti stazionari previsti per il dato cammino di reazione. In accordo con quanto proposto da *Eyring* e *Polanyi*[22] si può immaginare che in una semplice trasformazione *one-step* dal reagente al prodotto si passi da una struttura di minimo energetico (reagente) ad un'altra (prodotto) attraverso una struttura di massimo energetico che prende il nome di *stato di transizione.* Lo stato di transizione per il ruolo che svolge, cioè di struttura ad elevato contenuto energetico e di transizione tra quella di un minimo e quella del minimo successivo, è stato definito come il massimo lungo la curva a minima energia che connette reagenti e prodotti. Una simile trasformazione corrisponde sicuramente ad una variazione di energia che, poiché dipendente da un certo numero di variabili, dovrebbe essere rappresentata in uno spazio multidimensionale. Molti studi fatti in questa direzione hanno dimostrato come la reazione possa essere seguita tramite un'unica grandezza (comunque difficile da determinare) chiamata *coordinata di reazione*. Con questa approssimazione si può costruire un profilo di energia potenziale in funzione della coordinata di reazione prescelta (Figura 2.6).

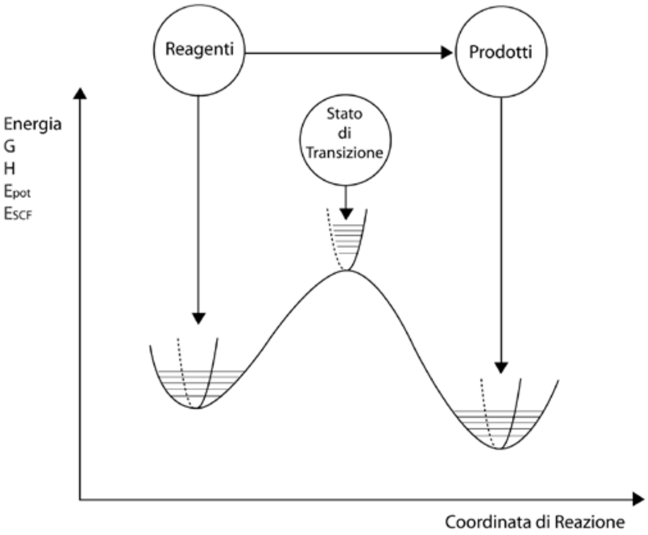

Figura 2.6: Variazione dell'energia in funzione della coordinata di reazione.

La trattazione teorica dei cammini di reazione richiede una conoscenza dettagliata dell'energia potenziale di un sistema molecolare in funzione di tutti gradi di libertà, in quanto per studiare le geometrie di equilibrio di ciascun minimo si fa uso dell'approssimazione di *Born-Oppenheimer;*[1] in questo modo la superficie di energia potenziale è indipendente dalla massa dei nuclei. Conoscere l'energia potenziale di un sistema costituito da *N* atomi non è una cosa banale. L'ipersuperficie di energia potenziale che rappresenta la variazione dell'energia dell'intero sistema dipende da troppi parametri per poter essere facilmente riportata in un grafico; inoltre, la funzione dell’energia molecolare analitica non è nota e deve essere costruita punto per punto.

Proprio questa ultima evidenza ne rende impossibile la rappresentazione della superficie nella sua totalità. Se ad esempio si vuole analizzare un sistema semplice costituito da 9 atomi, e quindi dotato di 21 gradi di libertà, considerando una griglia di 6 punti per ogni grado interno si dovrebbero realizzare 6^{21} calcoli, ovvero
$10.^{16}$ Supponendo idealmente che l’energia di ogni punto possa essere ottenuta in 1 secondo, l’intero calcolo richiederebbe 10^{16} secondi, ovvero circa 10^{9} anni.
Immaginando di iniziare un calcolo di questo tipo nell’era dei dinosauri, oggi non sarebbe ancora terminato. Questo paradosso è noto appunto come ‘paradosso del dinosauro’. Ciò implica ovviamente la necessità di ricercare un altro iter risolutivo.
Il superamento di tale problematica è possibile passando da una superficie multidimensionale ad un grafico in due dimensioni.

2.5.1 Metodi per la ricerca dei minimi e degli stati di transizione

Poiché la costruzione delle ipersuperfici di energia potenziale punto per punto non è possibile, lo studio della funzione di energia potenziale dei nuclei consiste nella caratterizzazione dei punti stazionari, ovvero minimi, massimi e punti di sella, attraverso le loro derivate prime e seconde. Per una funzione a più variabili, le derivate prime rispetto a ciascuna di esse generano un vettore detto *gradiente*, mentre le derivate seconde rappresentano gli elementi che costituiscono la matrice detta *Hessiano*.
Un punto stazionario, per una funzione ad una sola variabile, è il punto nel quale la derivata è nulla, mentre per una funzione in due o più dimensioni esso è il punto in cui si annulla la derivata prima rispetto a tutte le variabili. La natura dei punti stazionari può essere stabilita dal segno della derivata seconda, positiva per un minimo e negativa per un massimo, per sistemi monodimensionali e dagli autovalori della matrice dell’*Hessiano* per sistemi multidimensionali. Se gli autovalori sono tutti positivi il punto stazionario è un minimo locale, se sono tutti negativi si tratta di un massimo locale, se vi è un solo autovalore negativo il punto stazionario è un *punto di sella di ordine uno*, ossia un massimo in una direzione ed un minimo in tutte le altre direzioni ad essa perpendicolari e corrisponde ad uno stato di transizione.
Per la minimizzazione non vincolata di una funzione non lineare e per la ricerca degli stati di transizione di più variabili sono stati messi a punto un grande numero di metodi.

Fra le caratteristiche che un algoritmo di minimizzazione dovrebbe possedere ritroviamo, sicuramente: la velocità di convergenza verso il minimo, la stabilità ed il costo computazionale soprattutto in termini di calcolo.

2.5.2 Meccanismi di reazione che coinvolgono più di uno stato di spin

Qualche anno fa, Schröder, Shaik e Schwarz hanno introdotto un concetto fondamentale nell'interpretazione della reattività chimica e dei meccanismi di reazione che prevedono il coinvolgimento di metalli, formulando il paradigma della "Two State Reativity" (TSR).[23]

Fino ad allora, l'interpretazione dei profili energetici relativi ai meccanismi di reazione era fondata sul concetto di conservazione dello spin, secondo il quale gli stadi cineticamente determinanti erano collocati su superficie di energia potenziale caratterizzate da una molteplicità di spin uniforme. Si fa riferimento a questi processi come ai meccanismi che evolvono in termini di Single-State Reactivity (SRR).

In un processo chimico costituito da una sequenza di processi, lo stadio cineticamente determinante (RDS, *Rate Determining Step*) corrisponde alla reazione elementare più lenta. Tale *step* impone un limite superiore alla velocità massima dell'intero evento reattivo.

E' stato rilevato che nei sistemi organometallici[24,25] spesso la reazione può evolvere in più di uno stato elettronico, per cui più di una superficie di spin può connettere reagenti e prodotti. Il fenomeno di due stati di differente molteplicità che determinano il percorso a minore energia di una reazione è classificato come *Two-State Reactivity*. La *TSR* è infatti in grado di stabilire i cammini a minore energia per sistemi la cui evoluzione sarebbe altrimenti difficile da comprendere e l'inversione di spin può agire come collo di bottiglia nel determinare la velocità di reazione e le percentuali di formazione dei prodotti.

Per comprendere l'operatività del paradigma *TSR* è necessario individuare i meccanismi attraverso i quali l'eccitazione elettronica può modificare la chimica di una data specie.

Infatti, una reazione che sia, per esempio, endotermica per lo stato fondamentale dei reagenti, può divenire esotermica, e quindi rilevabile sperimentalmente, se considerata a partire dallo stato eccitato dei reagenti.

Il caso della *TSR* per un certo numero di reagenti e prodotti necessita di alcuni particolari requisiti. Il primo prerequisito è uno stato fondamentale ad alto spin dei reagenti ed uno stato eccitato a basso spin separati ragionevolmente da un piccolo intervallo di energia. Questa è una situazione riscontrata in alcuni composti organometallici coordinativamente insaturi ed in molte specie inorganiche. Per esempio, alcuni cationi dei metalli di transizione nudi hanno stati fondamentali ad alto spin ad energia non molto più bassa di stati a basso spin. Il secondo requisito è che la struttura dello stato di transizione che determina la velocità della reazione presenti una molteplicità di spin diversa da quella dei reagenti nello stato fondamentale. Infine, a determinare la distribuzione dei prodotti deve essere l’azione reciproca delle due superfici di spin.

Se i meccanismi e le entalpie di reazione per lo stato fondamentale e per lo stato eccitato sono simili su entrambe le superfici, la superficie per lo stato eccitato si mantiene sempre al di sopra di quella corrispondente allo stato fondamentale (postulato di Hammond)[26,27] dei reagenti lungo tutto il cammino di reazione, come in figura 2.7 (a).

Se i meccanismi sono simili, ma l’entalpia di reazione per lo stato eccitato è più grande di quella relativa ai reagenti nello stato fondamentale è probabile che si verifichi un incrocio sulle superfici dopo il superamento della barriera relativa allo stato di transizione,come in figura 2.7 (b).

Entrambe queste situazioni (a e b) possono essere descritte in termini di *SSR*, perché l’inversione di spin nel secondo dei due casi può essere compensata dal fattore pre-esponenziale in una descrizione del tipo *Arrhenius*.

Quando i due meccanismi suddetti differiscono, essendo la superficie relativa allo stato eccitato molto più piatta dalla parte dei reagenti, un incrocio tra le superfici dovrebbe verificarsi prima del superamento della barriera di energia associata allo stato di transizione. Questa rappresenta una tipica situazione per una descrizione del cammino di reazione in termini di *TSR*, come in figura 2.7 (c).

Esiste un quarto caso nel quale lo stato fondamentale di reagenti e prodotti coincide, ma è, in questo caso, lo stato di transizione che li separa ad essere più stabile in uno stato eccitato, come in figura 2.7 (d).

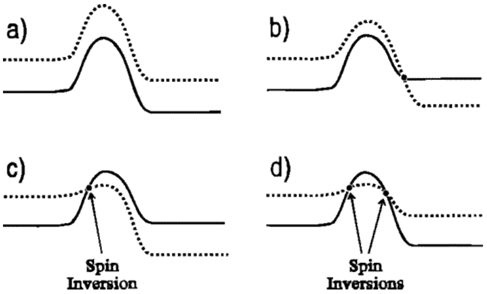

Fig 2.7 Possibili cammini di reazione a più bassa energia: il grafico in linea continua è la PES relativa allo stato fondamentale del sistema, mentre il profilo tratteggiato corrisponde al primo stato eccitato.

Un altro parametro rilevante nella valutazione delle reattività di tipo SSR e TSR è l'intersezione tra le due superfici mediante l'accoppiamento spin-orbita.[28,29]

2.6 Analisi dei legami

Con l'obiettivo di ottenere una visione più approfondita dei meccanismi di attivazione dei legami C-H e C-C da parte di cationi degli attinidi, ed in particolare di capire il ruolo svolto dagli elettroni 5f e 6d nel processo catalitico, si è proceduto ad analizzare le caratteristiche di legami di diverse specie, intermedi e stati di transizione, coinvolti in alcune reazioni studiate. Con questo obiettivo si sono utilizzati sia metodologie più tradizionali, basate sull'analisi della funzione d'onda nello spazio orbitalico, quale il metodo NBO (Natural Bond Orbital), che metodologie meno tradizionali, basate sull'analisi topologica dei legami chimici.

2.6.1 Teoria topologica del legame chimico

I concetti di legame e di coppia elettronica, che sono spesso utilizzati in chimica, non corrispondono ad alcuna osservabile di cui si può determinare il valore di aspettazione nel senso della meccanica quantistica. Appartengono invece ad una conoscenza per così dire "intuitiva" della materia definita dai chimici sulla base dell'esperienza e sono diventati i punti basilari di un sistema esplicativo grazie alla validità della *teoria di Lewis*.[30] Il successo dell'idea di *Lewis* è principalmente dovuto alla sua efficienza ed alla sua semplice formulazione in termini di concetti puramente chimici, anche se tale teoria non è stata rispettata dagli approcci VB *(teoria del legame* *di valenza)* di *Slater* e *Pauling*[31] e MO *(teoria degli orbitali molecolari)* di *Mulliken* e Hund.[32]

Il modello VSEPR di *Gillespie*,[33] nato successivamente è invece lo sviluppo naturale della teoria di *Lewis* verso la comprensione della geometria molecolare.

La funzione d'onda fornisce una descrizione accurata della struttura elettronica di un qualsivoglia sistema molecolare, ma è ben lungi dal fornire un'interpretazione fisica semplice ed immediata.

La possibilità di tradurre in un linguaggio chimico comprensibile le informazioni che pur sono contenute nella funzione d'onda, è ricondotta all'interpretazione che si attribuisce al quadrato della funzione d'onda come una misura della distribuzione di probabilità delle particelle nel sistema molecolare.

Lo scopo della teoria topologica del legame chimico è, infatti, quello di trovare un modello matematico dell'approccio di *Lewis*. Il primo passo in questa direzione è stato fatto da *Daudel* ed i suoi collaboratori,[34] i quali hanno tentato di definire propriamente le regioni chimicamente rilevanti delle molecole. Ma, è solo negli anni successivi, con l'avvento della teoria degli *Atomi nelle Molecole* di *Bader*[35] (AIM, *Atoms in Molecules*) che si è riusciti a compiere un significativo passo in avanti. In questa teoria, l'analisi del gradiente della densità elettronica fornisce una partizione dello spazio molecolare in *basin* di *attrattori* che rappresentano massimi locali della densità elettronica e sono generalmente localizzati in corrispondenza dei nuclei. I punti critici del gradiente della densità elettronica, ossia i punti in corrispondenza dei quali $\nabla\rho(r) = 0$, permettono di definire una rete di legami detta "grafo molecolare" e quindi, in ambito topologico, una struttura molecolare che generalmente è in accordo con quella che si può tracciare utilizzando il solo "intuito chimico". Questo tipo di approccio, tuttavia, non permette di studiare reazioni semplici come la rottura omolitica di una molecola biatomica, poiché la configurazione nucleare corrisponde ad una singola struttura molecolare e si è reso necessario ricorrere ad altre funzioni locali, che sono state chiamate "funzioni di localizzazione", allo scopo di caratterizzare legami e *lone pair* nelle molecole.

In questo lavoro di tesi è stato utilizzato anche un metodo di analisi del legame proposto da *Silvi* e *Savin*[36] che fa uso, fra le possibili funzioni di localizzazione, di una versione opportunamente modificata di quella proposta da *Becke e Edgecombe*.[37]

Tale funzione, denominata *ELF* (*Electron Localization Function*), possiede il merito di partizionare lo spazio molecolare in maniera coerente con la descrizione di *Lewis* del legame chimico e con la teoria *VSEPR*.

Per ricavare le informazioni sulla funzione di localizzazione elettronica è utile definire una probabilità condizionale mediata sfericamente. Per probabilità condizionale si intende che se un elettrone di spin σ è localizzato con certezza nella posizione *1*, definita posizione di riferimento, la probabilità "condizionale" di trovare un secondo elettrone con lo stesso spin in posizione *2* viene ottenuta dividendo la "*pair probability*" per la densità totale di spin σ nella posizione *1*:

$$P^{\sigma\sigma}_{cond}(1,2) = P^{\sigma\sigma}_{2}(1,2)/\rho_\sigma(1) = \rho_\sigma(2) - \frac{\left|\rho_1^\sigma(1,2)\right|^2}{\rho_\sigma(1)} \tag{2.8}$$

essendo la probabilità (*pair probability*) di trovare due elettroni con lo stesso spin σ simultaneamente nelle posizioni *1* e *2* in un sistema multielettronico definita, dalla teoria di *Hartree-Fock,* come

$$P_2^{\sigma\sigma}(1,2) = \rho_\sigma(1)\rho_\sigma(2) - \left|\rho_1^\sigma(1,2)\right|^2 \tag{2.9}$$

dove

$$\rho_1^\sigma(1,2) = \sum_i^\sigma \psi_i^*(1)\psi_i(2) \tag{2.10}$$

La probabilità condizionale mediata sfericamente può così essere espressa mediante un'espansione in serie di *Taylor*:

$$P^{\sigma\sigma}_{cond}(\mathbf{r},\mathrm{s}) = \frac{1}{3}\left|\tau_\sigma - \frac{1}{4}\frac{\left|\nabla\rho^\sigma(\mathbf{r})\right|^2}{\rho_\sigma}\right|\mathrm{s}^2 + \ldots \tag{2.11}$$

dove (**r**,s) indica la media su una shell di raggio s intorno al punto di riferimento **r e**

$$\tau_\sigma = \sum_i^\sigma \left|\nabla\varphi_i\right|^2 \tag{2.12}$$

è la densità di energia cinetica. Il coefficiente del termine quadratico dell'espansione rappresenta la cosiddetta densità di energia cinetica locale di *Pauli*, ossia l'eccesso di energia cinetica che gli elettroni possiedono, in base al principio di esclusione di *Pauli*, in quanto fermioni rispetto ad un sistema di bosoni con la medesima densità.

A questo punto, l'informazione sulla localizzazione elettronica può essere ricavata tenendo conto che più piccola è la probabilità di trovare un secondo elettrone con il medesimo spin vicino al punto di riferimento, più localizzato sarà l'elettrone di riferimento. Ciò significa che la localizzazione elettronica è legata direttamente al valore assunto dalla quantità:

$$D_\sigma = \tau_\sigma - \frac{1}{4}\frac{\left|\nabla \rho^\sigma(r)\right|^2}{\rho^\sigma} \qquad (2.13)$$

che essendo definita mediante una densità di probabilità, è necessariamente non negativa.

Poiché la relazione fra la funzione di localizzazione e l'equazione (2.13) è inversa, un'alta localizzabilità implica un valore di D_σ piccolo; inoltre, da quest'ultima relazione non vengono fissati i limiti di variabilità della funzione di localizzazione. *Becke* e *Edgecombe* hanno pertanto proposto l'introduzione di una funzione alternativa:

$$\eta(\mathbf{r}) = \left(1 + \chi_\sigma^2\right)^{-1} \qquad (2.14)$$

dove $\chi_\sigma = \frac{D_\sigma}{D_\sigma^0}$ e D_σ^0 corrisponde all'energia cinetica di un gas omogeneo di elettroni con densità di spin uguale $\rho_\sigma(r)$. Il rapporto χ_σ è indice di localizzazione adimensionale calibrato rispetto alla densità di un gas omogeneo scelto come riferimento. L'intervallo di valori possibili per la funzione *ELF* è quindi compreso fra *0* e *1*, con il limite superiore per $\eta(\mathbf{r}) = 1$ corrispondente ad un elettrone perfettamente localizzato.

Quando gli elettroni sono isolati o formano coppie con spin antiparalleli, il principio di *Pauli* ha poca influenza sul loro comportamento e l'energia cinetica locale in eccesso possiede un valore basso, mentre ai confini fra tali regioni la probabilità di trovare elettroni con lo stesso spin vicini gli uni agli altri è alta e l'energia cinetica in eccesso possiede un valore elevato. L'analisi del gradiente della funzione *ELF* permette, allora, di localizzare i cosiddetti *attrattori* e i *basin*, che possiedono un significato chimico evidente. Gli *attrattori* rappresentano massimi locali della funzione di localizzazione elettronica, mentre il *basin* è la regione di spazio assegnata a ciascun massimo locale di $\eta(\boldsymbol{r})$. Esistono, fondamentalmente due tipi di *basin*: di *core* e di *valenza*, dei quali i primi sono localizzati immediatamente a ridosso dei nuclei ed i secondi nella regione di spazio rimanente. La struttura ricavabile dai *basin* di core riproduce molto bene le shell atomiche più interne. Un *basin* di *valenza*, invece, è caratterizzato dal suo cosiddetto *ordine sinaptico*, ossia dal numero di *basin* di *core* con i quali condivide i confini (tabella 2.9). In questa rappresentazione un *basin* monosinaptico corrisponde ad una coppia di non legame nella rappresentazione di Lewis, mentre *basin* di- e poli-sinaptici corrispondono ai legami fra gli atomi.

Ordine sinaptico	Nomenclatura	Simbolo
0	Core	C(X_i)
1	Monosinaptico	V(X_i)
2	Disinaptico	V(X_i, Y_j)
≥3	Polisinaptico	V(X_i, $Y_{j,\dots}$)

Tab. 2.9 Classificazioni dei diversi basin secondo il loro ordine sinaptico

Per un dato sistema in un certo stato elettronico esiste, quindi, fra la descrizione topologica e quella di *Lewis* una corrispondenza uno a uno che permette di accedere al modello matematico atto al superamento dello stesso modello di *Lewis*. L'integrazione della densità monoelettronica e della *pair probability* sul volume Ω_i dell'iesimo *basin* restituisce la popolazione N_i del *basin* stesso:

$$\overline{N}_i = \int_{\Omega_i} \rho(r)dr \qquad (2.15)$$

$$\overline{N}_{ij} = \int_{\Omega_i}\int_{\Omega_j} P_{cond}^{\sigma\sigma}(r_1, r_2)dr_1 dr_2 \qquad (2.16)$$

E la sua varianza

$$\sigma^2(\overline{N}_i) = \overline{N}_{ij} - \overline{N}_i(\overline{N}_i - 1) \qquad (2.17)$$

La connessione fra i punti critici ($\nabla\eta(\boldsymbol{r}) = 0$) del gradiente della funzione *ELF* determina il cosidetto *grafo molecolare*, cioè l'organizzazione dei *basin* di *core* e di *valenza*, caratterizzato dal numero di *attrattori*, denominato *numero morfico* (μ) .

2.6.2 Analisi “Natural Bond Orbital (NBO)”

L’altro approccio utilizzato in questo lavoro di tesi per l’analisi dei legami chimici coinvolti è “*Natural Bond Orbital*”.[38]

Il programma NBO esegue l’analisi di legame di una funzione d’onda multi elettronica in termini di funzione d’onda localizzata corrispondente ad un centro (lone pairs) o a due centri (legame) degli elementi della struttura di Lewis. Esegue la determinazione degli orbitali atomici naturali (NAOs), orbitali naturali ibridi (NHOs), orbitali naturali di legame (NBOs) orbitali molecolari localizzati naturali (NLMOs), partendo da un set di base di partenza $\{\chi_i\}$

Input-basis → NAOs → NHOs → NBOs →NLMOs (2.18)

Gli NBOs sono ottenuti come autofunzione della matrice densità e sono “naturali” nel senso di convergenza ottimale.

Il set NBOs ad alta occupazione, rappresenta la “struttura naturale di Lewis”, effetti di delocalizzazione appaiono come deboli allontanamenti da questa struttura.

Ogni passo della sequenza come riportato in (2.8) comporta un set ortonormale che attraversa lo spazio e può essere usato per dare una rappresentazione esatta della funzione d’onda e calcolare i valori di aspettazione del sistema (proprietà).

La generale trasformazione NBOs si adatta bene a descrivere gli effetti covalenti della molecola e le interazioni donatore accettore.

Bibliografia

1. M. Born, J. R. Oppenheimer, *Ann. Phys.*, **84**, 457 (1927).
2. I. N. Levine, third edition, Allyn and Bacon Inc., **7** Wells Avenue, Newton, Massachussets 02159, (1983).
3. P. Hohenberg, W. Kohn, *Phys. Rev. B*, **136**, 864 (1964).
4. W. Kohn, L.J. Sham, *Phys. Rev. A*, **140**, 1133 (1965).
5. S.H. Vosko, L. Wilk, M. Nusair, *Can. J. Phys.*, **58**, 1200 (1980).
6. J. P. Perdew, *Phys. Rev. B*, **33**, 8822 (1986).
7. A. D. Becke, *Phys. Rev. A*, **38**, 3098 (1988).
8. C. Lee, W.Yang, R.G. Parr, *Phys. Rev. B*, **37**, 785 (1988).
9. A. Becke, *J. Chem. Phys.*, **98**, 5648 (1993).
10. (a) J. P. Perdew, *Phys. Rev.B*, **44**, 10221 (1991)**;** (b) J. P. Perdew, Y. Wang, *ibidem* **45**, 13244 (1992).
11. A.Foldy, S.Wouthysen, *Phys.Rev.*, **78**, 29 (1950).
12. M. Douglas, N. M. Kroll, *Ann. Phys. (NY)*, **82**, 89 (1974).
13. (a) E. Van Lenthe, E. J. Baerends, J.G Snijders, *J. Chem. Phys.*, **99**, 4597 (1993); (b) E. Van Lenthe, E. J. Baerends, J.G Snijders, *J. Chem. Phys.*, **101**, 9783 (1994); (c) E. Van Lenthe, E. J. Baerends, J.G Snijders, *J. Chem. Phys.*, **110**, 8943 (1999).
14. (a) G. te Velde, F. M. Bickelhaupt, S. J. A van Gisbergen, C. Fonseca Guerra, E. J. Baerends, J. G. Snijders, T. Ziegler, *J. Comput. Chem.*, **22**, 931 **(**2001); (b) C. Fonseca Guerra, J. G. Snijders, G. te Velde, E. Baerends, J. *Theor. Chem. Acc.*, **99**, 391 (1998); (c) ADF2004.01, SCM, Theoretical Chemistry, Vrije Universiteit, Amsterdam, The Netherlands, http://www.scm.com.
15. Gaussian 03, Revision C.02, M. J. Frisch, G. W. Trucks, H. B. Schlegel, G. E. Scuseria, M. A. Robb, J. R. Cheeseman, J. A. Montgomery, Jr., T. Vreven, K. N. Kudin, J. C. Burant, J. M. Millam, S. S. Iyengar, J. Tomasi, V. Barone, B. Mennucci, M. Cossi, G. Scalmani, N. Rega, G. A. Petersson, H. Nakatsuji, M. Hada, M. Ehara, K. Toyota, R. Fukuda, J. Hasegawa, M. Ishida, T. Nakajima, Y. Honda, O. Kitao, H. Nakai, M. Klene, X. Li, J. E. Knox, H. P. Hratchian, J. B. Cross, V. Bakken, C. Adamo, J. Jaramillo, R. Gomperts, R. E. Stratmann, O. Yazyev, A. J. Austin, R. Cammi, C. Pomelli, J. W. Ochterski, P. Y. Ayala, K. Morokuma, G. A. Voth, P. Salvador, J. J. Dannenberg, V. G. Zakrzewski, S. Dapprich, A. D. Daniels, M. C. Strain, O. Farkas, D. K. Malick, A. D. Rabuck, K. Raghavachari, J. B. Foresman, J. V. Ortiz, Q. Cui, A. G. Baboul, S. Clifford, J. Cioslowski, B. B. Stefanov, G. Liu, A. Liashenko, P. Piskorz, I. Komaromi, R. L. Martin, D. J. Fox, T. Keith, M. A. Al-Laham, C. Y. Peng, A. Nanayakkara, M. Challacombe, P. M. W. Gill, B. Johnson, W. Chen, M. W. Wong, C. Gonzalez, and J. A. Pople, Gaussian, Inc., Wallingford CT, 2004.
16. D.E. Ellis, *Int. J. Quant. Chem. 2S*, **35**, (1968).
17. P.M. Boerrigter, G. te Velde, E.J. Baerends, *Int. J. Quantum Chem.*, **33**, 87 (1988).
18. G. te Velde, E.J. Baerends, *J. Comp. Phys.*, **99**, 84 (1992).
19. (a) M. Garcia-Hernandez, C. Lauterbach, S. Krüger, A. Matveev, N. Rösch, J. Comput. Chem., **23**, 834 (2002); (b) W. A. de Jong, R. J. Harrison, J. A. Nichols, D. A. Dixon, *Theor. Chem. Acc.*, **107**, 22, (2001); (c) Y.-K. Han, K. Hirao, J. Chem. Phys, 113, 7345 (2000); (d) N. Ismail, J.-L. Heully, T. Saue, J.-P. Daudey, C. J. Marsden, *Chem. Phys. Lett.*, **300**, 296 (1999).
20. (a) M. C. Michelini, N. Russo, E. Sicilia, *Angew. Chem. Int. Ed.*, **45**, 1095 (2006); (b) M. C. Michelini, N. Russo, E. Sicilia, *J. Am. Chem. Soc.*, **129**, 4229 (2007) (c) G.Mazzone, M. C. Michelini, N. Russo, E. Sicilia, *Inorg. Chem.*, **47**, 2083 (**2008**); (d) M. E .Alikhani, M. C. Michelini, N. Russo, B. *J* .Silvi, *Phys. Chem. A*, **112**, 12966 (2008).
21. (a) http://www.theochem.unistuttgart.de/pseudopotentiale/; (b) W. Külchle, M. Dolg, H. Stoll, H. Preuss, *J. Chem. Phys.*, ***100***, 7535 (1994).
22. H. Eyring, M, Polanyi, *Z. Phys Chem.*, **B12**, 279 (1931).

23. D. Schröder, S. Shaik, H. Schwarz, *Acc. Chem. Res.*, **33**, 139 (2000).
24. S. Shaik, D. Danivich, A. Fiedler, D. Schröder, H. Schwartz, *Helv. Chim. Acta*, **78**, 1393 (1995).
25. S. Shaik, M. Filatov, D. Schröder, H. Schwartz, *Chem. Eur. J.*, **4**, 193 (1998).
26. G. S. Hammond, *J. Am. Chem. Soc.*, **77**, 334 (1955).
27. J. E. Leffler, *Science*, **117**, 340 (1952).
28. E. D. German, I. Efremenko, M. Sheintuch, *J. Phys. Chem. A*, **105**, 11312 (2001).
29. C. R. Landis, C. M. Morales, S. S. Stahl, *J. Am. Chem. Soc.*, **126**, 16302 (2004).
30. G.N. Lewis, Dover, New York, (1966).
31. (a) J. C. Slater, *Phys. Rev.*, **41**, 255, (1931); (b) J. C. Slater, *Phys. Rev.*, **38**, 1109 (1931); (c) J. C. Slater, *Phys. Rev.*, **37**, 481 (1931); (d) L. Pauling, *J. Am. Chem. Soc.*, **53**, 1367 (1931); (e) L. Pauling, *J. Am. Chem. Soc.*, **53**, 3225 (1931).
32. (a) Mulliken, *Phys. Rev*. **32**, 186 (1928); (b) R. S. Mulliken, *Phys. Rev*. **32**, 761 (1928); (c) R. S. Mulliken, *Phys. Rev.*, **33**, 730 (1929); (d) R. S. Mulliken, *Phys. Rev.*, **41**, 49 (1932); (e) F. Hund, *Z. Phys.*, **73**, 1 (1931); (f) F. Hund, *Z. Phys.*, **74**, 1 (1932); (g) F. Hund, *Z. Phys.*, **51**, 759 (1928).
33. R.J. Gillespie, Van Nostrand Reinhold, London, (1972).
34. (a) R. Daudel, Gauthier-Villars, Paris, (1957) ; (b) R. Daudel, Editions du Centre National de la Recherche Scientifique, Paris, (1971) ; (c) R. Daudel, Reidel, Dordrecht, (1974) ;(d) R. Daudel, R.F.W. Bader, D.S. Borrett, *Can. J. Chem.*, **52**, 1310 (1974); (d) C. Aslangul, R. Constanciel, R. Daudel, P. Kottis, *Ad. Quant. Chem.* Academic Press, New York, **6,** 93 (1972).
35. (a) R.F.W. Bader, S.G. Anderson, A. J Duke, *J. Am. Chem. Soc.*, **101**, 1989 (1979); (b) R. F.W. Bader, Oxford University Press Oxford, (1990).
36. B. Silvi, A. Savin, *Nat.*, **371**, 683 (1994).
37. A. D. Becke, K.E. Edgecombe, *J.Chem. Phys.*, **92**, 5397 (1990).
38. (a) A. E. Reed, F. Weinhold, *J. Chem. Phys.*, **83**, 1736 (1985); (b) A. E. Reed, L. A Curtiss, F. Weinhold, *Chem. Rev.*, **88**, 899 (1988).

3

Studio teorico di reazioni in fase gassosa di $Th^{+(2+)}$;$U^{+(2+)}$ con CH_4, C_2H_6, C_3H_8

Introduzione

L'attivazione dei legami C-H e C-C da parte di cationi dei metalli di transizione è stata ampiamente analizzata in passato, soprattutto per quanto riguarda il metano e gli alcani più piccoli.[1-5]

L'indagine sperimentale sistematica, confermata anche da studi teorici, ha stabilito che il passaggio dominante nel meccanismo di reazione di qualunque processo relativo all'attivazione di legami prototipi, C-H, C-C, è quello di inserzione del metallo nel legame da attivare. Ovvero, data una specie contenente un metallo di transizione M, che per convenzione viene chiamata [M], e dato un legame prototipo R-H di un idrocarburo, il passaggio chiave risulta essere:

$$[M] + R\text{-}H \longrightarrow R\text{-}[M]\text{-}H$$

Diversi studi realizzati sui monocationi di metalli di transizione, hanno confermato tale meccanismo d'inserzione,[6-11] mentre per i dicationi, Freiser e collaboratori,[12-15] seguendo i lavori di Tonkyn e Weisshaar[16-17] hanno proposto meccanismi di reazione diversi per cationi con configurazioni elettroniche di tipo d^2 (Zr^{2+}) e d^3 (Nb^{2+}, Ta^{2+}), da quelli con configurazione eletronica d^1 (Sc^{2+}, Y^{2+}, La^2). Nel primo caso, il meccanismo evolve attraverso la classica inserzione ossidativa, con formazione di intermedi del tipo $\{H\text{-}M^{2+}\text{-}C\}$ o $\{C\text{-}M^{2+}\text{-}C\}$, mentre nell'ultimo caso la reazione avviene attraverso un meccanismo radicalico, mediante l'astrazione di un atomo di H. In particolare è stata utilizzata una curva di energia potenziale, derivata dal modello Landau-Zener,[18] per spiegare il meccanismo di reazione osservato. I reagenti M^{2+} + RH seguono una curva di energia potenziale attrattiva ione-dipolo indotto, mentre i relativi prodotti, $M^+ + RH^+$ (trasferimento di elettroni), $MH^+ + R^+$ (trasferimento di idruro) o $MCH_3^+ + (RH\text{-}CH_3)^+$ (trasferimento di metile) seguono una curva di energia potenziale puramente repulsiva. L'esotermicità di queste reazioni definisce il punto d'incroccio fra le due curve di energia potenziale. Se la reazione non è sufficientemente esotermica, il punto d'incroccio fra le due curve cade a lunghe distanze, e di conseguenza questi tre tipi di trasferimento non possono avvenire. In questo caso, i cationi M^{2+} possono superare il punto d'incrocio dando come risultati prodotti con carica +2.

Studi più recenti riguardanti elementi dei gruppi 4f; ed in particolare reazioni di idrocarburi con ioni lantanidi (Ln^+), hanno messo in rilievo il ruolo degli elettroni 4f nei processi di attivazione di legami: sono necessari almeno due elettroni non f al fine di attivare gli alcani, e di conseguenza, l'efficienza di attivazione di idrocarburi, da parte dei cationi Ln^+ in fase gassosa, è correlata all'energia di promozione dallo stato fondamentale allo stato eccitato a più bassa energia, avente configurazione elettronica [Xe] $4f^{n-2}5d^16s^1$.[19]

Per gli ioni dicationici dei lantanidi,[20-21] l'energia di promozione ad una configurazione con due elettroni non 4f è molto più alta di quella per gli ioni monocationici, e la reattività verso alcuni idrocarburi è attribuita alla configurazione accessibile d^1 e a un meccanismo radicalico, che non comporta un'inserzione diretta nel legame C-C o C-H, simile a quello proposto da Freiser e collaboratori per i cationi dei metalli di transizione con configurazione elettronica d^1.[12-15]

Una relazione analoga è stata proposta anche per gli attinidi.[22] L'efficienza degli ioni An^+ (An = Th, Pa, U, Np, Pu, Pu, Am, Cm, Bk, Cf, Es) ad attivare idrocarburi attraverso un'inserzione ossidativa può essere correlata con l'energia richiesta dallo ione An^+ per la transizione dallo stato fondamentale al primo stato eccitato con configurazione $5f^{n-2}6d7s$;[23] indicando che pure la reattività degli ioni attinidi in fasse gassosa è legata alla loro struttura elettronica.

L'attivazione di idrocarburi procede attraverso l'inserzione ossidativa del legame C-H o C-C per formare un'intermedio del tipo $\{C-An^+-H\}$ o $\{C-An^+-C\}$. La ridotta reattività degli elementi transuranici, dal Pu all'Es, sono state attribuite alle alte energie di promozione dallo stato fondamentale ad uno stato eccitato del tipo $5f^{n-2}6d7s$.

Il nostro lavoro è stato incentrato sullo studio teorico della reattività in fase gassosa di alcuni cationi della serie degli attinidi,[24] in particolare $Th^{+(2+)}$ e $U^{+(2+)}$ con metano ed etano, e Th^{2+} e U^{2+} con propano. Il principale interesse è stato quello di ottenere una conoscenza dettagliata del processo di attivazione dei legami C-H e C-C attraverso l'utilizzo di metodi teorici basati sulla teoria del funzionale della densità, con l'obiettivo di analizzare la reattività dei cationi metallici, che in assenza di fattori perturbativi correla direttamente con la loro struttura elettronica.

Per la realizzazione di questo lavoro si è partiti da dati sperimentali presenti in letteratura per le reazioni dei cationi monopositivi con metano ed etano,[23] e da dati sperimentali che si hanno a disposizione grazie alla collaborazione iniziata da qualche anno con due gruppi sperimentali (Unidade de Ciências Químicas e

Radiofarmacêuticas, Instituto Tecnológico e Nuclear, Portugal, e Chemical Sciences Division, Lawrence Berkeley National Laboratory, Berkeley, USA) per le reazioni dei cationi dipositivi con metano, etano, e propano.[24c] Questo confronto diretto con i dati sperimentali ottenuti in fase gassosa, hanno permesso di testare l'affidabilità del metodo teorico utilizzato.

3.1 Reazioni dei cationi $Th^{+(2+)}$ e $U^{+(2+)}$ con metano ed etano

Nella tabella 3.1 sono riportati i dati sperimentali[23c, 24c] per le reazioni tra i cationi $An^{+\,(2+)}$ (An = Th,U) e metano ed etano. Il metano viene attivato dai cationi Th^+ e Th^{2+} per formare il carbene attraverso l'eliminazione di H_2, mentre entrambi i cationi, U^+ e U^{2+}, risultano inerti. L'etano viene invece attivato dai cationi Th^+ (singola e doppia deidrogenazione), Th^{2+} (doppia deidrogenazione) e U^{2+}(singola deidrogenazione).

L'obiettivo principale di questo studio teorico è stato quello di studiare in dettaglio i meccanismi di tali reazioni e ricavare possibili similitudini e differenze utili per la comprensione dei diversi comportamenti osservati sperimentalmente. Il meccanismo di deidrogenazione del metano è simile per tutte e quattro le reazioni studiate, come indicato dai corrispondenti profili di energia potenziale (pubblicazioni I e III). La reazione inizia con l'inserzione del metallo nel legame C-H per formare un intermedio metil-idruro {$H\text{-}An^{+\,(2+)}\text{-}CH_3$}, dopo il superamento della barriera di attivazione associata (TS1). Da questo intermedio la reazione evolve attraverso la formazione di uno stato di transizione a quattro centri (TS2) che produce un secondo intermedio di inserzione, {$(H_2)An^{+(2+)}\text{-}CH_2$}, in cui la molecola di H_2 è già formata, proseguendo verso il rilascio di H_2 senza barriera.

$An^{+\,(2+)}$	CH_4			C_2H_6		
	Products	***k***	***k*/*k*COL**	**Products**	***k***	***k*/*k*COL**
$Th^{+\,(a)}$	$ThCH_2^+$ (100)	0.01	0.009	$ThC_2H_4^+$ (55) $ThC_2H_2^+$ (45)	0.11	0.12
$Th^{2+\,(b)}$	$ThCH_2^{2+}$ (100)	0.22	0.11	$ThC_2H_2^{2+}$(100)	0.28	0.15
$U^{+\,(a)}$	Non reagisce	<0.001	<0.001	Non reagisce	<0.001	<0.001
$U^{2+\,(b)}$	Non regisce	<0.001	<0.001	$UC_2H_4^{2+}$ (100)	0.34	0.18

Tab. 3.1: Prodotti di distribuzione (%), costanti di velocità (k, in unità

10^{-9}cm^{3}molecola^{-1}s^{-1}) ed efficienza di reazione (k/k$_{COL}$). (a) Rif. 23c. (b) Rif 24c.

A differenza di quanto avviene per il metano, Th^+, Th^{2+} e U^{2+} reagiscono con l'etano con efficienze paragonabili e prodotti di distribuzione diversi (tabella 3.1). Il meccanismo per l'attivazione del legame C-H dell'etano da parte dei cationi mono e dipositivi procede con alcune differenze; in particolare, dopo la formazione del primo intermedio d'inserzione $\{H{-}An^+{-}C_2H_5\}$, la reazione per i monocationi evolve con un riarrangiamento intramolecolare per produrre un nuovo intermedio di reazione, in cui il secondo atomo di idrogeno viene trasferito dal C al centro metallico $\{(H)_2An^+{-}C_2H_4\}$ e, successivamente, verso la formazione di un terzo intermedio $\{(H_2)An^+{-}C_2H_4\}$ in cui la molecola H_2 è già formata. La reazione coinvolge, quindi, il superamento tre stati di transizione. In contrasto, nel caso della reazione dei dicationi, dopo la formazione del primo intermedio, $\{H{-}An^{2+}{-}C_2H_5\}$, la reazione evolve direttamente verso la formazione del l'intermedio finale, $\{(H_2)An^{2+}{-}C_2H_4\}$, dopo il superamento di uno stato di transizione a quattro centri. In questo caso la reazione coinvolge soltanto due stati di transizione. La seconda deidrogenazione segue lo stesso meccanismo della prima, con la medesima differenza fra i cationi An^+ e An^{2+}.

E' stato considerato anche il processo di attivazione del legame C-C dell'etano da parte dei cationi $An^{+(2+)}$, il quale porta all'eliminazione di CH_4. La reazione inizia con la formazione di un addotto iniziale, $An(C_2H_6)^{+(2+)}$, uguale per entrambi i cammini di reazione (eliminazione di CH_4 e deidrogenazione), il quale si riorganizza per formare una specie dimetile, $\{CH_3{-}An^{+(2+)}{-}CH_3\}$, in cui è avvenuta l'inserzione del legame C-C da parte del metallo. La specie formata, è quasi sempre il minimo globale della reazione, e coinvolge una barriera di attivazione notevolmente più alta di quella corrispondente alla formazione del primo intermedio per la deidrogenazione, $\{H\text{-}An^{+(2+)}\text{-}CH_3\}$. Da questo intermedio la reazione evolve verso un altro complesso stabile, $\{(CH_4)An^{+(2+)}{-}CH_2\}$, precursore per l'eliminazione di metano. In alcuni casi (Th^+, Th^{2+}), il processo di eliminazione di CH_4 è esotermico ma la reazione non avviene presumibilmente per impedimento cinetico; in altri casi (U^+, U^{2+}) la reazione è sia termodinamicamente che cineticamente sfavorevole. Altri prodotti di reazione sono stati considerati: $AnH^{+(2+)}$, $AnC_2H_5^{+(2+)}$ e $AnC_2H_3^{+(2+)}$. Essi possono essere ottenuti per semplice rottura dei legame An-C e An-H dei diversi intermedi di reazione. Nella maggior parte dei casi la formazione di questi prodotti è risultata endotermica. Nel caso delle reazioni riguardanti i dicationi, si sono pure presi in considerazione i prodotti derivanti dalla separazione di carica, quali $AnH^+ + CH_3^+$ e $AnH^+ + C_2H_5^+$, i quali, sebbene risultino in alcuni casi esotermici, coinvolgono barriere di attivazione molto elevate.

3.2 Reazioni dei cationi Th^{2+} e U^{2+} con propano

I risultati teorici hanno dimostrato che tutti i prodotti ottenuti sperimentalmente procedono tramite inserzione ossidativa, e sono stati fondamentali per costatare che l'energetica calcolata per l'inserzione dei cationi dipositivi è del tutto coerente con il modello empirico che correla l'efficienza d'inserzione e l'energia necessaria per promuovere lo ione An^{2+} dal GS ad uno stato eccitato con due elettroni non 5f ($6d^2$).

Le reazioni di attivazione di propano sono notevolmente più complesse rispetto a quelle di metano ed etano, dovuto al maggior numero di prodotti/meccanismi di reazione possibili. Come si può vedere dalla tabella 3.2, i dati sperimentali[29c] indicano la formazione di tre prodotti differenti nel caso di Th^{2+} e quattro per l'U^{2+} , e solo la formazione del prodotto $AnCH_3^+$ è comune a tutte e due. Sono stati esaminati diversi meccanismi di reazione relativi alla formazione di tutti i possibili prodotti, per tutte i due cationi studiati. In tutti i processi analizzati si è costatato che i meccanismi di reazione sono simili per tutti i due i cationi, ma differiscono in modo fondamentale dal punto di vista della loro energetica. Per quanto concerne i meccanismi di deidrogenazione, i risultati teorici indicano che mentre il Th^{2+} procede verso il prodotto di doppia deidrogenazione con barriere di attivazione che sono al di sotto dell'asintoto rappresentato dai reagenti, l'elevata barriera di attivazione associata all'inserzione nel legame C-H da parte del U^{2+}, sposta il profilo di energia potenziale verso energie molto più alte di quelle corrispondenti al catione Th^{2+}, permettendo che avvenga soltanto la prima deidrogenazione in modo esotermico.

Analogamente a quanto visto per l'attivazione del legame C-H, i meccanismi di reazione dei due cationi per l'attivazione del legame C-C sono piuttosto simili, e la principale differenza è lo spostamento dei profili di energia potenziale delle reazioni del catione U^{2+} verso valori energetici più alti rispetto a quelli del Th^{2+}, per cui nel caso della reazione di U^{2+} e C_3H_8, ad esempio, si osserva soltanto eliminazione di CH_4, mentre per il Th^{2+} l'eliminazione di CH_4 è seguita dall'eliminazione esotermica di H_2.

An^{2+}	**C_3H_8**		
	Products	***k***	***k*/*k*$_{COL}$**
Th^{2+}	$ThC_3H_4^{2+}$ (55) $ThC_2H_2^{2+}$ (35) $ThCH_3^{+}$ (10)	0.26	0.13
U^{2+}	$UC_3H_6^{2+}$ (40) $UC_2H_4^{2+}$ (15) UH^{+} (10) UCH_3^{+} (35)	0.42	0.22

Tab 3.2: Prodotti di distribuzione (%), costanti di velocità (k, in unità 10^{-9}cm^{3}molecola^{-1}s^{-1}), e efficienza di reazione (k/k$_{COL}$). Rif 24c.

Questo spostamento dei profili di energia potenziale delle reazioni che coinvolgono il catione U^{2+} verso energie più alte rispetto di quelle del catione Th^{2+} è una conseguenza delle diverse energie relative dei primi intermedi di reazione, e si è verificato in tutte le reazione studiate. Infatti, questo spostamento verso energie più alte risulta di fondamentale importanza per la comprensione della diversa reattività osservata sperimentalmente.

I risultati teorici ottenuti utilizzando il livello di teoria B3LYP/SDD sono in accordo con i dati sperimentali, e permettono di razionalizzare la diversa reattività osservata sperimentalmente. Chiaramente, la semplice analisi delle caratteristiche dei diversi profili di energia potenziale, è insufficiente per predire o giustificare la diversa distribuzione dei prodotti osservati in ogni caso. Per superare questa limitazione, bisognerebbe utilizzare metodologie basate sulla dinamica molecolare, il che risulta molto complesso nel caso di reazioni in cui ci sono incroci fra superficie di spin differenti.[25]

3.3 Efficienza di attivazione e configurazione elettronica dello stato fondamentale

Il confronto dei risultati, sia teorici che sperimentali,[23-24] riguardanti l'efficienza di attivazione di metano, etano e propano da parte dei cationi mono (Th^{+} e U^{+}) e dipositivi (Th^{2+} e U^{2+}), permette di estrarre importanti conclusioni riguardanti l'influenza della configurazione elettronica dello stato fondamentale dei cationi, nel processo di attivazione dei legami.

Un'analisi dell'energia liberata durante formazione del complesso catione-legante iniziale, $An^{+(2+)}$-C_xH_y (tabella 3.3), evidenza che questa energia è maggiore per i dicationi e cresce con l'aumento delle dimensioni (e quindi della polarizabilità) dell'alcano considerato. Si potrebbe, quindi, prevedere che la energia addizionale fornita al sistema durante le reazione con i cationi dipositivi potrebbe permettere meccanismi di reazione che non sarebbero possibili per i monocationi con caratteristiche elettroniche altrettanto simili.

$An^{+(2+)}$-C_xH_y	**Th^+**	**Th^{2+}**	**U^+**	**U^{2+}**
CH_4	-31	-120	-22	-103
C_2H_6	-33	-160	-19	-131
C_3H_8	-	-215	-	-177

Tab. 3.3 Energia di formazione del complesso $An^{+(2+)}$-C_xH_y calcolate a livello B3LYP/SDD

In tabella 3.4 sono riportate l'energie necessarie per portare i cationi Th^+, Th^{2+}, U^+ e U^{2+} dai loro stati fondamentale agli stati eletronici eccitati di più bassa energia con una configurazione elettronica con due elettroni non 5f.

Il catione Th^+ è risultato più reattivo nei confronti del legame C-H del metano ed etano, e la sua efficienza può essere associata al fatto che il catione nel suo stato fondamentale possiede una configurazione elettronica ($6d^27s$) adatta all'inserzione del catione nel legame. Per il Th^{2+} la configurazione $6d^2$ è quasi degenere (1 kJ/mol) allo stato fondamentale $5f^16d^1$, mentre per il catione U^{2+} lo stato fondamentale ha una configurazione elettronica $5f^4$, con la configurazione del primo stato eccitato $5f^36d^1$ a 3 kJ/mol, e la configurazione $5f^26d^2$ a 232 kJ/mol.

	GS	ES	RE
Th^+	$6d^27s$	-	-
Th^{2+}	$5f^16d^1$	$6d^2$	1

U$^+$	5f^{3}7s^2	5f^{3}6d7s 5f^{3}6d^2	4 55
U^{2+}	5f^4	5f^{2}6d^2	232

Tab 3.4: Energie relative (RE) in kJ/mol dello stato eccitato a più bassa energia con 2 elettroni non-5f (ES) e lo stato fondamentale (GS)[26]

In base al modello empirico proposto per i cationi monopositivi, An$^+$, si potrebbe quindi, prevedere che l'inserzione del catione U^{2+} nei legami è quella meno favorita dalla configurazione elettronica. Nella tabella 3.5 sono riportati i valori corrispondenti alla energie di inserzione (ΔE_i), calcolate come la differenza fra la energia del complesso iniziale catione-legante, An^{2+}-C$_x$H$_y$, e l'energia del primo intermedio d'inserzione, {H-An^{2+}-C} o {C-An^{2+}-C}, per i cationi Th^{2+} e U^{2+} nelle reazioni di attivazione dei legami C-H e C-C del metano, etano e propano. Le differenze fra i valori ottenuti per il catione Th^{2+} e quelle corrispondenti al catione U^{2+} ($\Delta E_i[U^{2+}]$ - $\Delta E_i[Th^{2+}]$) variano tra 184 e 261 kJ/mol, cioè ragionevolmente vicini al valore 230 kJ/mol, necessario per la promozione del catione U^{2+} dalla configurazione dello stato fondamentale allo stato eccitato.

Questa correlazione tra l'efficienza dei meccanismi d'inserzione e l'energie di promozione è consistente con il modello empirico che prevede la necessità di una promozione dei cationi dai suoi stati fondamentali a stati eccitati aventi due elettroni non 5f, e può essere di grande utilità per comprendere e prevedere la reattività degli ioni attinidi in fase gassosa.

C$_x$H$_y$	**$\Delta E_i[Th^{2+}]$**	**$\Delta E_i[U^{2+}]$**	**$\Delta E_i[U^{2+}]$ - $\Delta E_i[Th^{2+}]$**
CH$_4$			
C-H	-75	150	225
C$_2$H$_6$			
C-H	-92	110	202
C-C	-156	50	206
C$_3$H$_8$			
C-H	-100	94	194
C-C$^{(a)}$	-145	39	184
C-C$^{(b)}$	-167	94	261

Tab 3.5: Energie d'inserzione dei legami C-H e C-C da parte dei cationi Th^{2+} e U^{2+}, calcolate a livello B3LYP/SDD (Ref 24c).
(a) e (b) corrispondono a diversi meccanismi di inserzione nel legame C-C del propano.

3.4 Confronto fra i diversi livelli di teoria utilizzati

Per analizzare le reazioni di Th^+ e U^+ con metano ed etano sono stati scelti due differenti approcci della teoria del funzionale densità.

Nel primo approccio si è utilizzato il funzionale di scambio e correlazione ibrido B3LYP, insieme al potenziale effettivo di core relativistico Stuttgart/Dresden (SDD) (come implementati nel codice Gaussian03). Per il C e l'H, invece è stato impiegato il set di funzione di base 6-311++G(d,p). Nel secondo approccio gli effetti relativistici sono stati introdotti attraverso l'approssimazione ZORA (come implementata nel codice ADF); in questo caso si è utilizzato il potenziale di scambio e correlazione PW91, e come set di base le funzioni di Slater triple ZETA con funzioni di polarizzazione (TZ2P), e l'approccio *frozen core* per descrivere gli elettroni dei gusci più interni (fino al livello 5d frozen per Th/U e 1s per il C).[27]

Attraverso il confronto dei risultati ottenuti con i due livelli di teoria utilizzati si è rilevato che in molti casi le energie relative calcolate con i diversi metodi sono considerevoli.[24a,b] Bisogna sottolineare che i due metodi scelti si differenziano sia per il tipo di funzionale utilizato, che per il numero di elettroni di core (60 elettroni nella approssimazione B3LYP/SDD, e 78 nell'approccio PW91/ZORA), ed il modo in cui le correzioni relativistiche sono introdotte. Risultati simili sono stati riportati in lavori precedenti, e l'utilizzo di un terzo livello di teoria (PW91/SDD) ha permesso di concludere che le differenze energetiche sono, almeno in parte, dovute al diverso funzionale di scambio e correlazione utilizzato.[28]

Per approfondire l'origine di queste differenze energetiche, tutti i profili di energia potentiale per le reazioni dell'etano con i cationi monopositivi (pubblicazione II), sono state ricalcolate utilizzando come asintoto i prodotti anziché i reagenti. Si è notato che le differenze energetiche ottenute con i due livelli di teoria sono notevolmente diminuite per la maggior parte degli intermedi di reazione e prodotti, mentre la differenza non è migliorata per quanto riguarda l'energia relativa del complesso iniziale ed i reagenti. Questo risultato ha portato alla conclusione che le differenze nei valori di energie relative calcolate con i diversi livelli di teoria, sono, almeno parzialmente, dovute alla scelta dei reagenti ($An^{+(2+)} + C_xH_y$) come asintoti per i calcoli dei profili di energia potenziale. Bisogna sottolineare che nella fase iniziale del processo d'inserzione, avvengono i cambiamenti più drastici nell'intorno chimico dei cationi, e quindi nel numero di ossidazione formale del catione. Studi teorici precedenti hanno sottolineato la difficoltà della DFT nel descrivere reazioni chimiche che coinvolgono cambiamenti di stati di ossidazione formali.[29]

Il confronto dei risultati ottenuti con i due approcci teorici utilizzati indica che il livello B3LYP/SDD è quello che riproduce meglio i dati sperimentali. Per questo motivo le reazioni dei dicationi con metano, etano e propano sono stati studiate solo a livello B3LYP/SDD.

Bibliografia

1. (a) M. A. Tolbert, J. L. B. Beauchamp, *J. Am. Chem. Soc.*, 106, 8117 **(**1984); (b) Armentrout, P. B.; Beauchamp, J. L. *Acc. Chem. Res.*, **22**, 315 **(**1989); (c) P. B. Armentrout, *Science*, **251**, 175 (1991); (d) J. C. Weisshaar, *Acc. Chem. Res.*, **26**, 213 (1993); (e) F. Liu, X.-G. Zhang, P. B. Armentrout, *Phys. Chem. Chem. Phys*, **7**, 1054 (2005).
2. (a) N.Russo, E.Sicilia, *J. Am. Chem. Soc.*, **123**, 2588 (2001**);** (b) E.Sicilia, N. Russo, *J. Am. Chem. Soc.* **124**, 1471 (2002); (c) M. C.Michelini, N. Russo, E.Sicilia, *J. Phys. Chem. A*, **106**, 8937 **(**2002); (d) M. C. Michelini, E.Sicilia, N. Russo, M. E.Alikhani, B. Silvi, *J. Phys. Chem. A*, **107**, 4862 (2003); (e) S.Chiodo, O. Kondakova, M. C.Michelini, N.Russo, E. Sicilia, *J. Phys. Chem. A*, **108**, 1069 (2004).
3. (a) K. K. Irikura, J. L. Beauchamp, *J. Am. Chem. Soc.*, **111**, 75 (1989); (b) K. K. Irikura, J. L. Beauchamp, *J. Am. Chem. Soc.*, **113**, 2769 (1991); (c) K. K. Irikura, J. L. Beauchamp, *J. Phys. Chem.* **95**, 8344 (1991).
4. (a) S. W. Buckner, T. J. MacMahon, G. D. B. S. Byrd, *Inorg. Chem.*, **28**, 3511 (1989); (b) J. K. Perry, G.Ohanessian, W. A. Goddard, III. *Organometallics*, **13**, 1870 (1994); (c) C.Heinemann, R. H.Hertwig, R.Wesendrup, W.Koch, H.Schwarz, *J. Am. Chem. Soc.*, **117**, 495 (1995); (d) C.Heinemann, R.Wesendrup, H.Schwarz, *Chem. Phys. Lett.*, 239, 75 (1995).
5. (a) X.-G. Zhang, R.Liyanage, P. B. Armentrout, *J. Am. Chem. Soc.*, **123**, 5563 (2001); (b) M. M. Armentrout, F.-X. Li, P. B. Armentrout, *J. Phys. Chem. A*, **108**, 9660 (2004); (c) L. G.Parke, C. S.Hinton, P. B. Armentrout, *Int. J. Mass Spectrom.*, **254**, 168 (2006); (d) P. B.Armentrout, S.Shin, R. Liyanage, *J. Phys. Chem. A*, **110**, 1242 (2006); (e) L. G. Parke, C. S.Hinton, P. B. Armentrout, *J. Phys. Chem. C*, **111**, 17773 (2007).
6. K.Eller, H.Schwarz, *Chem. Rev.*, **91**, 1121 (**1991).**
7. H.Schwarz, *Angew. Chem.*, **42** 4442 (2003)
8. Armentrout, P. B. *Int. J. Mass Spectrom.*, **227**, 289 (2003).
9. L.Operti, R.Rabezzana, *Mass Spectrom. Rev.*, **25** 483 (2006).
10. a) Y.Huang, M. B.Wise, D. B. Jacobson, B. S. Freiser, *Organometallics*, **6**, 346 (1987); (b) J. B.Schilling, J. L. Beauchamp, *J. Am. Chem. Soc.*, **110**, 15 (1988); (c) L. S.Sunderlin, P. B. Armentrout, *J. Am. Chem. Soc.* **111**, 3845 (1989).
11. L. M. Roth, B. S. Freiser, *Mass Spectrom. Rev.*, **10**, 303 (1991).
12. Freiser, B. S. *Acc. Chem. Res.*, **27**, 353 (1994)
13. Y. D.Hill, Y.Huang, T. Ast, B. S. Freiser, *Rapid Commun. Mass Spectrom.*, **11**, 149 (1997).
14. Y. A.Ranasinghe, T. J.MacMahon, B. S.Freiser, *J. Am. Chem. Soc.*, **114**, 9112 (1992)
15. Y. D.Hill, Y.Huang, T.Ast, , B. S. Freiser *Rapid Commun. Mass Spectrom.*, **11**, 149 (1997).
16. R.Tonkyn, J. C. Weisshaar, *J. Am. Chem. Soc.*, ***108***, 7128 (1986).
17. J.Weisshaar, C. *Acc. Chem. Res.*, *26*, 213 (1993).
18. K. G. Spears, G. C.Fehsenfeld, M.McFarland, E. E. Ferguson, *J. Chem. Phys.*, **56**, 2562 (1972).
19. H. H. Cornehl, C. Heinemann, D. Schroeder, H. Schwarz, *Organometallics*, **14**, 992 (1995).
20. Y. A.Ranasinghe, T.J.MacMahon, B. S. Freiser, *J. Am. Chem. Soc.*, **114**, 9112 (1992).
21. J.Marçalo, M.Santos, A.Pires , J. K.Gibson, R. G. Haire, *J. Phys. Chem. A*, **112**, 12647 (2008).
22. J. K. Gibson, *Int. J. Mass Spectrom.*, ***214***, 1 (2002).
23. (a) C. Heinemann, H.H. Cornehl,H. Schwarz *J. Organometall. Chem.* **501**, 201 (1995); (b) J. Marçalo, J.P. Leal, A. Pires de Matos *Int. J. Mass Spectrom. Ion Processes* **157/158**, 265 (1996); (c) J. K.Gibson, R. G. Haire, J.Marçalo, M. Santos, A. Pires de Matos, M. K.Mrozik, R. M. Pitzer, B.E. Bursten, *Organometallics*, **26**, 3947 (2007).

24. (a) E. Di Santo, M. C. Michelini, N. Russo, *Organometallics*, **28**, 3716 (2009) (b) E. Di Santo, M. C. Michelini, N. Russo, *J. Phys. Chem. A* **113**, 14699 **(**2009); (c) E. Di Santo, M. Santos, M. C. Michelini, J. Marcalo, J. K. Gibson, N. Russo *submitted*
25. J. Zhou, H. Bernhard Schlegel; *J. Phys. Chem. A*, **114**, 8613 (2010).
26. J. Blaise, J.-F.Wyart, *Tables Internationales de Constantes : Paris* (1992).
27. vedi 2°capitolo
28. (a) M. C. Michelini, N. Russo, E. Sicilia, *Angew. Chem., Int. Ed*, **45**, 1095 (2006); (b) M. C. Michelini, N. Russo, E. Sicilia, *J. Am. Chem. Soc.*, **129**, 4229 (2007); (c) M. E. Alikhani, M. C. Michelini, N. Russo, B. Silvi, *J. Phys. Chem. A*, **112**, 12966 (2008); (d) G. Mazzone, M. C. Michelini, N. Russo, E. Sicilia, *Inorg. Chem.*, **47**, 2083 (2008).
29. V. Vallet, B. Schimmelpfennig, L. Maron, C. Teichteil, T. Leininger, O. Gropen, I.Grenthe, U.Wahlgren, *Chem. Phys.*, **244**, 185 (1999).

Appendice

Pubblicazione I

Methane C-H bond activation by gas-Phase Th^+ and U^+: reaction mechanisms and bonding analysis.

Emanuela Di Santo, Maria del Carmen Michelini, Nino Russo

Organometallics **2009,** 28**,** 3716-3726.

3716 *Organometallics* **2009,** *28,* 3716–3726
DOI: 10.1021/om900156f

ORGANOMETALLICS
Article

Methane C−H Bond Activation by Gas-Phase Th^+ and U^+: Reaction Mechanisms and Bonding Analysis

Emanuela Di Santo, Maria del Carmen Michelini,* and Nino Russo*

Dipartimento di Chimica and Centro di Calcolo ad Alte Prestazioni per Elaborazioni Parallele e Distribuite-Centro d'Eccellenza MURST, Università della Calabria, I-87030 Arcavacata di Rende, Italy

Received February 27, 2009

Th^+ is the only actinide ion that activates exothermically the strong C−H bonds of methane in the gas phase. In contrast, U^+, as well as all of the rest of the experimentally studied An^+ cations, is inert in the reaction with CH_4. In this work, the activation of methane by thorium and uranium monocations was investigated using two different density functional theory approaches. The reaction mechanisms and the corresponding potential energy profiles were analyzed in detail. From the formation of the initial ion−molecule adduct, the $Th^+ + CH_4$ reaction pathway evolves completely along the doublet spin surface, whereas that of $U^+ + CH_4$ involves solely the quartet bare cation ground spin state. The bonding properties of all of the species involved in the reaction pathways were investigated in terms of diverse analyses including natural bond orbital, atoms in molecules, and electron localization function. The dehydrogenation products ($Th^+{=}CH_2$ and $U^+{=}CH_2$) as well as the last insertion intermediates are characterized by the presence of α-agostic geometries.

1. Introduction

The activation of the C−H bond in methane is an industrial process of great interest because it is the first step in converting natural gas into a transportable liquid feedstock.[1] A number of experimental and theoretical studies on the reactivity of bare transition metal ions with methane have provided a wealth of insight concerning the C−H bond activation process.[2−6] Those studies have demonstrated that none of the first- or second-row transition metal (TM) ions react with methane at thermal energies. In contrast, it was shown that several of the third-row transition metal ions (Ta^+, W^+, Os^+, Ir^+, and Pt^+) react exothermically to dehydrogenate methane.[4−6] In a recent series of papers,[6] Armentrout and co-workers have revisited, both experimentally and theoretically, the reactivity of most of the third-row TM monocations (Hf^+,[6c] Ta^+,[6g] W^+,[6e] Re^+,[6b] Ir^+,[6f] Pt^+,[6a] and Au^+[6d]) with CH_4. The differences in reactivity have been explained on the basis of the different electronic configurations of the bare cations and on the grounds of an unfavorable thermochemical formation of the cationic carbene complex MCH_2^+.

---

*To whom correspondence should be addressed. E-mail: nrusso@unical.it; mc.michelini@unical.it.

(1) (a) Arakawa, H.; Aresta, M.; Armor, J. N.; Barteau, M. A.; Beckman, E. J.; Bell, A. T.; Bercaw, J. E.; Creutz, C.; Dinjus, E.; Dixon, D. A.; Domen, K.; DuBois, D. L.; Eckert, J.; Fujita, E.; Gibson, D. H.; Goddard, W. A.; Goodman, D. W.; Keller, J.; Kubas, G. J.; Kung, H. H.; Lyons, J. E.; Manzer, L. E.; Marks, T. J.; Morokuma, K.; Nicholas, K. M.; Periana, R.; Que, L.; Rostrup−Nielson, J.; Sachtler, W. M. H.; Schmidt, L. D.; Sen, A.; Somorjai, G. A.; Stair, P. C.; Stults, B. R.; Tumas, W. *Chem. Rev.* **2001**, *101*, 953. (b) Crabtree, R. H. *J. Chem. Soc., Dalton Trans.* **2001**, 2437. (c) Labinger, J. A.; Bercaw, J. E. *Nature* **2002**, *417*, 507. (d) Bergman, R. G. *Nature* **2007**, *446*, 391. (e) Schwarz, H. *Int. J. Mass Spectrom.* **2004**, *237*, 75. (f) Schröder, D.; Schwarz, H. *Proc. Natl. Acad. Sci. U.S.A.* **2008**, *105*, 18114.

(2) See for instance: (a) Tolbert, M. A.; Beauchamp, J. L. B. *J. Am. Chem. Soc.* **1984**, *106*, 8117. (b) Armentrout, P. B.; Beauchamp, J. L. *Acc. Chem. Res.* **1989**, *22*, 315. (c) Armentrout, P. B. *Science* **1991**, *251*, 175. (d) Weisshaar, J. C. *Acc. Chem. Res.* **1993**, *26*, 213. (e) Liu, F.; Zhang, X.-G.; Armentrout, P. B. *Phys. Chem. Chem. Phys.* **2005**, *7*, 1054.

(3) See for instance: (a) Russo, N.; Sicilia, E. *J. Am. Chem. Soc.* **2001**, *123*, 2588. (b) Sicilia, E.; Russo, N. *J. Am. Chem. Soc.* **2002**, *124*, 1471. (c) Michelini, M. C.; Russo, N.; Sicilia, E. *J. Phys. Chem. A* **2002**, *106*, 8937. (d) Michelini, M. C.; Sicilia, E.; Russo, N.; Alikhani, M. E.; Silvi, B. *J. Phys. Chem. A* **2003**, *107*, 4862. (e) Chiodo, S.; Kondakova, O.; Michelini, M. C.; Russo, N.; Sicilia, E. *J. Phys. Chem. A* **2004**, *108*, 1069.

(4) (a) Irikura, K. K.; Beauchamp, J. L. *J. Am. Chem. Soc.* **1989**, *111*, 75. (b) Irikura, K. K.; Beauchamp, J. L. *J. Am. Chem. Soc.* **1991**, *113*, 2769. (c) Irikura, K. K.; Beauchamp, J. L. *J. Phys. Chem.* **1991**, *95*, 8344. (d) Irikura, K. K.; Goddard, W. A.III *J. Am. Chem. Soc.* **1994**, *116*, 8733.

(5) (a) Buckner, S. W.; MacMahon, T. J.; Byrd, G. D. B. S. *Inorg. Chem.* **1989**, *28*, 3511. (b) Ranasinghe, Y. A.; MacMahon, T. J.; Freiser, B. S. *J. Phys. Chem.* **1991**, *95*, 7721. (c) Blomberg, M. R. A.; Siegbahn, P. E. M.; Svensson, M. *J. Phys. Chem.* **1994**, *98*, 2062. (d) Perry, J. K.; Ohanessian, G.; Goddard, W. A.III *Organometallics* **1994**, *13*, 1870. (e) Wesendrup, R.; Schröeder, D.; Schwarz, H. *Angew. Chem., Int. Ed.* **1994**, *33*, 1174. (f) Irikura, K. K.; Goddard, W. A.III *J. Am. Chem. Soc.* **1994**, *116*, 8733. (g) Heinemann, C.; Hertwig, R. H.; Wesendrup, R.; Koch, W.; Schwarz, H. *J. Am. Chem. Soc.* **1995**, *117*, 495. (h) Pavlov, M.; Blomberg, M. R. A.; Siegbahn, P. E. M. *J. Phys. Chem. A* **1997**, *101*, 1567. (i) Heinemann, C.; Schwarz, H.; Koch, W.; Dyall, K. *Chem. Phys.* **1996**, *104*, 4642. (j) Heinemann, C.; Wesendrup, R.; Schwarz, H. *Chem. Phys. Lett.* **1995**, *239*, 75. (k) Achatz, U.; Beyer, M.; Joos, S.; Fox, B. S.; Nieder-Schatteburg, G.; Bondybey, V. E. *J. Phys. Chem. A* **1999**, *103*, 8200. (l) Heinemann, C.; Koch, W.; Schwarz, H. *Chem. Phys. Lett.* **1995**, *245*, 509. (m) Holthausenm, M. C.; Heinemann, C.; Cornehl, H. H.; Koch, W.; Schwarz, H. *J. Chem. Phys.* **1995**, *102*, 4931.

(6) (a) Zhang, X.-G.; Liyanage, R.; Armentrout, P. B. *J. Am. Chem. Soc.* **2001**, *123*, 5563. (b) Armentrout, M. M.; Li, F.-X.; Armentrout, P. B. *J. Phys. Chem. A* **2004**, *108*, 9660. (c) Parke, L. G.; Hinton, C. S.; Armentrout, P. B. *Int. J. Mass Spectrom.* **2006**, *254*, 168. (d) Li, F.-X.; Armentrout, P. B. *J. Chem. Phys.* **2006**, *125*, 133114. (e) Armentrout, P. B.; Shin, S.; Liyanage, R. *J. Phys. Chem. A* **2006**, *110*, 1242. (f) Li, F.-X.; Zhang, X.-G.; Armentrout, P. B. *Int. J. Mass Spectrom.* **2006**, *255−256*, 279. (g) Parke, L. G.; Hinton, C. S.; Armentrout, P. B. *J. Phys. Chem. C* **2007**, *111*, 17773.

The reaction of Hf^+ with methane is endothermic, and theoretical computations indicate that Hf^+ retains its ground state (GS) configuration throughout the dehydrogenation reaction. It has been concluded that the inefficiency of the reaction can be attributed to the unfavorable doubly occupied 6s-orbital in the ^2D ($6s^25d^1$) GS.[6c] Ta^+ was found to be highly reactive with methane over a wide range of kinetic energies. The reaction is exothermic, and the relatively low efficiency has been attributed to the necessity of spin changes that take place during the reaction.[6g] In contrast, it was shown that Re^+ produces $ReCH_2^+$ efficiently in a slightly endothermic process, and theoretical calculations indicate that the reaction involves three facile spin changes between three different spin surfaces (septet, quintet, and triplet).[6b]

W^+ was reported as one of the most reactive second-row TM ions.[4b,6e] Ground state W^+ ions were found to react with CH_4 over a wide range of kinetic energies, and at low energies the dehydrogenation process was found to be slightly exothermic. Theoretical computations have shown that the dehydrogenation of methane by W^+ requires at least one spin change (and possibly two changes) along the lowest-energy path available. Ir^+ dehydrogenates methane in an exothermic and very efficient reaction.[6f] As in the case of Re^+,[6b] the reaction pathways involves more than one spin surface.

Several experimental and theoretical studies on the activation of methane by Pt^+ have been reported in the literature.[4b,4d,5e,5g−5m,6a] The dehydrogenation reaction of methane by Pt^+ is exothermic and efficient, and the reaction evolves along the doublet ground state potential energy surface.[6a]

Early experimental studies of reactions of lanthanide (Ln) ions with hydrocarbons in the gas phase have shown the importance of this type of chemical reactivity analysis in elucidating the role of electronic structures of 4f-element ions in inducing bond activation.[7] In the case of lanthanide cations it was pointed out that at least two non-f-electrons are required in order to activate alkanes. Further, it was found that the efficiency of activation of hydrocarbons by Ln^+ in the gas phase correlates with the promotion energy from the ground state electronic configuration to the lowest-lying [Xe] $4f^{n-2}5d^16s^1$ configuration. In a very recent experimental study,[7e] the gas-phase reactivity of doubly charged lanthanide cations with alkanes and alkenes was studied by Fourier transform ion cyclotron resonance mass spectrometry (FTICR-MS). It was found that the only Ln^{2+} ions that activate the hydrocarbons to form doubly charged ions were La^{2+}, Ce^{2+}, Gd^{2+}, and Tb^{2+}, all of which have ground states or low-lying d^1 electronic configurations. The remaining Ln^{2+} ions reacted via transfer channels or adduct formation.

The activation of small alkanes and alkenes by bare actinide (An) cations (Th^+ through Cm^+) was systematically examined using FTICR-MS.[8] For the reaction with CH_4 the experiments indicate that the only An^+ that reacts is Th^+, giving exclusive elimination of H_2 with a rather low efficiency ($k/k_{COL} = 0.009$).[8] These results agree with earlier experimental studies (FTICR-MS) of the activation of alkanes and alkenes by thorium cations, which indicated that thermalized Th^+ ions react with methane to form $ThCH_2^+ + H_2$.[9] Very early studies of the reactivity of uranium ions with CD_4[10] have shown that the endothermic reaction leads to the formation of UD^+. The most recent experimental results[8] indicate that U^+ is unreactive at thermal energies with CH_4 within the detection limit ($k/k_{COL} < 0.001$).

As part of an ongoing project on the H−C and C−C bond activation of small alkanes and alkenes by gas-phase bare actinide cations, we have studied the activation of the methane C−H bond by Th^+ and U^+ cations. The main goal of this work was to perform a detailed study of the reaction mechanisms, with the aim to analyze similarities and differences that could provide insight into the different reaction efficiencies. With this aim, we have also performed an extensive study of the bonding properties of all of the species involved in the studied reactions.

2. Computational Details

On the basis of the performance observed in our previous studies of the reaction of uranium and thorium cations with water and N_2O,[11] two different approaches of density functional theory (DFT) were used to perform this study. First, the zero-order regular approximation (ZORA) was used together with the PW91 functionals (for exchange and correlation)[12] and the TZ2P basis set as implemented in the ADF package[13] (we refer to this level of theory as PW91/ZORA hereafter). Second, the B3LYP[14] hybrid functional was employed together with the Stuttgart−Dresden relativistic effective core potential (small core)/basis sets.[15] The 6-311 + + G(d,p) basis sets of Pople and co-workers[16] were employed for C and H atoms (B3LYP/SDD,

---

(7) (a) Huang, Y.; Wise, M. B.; Jacobson, D. B.; Freiser, B. S. *Organometallics* **1987**, *6*, 346. (b) Schilling, J. B.; Beauchamp, J. L. *J. Am. Chem. Soc.* **1988**, *110*, 15. (c) Sunderlin, L. S.; Armentrout, P. B. *J. Am. Chem. Soc.* **1989**, *111*, 3845. (d) Cornehl, H. H.; Heinemann, C.; Schroeder, D.; Schwarz, H. *Organometallics* **1995**, *14*, 992. (e) Marçalo, J.; Santos, M.; Pires , A.; Gibson, J. K.; Haire, R. G. *J. Phys. Chem. A* **2008**, *112*, 12647.

(8) Gibson, J. K.; Haire, R. G.; Marçalo, J.; Santos, M.; Pires , A.; Mrozik, M. K.; Pitzer, R. M.; Bursten, B. E. *Organometallics* **2007**, *26*, 3947.

(9) Marçalo, J.; Leal, J. P.; Pires , A. *Int. J. Mass Spectrom. Ion Processes* **1996**, *157*/*158*, 265.

(10) (a) Armentrout, P. B.; Hodges, R. V.; Beauchamp, J. L. *J. Chem. Phys.* **1977**, *66*, 4683. (b) Armentrout, P.; Hodges, R.; Beauchamp, J. L. *J. Am. Chem. Soc.* **1977**, *99*, 3162.

(11) (a) Michelini, M. C.; Russo, N.; Sicilia, E. *Angew. Chem., Int. Ed.* **2006**, *45*, 1095. (b) Michelini, M. C.; Russo, N.; Sicilia, E. *J. Am. Chem. Soc.* **2007**, *129*, 4229. (c) Mazzone, G.; Michelini, M. C.; Russo, N.; Sicilia, E. *Inorg. Chem.* **2008**, *47*, 2083. (d) Alikhani, M. E.; Michelini, M. C.; Russo, N.; Silvi, B. *J. Phys. Chem. A* **2008**, *112*, 12966.

(12) (a) Burke, K.; Perdew, J. P.; Wang Y. In *Electronic Density Functional Theory: Recent Progress and New Directions*; Dobson, J. F., Vignale, G., Das, M. P., Eds.; Plenum: New York, 1998. (b) Perdew, J. P. In Electronic Structure of Solid '91; Ziesche, P., Eschrig, H., Eds.; Akademie Verlag: Berlin, 1991; p 11. (c) Perdew, J. P.; Burke, K.; Wang, Y. Phys. Rev. B 1996, 54, 16533. (d) Perdew, J. P.; Chevary, J. A.; Vosko, S. A.; Jackson, K. A.; Pederson, M. R.; Singh, D. J.; Fiolhais, C. Phys. Rev. B 1992, 46, 6671. (e) Perdew, J. P.; Chevary, J. A.; Vosko, S. H.; Jackson, K. A.; Pederson, M. R.; Singh, D. J.; Fiolhais, C. Phys. Rev. B 1993, 48, 4978.

(13) (a) te Velde, G.; Bickelhaupt, F. M.; van Gisbergen, S. J. A.; Fonseca Guerra, C.; Baerends, E. J.; Snijders, J. G.; Ziegler, T. *J. Comput. Chem.* **2001**, *22*, 931. (b) Fonseca Guerra, C.; Snijders, J. G.; te Velde, G.; Baerends, E. J. *Theor. Chem. Acc.* **1998**, *99*, 391. (c) *ADF2004.01*; SCM, Theoretical Chemistry, Vrije Universiteit: Amsterdam, The Netherlands, http://www.scm.com.

(14) (a) Becke, A. D. *J. Chem. Phys.* **1993**, *98*, 5648. (b) Lee, C.; Yang, W.; Parr, R. G. *Phys. Rev. B* **1988**, *37*, 785.

(15) (a) http://www.theochem.unistuttgart.de/pseudopotentiale/. (b) Küchle, W.; Dolg, M.; Stoll, H.; Preuss, H. *J. Chem. Phys.* **1994**, *100*, 7535.

(16) (a) Krishnan, R.; Binkley, J. S.; Seeger, R.; Pople, J. A. *J. Chem. Phys.* **1980**, *72*, 650. (b) Blaudeau, J.-P.; McGrath, M. P.; Curtiss, L. A.; Radom, L. *J. Chem. Phys.* **1997**, *107*, 5016. (c) Clark, T.; Chandrasekhar, J.; Schleyer, P. V. R. *J. Chem. Phys.* **1983**, *74*, 294.

SDD = Stuttgart−Dresden relativistic effective core potential). The B3LYP/SDD calculations were carried out using the Gaussian03 package.[17] Spin−orbit effects were not treated explicitly in this work.

Computations of open-shell systems were performed using spin-unrestricted methods. Spin contamination problems were found only for some doublet spin species. At the B3LYP/SDD level, the problem was solved after annihilation of the first spin contaminant, as $\langle S^2\rangle_A$ values never exceeded 10% of the exact value. At PW91/ZORA it was not possible to solve this problem, as this tool is not implemented in the ADF package. Therefore, there is important spin contamination in all of the doublet spin structures involved in the $U^+ + CH_4$ pathway. However, as will be shown in the next section, the $U^+ + CH_4$ reaction evolves completely along the quartet spin surface and the doublet potential energy profile (PEP) is quite high in energy. In the case of the $Th^+ + CH_4$ pathway the only doublet structure that presents strong contamination problems at PW91/ZORA is the initial adduct, Th^+-CH_4 (**I**). As previously mentioned, in the case of B3LYP/SDD level calculations the problem was solved after annihilation of the first spin contaminant.

All the structures were fully optimized, and the nature of the stationary points was characterized by a vibrational analysis performed within the harmonic approximation. The zero-point vibrational energy corrections were included in all the reported relative energies. We have ensured that every transition state has only one imaginary frequency, and intrinsic reaction coordinate (IRC) calculations were performed to confirm that the transition states connect reactants and products.

For both studied reactions, the ground and lowest-lying excited spin states of the bare cations were considered. Therefore, we have studied quartet and doublet spin states for the $Th^+ + CH_4$ reaction, and quartet, sextet, and doublet states in the case of $U^+ + CH_4$.

The bonding properties of all of the key minima and transition states involved in the reaction pathways were studied using topological methodologies. In particular, we have employed the topological analysis of the electron localization function (ELF)[18a] as proposed by Silvi and Savin.[18b] ELF grids and basin integrations were computed with the TopMod package.[19] Bonding and electronic properties were also explored using the atoms-in-molecules (AIM) approach.[20] In particular, we have analyzed the main properties of the (3,−1) bond critical points (bcp) in the gradient field of the electron density. The bcp's were localized with the EXTREME program (part of the AIMPAC package).[20] We have complemented the information obtained from topological methodologies with the description of the species provided by natural bond orbital (NBO) analysis.[21]

3. Results and Discussion

3.1. Bare Cations. At the PW91/ZORA level of theory the bare Th^+ GS has a quartet spin state derived from the $[Rn]6d^27s$ configuration, whereas at the B3LYP/SDD level the doublet $[Rn]5f7s^2$ configuration is the lowest-energy electronic configuration, with the quartet $[Rn]6d^27s$ at around 24 kJ/mol higher in energy. The GS level of the Th^+ cation is actually not identified in the Blaise and Wyart tables[22] due to a strong multiconfiguration mixing. The ground level has a mixed $^4F-^2D$ character.

According to the Blaise and Wyart tables, the lowest-energy U^+ has a $[Rn]5f^37s^2$ electronic configuration and is followed closely by several sextet spin states.[22] In this case, the experimental bare cation levels are better reproduced by B3LYP/SDD computations. The calculated GS has in fact a $[Rn]5f^37s^2$ electronic configuration (quartet state) and is followed by two sextet states very close in energy, $[Rn]5f^36d7s$ at 6 kJ/mol and the $[Rn]5f^47s$ state at 17 kJ/mol, whereas the $[Rn]5f^37s^2$ doublet spin state is much higher in energy (around 71 kJ/mol over the quartet GS). At the PW91/ZORA level the computed GS has a $[Rn]5f^47s$ (sextet) configuration, whereas the $[Rn]5f^37s^2$ (quartet) was found at 55 kJ/mol over the GS.

The details of the calculated bare cation energy gaps have been reported elsewhere,[11a,11c] and the results are collected in Table S1 (Supporting Information) together with the experimental lowest-energy levels for each configuration, taken from ref 22. It should be noted that the computed energies are better interpreted as an average over all possible J-states of a given electronic configuration, whereas the experimental energies were taken as the lowest J-state energy of each configuration.

In the case of Th^+, therefore, the different levels of theory used in this work do not agree in the spin state of the bare cation GS; however they agree in that the reaction pathway evolves on the doublet spin state surface after the formation of the initial ion−molecule complex (see next section). The $U^+ + CH_4$ reaction evolves clearly along the quartet ground bare cation spin state (sextet and quartet spin state are practically degenerate for the initial U^+-CH_4 complex at the PW91/ZORA level). At both levels of theory the relative energies (Figures 2 and 4) of all the species were calculated with respect to the computed bare cation GSs.

3.2. Reaction Mechanisms. The activation of CH_4 by transition metal cations is generally explained using an oxidative addition mechanism in which the metal inserts into the C−H bond to form a hydrido−methyl insertion intermediate ($H-M^+-CH_3$), whose formation is often the key step of the whole process. From that intermediate the H_2 elimination takes place through the formation of a four-centered transition state that yields a second insertion intermediate, $(H_2)M^+{=}CH_2$, in which the H_2 molecule is already formed, or through the formation of a methylidene metal dihydride intermediate, $(H)_2M^+{=}CH_2$, in which both H atoms are independently bonded to the metal cation. We have followed the same scheme to analyze the reaction of An^+ (An = Th, U) with methane. Two other reaction channels were also investigated: the elimination of H and CH_3 fragments to obtain $AnCH_3^+$ and AnH^+, respectively.

In Figure 1 are presented all the geometrical structures corresponding to the minima and transition states (lowest-energy spin states) involved in the $Th^+ + CH_4$ reaction, whereas in Figure 2 is sketched the corresponding PEP. The reaction starts with the exothermic formation of the Th^+-CH_4 association complex (**I**). As previously mentioned, despite the disagreement in the assignment of the Th^+ GS at

---

[17] Frisch, M. J.; et al. *Gaussian 03*. See Supporting Information for full citation.

[18] (a) Becke, A. D.; Edgecombe, K. E. *J. Chem. Phys.* **1990**, *92*, 5397. (b) Silvi, B.; Savin, A. *Nature* **1994**, *371*, 683.

[19] (a) Noury, S.; Krokidis, X.; Fuster, F.; Silvi, B. *TopMod Package*; Paris, 1997. (b) Noury, S.; Krokidis, X.; Fuster, F.; Silvi, B. *Comput. Chem.* **1999**, *23*, 597.

[20] Bader, R. W. F. *Atoms in Molecules. A Quantum Theory*. Clarendon, Oxford, 1990.

[21] (a) Reed, A. E.; Weinhold, F. *J. Chem. Phys.* **1985**, *83*, 1736. (b) Reed, A. E.; Curtiss, L. A.; Weinhold, F. *Chem. Rev.* **1988**, *88*, 899.

[22] Blaise, J.; Wyart, J.-F. International Tables of Selected Constants, Energy Levels and Atomic spectra of Actinides, Vol. *20*, *Tables of Constants and Numerical Data*; Paris, 1992, taken from http://www.lac.u-psud.fr/Database/Contents.html.

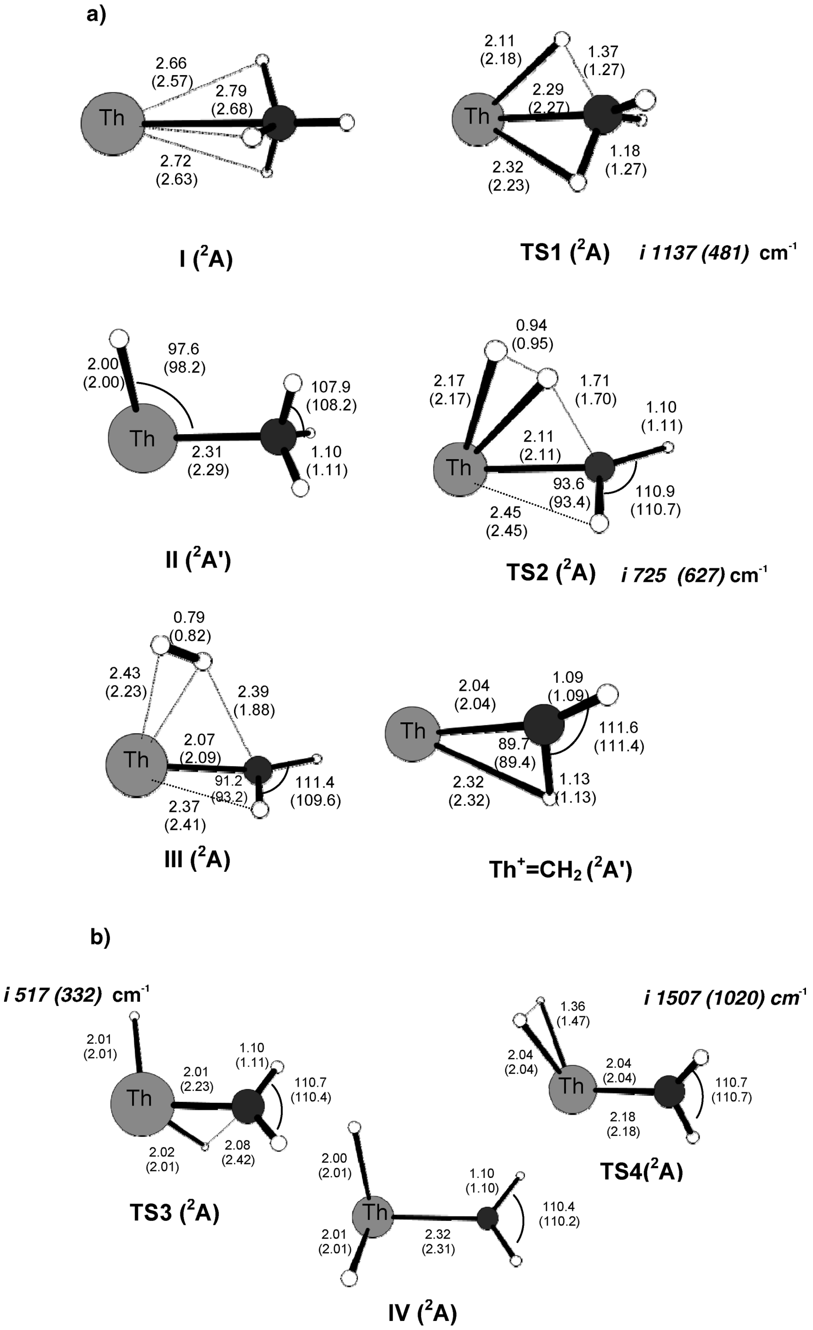

Figure 1. Geometrical parameters of all of the minima and transition states (lowest-energy spin state species) involved in the reaction of Th^+ with CH_4, at the B3LYP/SDD (PW91/ZORA) level of theory. Bond lengths are in angstroms and angles are in degrees.

the different levels of theory used in this work, all of the minima and transition states involved in the dehydrogenation reaction from the initial Th^+-CH_4 adduct to the products have a doublet spin state, at both levels of theory. The quartet surface remains higher in energy throughout the entire PEP, such that coupling between the surfaces is anticipated to be unimportant in the observed reactivity.

After rising to the first transition state (**TS1**), a hydrogen atom is shifted from the carbon atom to the metal, leading to a hydrido-metal intermediate (**II**), $H-Th^+-CH_3$. This structure is the global minimum of the PEP. The reaction proceeds toward the formation of the dehydrogenation products through the formation of a concerted four-center transition state (**TS2**). After the surpassing of this transition state, the system evolves to the formation of a second insertion intermediate, $(H_2)Th^+{=}CH_2$, in which the H_2 molecule is already formed. We have also taken into account the possible formation of the dihydride thorium methylidene, $(H)_2Th^+{=}CH_2$, isomer (**IV**). This structure is formed after the surpassing of a different transition state (**TS3**) that is very close energetically to **TS2**, and in order to form the last insertion intermediate (**III**) the system has to surpass another transition state (**TS4**), which was found to be higher in energy (+30.4 kJ/mol at B3LYP/SDD level). This alternative pathway (**II** → **TS3** → **IV** → **TS4** → **III**) is shown in dashed lines in Figure 2, and the structures involved (**TS3**, **IV**, and **TS4**) are collected in Figure 1b. For $Th^+ + CH_4$ the dehydrogenation process shows an exothermicity of almost 43 kJ/mol at the B3LYP/SDD level (118 kJ/mol at the PW91/ZORA). At the B3LYP/SDD level of

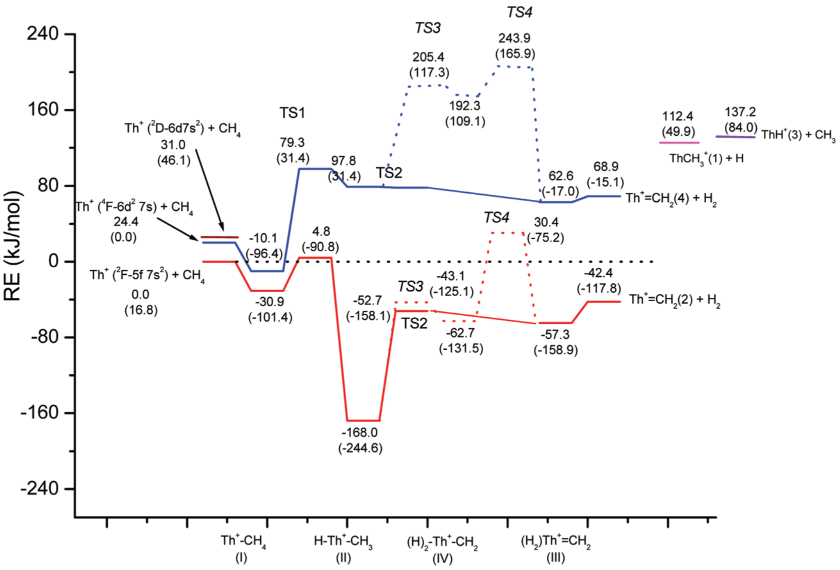

Figure 2. Potential energy profiles for the reaction of $Th^+ + CH_4$ at the B3LYP/SDD (PW91/ZORA) level of theory, corresponding to the quartet and doublet spin states.

theory the only transition state barrier that is over the asymptote limit is the first one, at almost +5 kJ/mol. The rest of the structures involved in the reaction pathway are well below the reactants asymptote. As can be seen in Figure 2, the quartet state PEP is quite high in energy.

We have also considered the formation of two other reaction products: $ThCH_3^+ + H$ and $ThH^+ + CH_3$. Both processes are endothermic. The formation of $ThCH_3^+ + H$ involves an endothermicity of 112 kJ/mol, whereas in the case of $ThH^+ + CH_3$ that value increases to 137 kJ/mol (B3LYP/SDD level). $ThCH_3^+$ has a $^1A_1$ ground state, which is followed very close in energy (+9 kJ/mol) at the B3LYP/SDD level by a triplet spin state isomer. At the ZORA/PW91 level the energetic ordering of the $ThCH_3^+$ triplet and singlet states is inverted, as the triplet state is the GS with the singlet isomer 31 kJ/mol higher in energy. ThH^+ has a $^3\Delta$ GS at both levels of theory and is followed by a $^1\Sigma^+$ isomer very close in energy (+2 kJ/mol at the B3LYP/SDD level). We note, however, that in both cases ($ThCH_3^+$ and ThH^+) the B3LYP/SDD GSs were determined only after the wave function stability was checked and the instability problems were solved. At the ZORA/PW91 level it was not possible to check the stability of the wave functions, as this tool is not implemented in the ADF package.

In a recent theoretical work,[23] the reactivity of neutral lanthanides and thorium bare atoms with CH_4 was studied at the DFT and Hartree–Fock levels of theory. In particular, at the DFT level the hybrid B3LYP functional was used together with the CRENBL pseudopotential for the Th atom. The authors report only the initial oxidation process, namely, the insertion of the metal atom into the C–H bond of CH_4 with the consequent formation of the first insertion intermediates, $H-Ln-CH_3$ and $H-Th-CH_3$. At the B3LYP/CRENBL level of theory the insertion of the $[5f^0]$ $7s^26d^2$ thorium into the methane C–H bond was predicted to be an exothermic process and essentially barrierless. In particular, the reaction energy for the formation of the insertion intermediate was calculated to be 181 kJ/mol, and the activation energy was 9 kJ/mol. These values are comparable with our computations at the B3LYP/SDD level, as the formation of the $H-Th^+-CH_3$ insertion intermediate involves a release of 168 kJ/mol, with an activation barrier of almost 5 kJ/mol (B3LYP/SDD level, see Figure 2). The geometrical properties of the transition state (*trans* planar conformation) and the eclipsed structure of the insertion intermediate, $H-Th-CH_3$,[23] are very close to the corresponding charged species computed in this work, the major difference being in the Th–C distance, which in the case of the charged species is shorter by ca. 0.1–0.2 Å.

As previously mentioned, for the $U^+ + CH_4$ reaction we have considered three different spin states, namely, the quartet bare cation GS and the sextet and doublet excited states. The dehydrogenation reaction, however, evolves completely along the quartet spin state.

Our calculations indicate that the mechanism is similar to that previously described for the $Th^+ + CH_4$ reaction; however, the energetics of the reaction is quite different. At the B3LYP/SDD level the formation of $U^+{=}CH_2$ is endothermic by almost 71 kJ/mol. The reaction barriers as well as the last reaction intermediate are well over the limit represented by the reactants. The results obtained at the B3LYP/SDD level justify the nondetection of reactivity during the FTICR-MS experiments, which are able to detect only exothermic and thermoneutral reactions. The geometrical structures of all of the transition states and intermediates involved in the $U^+ + CH_4$ reaction are presented in Figure 3, whereas the corresponding PEP is sketched in Figure 4. For the $U^+ + CH_4$ reaction we have not included the structures corresponding to the alternative dehydrogenation pathways, namely, those involving the dihydrometal-methylidene, $(H)_2U^+{=}CH_2$, intermediate because those structures are much higher in energy.

As can be seen in Figures 2 and 4, in both studied reactions the relative energies obtained at PW91/ZORA are systematically larger (and negative) than the corresponding B3LYP/SDD values. These differences range from 65 to 120 kJ/mol. We have found similar results in our previous works.[11]

With the aim to further analyze the performance of the theoretical methodologies used in this work, we have also

---

[23] de Almeida, K. J.; Cesar, A. *Organometallics* **2006**, *25*, 3407.

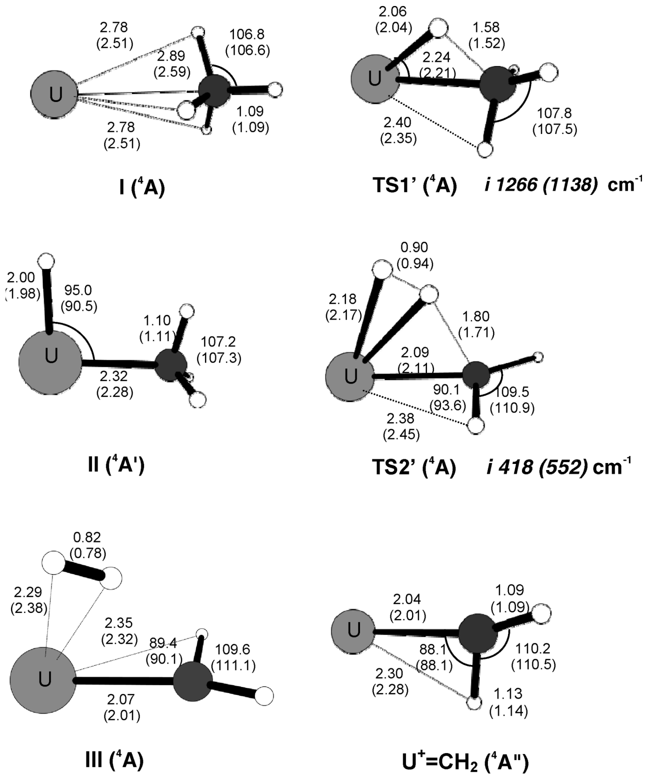

Figure 3. Geometrical parameters of all of the minima and transition states (lowest-energy spin state species) involved in the reaction of U^+ with CH_4, at the B3LYP/SDD (PW91/ZORA) level of theory. Bond lengths are in angstroms and angles are in degrees.

computed the bond dissociation energies (BDE) of different An^+-R species (R = H, CH_2, CH_4, C_2H_2, C_2H_4, C_2H_6; An = Th, U) and compared our results with experimental estimations, when available. The estimated experimental values correspond to lower limits implied by the observed reactions, with the only exception of the UH^+ BDE, for which the computed value agrees reasonably well with the experimental value reported in an early experimental work by Armentrout et al. (see Supporting Information).[10] Therefore the comparison that can be done is quite rough and cannot give further insight into the accuracy of the different levels of theory employed in this work. The obtained results are included as Supporting Information (Tables S2 and S3) and show that the BDE values obtained at the PW91/ZORA level are systematically higher than those obtained at the B3LYP/SDD level. In all cases, and at both levels of theory, the calculated values fall in the range implied from the experimental estimations.

3.3. Comparison with the Activation of Methane by Third-Row Transition Metal Cations. In an early experimental work, Irikura and Beauchamp showed that some bare third-row transition metal ions M^+ (M = Ta, W, Os, Ir, Pt) react exothermically with CH_4 to yield the corresponding carbene complexes $M^+(CH_2)$.[4] None of the first- or second-row transition metal ions react with methane at thermal energies, and the dramatic difference in reactivity is partially attributable to thermodynamic differences. The metal−methylene bond energies are much stronger for the third-row metals, which has been related to the lanthanide contraction that alters the relative sizes of the valence s- and d-orbitals.[24] As a consequence of the stronger metal methylene bond energies, the dehydrogenation reaction is exothermic for third-row metals. The catalytic oxidation process only proceeds exothermically if the bond dissociation energy for the metal cation to triplet ground state methylene exceeds 464 kJ/mol.[25] However, not all of the third-row transition metal ions react exothermically with methane; the early La^+ and Hf^+ along with Re^+ and Au^+ have been shown to be quite inactive. The differences in reactivity have been explained on the basis of the different electronic configurations of the bare cations and on the grounds of an unfavorable thermochemical formation of the cationic carbene complex, $M-CH_2^+$.[6]

A comparison of the reactivity of the members of group 4 (Ti^+, Zr^+, Hf^+) with CH_4 indicates that the reactions of the first two members of the group are endothermic, with an increase of efficiency on going from Ti^+ to Zr^+.[26a,26b,2b] Zr^+ was observed to react with methane at thermal energies in an early work performed by Freiser et al.,[5b] using ion cyclotron resonance (ICR) mass spectrometry techniques. More recently Armentrout and collaborators[26b] have investigated the reaction of Zr^+ and CH_4 over a wide range of kinetic energies, therefore examining both endothermic and exothermic processes, and have shown that the reaction is slightly endothermic. In both cases the reaction involves a crossing between the quartet (bare cations GS) and doublet surfaces. The GS of Th^+ (^4F, $6d^27s^1$) has a half-filled valence orbital, like the earlier members of group 4, Ti^+(^4F, $3d^24s^1$) and Zr^+ (^4F, $4d^25s^1$), both of which are the most reactive cations of the first and second TM series, respectively. On the contrary, Hf^+(^2D, $5d^16s^2$) has a doubly occupied 6s-orbital and retains its doublet GS configuration all along the dehydrogenation pathway.[6c] A qualitative interpretation of the activation process based on a simple acceptor−donor model implies the necessity of an electronic configuration on the metal ion having an acceptor orbital into which the electrons of the bond to be broken can be donated. The low reactivity of Hf^+(^2D) has been then attributed to the unfavorable electronic configuration, which results in a high barrier for the oxidative addition of a C−H bond and a relatively weak Hf^+-CH_2 bond.[6c]

A similar comparison between the members of the group 6, Cr^+(^6S, $3d^5$), Mo^+(^6S, $4d^5$), and W^+(^6D, $6s^15d^4$), demonstrate that the efficiencies of the dehydrogenation processes differ dramatically among the three metals and that most of these differences in reactivity can be simply understood on the basis of differences in thermochemistry.[6e,26b,26c] The only member of the series that reacts exothermically with methane is W^+,[6e] whereas the reaction is somewhat endothermic for Mo^+[26c] and more so for Cr^+.[26c,3b] The methane dehydrogenation by the two earlier TMs of group 6 have been shown to proceed through an intersystem crossing between the sextet bare cation GS and quartet excited spin surfaces, whereas in the case of W^+ the possibility of more than one spin change has been reported.[6e] Contrarily, the methane dehydrogenation activated by U^+(^4I, $5f^37s^2$) ions is an endothermic reaction

---

(24) Ohanessian, G.; Brusich, M. J.; Goddard, W. A.III *J. Am. Chem. Soc.* **1990**, *112*, 7179.

(25) Lias, S. G.; Bartmess, J. E.; Lieberman, J. F.; Holmes, J. L.; Levin, R. D.; Mallard, W. G. *J. Phys, Chem. Ref. Data* **1988,** *17*, Suppl. 1.

(26) (a) Sunderlin, L. S.; Armentrout, P. B. *J. Phys. Chem.* **1988**, *92*, 1209. (b) Armentrout, P. B.; Sievers, M. R. *J. Phys. Chem. A* **2003**, *107*, 4396. (c) Armentrout, P. B. *J. Phys. Chem. A* **2006**, *110*, 8327. (d) Georgiadis, R.; Armentrout, P. B. *J. Phys. Chem.* **1988**, *92*, 7067.

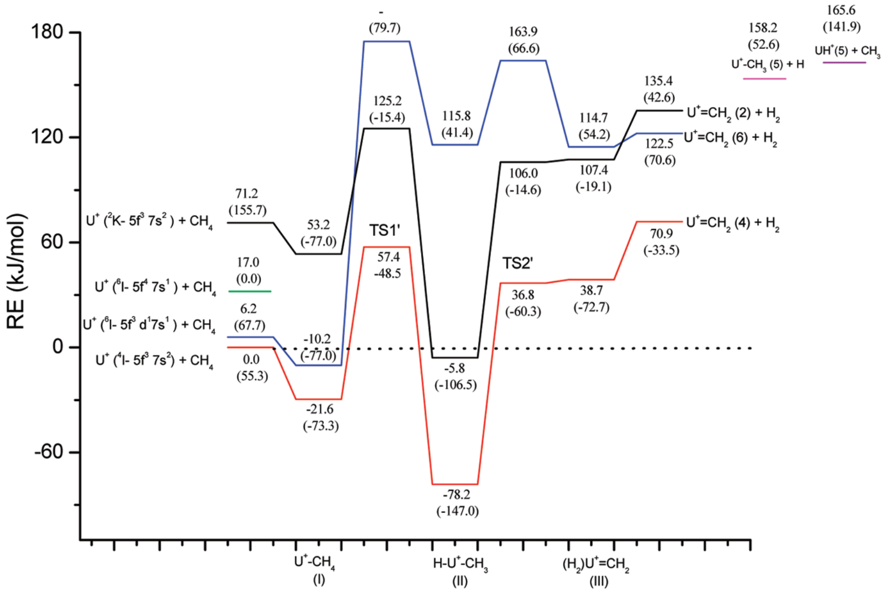

Figure 4. Potential energy profiles for the reaction of $U^+ + CH_4$ at the B3LYP/SDD (PW91/ZORA) level of theory, corresponding to the quartet, sextet, and doublet spin states.

(B3LYP/SDD results) that evolves along the quartet bare cation GS spin state.

3.4. Geometrical and Bonding Properties. The most relevant geometrical parameters of all of the minima and transition states (lowest-energy spin states) are reported in Figures 1 and 3. As can be seen in those figures the initial adducts are characterized by slightly distorted η^3-coordination modes. The **TS1** structures can be described as η^2-distorted structures in which, besides the H atom that is being transferred, a second H atom is also quite close to the metal atom. The structures of both hydrido-metal intermediates are eclipsed, whereas the last three structures (**TS2**, second insertion intermediate (**III**), and the An^+=CH_2 products) are characterized by the presence of agostic geometries. Many early transition metal alkylidenes exhibit agostic geometries, and similar geometrical distorsions were also reported in neutral methylidene metal dihydrides (Th, U).[27] The An−C−H agostic angle is of 93.6° in **TS2** (90.1° in **TS2′**), and in both cases there is a slight diminishing of that value on going from these structures to the An^+=CH_2 reaction products. The same trend is observed for the An−H agostic distance, which has a value of 2.45 Å in **TS2** and 2.38 Å in **TS2′**, and diminishes to 2.32 Å in Th^+=CH_2 and 2.30 Å in U^+=CH_2. Typical metal−hydrogen agostic distances range between 1.85 and 2.40 Å. In all cases the elongation of the agostic C−H bond was found to be about 0.04 Å (1.13 Å vs 1.09 Å for the second C−H bond).

The bonding properties of all of the species involved in the studied reaction pathways have been investigated using two different topological methodologies (AIM, ELF) as well as using the natural bond orbital analysis. A short description of the ELF and AIM methodologies and their use in bonding analysis is included in the Supporting Information. In Table 1 are presented the natural population analysis (NPA) metal charges and the corresponding metal valence populations of all of the species involved in the $Th^+ + CH_4$ and $U^+ + CH_4$ reaction pathways. The ELF localization domains (η = 0.65) of the lowest-energy minima and transition states corresponding to the $Th^+ + CH_4$ reaction pathway are collected in Figure 5, whereas those corresponding to $U^+ + CH_4$ are reported in Figure 6. We have also reported the metal charges as calculated from AIM analysis. As can be seen in Table 1, in all cases the metal charges on equivalent species are always very close (the difference is at most 0.1 e). Those values increase from +1.00 in the initial

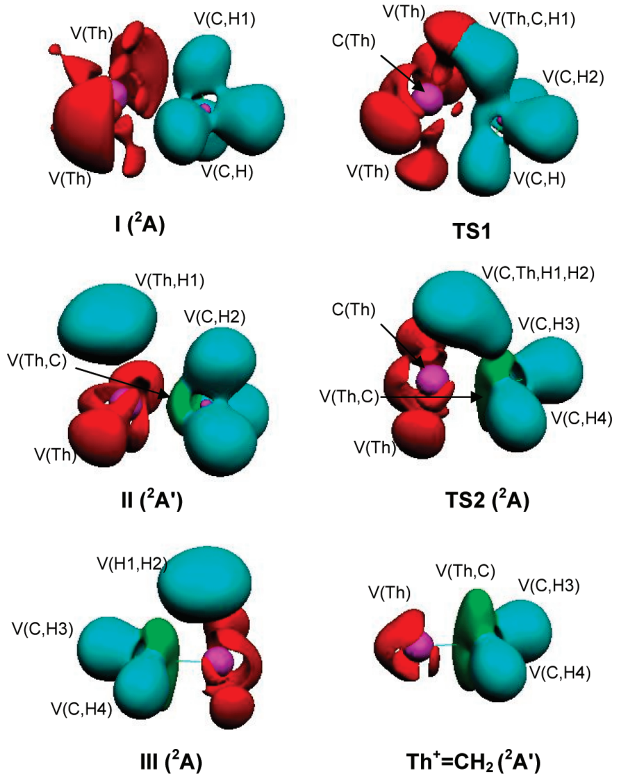

I (^{2}A) **TS1**

II (^{2}A′) **TS2 (^{2}A)**

III (^{2}A) **Th^+=CH_2 (^{2}A′)**

Figure 5. ELF localization domains (η = 0.65) of the lowest-energy minima and transition states corresponding to the $Th^+ + CH_4$ reaction pathway.

---

[27] (a) Roos, B. O.; Lindh, R.; Cho, H.-G.; Andrews, L. *J. Phys. Chem. A* **2007**, *111*, 6420. (b) Lyon, J. T.; Andrews, L.; Malmqvist, P.-A.; Roos, B. O.; Yang, T.; Bursten, B. E. *Inorg. Chem.* **2007**, *46*, 4917. (c) Lyon, J. T.; Andrews, L.; Hi, L. *Inorg. Chem.* **2008**, *47*, 1435.

complex to around +2.00 in the first insertion intermediate. The rest of the structures, from **TS2** to the final products, are characterized by a charge close to +2.00 on the metal center. NPA metal charges are systematically more positive than the corresponding AIM values by between 0.12 and 0.35 e.

NBO analysis shows that in the initial Th^+-CH_4 (^2A) ion−molecule complex the unpaired electron located on the metal occupies a hybrid orbital (50% d-character, 50% f-character), whereas the metal lone pair is localized on a hybrid orbital that has mainly s-character (70%). In all the rest of the Th^+ species the unpaired electron is located on s−d−f hybrid orbitals. The percentage of s-character grows steadily from 55% in **TS1** to 86% in the products, whereas the d-character diminishes from 39% in **TS1** to 12% in $Th^+{=}CH_2$. The contribution of f-orbitals to those hybrids is really very low (between 0 and 6% depending of the species). In contrast, the uranium unpaired electrons are pure f in all the studied species.

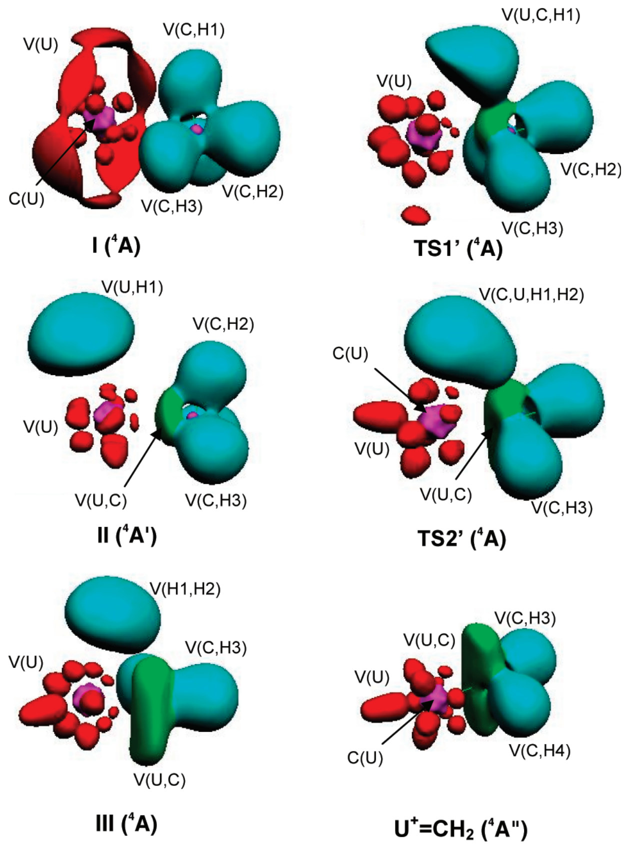

Figure 6. ELF localization domains (η = 0.65) of the lowest-energy minima and transition states corresponding to the $U^+ + CH_4$ reaction pathway.

According to the NBO analysis, the An^+-C σ-bonds are usually formed from s−d−f metal hybrid orbitals and s−p hybrids of carbon atom. The most notable difference between the Th- and the U-containing species is the greater d-character of the thorium hybrids (generally around 10%). π-Bonds, which are present only in the last insertion intermediates, $(H_2)An^+{=}CH_2$, and in the $An^+{=}CH_2$ reaction products, are formed from pure p-orbitals of oxygen and d−f metal hybrids. We have included the NBOs corresponding to the An^+-C bonds for some of the studied species as Supporting Information (Tables S4 and S5).

Th^+-CH_4 and U^+-CH_4. The metal valence populations indicate that the configuration of the Th^+ cation in the initial complex has a mixed configuration (see Table 1). In contrast, the U^+ configuration in the U^+-CH_4 adduct is very close to that of the GS bare cation ($[Rn]5f^37s^2$).

The ELF topological analysis indicates that there is no covalent bond formation between the fragments, as evidenced by the absence of a disynaptic valence basin between the metal and the CH_4 molecule (see Tables 2 and 3), confirming that the interaction between the partners can be considered an electrostatic interaction. This result agrees with AIM analysis (Tables 4 and 5), which shows the presence of a (3,−1) bcp between the Th and C atoms, with a very low charge density (ρ(bcp) = 0.031 au in the case of Th^+-CH_4 and 0.022 au in U^+-CH_4), and $\nabla\rho$ (bcp) values that are small and positive (around 0.09 au in both cases).

It has been previously reported that ELF analysis fails to provide a clear core−valence separation in the case of U atoms.[11d] Naturally, the same problem arises in the case of thorium. However, the sum of core and valence population, C(An) + V(An), clearly corresponds to the number of outer-shell electrons (29 electrons in the case of Th^+ and 31 in U^+). ELF and AIM analysis were performed using wave functions obtained at the B3LYP/SDD level, therefore using 60-electron SDD core pseudopotentials. For the initial An^+-CH_4 structures the C(An) + V(An) populations remain without variations, which indicates that there is no charge transfer between the two moieties. It can be observed from Tables 2 and 3 that for the rest of the U^+ structures those values always remain close to 29.5 electrons, whereas in the case of Th^+ those values change notably along the species,

Table 1. AIM (Atoms in Molecules) Charges, NPA (Natural Population Analysis) Charges, and Metal Valence Populations for All Minima and Transition States Computed at the B3LYP/SDD Level of Theory

			metal valence populations		
species (spin multiplicity)	AIM charges	NPA charges	7s	5f	6d
Th^+-CH_4 (2)	1.00	1.00	1.39	0.49	1.11
U^+-CH_4 (4)	1.00	0.98	1.71	3.23	0.08
TS1 (2)	1.38	1.54	1.12	0.37	0.99
TS1′ (4)	1.48	1.60	0.77	3.19	0.45
$H-Th^+-CH_3$ (2)	1.93	2.19	0.80	0.18	0.83
$H-U^+-CH_3$ (4)	2.03	2.21	0.30	3.09	0.42
TS2 (2)	1.80	2.08	0.77	0.28	0.90
TS2′ (4)	1.83	2.08	0.17	3.22	0.55
$(H_2)Th^+{=}CH_2$ (2)	1.75	2.10	0.73	0.24	0.95
$(H_2)U^+{=}CH_2$ (4)	1.82	2.10	0.12	3.20	0.60
$Th^+{=}CH_2$ (2)	1.82	2.09	0.88	0.24	0.00
$U^+{=}CH_2$ (4)	1.88	2.12	0.08	3.18	0.60

Table 2. Basin Populations, $\overline{N}$, Together with the Corresponding Variances, σ^2, of All Species Involved in the $Th^+ + CH_4$ Reaction Pathway

	I (^{2}A)		**TS1** (^{2}A)		**II** (^{2}A′)		**TS2** (^{2}A)		**III** (^{2}A)		$Th^+{=}CH_2$ (^{2}A′)	
basin	$\overline{N}$	σ^2	$\overline{N}$	σ^2	$\overline{N}$	σ^2	$\overline{N}$	σ^2	$\overline{N}$	σ^2	$\overline{N}$	σ^2
C(Th) + V(Th)	29.01	10.90	28.55	10.48	26.50	8.95	27.54	8.98	27.50	9.05	27.28	9.51
C(C)	2.09	0.26	2.09	0.26	2.09	0.26	2.08	0.26	2.09	0.26	2.09	0.26
V(C,H1)	1.98	0.71										
V(C,H2)	1.98	0.71	1.98	0.72	1.95	0.71						
V(C,H3)	1.98	0.71	1.92	0.78	1.96	0.71	1.65	0.74	1.92	0.76	1.89	0.76
V(C,H4)	1.93	0.66	2.00	0.66	1.94	0.71	1.69	0.76	2.05	0.68	2.04	0.68
V(Th,C)					2.26	1.26	3.03	1.55	1.75	1.06	1.81	1.10
V(Th,C)									1.61	1.01	1.83	1.11
V(Th,C,H1)			2.43	1.11								
V(H1,Th)					2.25	0.69						
V(C,Th,H1,H2)							2.87	1.74				
V(H,H)									1.86	0.35		

Table 3. Basin Populations, $\overline{N}$, Together with the Corresponding Variances, σ^2, of All Species Involved in the $U^+ + CH_4$ Reaction Pathways

	I (^{4}A)		**TS1′** (^{4}A)		**II** (^{4}A′)		**TS2′** (^{4}A)		**III** (^{4}A)		$U^+{=}CH_2$ (^{4}A″)	
basin	$\overline{N}$	σ^2	$\overline{N}$	σ^2	$\overline{N}$	σ^2	$\overline{N}$	σ^2	$\overline{N}$	σ^2	$\overline{N}$	σ^2
C(U) + V(U)	31.01	12.77	30.1	12.49	29.51	11.98	29.65	11.94	29.65	11.84	29.57	11.81
C(C)	2.10	0.26	2.09	0.26	2.09	0.26	2.09	0.26	2.09	0.26	2.09	0.26
V(C,H1)	1.98	0.69										
V(C,H2)	1.99	0.70	1.96	0.74	1.97	0.70						
V(C,H3)	1.99	0.69	1.94	0.74	1.98	0.70	1.65	0.78	1.94	0.75	1.90	0.75
V(C,H4)	1.93	0.66	2.04	0.74	1.97	0.70	1.72	0.80	2.07	0.68	2.05	0.68
V(U,C)			1.22	0.84	1.71	0.98	2.94	1.48	1.45	0.93	1.67	0.99
V(U,C)									1.67	0.99	1.68	1.00
V(U,C,H1)			1.65	0.78								
V(H,U)					1.78	0.42						
V(C,U,H1,H2)							2.79	1.48				
V(H,H)									2.07	0.68		

Table 4. Topological Properties of the Charge Density Calculated at the (3,−1) Bond Critical Points for All Species Involved in the $Th^+ + CH_4$ Reaction Pathway[a]

	I (^{2}A)		**TS1** (^{2}A)		**II** (^{2}A′)		**TS2** (^{2}A)		**III** (^{2}A)		$Th^+{=}CH_2$ (^{2}A′)	
bond	ρ(bcp)	$\nabla^2\rho$(bcp	ρ(bcp)	$\nabla^2\rho$(bcp)	ρ(bcp)	$\nabla^2\rho$(bcp)	ρ(bcp)	$\nabla^2\rho$(bcp)	ρ(bcp)	$\nabla^2\rho$(bcp)	ρ(bcp)	$\nabla^2\rho$(bcp)
Th−C	0.031	0.092	0.113	0.067	0.125	−0.027	0.159	0.062	0.173	0.055	0.185	0.034
C−H1	0.273	−0.919	0.151	−0.211								
C−H2	0.265	−0.850	0.258	−0.806	0.259	−0.812	0.246	−0.716	0.242	−0.684	0.239	0.660
C−H3	0.265	−0.850	0.221	−0.569	0.259	−0.812	0.081	0.009				
C−H4	0.265	−0.850	0.276	−0.948	0.259	−0.812	0.272	−0.919	0.272	−0.919	0.271	−0.911
Th−H(1)			0.113	0.067	0.110	−0.052	0.067	0.109	0.037	0.115		
H(1)−H(2)							0.167	−0.424	0.238	−0.882		

[a] ρ_b and $\nabla^2\rho_b$ in au. The corresponding values for the free CH_4 molecule are ρ(bcp) C−H = 0.272 au; $\nabla^2\rho$(bcp) C−H = −0.899 au; for H_2 ρ(bcp) = 0.261 au; $\nabla^2\rho$(bcp) = −1.056 au.

Table 5. Topological Properties of the Charge Density Calculated at the (3,−1) Bond Critical Points for All Species Involved in the $U^+ + CH_4$ Reaction Pathway[a]

	I (^{4}A)		**TS1′** (^{4}A)		**II** (^{4}A′)		**TS2′** (^{4}A)		**III** (^{4}A)		$U^+{=}CH_2$ (^{4}A″)	
bond	ρ(bcp)	$\nabla^2\rho$(bcp)	ρ(bcp)	$\nabla^2\rho$(bcp)	ρ(bcp)	$\nabla^2\rho$(bcp)	ρ(bcp)	$\nabla^2\rho$(bcp)	ρ(bcp)	$\nabla^2\rho$(bcp)	ρ(bcp)	$\nabla^2\rho$(bcp)
U−C	0.022	0.080	0.119	0.085	0.100	0.028	0.157	0.115	0.163	0.120	0.174	0.116
C−H1	0.266	−0.859	0.103	−0.039								
C−H2	0.266	−0.859	0.243	−0.699	0.266	−0.850	0.069	0.037				
C−H3	0.266	−0.859	0.278	−0.957	0.266	−0.850	0.272	−0.913	0.239	−0.664	0.236	−0.638
C−H4	0.272	−0.914	0.243	−0.699	0.266	−0.850	0.241	−0.678	0.271	−0.908	0.270	−0.900
U−H(1)			0.012	0.085	0.073	0.018						
H(1)−H(2)							0.183	−0.513	0.221	−0.755		

[a] ρ_b and $\nabla^2\rho_b$ in au. The corresponding values for the free CH_4 molecule are ρ(bcp) C−H = 0.272 au; $\nabla^2\rho$(bcp) C−H = −0.899 au; for H_2 ρ(bcp) = 0.261au; $\nabla^2\rho$(bcp) = −1.056 au.

reaching the lowest value in the first insertion intermediate (C(Th) + V(Th) = 26.5 e). This is an indication of a greater involvement of Th^+ valence electrons in the bond formation (as much as 2.5 e) compared to U^+ (not more than 1.5 e).

TS1 and TS1′. The ELF topological analysis of these structures shows that in both cases the first C−H bond breaking takes place at this stage of the reaction. This fact is evidenced by the lack of the V(C,H1) basin (see Tables 2 and 3) that is replaced by a trisynaptic V(Th,C, H1) basin with a population of 2.43 e, and a V(U,C,H1) basin in **TS1′** with 1.65 e. In both structures, therefore, the H atom being transferred belongs to a 3c-2e bond. We note, however, that the atomic electron contribution to that basin population comes mostly from the H atom in the case of the uranium structure (1.22 e) with small contributions from C (0.08 e) and U (0.34 e) atoms, whereas in the case of Th^+ the main contributors are the carbon (1.21 e) and the H atom (1.02 e). In the case of **TS1′** the U−C bond is already formed, as evidenced by the presence of a disynaptic V(C,U) basin with an electron population of 1.22 e. This basin is absent in the case of **TS1**. From a topological point of view, therefore, **TS1′** is much closer to the next minimum ($H-U^+-CH_3$) than **TS1**. As in the case of the first complex, the spin density is always localized on the metal atom.

According to AIM analysis, there is a strong lowering of the C−H(1) ρ(bcp) (0.15 au), whereas the Laplacian of the charge density is still negative but quite smaller than the corresponding values for the rest of the C−H bonds. The breaking of the first C−H bond is therefore supported by AIM analysis. There is also an important increasing of the ρ(bcp) at the An^+-C bond (around 0.11 au in both cases) (see Table 5). In both structures a bond critical point was localized between the metal atom and the hydrogen atom that is being transferred with a $\rho(\text{bcp}) = 0.113$ au (Th) and 0.012 au (U). In the case of **TS1**, the Laplacian of the charge density is small and negative (−0.057 au), whereas in **TS1′** that value is small and positive (+0.085 au).

The formation of the first transition state involves a charge transfer from the metal atom to the hydrogen atom that is being transferred (AIM charges around −0.2 e in both structures). As a consequence, the AIM charges on the metal center increase up to +1.38 (**TS1**) and +1.48 (**TS1′**), respectively (Table 1).

$H-Th^+-CH_3$ and $H-U^+-CH_3$. The formation of the first insertion intermediate provokes a further redistribution of charge and important topological changes. ELF analysis shows that in $H-An^+-CH_3$ (An = Th, U) structures the trisynaptic valence basin dissapears, being replaced by a disynaptic V(H1,An) basin, with a population of 2.25 e in $H-Th^+-CH_3$ and 1.78 e for $H-U^+-CH_3$. This is an indication of the formation of the An−H bond. The contribution to the V(H1,An) electron population coming from Th is around 33%, whereas that of U is much lower (almost 13% of the total basin population). These structures are also characterized by the presence of a disynaptic V(An,C) valence basin with a population close to two electrons, which represent a single covalent bond between the metal and carbon atoms. The contribution of Th to the V(Th,C) basin population is around 35%, whereas U contributes only 12% of the V(U,C) basin population, which is an indication of the presence of very polarized covalent bonds, as concluded also from the polarization coefficients of the corresponding NBO orbitals (Tables S3 and S4). As previously mentioned, the higher involvement of the electron charge in the case of the thorium structures is also evidenced by the strong lowering of the C(Th) + V(Th) value, which reaches a minimum in this intermediate (26.5 e; see Table 2).

This view is supported by AIM analysis, as indicated by the presence of a (3,−1) critical point between Th and H atoms, with a negative value of the Laplacian of the charge density (−0.052 au). In the case of the uranium structure the charge density on that bcp is slightly lower (0.073 au) compared with that of Th (0.113 au), and the Laplacian is small and positive (0.018 au).

The charge carried by the metal center has further increased. The AIM charge is +1.93 in the case of $H-Th^+-CH_3$ and +2.03 in $H-U^+-CH_3$. The natural charge distribution of both intermediates indicates that the transferred H atom is negatively charged (ca. −0.58 e in both structures).

TS2 and TS2′. The most notable topological feature of these structures is the presence of a polysynaptic basin, V(C, An,H1,H2), with an electron population close to three electrons. However, the electron contribution coming from the metal atoms is very small (around 0.07 e in both cases), and the increased population is due mainly to the high electron delocalization between this basin and the V(C,H3) and V(C,H4) ones. In both structures there is a V(An,C) disynaptic basin with a population of around 3.00 e, which indicates that the An−C bond can be considered intermediate between a single and double bond. Consistently, there is an increase of the charge density at the An−C bcp (Tables 4 and 5). This value increases steadily from the initial adduct to the dehydrogenation products. The two remaining valence basins correspond to the C−H bonds and have electron populations quite depleted (around 1.65 e) due to the great electron delocalization with the polysynaptic V(C,An,H1,H2) basin.

$(H_2)Th^+{=}CH_2$ and $(H_2)U^+{=}CH_2$. The ELF analysis of these reaction intermediates shows that the type of basins and electron populations are similar to those corresponding to the $An^+{=}CH_2$ products, in addition to a disynaptic V(H1,H2) basin with an electron population very close to two electrons. It is evident, therefore, that the H_2 molecule is already formed and that these structures can be considered as formed from two fragments, $Th^+{=}CH_2$ (or $U^+{=}CH_2$) and H_2. The ELF description of the second insertion intermediate is supported by the AIM analysis, which shows that the charge density and the Laplacian values for the H(1)−H(2) bcp are comparable to the corresponding values for the free H_2 molecule. The same properties for the An=C bcp's are comparable to those corresponding to the bare $An^+{=}CH_2$ products (see Tables 4 and 5).

$Th^+{=}CH_2$ and $U^+{=}CH_2$. ELF analysis indicates that both structures are characterized by the presence of two V(An,C) disynaptic valence basins with electron populations of 1.8 e ($Th^+{=}CH_2$) and 1.7 e ($U^+{=}CH_2$), respectively. These basins represent the An−C double bonds (see Tables 2 and 3), which have an important ionic character, as evidenced by the low contribution of the metal atoms to the basin population (almost 24% of the total population in the case of Th and 16% in the case of U).

The charge density at the $An^+{=}C$ (3,−1) bcp reaches a maximum in these species (around 0.18 au), whereas $\nabla^2\rho(r)$ at that point is still small and positive (Tables 4 and 5). No (3,−1) bcp was found between the metal atoms and the agostic H atom. Previous theoretical studies[28] have shown that neither of the topological methodologies used here (AIM, ELF) give evidence of an interaction between the metal center and the agostic H atom. NBO studies of transition metal species containing agostic geometries similar to those found in $Th^+{=}CH_2$ and $U^+{=}CH_2$ have justified

---

[28] (a) Vidal, I.; Melchor, S.; Alkorta, I.; Elguero, J.; Sundberg, M. R.; Dobado, J. A. *Organometallics* **2006**, *25*, 5638. (b) Berkäine, N.; Reinhardt, P.; Alikhani, M. E. *Chem. Phys.* **2008**, *343*, 241.

the higher stability of the distorted structures on a delocalization process that is evidenced through $\sigma_{CH} \rightarrow n^*_M$ hyperconjugation processes.[28b] However, no indication of this kind of second-order perturbation analysis stabilization was detected in the species studied in this work.

According to the NBO analysis, the An=C bond in both methylidenes can be described as a double bond. The σ-bond is formed from a thorium hybrid orbital that has 67% d- and 23% f-character (including also a very small contribution of p-orbitals) and $s_{31\%}-p_{69\%}$ hybrid orbitals of the carbon atom. In the case of uranium the hybridization involves also a small percentage of s- and p-orbitals ($d_{59\%}-f_{26\%}-s_{9\%}-p_{5\%}$). The π-bond is formed from a $d_{77\%}-f_{23\%}$ hybrid orbital in the case of Th and $d_{65\%}-f_{35\%}$ for U, both of which interact with pure p carbon orbitals. The description of the bond obtained at the present level of theory involves, therefore, an important participation of 5f-orbitals in both reaction products. The polarization coefficients (e.g., 0.9 for C and 0.5 for An; see Tables S4 and S5) indicate that the An−C bond can be considered as a highly polarized covalent bond. The unpaired electron is located on a hybrid orbital that has mainly s-character (86%) in the case of $Th^+=CH_2$, whereas for $U^+=CH_2$ the three unpaired electrons are located on pure f-orbitals.

The computed Th−C bond dissociation energy (BDE) $Th^+=CH_2$ is notably higher than the corresponding value for $U^+=CH_2$. In particular at the B3LYP/SDD level the Th−C BDE is 491 kJ/mol (577 kJ/mol at PW91/ZORA), compared to the 378 kJ/mol (493 kJ/mol at PW91/ZORA) obtained for the U−C BDE. We note that the estimations of the bond dissociation enthalpy limit implied from the observed reactions indicate that the Th−C BDE of $Th^+=CH_2$ is ≥ 460.4 kJ/mol.[8] The greater strength of the Th−C bond is evidenced in ELF analysis by a higher electron population of the V(Th,C) valence basins (Tables 2 and 3), whereas AIM analysis shows a greater value of the charge density (0.185 au) at the Th−C bond critical point compared to the corresponding value for the U−C bond (0.174 au).

4. Conclusions

The main conclusions drawn from this work can be summarized as follows.

4.1. Energetic Results. The $Th^+ + CH_4$ dehydrogenation reaction evolves on the doublet spin surface from the formation of the Th^+-CH_4 initial adduct. The reaction was found to be exothermic (almost 43 kJ/mol at the B3LYP/SDD level) with a very small barrier over the reactants asymptote (+5 kJ/mol at the B3LYP/SDD level). From the present computations the low efficiency of the $Th^+ + CH_4$ reaction could be justified only by the previously mentioned initial activation barrier. U^+ retains its quartet ground spin state configuration throughout the whole dehydrogenation process. At the B3LYP/SDD level the reaction is endothermic by almost 71 kJ/mol with reaction barriers well above (+57.4 kJ/mol) the limit represented by the reactants ($U^+[5f^3 7s^2] + CH_4$). Therefore, even when the dramatic difference in reactivity between Th^+ and U^+ is mainly attributable to thermodynamic differences, there is also some kinetic hindrance during the initial $U^+ + CH_4$ oxidation process. This result justifies the nondetection of reactivity for U^+ at thermal reactions.

For both reactions the first insertion intermediate, $H-An^+-CH_3$, is the global minimum of the potential energy profiles, and its formation is an exothermic process, in both studied reactions. The other possible reaction channels (formation of $AnCH_3^+ + H$ or $AnH^+ + CH_3$) were found to be highly endothermic for both reactions (between 112 and 170 kJ/mol at B3LYP/SDD).

The metal−methylidene binding energies were also computed. For $Th^+=CH_2$ that value was found to be 491 kJ/mol, whereas the corresponding value for $U^+=CH_2$ is 378 kJ/mol (B3LYP/SDD computations).

4.2. Bonding Analysis. From a topological point of view, the evolution of the bonding along both studied reactions is qualitatively similar. Quantitatively, however, the higher involvement of the thorium electron density in the formation of the bonding is evident, as demonstrated by the important diminishing of the C(Th) + V(Th) electron population (ELF analysis). That value reaches a minimum in the $H-Th^+-CH_3$ insertion intermediate. ELF analysis shows that both H atom transfers take place through the formation of polysynaptic basins. The breaking of the first C−H bond is facilitated by the transfer of electron density from the valence metal basins to the V(C,H) basin of methane, resulting in the formation of a trysinaptic V(An,C,H) basin containing two electrons (3c-2e bond). The second transfer takes place through the formation of a polysynaptic basin that involves both H atoms, as well as the metal and carbon atoms. The last insertion intermediate, $(H_2)An^+=CH_2$, as well as the $An^+=CH_2$ reaction products are characterized by the presence of agostic geometries.

Acknowledgment. This research was funded by the Università della Calabria.

Supporting Information Available: Computed bare cation energy gaps, BDEs for different An^+-R species, and NBO analyses of some of the species involved in the studied reaction pathways. This material is available free of charge via the Internet at http://pubs.acs.org.

Supporting Information

Methane C-H Bond Activation by Gas-Phase Th^+ and U^+: Reaction Mechanisms and Bonding Analysis

Emanuela Di Santo, Maria del Carmen Michelini, and Nino Russo

Dipartimento di Chimica and Centro di Calcolo ad Alte Prestazioni per Elaborazioni Parallele e Distribuite-Centro d'Eccellenza MURST, Università della Calabria, I-87030 Arcavacata di Rende, Italy

Table of Contents:

AIM and ELF analysis

Table S1 Relative energies, in kJ/mol, of the low energy excited states of the Th^+ and U^+ cations with respect to the corresponding ground states.

Table S2 Calculated and experimental estimations of bond dissociation energies (BDE, in kJ/mol) for different Th^+-R species (R= CH_2, CH_4, C_2H_2, C_2H_4, C_2H_6)

Table S3 Calculated bond dissociation energies (BDE, in kJ/mol) for different U^+-R species (R= CH_2, CH_4, C_2H_2, C_2H_4, C_2H_6)

Table S4 Natural Bond Orbital Analysis of Th^+–C for some of the species involved in the Th^++CH_4 pathway.

Table S5 Natural Bond Orbital Analysis of U^+–C for some of the species involved in the U^++CH_4 pathway.

AIM Analysis

The atoms-in-molecules (AIM) theory[1] reveals insightful information on the nature of bonds. This theory is based on the critical points (CP) of the electronic density, $\rho(\mathbf{r})$. These are points where the gradient of the electronic density, $\nabla\rho(\mathbf{r})$, vanishes and are characterized by the three eigenvalues (λ_1, λ_2, λ_3) of the Hessian matrix of $\rho(\mathbf{r})$. The CPs are labeled as (r,s) according to their rank, r (number of nonzero eigenvalues), and signature, s (the algebraic sum of the signs of the eigenvalues).

Four types of CPs are of interest in molecules: (3,-3), (3,-1), (3,+1), and (3,+3). A (3,-3) point corresponds to a maximum in $\rho(\mathbf{r})$ and occurs generally at the nuclear positions. A (3,+3) point indicates electronic charge depletion and is known as cage CP. (3,+1) points, or ring CP, are merely saddle points. Finally, a (3,-1) point or bond critical point (BCP), is generally found between two neighboring nuclei indicating the existence of a bond between them. Several properties that can be evaluated at a bond critical point (BCP) constitute very powerful tools to classify the interactions between two fragments.

The two negative eigenvalues of the Hessian matrix (λ_1 and λ_2) at the BCP measure the degree of contraction of $\rho(\mathbf{r})$ perpendicular to the bond toward the critical point, while the positive eigenvalue (λ_3) measures the degree of contraction parallel to the bond and from the BCP toward each of the neighboring nuclei. Unequal values of λ_1 and λ_2 at (3,-1) BCP´s denote an anisotropic spread of electrons quantified through the concept of ellipticity: $\varepsilon = \lambda_1/\lambda_2 - 1$, (with $\lambda_1 > \lambda_2$) where values of $\varepsilon >> 1$ can be indicative of π bonding. Calculated properties at the BCP of the electronic density are labeled with the subscript 'b' throughout the work.

In the AIM theory atomic interactions are classified according to two limiting behaviors, namely, shared interactions and closed-shell interactions. Shared interactions are characteristic of covalent and polarized bonds and their main features are large values of ρ_b, $\nabla^2\rho_b < 0$ and $E_b < 0$, E_b being the local electronic energy density of the system calculated at the BCP and defined as the sum of the local kinetic energy density and the local potential energy density, both computed at the BCP. In contrast, closed-shell interactions, useful to describe ionic bonds, hydrogen bonds, and van der Waals interactions, are characterized by small values of ρ_b, $\nabla^2\rho_b > 0$ and $E_b > 0$. Within the framework of AIM analysis the variance, $\sigma^2(\Omega_A)$ of the atomic basin populations can be spread in terms of the contribution from other basins, the covariance, $\mathrm{cov}(\Omega_{A,}\ \Omega_B)$, which has a clear relationship with the so-called delocalization index, $\delta(\Omega_{A,}\ \Omega_B)$[2a,b]

$$\mathrm{cov}(\Omega_{A,}\ \Omega_B) = -\ \delta(\Omega_{A,}\ \Omega_B)/2$$

The delocalization index accounts for the electrons delocalized or shared between the basins Ω_A and Ω_B. In the single determinant approach this index is exactly the topological bond order defined by Ángayán and co-workers.[2c] We must mention, however, that even when for molecular bonds with equally shared pairs a simple relationship between the delocalization index and the formal bond order (number of Lewis bonded pairs) has been generally found,[2d] for polar bonds there is no longer such a simple relationship. It has been shown that the delocalization index tend to decrease with the increased electronegativity difference of the atoms involved in the bond. There has been some discussion in the past regarding the use of this index as a covalent bond order.[2d,e]

ELF Analysis

The Electron Localization Function (ELF) analysis is based on the topology of the gradient vector field of the Becke and Edgecombe[3] electron localization function, as implemented by Silvi and Savin.[4] The ELF has been suggested to be a measure of the excess of kinetic energy density due to the Pauli repulsion[5]

$$\eta(r) = \frac{1}{1 + (\frac{D_\sigma(r)}{D_\sigma^0(r)})}$$

where D_σ (r) is the local excess kinetic energy density due to Pauli repulsion and $D_\sigma{}^0$ (r) is the kinetic energy density of a reference homogeneous electron gas of the same electron
density, a value that essentially acts as a renormalization factor.

Values of $\eta(r)$ thus range from 0 to 1 with larger values denoting larger electron localization, i.e., a higher probability of finding electrons alone or in pairs of antiparallel spin. The gradient field of the ELF, $\nabla\eta(r)$, can be also used to partition the space into localization basins, Ω_A.[4] Each of these basins contains a (3,-3) critical point of $\eta(r)$, also referred to as an attractor, which may or may not contain an atomic center. Basins are visualized for any given isodensity value of $\eta(r) = f$, which in turn encompass regions of $\eta(r) \geq f \leq 1$. Basins are classified as either (1) core basins, C(A), encompassing a nucleus ($Z > 2$) and core electrons, or as (2) valence basins, V(A,...), encompassing valence shell electrons.[4] Valence basins are furthermore categorized by their synaptic order which refers to the number of core basins with which they share a common boundary. A monosynaptic basin, V(A), encompasses lone pairs while a polysynaptic basin, V(A,...), encompasses electrons involved in bi- or polycentric bonds. The presence of a di- or polysynaptic basin is indicative of a shared interaction of electrons (covalent, dative, or metallic bonds), while its absence denotes a closed-shell interaction (ionic, van der Waals or hydrogen bond). Basin-related properties are calculated by integrating a certain property over the volume of the basin. For instance, the electronic population of a synaptic basin, $\bar{N}(\Omega_A)$, is obtained as the integral of the one-electron density over the basin Ω_A. The variance of the basin population,

$\sigma^2[\bar{N}(\Omega_A)]$, which is the square of the standard deviation of the population, represents the quantum-mechanical uncertainty of the basin population and is a consequence of the delocalization of electrons. It has the meaning of an excess in the number of pairs due to the interaction of Ω_A with other basins, and is usually written as the sum of contributions of all other basins. Within ELF analysis a multiple bond is characterized by a basin population $\bar{N}(\Omega_A)$ higher that 2.0 electrons and a variance $\sigma^2[\bar{N}(\Omega_A)]$ lesser than the corresponding basin population. The topological representation obtained from ELF analysis, is usually interpreted in terms of superposition of mesomeric structures.[6]

References

(1) R. F. W.Bader, *Atoms in Molecules. A Quantum Theory*, Oxford, University Press, 1990.

(2) (a) Fradera, X.; Austen, M. A.; Bader, R. F. W. *J. Phys. Chem. A* **1999**, *103*, 304. (b) Fradera, X.; Poater, J.; Simon, S.; Duran, M.; Solà, M. *Theor. Chem. Acc.* **2002**, *108*, 214.(c) Ángayán, J.G.; Loos, M.; Mayer, I *J. Phys. Chem.* **1994**, *98*, 5244. (d) Poater, J.; Duran, M.; Solà, M.; Silvi, B. *Chem. Rev.* **2005**, *105*, 3911 (e) Fradera, X.; Solà, M. *J. Comput. Chem.* **2002**, *23*, 1347.

(3) Becke, A. D.; Edgecombe, K. E. *J. Chem. Phys.* **1990,** *92,* 5397.

(4) (a) Silvi, B.; Savin, A. *Nature* **1994**, *371*, 683; (b) Savin, A.; Silvi, S.; Colonna, F. *Can. J. Chem.* **1996**, *74*, 1088.

(5) Savin, A.; Flad, J.; Preuss, H.; von Schnering, H. G. *Angew. Chem.* **1992,** *104*, 185.

(6) (a) Silvi, B. *Phys Chem. Chem. Phys*, **2004**, *6,* 256; (b) Lepetit, C.; Silvi, B.; Chauvin, R. *J. Phys. Chem. A* **2003**, *107*, 464. (c) Pilme, J.; Silvi, B.; Alikhani, M. E. *J. Phys. Chem. A* **2005**, *109*, 10028.

Full citation of Reference 17 :

Gaussian 03, Revision C.02, Frisch, M. J.; Trucks, G. W.; Schlegel, H. B.; Scuseria, G. E.; Robb, M. A.; Cheeseman, J. R.; Montgomery, Jr., J. A.; Vreven, T.; Kudin, K. N.; Burant, J. C.; Millam, J. M.; Iyengar, S. S.; Tomasi, J.; Barone, V.; Mennucci, B.; Cossi, M.; Scalmani, G.; Rega, N.; Petersson, G. A.; Nakatsuji, H.; Hada, M.; Ehara, M.; Toyota, K.; Fukuda, R.; Hasegawa, J.; Ishida, M.; Nakajima, T.; Honda, Y.; Kitao, O.; Nakai, H.; Klene, M.; Li, X.; Knox, J. E.; Hratchian, H. P.; Cross, J. B.; Bakken, V.; Adamo, C.; Jaramillo, J.; Gomperts, R.; Stratmann, R. E.; Yazyev, O.; Austin, A. J.; Cammi, R.; Pomelli, C.; Ochterski, J. W.; Ayala, P. Y.; Morokuma, K.; Voth, G. A.; Salvador, P.; Dannenberg, J. J.; Zakrzewski, V. G.; Dapprich, S.; Daniels, A. D.; Strain, M. C.;

Farkas, O.; Malick, D. K.; Rabuck, A. D.; Raghavachari, K.; Foresman, J. B.; Ortiz, J. V.; Cui, Q.; Baboul, A. G.; Clifford, S.; Cioslowski, J.; Stefanov, B. B.; Liu, G.; Liashenko, A.; Piskorz, P.; Komaromi, I.; Martin, R. L.; Fox, D. J.; Keith, T.; Al-Laham, M. A.; Peng, C. Y.; Nanayakkara, A.; Challacombe, M.; Gill, P. M. W.; Johnson, B.; Chen, W.; Wong, M. W.; Gonzalez, C.; and Pople, J. A.; Gaussian, Inc., Wallingford CT, 2004.

Table S1 Relative energies, in kJ/mol, of the low energy excited states of the Th^+ and U^+ cations with respect to the corresponding ground states. Spin multiplicity is given in parenthesis.

Th^+	Expt.[a]	PW91/ZORA[c]	B3LYP/SDD[c]
[Rn]$6d^27s$ (4)	**0.0** (^4F-^2D)[b]	**0**	24
[Rn]$6d7s^2$ (2)	49.2(^4F-^2D)[b]	46	31
[Rn].$5f7s^2$ (2)	53.7	17	**0**
[Rn]5f6d7s (4)	73.8	40	57
[Rn] $6d^3$ (4)	83.8	69	97
U^+	Expt.[a]	PW91/ZORA[d]	B3LYP/SDD[d]
[Rn]$5f^37s^2$ (4)	**0.0**	55	**0**
[Rn]$5f^36d7s$ (6)	3.5	68	6
[Rn] $5f^47s$ (6)	55.8	**0**	17
[Rn]$5f^37s^2$ (2)	115.9	156	71

[a] Lowest energy levels of each configurations taken from Blaise, J.; Wyart, J.-F. International Tables of Selected Constants, Energy Levels and Atomic spectra of Actinides, Vol. 20, Tables of Constants and Numerical Data, Paris, 1992, taken from http://www.lac.u-psud.fr/Database/Contents.html.

[b] The GS level is not actually identified in the experimental tables due to strong configuration mixing. The [Rn]$6d^27s$ (^4F) and the[Rn]$6d7s^2$ (^2D) configurations accounts for less than 50 % of the eigenfunction.

[c] Taken from Mazzone, G.; Michelini, M. C.; Russo, N.; Sicilia, E. *Inorg. Chem.* **2008**, *47*, 2083.

[d] Taken from Michelini, M. C.; Russo, N.; Sicilia, E. *Angew. Chem. Int. Ed.* **2006**, *45*, 1095.

Table S2 Calculated and experimental estimations of bond dissociation energies (BDE, in kJ/mol) for different Th^+-R species (R= CH_2, CH_4, C_2H_2, C_2H_4, C_2H_6) [a]

Species (Multiplicity)	**This work B3LYP/SDD**	**This work PW91/ZORA**	**Expt** [b]
$Th^+= CH_2$ (2)	491.2	577.3	≥ 460.4[c] ≥ 465[d]
$Th^+–CH_4$ (2)	30.9	101.4	-
$Th^+–C_2H_2$ (2)	321.0	415.3	≥ 312.0[c]
$Th^+–C_2H_4$ (2)	233.8	333.0	≥ 136.3[c]
$Th^+–C_2H_6$ (2)	33.4	124.9[e]	-
$Th–H^+$	287.2	337.2	-

[a] Energies were calculated from the energy difference between the Th^+-R absolute energy and the corresponding values for the Th^+ + R asymptotes, with all the species in their GSs. All BDE values include zero point energy corrections.

[b] Bond dissociation enthalpy limits implied from the observed reactions.

[c] Marçalo, J.; Leal, J. P.; Pires de Matos, A. *Int. J. Mass Spectrom. and Ion Processes* **1996**, *157/158*, 265.

[d] Gibson, J. K.; Haire, R. G.; Marçalo, J.; Santos, M.; Pires de Matos, A.; Mrozik, M. K.; Pitzer, R. M, Bursten, B. E. *Organometallics* **2007**, *26*, 3947.

[e] At PW91/ZORA the GS is a quartet state followed very close in energy (+ 4 kJ/mol) by a doublet spin state isomer.

Table S3 Calculated and experimental estimations of bond dissociation energies (BDE, in kJ/mol) for different U^+-R species (R= CH_2, CH_4, C_2H_2, C_2H_4, C_2H_6) [a]

Species (Multiplicity)	**This work B3LYP/SDD**	**This work PW91/ZORA**	**Expt**[d]
$U^+=CH_2$ (4)	377.9	493.1	-
$U^+–CH_4$ (4)	21.6	77.0[b]	-
$U^+–C_2H_2$ (4)	178.6	322.4	-
$U^+–C_2H_4$ (4)	124.5	248.7	-
$U^+–C_2H_6$ (4)	19.2	95.7[c]	-
$U–H^+$	227.2	284.1	280 ± 19

[a] Energies were calculated from the energy difference between the U^+-R absolute energy and the corresponding values for the U^+ + R asymptotes, with all the species in their GSs. All BDE values include zero point energy corrections.
[b] At PW91/ZORA the GS is a sextet state followed very close in energy (+ 3 kJ/mol) by a quartet spin state isomer.
[c] At PW91/ZORA the GS is a sextet state followed close in energy (+ 10 kJ/mol) by a quartet spin state isomer.
[d] Armentrout, P.; Hodges, R. and Beauchamp, J. L. *J. Am. Chem. Soc.* **1977**, *99*, 3162.

Table S4 Natural Bond Orbital Analysis corresponding to the Th^+-C bond for some of the species involved in the $Th^+ + CH_4$ pathway.[a]

Species (State)	Alpha Spin Orbitals	Beta Spin Orbitals
II (^{2}A')	BD (Th–C) = 0.9 $[s_{18\%} - p_{82\%}]_C + 0.5\ [d_{64\%} - f_{21\%} - s_{12\%}]_{Th}$ LP: Th $(s_{61\%}\text{-}d_{34\%})$	BD (Th–C) = 0.9 $[s_{19\%} - p_{81\%}]_C + 0.4\ [d_{57\%} - f_{20\%} - s_{20\%}]_{Th}$
TS2 (^{2}A)	BD (Th–C) = 0.9 $[s_{2\%} - p_{98\%}]_C + 0.5\ [d_{61\%} - f_{33\%} - s_{7\%}]_{Th}$ LP: Th $(s_{61\%}\text{-}d_{33\%}\text{-}f_{4\%})$	BD (Th–C) = 0.9 $[s_{2\%} - p_{98\%}]_C + 0.5\ [d_{54\%} - f_{29\%} - s_{17\%}]_{Th}$
III (^{2}A)	BD (Th–C) = 0.9$[s_{31\%} - p_{68\%}]_C + 0.5\ [d_{67\%} - f_{23\%} - s_{7\%}]_{Th}$ BD (Th–C) = 0.9 $[p]_C + 0.5[d_{67\%} - f_{23\%}]_{Th}$ LP: Th $(s_{67\%}\text{-}d_{30\%}\text{-}f_{3\%})$	BD (Th–C) = 0.9 $[s_{32\%} - p_{68\%}]_C + 0.4\ [d_{59\%} - f_{23\%} - s_{14\%}]_{Th}$ BD (Th–C) = 0.9 $[p]_C + 0.5[d_{75\%} - f_{23\%}]_{Th}$
Th^+=CH_2 (^{2}A')	BD (Th–C) = 0.9 $[s_{31\%} - p_{69\%}]_C + 0.5\ [d_{67\%} - f_{23\%} - p_{5\%}]_{Th}$ BD (Th–C) = 0.9 $[p]_C + 0.5[d_{77\%} - f_{23\%}]_{Th}$ LP: Th $(s_{86\%}\text{-}d_{12\%}\text{-}f_{2\%})$	BD (Th–C) = 0.9 $[s_{32\%} - p_{68\%}]_C + 0.5\ [d_{60\%} - f_{25\%} - s_{10\%}]_{Th}$ BD (Th–C) = 0.9 $[p]_C + 0.5[d_{76\%} - f_{24\%}]_{Th}$

[a] BD: bonding orbital, LP: unpaired electron orbital.

Table S5 Natural Bond Orbital Analysis corresponding to the U^+-C bond for some of the species involved in the U^++CH_4 pathway. [a]

Species (State)	Alpha Spin Orbitals	Beta Spin Orbitals
II (^{4}A’)	BD (U–C) = $0.9\ [s_{16\%} - p_{84\%}]_C + 0.4\ [d_{55\%} - f_{23\%} - s_{20\%}]_U$ 3 LP: U (pure f orbitals)	BD (U–C) = $0.9\ [s_{16\%} - p_{84\%}]_C + 0.4\ [d_{56\%} - f_{18\%} - s_{24\%}]_U$
TS2 (^{4}A)	BD (U–C) = $0.8\ [s_{2\%} - p_{98\%}]_C + 0.5\ [d_{49\%} - f_{35\%} - s_{15\%}]_U$ 3 LP: U (pure f orbitals)	BD (U–C) = $0.9\ [s_{2\%} - p_{98\%}]_C + 0.5\ [d_{51\%} - f_{33\%} - s_{15\%}]_U$
III (^{4}A)	BD (U–C) = $0.9\ [s_{29\%} - p_{71\%}]_C + 0.5\ [d_{56\%} - f_{27\%} - s_{13\%}]_U$ BD (U–C) = $0.9\ [p]_C + 0.5\ [d_{64\%} - f_{32\%} - s_{4\%}]_U$ 3 LP: U (pure f orbitals)	BD (U–C) = $0.9\ [s_{31\%} - p_{69\%}]_C + 0.4\ [d_{51\%} - f_{30\%} - s_{15\%}]_U$ BD (U–C) = $0.9\ [p]_C + 0.5\ [d_{63\%} - f_{31\%} - s_{5\%}]_U$
U^+=CH_2 (^{4}A”)	BD (U–C) = $0.9\ [s_{29\%} - p_{71\%}]_C + 0.5\ [d_{59\%} - f_{26\%} - s_{9\%}]_U$ BD (U–C) = $0.9\ [p]_C + 0.5\ [d_{65\%} - f_{35\%}]_U$ 3 LP: U (pure f orbitals)	BD (U–C) = $0.9\ [s_{31\%} - p_{74\%}]_C + 0.4\ [d_{56\%} - f_{31\%} - s_{8\%}]_U$ BD (U–C) = $0.9\ [p]_C + 0.4\ [d_{70\%} - f_{30\%}]_U$

[a] BD: bonding orbital, LP: unpaired electron orbital.

Pubblicazione II

Activation of ethane C-H and C-C bonds by gas-phase Th^+ and U^+: a theoretical study.

Emanuela Di Santo, Maria del Carmen Michelini, Nino Russo

J.Phys.Chem. A **2009**, 113, 14699-14705.

J. Phys. Chem. A **2009,** *113,* 14699–14705

Activation of Ethane C−H and C−C Bonds by Gas Phase Th^+ and U^+: A Theoretical Study[†]

E. Di Santo, M. C. Michelini, and N. Russo*

Dipartimento di Chimica and Centro di Calcolo ad Alte Prestazioni per Elaborazioni Parallele e Distribuite-Centro d'Eccellenza MURST, Università della Calabria, I-87030 Arcavacata di Rende, Italy

Received: May 22, 2009; Revised Manuscript Received: August 11, 2009

Two different approaches of density functional theory were used to analyze the C−H and C−C bond activation mechanisms during the reaction of bare Th^+ and U^+ ions with ethane. We report a complete exploration of the potential energy surfaces taking into consideration different spin states. According to B3LYP/SDD computations the double dehydrogenation of C_2H_6 is thermodynamically favorable only in the case of Th^+. It is shown that the overall C−H and C−C bond activation processes are exothermic in the case of Th^+ and endothermic for U^+. In both cases, the C−C insertion transition state barrier exceeds the energy of the ground state reactants, preventing the observation of these species under thermal conditions.

1. Introduction

In the past decade a great body of studies has been performed on the reactivity of actinide cations with small molecules in the gas phase.[1−4] This research has been mainly carried out using mass spectroscopic techniques, which are able to provide thermochemical data as well as some insight into the reaction mechanisms.[1−3] The main goal of these studies has been to analyze the reactivity and bonding of the metal ions, which in the absence of perturbing factors correlate directly with their electronic structures and energetics. In early actinides it is particularly interesting to analyze the possible active role of the 5f electrons in reactivity. Recent theoretical calculations have permitted a detailed description of the reaction mechanisms of activation of small molecules by bare actinide cations.[4]

The activation of C−H and C−C bonds by transition metal (TM) ions in the gas phase has been an active area of research that provides fundamental information on reaction mechanisms, kinetics, and thermodynamics.[5]

A number of experimental and theoretical studies on the reactivity of bare transition-metal ions with methane have provided a wealth of insight concerning the C−H bond activation process.[6−10] Those studies have demonstrated that none of the first- or second-row transition metal ions reacts with methane at thermal energies. In contrast, it was shown that several of the third-row transition metal ions (Ta^+, W^+, Os^+, Ir^+, and Pt^+) react exothermically to dehydrogenate methane.[8−10] In a recent series of papers, Armentrout and co-workers have revisited, both experimentally and theoretically, the reactivity of most of the third-row TMs monocations (Hf^+, Ta^+, W^+, Re^+, Ir^+, Pt^+, and Au^+) with CH_4.[10]

Recent theoretical works[4e,11] have reported the reaction mechanisms of the interaction of actinide monocations with CH_4.

Ethane is the simplest alkane in which both the C−H and C−C bonds can be activated. Detailed experimental and theoretical studies of the reactivity of the first-[12] and second-row[13] transition metal ions with C_2H_6 have given insight into the electronic requirements of the metal for C−H and C−C bond activation. It was reported that the early members of the first-row TM series (Sc^+, Ti^+, and V^+) show no barrier and exhibit large cross sections for dehydrogenation of ethane, whereas for Fe^+, Co^+, and Ni^+ the reaction occurs with substantial activation barriers. For Cr^+, Mn^+, and Cu^+, no reaction is observed. Demethanation is observed only for the 3d metals Sc^+−Cr^+. It was generaly found that the reactivity is highly dependent on the spin state. In particular, in the cases in which the rate-determining step is the insertion of the metal into a C−H or a C−C bond, the electron spin conservation and electronic configuration restrict which reactant states are more active. Low-spin states are usually more efficient due to the spin-allowed reaction. For a recent review on this subject see ref 5e. For earlier reviews see refs 6b, 6d, and 14.

The reactivity of the 4d transition metal cations with C_2H_6 and higher alkanes has been much less studied, and only in a few cases were the reaction mechanisms studied in detail.[13]

The reactivity of thorium cations with alkanes and alkenes has been studied by Marçalo and co-workers using Fourier transform ion cyclotron resonance/mass spectrometry (FTICR-MS).[3a] It was found that Th^+ ions react exothermically with the studied alkanes and alkenes giving single and/or double dehydrogenation. In the particular case of ethane, the reaction leads to single and double dehydrogenation, with formation of $ThC_2H_4^+$ and $ThC_2H_2^+$ in a 1:1 ratio with a moderate efficiency. More recently, the gas-phase reactions of An^+ and AnO^+ ions (An = Th through Cm) with hydrocarbons has been systematically examined using FTICR-MS techniques.[3b] The results obtained for the reaction of Th^+ with C_2H_6 are in agreement with the earlier results obtained by Marçalo and collaborators.[3a] In the case of uranium the efficiency is under the detection limit ($k/k_{COL} \leq 0.001$).[3b]

Determining reaction mechanisms is one of the more challenging problems in computational chemistry. It has been shown that reactions involving gas-phase An^+ ions often involve crossings between surfaces of different spin states,[4] as usually occur in transition metal mediated reations. The idea of state-selective reactivity has been introduced, at first, by Armentrout and co-workers and the role of spin flip in organometallic chemistry has been underlined by the introduction of the so-called Two State Reactivity (TSR) paradigm.[6b,15] In the case of actinide chemistry the formal spin may vary during a reaction

---

[†] Part of the "Vincenzo Aquilanti Festschrift".

* Author to whom correspondence should be sent, nrusso@unical.it.

10.1021/jp9048154

without appreciably affect the rate due to the fact that weak spin−orbit coupling does not apply to the heavy metal ions and the requirement for spin-conservation is thereby relaxed.

In the framework of a more extended project[4] aiming to unravel the mechanistic details of catalytic processes for the activation of prototypical bonds mediated by bare actinide ions, we have analyzed the reaction of thorium and uranium monocations with ethane. Density functional theory (DFT) has been applied to characterize all the intermediates and first-order saddle points and to obtain a complete mechanistic scheme of the reactions.

The reaction mechanisms for the activation of both the C−C and C−H bonds have been studied according to the general scheme proposed for this kind of reaction that involves as the first step the formation of a metal−ligand adduct followed by an oxidative insertion of the metal center into a ligand molecule bond. The formation of the first insertion intermediate is usually the key step of the whole process, and its formation involves often a crossing between different spin surfaces. The next steps are migration of one or more atoms of the ligand molecule to the metal and reductive elimination of a small molecule provided that intermediates have sufficiently high lifetimes to undergo rearrangements. Bond breakings that are generally not accessible at thermal energies become dominant at high energies.

2. Computational Details

We have used two different approaches of DFT to analyze the reactions under study. This choice was made on the base of the performance observed in our previous studies of the bare actinide cations reactivity.[4] First, DFT in its three-parameter hybrid B3LYP[16] formulation was used together with the Stuttgart−Dresden basis set for the uranium atom (25s 16p 15d 7f)/[7s 6p 5d 3f] in combination with the 60 core electrons[17] relativistic effective core potential (RECP). This small-core RECP, so-called SDD pseudopotential, replaces the 60 electrons in the inner shells 1 through 4, leaving the explicit treatment of the $n = 5$ shell (5s 5p 5d and 5f), and also the 6s, 6p, 6d, and 7s valence electrons. The 6-311++G(d,p) basis set of Pople and co-workers was employed for the rest of the atoms[18] (we refer to these results as B3LYP/SDD, hereafter). These calculations were carried out with the GAUSSIAN 2003 package.[19]

Further calculations were done using the ADF2004.01 package.[20] The zero-order regular approximation (ZORA) was employed in ADF calculations. This approximation was used together with the PW91 functionals (exchange and correlation)[21] and triple-ζ (TZ2P) basis sets (PW91/ZORA level, hereafter). We have used the frozen-core approach as implemented in ADF to describe the inner electrons of thorium and uranium. Therefore, for both actinide cations all electrons up to 5d were considered as frozen, the remaining electrons constituted the active valence shell.

Full geometry optimizations were performed at both, B3LYP/SDD and PW91/ZORA levels, trying several initial geometries for each species. The nature of the calculated stationary points was characterized by a vibrational analysis performed within the harmonic approximation. The zero-point vibrational energy corrections were included in all the reported relative energies. We have ensured that every transition state has only one imaginary frequency and that the frequency connects reactants and products by means of IRC (intrinsic reaction coordinate) calculations. Unless otherwise mentioned, all energies and geometrical parameters reported in the next sections refers to the B3LYP/SDD results, whereas in all figures are reported the results obtained at both levels of theory. We have chosen the B3LYP/SDD computations as our reference results, due to the better agreement of these results with the existent experimental data. In section 4 we present a comparison of the results obtained at B3LYP/SDD and PW91/ZORA levels.

3. Results and Discussion

3.1. An^+ (An = Th, U) + C_2H_6: Bare Cations and Reaction Mechanisms. At the B3LYP/SDD level the doublet [Rn]5f7s^2 configuration is the lowest-energy electronic configuration of Th^+, with the quartet [Rn]6d^{2}7s 24 kJ/mol higher in energy, whereas at the PW91/ZORA level of theory the bare Th^+ ground state (GS) has a quartet spin state derived from the [Rn]6d^{2}7s configuration. The GS level of the Th^+ cation is actually not identified in the Blaise and Wyart tables[22] due to a strong multiconfiguration mixing. The ground level has a mixed $^4F-^2D$ character.

According to the Blaise and Wyart tables, the lowest-energy U^+ has a [Rn]5f^{3}7s^2 electronic configuration (quartet spin state) and is followed closely by several sextet spin states.[22] In this case, the experimental bare cation levels are better reproduced by B3LYP/SDD computations. The calculated GS has in fact a [Rn]5f^{3}7s^2 electronic configuration (quartet state) and is followed by two sextet states very close in energy, [Rn]5f^{3}6d7s at around 6 kJ/mol and the [Rn]5f^{4}7s state at 17 kJ/mol, whereas the [Rn]5f^{3}7s^2 doublet spin state is much higher in energy (around 71 kJ/mol over the quartet GS). At the PW91/ZORA level the computed GS has a [Rn]5f^{4}7s (sextet) configuration, whereas the [Rn]5f^{3}7s^2 (quartet) was found at 55 kJ/mol over the GS. The details of the calculated bare cations energy gaps have been reported elsewhere.[4a,c,e]

In our calculations we have explored the first and second dehydrogenation and the demethanation of C_2H_6 by bare Th^+ and U^+ cations. The activation of the first C−H bond yields to the formation of $AnC_2H_4^+$ (An = Th, U) with the release of one H_2 molecule, whereas the activation of the C−C bond yields to the formation of the methylidene complex, $AnCH_2^+$, and CH_4. The second dehydrogenation reaction, which starts with the reaction product of the first H_2 elimination, $AnC_2H_4^+$, involves the activation of two C−H bonds and leads to the formation of $AnC_2H_2^+$.

As in the case of the activation of alkanes by transition metal cations,[12,13] the proposed mechanisms involve an initial oxidative mechanism in which the cation An^+ inserts in the C−H or C−C bond to form a first insertion intermediate $C_2H_5-An^+-H$ or $CH_3-An^+-CH_3$. The reaction products can then be formed by reductive elimination of small molecules such as H_2 and CH_4 or by metal−hydrogen or metal−carbon bond cleavage, which usually takes place at high energies. From the $C_2H_5-An^+-H$ intermediate the dehydrogenation process evolves through the formation of a dihydride intermediate, $(H)_2An^+-C_2H_4$, which reductively eliminates H_2. The reaction mechanism involves the formation of a third intermediate, $(H_2)An^+-C_2H_4$ in which the H_2 molecule is already formed and prepared for the elimination. In contrast, the demethanation process involves only two transition states, the first one that yields to the formation of the previously mentioned dimethyl intermediate, $CH_3-An^+-CH_3$, and a second transition state that involves the transfer of an H atom between the methyl groups, to form the final adduct $(CH_4)An^+-CH_2$. We note that in most of the reaction pathways reported for the C−H bond activation of C_2H_6 by TM cations, the reaction mechanism does not involve a β-hydrogen shift resulting in dihydrido intermediates. Instead, the reactions usually proceed through a concerted saddle point connecting the C−H inserted species directly with a complex of the TM cation with molecular hydrogen and ethylene.

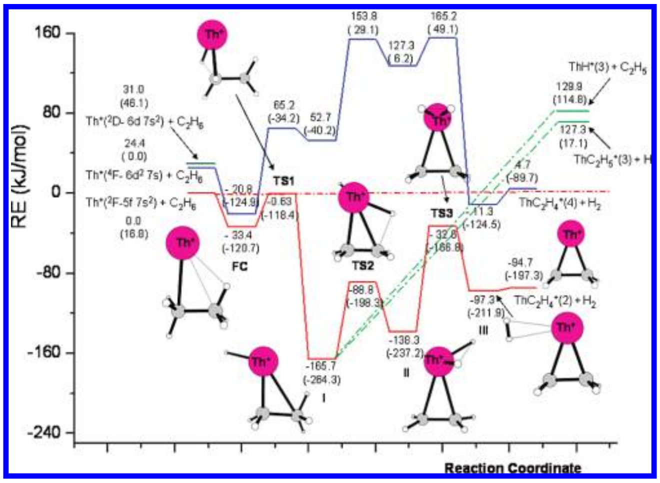

Figure 1. B3LYP/SDD (PW91/ZORA) quartet and doublet PESs for the first dehydrogenation of C_2H_6 by Th$^+$. Energies are in kJ/mol and relative to the ground-state reactants.

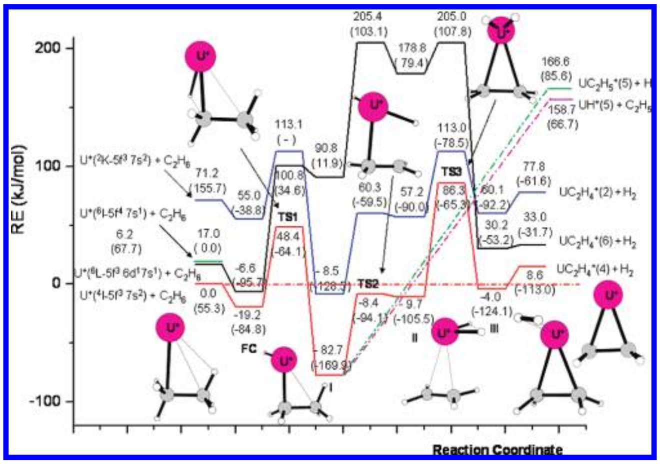

Figure 2. B3LYP/SDD (PW91/ZORA) quartet, sextet, and doublet PESs for the first dehydrogenation of C_2H_6 by U$^+$. Energies are in kJ/mol and relative to the ground-state reactants.

The second dehydrogenation reaction starts with the $AnC_2H_4^+$ adduct and as in the case of the first dehydrogenation reaction involves three transition states. The first one leads to the formation of the $C_2H_3-An^+-H$ intermediate, which after surpassing the second transition state yields a dihydride intermediate, $(H)_2An^+-C_2H_2$. Then the system evolves to the dehydrogenation products through the formation of the last insertion intermediate, $(H_2)An^+$-C_2H_2, which is basically formed from two moieties, H_2 and $An^+-C_2H_2$.

3.2. C−H Bond Activation: Formation of $ThC_2H_4^+ + H_2$ and $UC_2H_4^+ + H_2$. We will begin by discussing the interaction of An$^+$ (An = Th, U) cations with the C−H bond in ethane. As shown in Figures 1 and 2, the first step of the dehydrogenation reaction of ethane by bare An$^+$ cations is the exothermic formation of an $An(C_2H_6)^+$ complex. According to B3LYP/SDD results the reaction of $Th^+ + C_2H_6$ evolves completely along the doublet spin state, whereas at PW91/ZORA level we found that the doublet and quartet $Th(C_2H_6)^+$ structures are almost degenerate in energy, with the quartet state slightly favored. As discussed in the previous section (see also ref 4e), B3LYP/SDD and PW91/ZORA levels do not agree in the ordering of the Th$^+$ atomic states, and this is reflected also in the stability ordering of the initial complexes. However, both levels of theory agree in that the quartet spin surface becomes very high in energy throughout the rest of the PEP.

In the case of U$^+$ the reaction evolves completely along the quartet bare cation ground state (B3LYP/SDD). As explained below, at PW91/ZORA there is a double crossing between the doublet and quartet spin surfaces at the stage of the last transition state. The geometrical parameters corresponding to all the species involved in the reaction pathways at both studied levels of theory are reported as Supporting Information (Figures S1 and S2, respectively).

The reaction proceeds to form the first insertion intermediate $H-An^+-C_2H_5$ through the first-order saddle point **TS1** in which the cations are inserted into one of the C−H bonds. The imaginary frequencies (1051*i* cm^{-1} for Th and 1222*i* cm^{-1} for U), correspond to the C−H bond breaking. In both studied reactions this intermediate (**I**) is the global minimum of the potential energy profile and lies at −165.7 kJ/ml below the ground state reactants in the Th$^+$ reaction and at −82.7 kJ/mol in the U$^+$ reaction. The H−An bond distance is very close to the same distance in the corresponding hydrides: ThH$^+$ ($^3\Delta$, 1.99 Å) and UH$^+$ ($^5\Delta$, 1.97 Å).

Following the C−H bond insertion, the reaction proceeds through a second intramolecular rearrangement to yield a new intermediate, which can be described as a covalently bonded dihydrido complex, $(H)_2An^+-C_2H_4$, obtained by a hydrogen transfer from the second carbon atom to the metal center. In this complex the H−An bond distances are also very close to the corresponding values in the cationic hydrides (see Figures S1 and S2 in Supporting Information). These intermediates are formed after the system surpasses the second transition state, **TS2**, which are characterized by imaginary frequencies (768i cm^{-1} for Th$^+$ and 340i cm^{-1} for U$^+$) that involve the stretching of the C−H bond that is being broken. The lower stability of the second insertion intermediate (**II**) with respect to the first insertion intermediate (**I**) can be understood considering that Th$^+$ in its doublet spin state has only two electrons available for bonding; therefore, the transfer of the second H atom to form the dihydrido intermediate provokes a lengthening of the $Th^+-(C_2H_4)$ distances (2.58 and 2.64 Å, see Figure S1in Supporting Information). These distances are shortened after the H_2 molecule is formed (2.29 and 2.33 Å). U$^+$ in the quartet spin state is able to use two of its valence electrons to form bonds; therefore, the formation of the second insertion intermediate involves the same type of difficulties as the Th$^+$ species. As can be seen in Figure S2 (Supporting Information) the intermediate **II** in the quartet spin state is formed basically by two moieties, UH_2^+ and C_2H_4, which are about 3 Å. The C_2H_4 fragment is practically undistorted with respect to the equilibrium structure in the free molecule (the C−C distance of free C_2H_4 at the studied levels of theory is 1.33 Å). At this stage of the reaction the doublet spin state is quite low in energy, particularly at the PW91/ZORA level, but not enough to became the GS of this species. We note that for the **TS3** structure, the B3LYP/SDD and PW91/ZORA level of theory do not agree in the assignment of the ground spin state, as B3LYP/SDD favors the quartet state whereas PW91/ZORA indicates the doublet **TS3** structure as the GS. The surmised crossing between the doublet and quartet surfaces would be restricted exclusively to the **TS3** structure, as both levels of theory agree in that once the H_2 molecule is formed, the quartet spin state is clearly lower in energy.

The final intermediate, $(H_2)An^+-C_2H_4$, is formed after the last transition state is surmounted, **TS3**. In this structure the H−H distances are 1.25 (Th) and 1.13 Å (U), respectively. The imaginary frequencies are 1486*i* cm^{-1} in the case of Th$^+$ and 1169*i* cm^{-1} for U$^+$ and correspond to the expected H−H

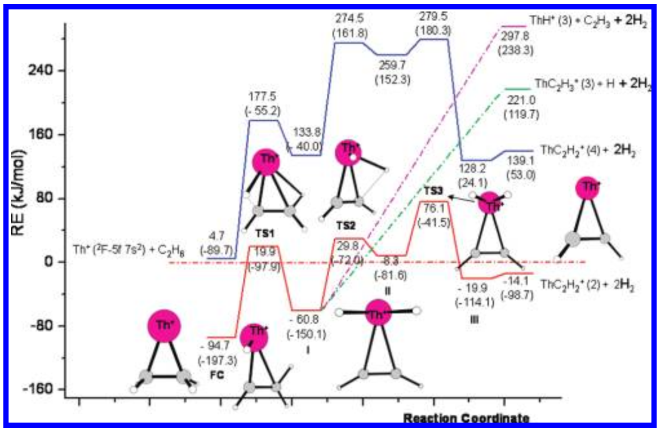

Figure 3. B3LYP/SDD (PW91/ZORA) quartet and doublet PESs for the second dehydrogenation of C_2H_6 by Th^+. Energies are in kJ/mol and relative to the ground-state reactants.

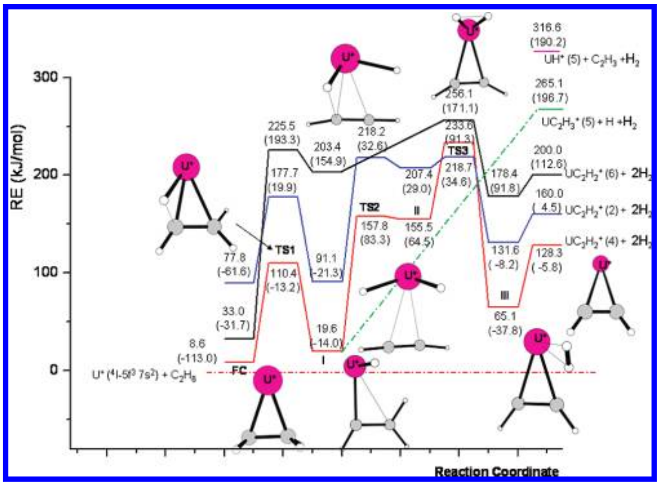

Figure 4. B3LYP/SDD (PW91/ZORA) quartet, sextet, and doublet PESs for the second dehydrogenation of C_2H_6 by U^+. Energies are in kJ/mol and relative to the ground-state reactants.

stretching that yields to the formation of H_2. In the last $(H_2)An^+{-}C_2H_4$ complex, the hydrogen molecule is already formed and electrostatically interacting between the cationic actinide−ethylene complex.

From the last intermediate, $(H_2)An^+{-}C_2H_4$, the hydrogen release is endothermic by about 3 kJ/mol in the case of Th^+ and 12.6 kJ/mol for U^+. The overall process is exothermic by about 95 kJ/mol for the reaction of Th^+ and endothermic by almost 9 kJ/mol for U^+.

Different alternative products were also analyzed. In particular, the $H{-}An^+{-}C_2H_5$ intermediate is an obvious choice for the formation of AnH^+ and $AnC_2H_5{}^+$ fragments that can be obtained by simple An−C and An−H bond breaking. Figure 1 shows that the formation of $ThC_2H_5{}^+$ (^3A) + H is endothermic by around 127 kJ/mol and the production of ThH^+ ($^3\Delta$) is endothermic by almost 130 kJ/mol. In the case of $U^+ + C_2H_6$ the endothermicity is slightly higher, in particular 158.7 kJ/mol (UH^+, $^5\Delta$) and 166.6 kJ/mol ($UC_2H_5{}^+$,^5A), respectively. The dehydrogenation of C_2H_6 by Th^+ involves transition barriers that in all cases lie below the reactants asymptote, so that the dehydrogenation process could dominate even at high kinetic energies. For U^+, B3LYP/SDD computations indicate that the first and the third reaction barriers are well over the limit represented by the reactants (48.4 and 86.3 kJ/mol, respectively).

3.3. Second Dehydrogenation: Formation of $ThC_2H_2{}^+$ + H_2 and $UC_2H_2{}^+$ + H_2. Spontaneous double dehydrogenation was experimentally observed in the reaction of $Th^+ + C_2H_6$;[3] therefore, we have also investigated the reaction mechanisms for the second dehydrogenation process, which yields $AnC_2H_2{}^+$ + H_2.

The reaction pathways for the second dehydrogenation start from the $AnC_2H_4{}^+$ reaction products of the first dehydrogenation. As for the first dehydrogenation, the reaction pathways to yield $AnC_2H_2{}^+ + H_2$ involve a three-step mechanism, which implies the surpassing of three transition states. For simplicity we present the reaction paths for the second elimination in separate pictures, Figures 3 and 4, for the reactions of Th^+ and U^+, respectively. As shown in those figures, the relative energies are calculated with respect to the $An^+ + C_2H_6$ GS reactants. The optimized geometries of all of the key minima and transition states involved in the second H_2 elimination are presented in Figures S3 and S4 (Supporting Information). The imaginary frequencies that characterize all of the transition states at both levels of theory are reported in the same figures.

The isomerization of the initial An^+−ethene adduct to the first insertion intermediate, $H{-}An^+{-}C_2H_3$, involves surpassing a transition structure in which one of the C−H bonds is elongated to about 1.6 Å, in both studied reactions. The imaginary vectors involve the elongation of this bond as well as the rotation of the C_2H_4 molecule, to approach to the planar structure that characterizes the $AnC_2H_3{}^+$ moiety in the following hydrate intermediate (see Figures S3 and S4 in Supporting Information). Along the reaction coordinate we found another transition state that involves the transfer of a second H atom that yields to the formation of a dihydride intermediate (**II**), $(H)_2An^+C_2H_2$, in which the metal−hydrogen distances are very close to 2.0 Å. From this intermediate the reaction evolves to the final $(H_2)An^+C_2H_2$ intermediate, through the surpassing of the last transition state, which is characterized by an imaginary frequency that involves the stretching of the H−H bond. For the same reasons stated in the previous section, also in this case the second insertion intermediate is destabilized with respect to the previous intermediate. In the case of the $U^+ + C_2H_6$ reaction the used levels of theory disagree in the assignation of the ground spin state for the **TS2** and the second intermediate (**II**). Also in this case the PW91/ZORA level favors the doublet spin state, whereas at the B3LYP/SDD level, the quartet spin state is the GS for these species. In summary, for Th^+ the second dehydrogenation evolves completely along the doublet spin surface, whereas in the case of U^+ the reaction evolves mostly on the quartet bare cation ground state, with a double crossing between the doublet and quartet spin surfaces. At the B3LYP/SDD level of theory the crossing takes place around the **TS3** structure, whereas according to the PW91/ZORA level the doublet spin surface is the GS from the formation of the first insertion intermediate (**I**) to the surpassing of **TS3**. Both levels of theory, however, agree that after the surpassing of the last transition state, the reaction evolves completely around the quartet state.

In contrast to the first dehydrogenation reaction, in both Th^+ and U^+ second dehydrogenation reactions, the intrinsic transition barriers associated with the breaking of the two C−H bonds are notably higher than the last one, associated to the formation of the H_2 molecule (see Table 1). The most notable difference between the cations is the higher intrinsic barrier for the second transition state for the reaction of U^+.

We must underline that all the barriers corresponding to the second dehydrogenation reaction are over the limit represented by the $An^+ + C_2H_6$ reactants. However, the relative energy of the barriers is quite low for Th^+. The whole $Th^+ + C_2H_6$ =

TABLE 1: Activation Barriers, in kJ mol^{-1}, of the Transition States Calculated at the B3LYP/SDD (PW91/ZORA) Level

$Th^+ + C_2H_6$	first dehydrogenation	second dehydrogenation	C−C bond activation
TS1[a]	32.8 (2.4)	114.6 (99.4)	105.5 (76.0)
TS2[b]	76.9 (66.0)	90.6 (78.0)	161.5 (126.5)
TS3[c]	105.7 (70.4)	67.8 (40.1)	

$U^+ + C_2H_6$	first dehydrogenation	second dehydrogenation	C−C bond activation
TS1[a]	67.6 (20.7)	101.8 (99.8)	124.5 (73.5)
TS2[b]	74.3 (75.8)	138.2 (53.9)	145.0 (70.4)
TS3[c]	96.0 (40.1)	63.2 (5.6)	

[a] Calculated as the energetic difference between the first transition state (TS1) and the first complex (FC), considering the GS species at each level of theory. [b] Calculated as the energetic difference between the second transition state (TS2) and the first intermediate (I), considering the GS species at each level of theory. [c] Calculated as the energetic difference between the third transition state (TS3) and the second intermediate (II), considering the GS species at each level of theory.

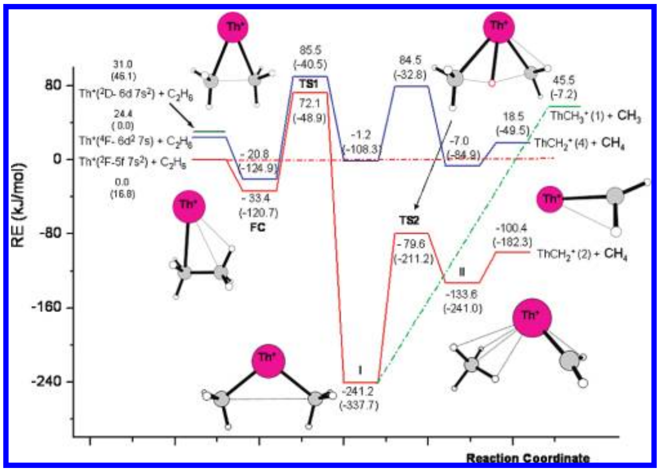

Figure 5. B3LYP/SDD (PW91/ZORA) quartet and doublet PESs for the C−C activation branch of the reaction of Th^+ with C_2H_6. Energies are in kJ/mol and relative to the ground-state reactants.

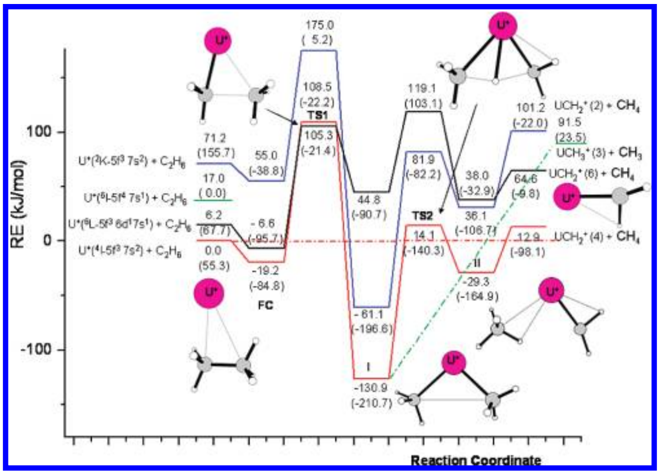

Figure 6. B3LYP/SDD (PW91/ZORA) quartet, sextet, and doublet PESs for the C−C activation branch of the reaction of U^+ with C_2H_6. Energies are in kJ/mol and relative to the ground-state reactants.

$ThC_2H_2^+ + 2H_2$ has an exothermicity of 14.1 kJ/mol, whereas the corresponding value for the reaction of U^+ is endothermic by 128.3 kJ/mol (B3LYP/SDD results).

3.4. C−C Bond Activation: Formation of $ThCH_2^+ + CH_4$ and $UCH_2^+ + CH_4$. The PES along the C−C bond activation branch of the $Th^+ + C_2H_6$ and $U^+ + C_2H_6$ reactions are displayed in Figures 5 and 6, respectively, while the corresponding geometrical structures are collected in Figures S5 and S6 (Supporting Information). As shown in Figures 5 and 6 (see also Figures 1 and 2), the initial $An(C_2H_6)^+$ complex is common to both dissociation channels (H_2 and CH_4 elimination). The adduct complex then rearranges to a dimethyl species (**I**), $CH_3-An^+-CH_3$, in which the cations are inserted into the C−C bond. This intermediate is the global minima of the potential energy profiles in both Th^+ and U^+ reactions. For the reaction of $Th^+ + C_2H_6$ the first transition state in its doublet ground spin state is located at around 72 kJ/mol (B3LYP/SDD) over the $Th^+(^2F) + C_2H_6$ asymptote and is characterized by one imaginary frequency of 575*i* cm^{-1}, corresponding to the C−C bond breaking and rotation of one of the CH_3 groups. The quartet and sextet spin state **TS1** structures are almost degenerate in energy (+108.5 and +105.3 kJ/mol) for the $U^+ + C_2H_6$ reaction (see Figure 6). The C−C distance is elongated to 1.93 Å in Th^+ **TS1** and 2.07 Å in U^+ **TS1**. The formation of the inserted dimethyl intermediate (**I**) is a very exothermic process in both studied reactions and involves a very high energy barrier.

Proceeding along the reaction coordinate, the intermediate (**I**) is converted into another stable ion−molecule complex, $(CH_4)An^+-CH_2$, which serves as the direct precursor for loss of methane. In these intermediates the methane moiety has a distorted η^3 coordination to the metal cation with one of the An^+-H distances quite shorter than the other two. The metal carbon distance is 2.88 Å (B3LYP/SDD) in $(CH_4)-ThCH_2^+$ and 2.77 Å in $(CH_4)-UCH_2^+$. In both structures the metal−methylidene distance is very close to the corresponding value in the carbene cation, 2.04 Å. The structures of the last intermediate (**II**) are characterized by the presence of agostic geometries. In this intermediate the $An^+=CH_2$ moieties are very close to the final $AnCH_2^+$ products. The bonding characteristics of the $An^+=CH_2$ structures have been discussed elsewhere.[4e] The doublet ground state $(CH_4)Th^+=CH_2$ complex is calculated to lie 133.6 kJ/mol below the reactants dissociation limit, while formation of the corresponding uranium species is calculated to be 29.3 kJ/mol.

The saddle point for the 1,3 hydrogen shift that directly converts the dimethyl complex into the $(CH_4)An^+=CH_2$ cation (**TS2**) is characterized by an imaginary frequency of 1345*i* cm^{-1} in the case of Th^+ and 1314*i* cm^{-1} for U^+ (B3LYP/SDD). The transition vector associated to these frequencies and the geometries of the transition structures are completely consistent with the 1,3 H-shift, which leads to the final complex (**II**). The relative energy of **TS2** with respect to the reactants is −79.6 kJ/mol (Th^+) and 14.0 kJ/mol (U^+). The structure of this transition state shows one of the An−C distances elongated by about 0.4 Å, while the carbene structure is almost formed. It must be noted that in **TS2** the metal atom participates to some extent to the hydrogen migration as implied by the short An−H distance (2.08 and 2.05 Å for the Th^+ and U^+ **TS2** structures, respectively).

The reductive elimination of methane from the last insertion intermediate, with formation of $An=CH_2^+$ is endothermic by around 33 kJ/mol for Th^+ and 42 kJ/mol for U^+. The whole demethanation process is exothermic by around 100 kJ/mol for the $Th^+ + C_2H_6$ reaction and endothermic by almost 13 kJ/mol for $U^+ + C_2H_6$.

From the $CH_3-An^+-CH_3$ intermediate the $AnCH_3^+ + CH_3$ products can be obtained through direct bond cleavage of one of the An−C bonds. Figures 5 and 6 show that this process is endothermic by 45.5 kJ/mol (Th^+) and 91.5 kJ/mol (U^+), respectively. Direct formation of $AnCH_3^+ + CH_3$ products is, therefore, energetically much more demanding than the tight **TS2** transition state for the 1,3 hydrogen shift.

The first transition state, **TS1**, is by far the most demanding point in the mechanistic scheme for the C−C bond activation, lying 72.1 and 105.3 kJ/mol above the $Th^+ + C_2H_6$ and $U^+ + C_2H_6$ reactants asymptotes, respectively. We conclude, therefore that the lacking of CH_4 elimination in the experiments is due to a kinetic impedance in the case of the $Th^+ + C_2H_6$ reaction, whereas for U^+ the reaction is unfavorable both thermodynamically and kinetically.

4. Comparison between the Different Levels of Theory

As reported in previous theoretical works,[4] a comparison of the relative energies calculated at the two different levels of theory used in this work, B3LYP/SDD and PW91/ZORA, indicates important differences that can be as high as 130 kJ/mol for the GS species of the $Th^+ + C_2H_6$ reaction and 185 kJ/mol in the case of the GS species of the $U^+ + C_2H_6$ reaction. This trend has been previously analyzed, and it was concluded that a significant part of the energy difference is due to the different functionals used in each approach.[4a,b]

In order to give further insight into the origin of these differences, we have recalculated the potential energy surfaces presented in Figures 1−6, using as the asymptote the reaction products in their corresponding ground states, instead of the reactants. The results are presented in Figures S7 to S12 (Supporting Information). It can be seen that the relative energies of the different species calculated at both levels of theory are now much closer, being the greater difference of 39 kJ/mol for the $Th^+ + C_2H_6$ reaction and 120 kJ/mol for the $U^+ + C_2H_6$ reaction. The largest difference between the relative energies calculated at the different levels of theory is now restricted to the relative energy of the $An^+ + C_2H_6$ reactants with respect to the new asymptotes (reaction products in their GSs).

These results seem to indicate that the main reason for the large difference between the relative energies calculated at the B3LYP/SDD and PW91/ZORA levels is the choice of the $An^+ + C_2H_6$ asymptote. We note that the formal oxidation numbers for all the Th^+ species from the formation of the first transition state in the case of the first dehydrogenation (and the C−C bond activation) and for all the species involved in the second dehydrogenation is III. The improvement in the agreement between the B3LYP/SDD and the PW91/ZORA relative energies when considering the reaction products as the reference energy can be considered as an indication of the difficulties of DFT to describe the energetics of reactions that involve important changes in the oxidation states. The same reasoning can be applied the to $U^+ + C_2H_6$ reaction, for which all the species in the first dehydrogenation paths as well as the C−C bond activation process have the same formal oxidation number (III) from the formation of the first transition state. Previous theoretical studies have underlined the shortcomings of DFT to describe quantitatively the energetics of reactions involving changes in the formal oxidation numbers.[23]

5. Summary and Conclusions

The following major conclusions can be inferred from the detailed exploration of the PES for the reaction of Th^+ and U^+ with C_2H_6.

Both hydrogen and methane elimination reactions start with the formation of the $An(C_2H_6)^+$ ion−molecule complex. According to B3LYP/SDD results, the dehydrogenation of C_2H_6 evolves completely along the doublet spin surface. The first H_2 elimination reaction is exothermic by almost 95 kJ/mol and the highest energy point en route to the products is the first C−H insertion transition state that has been located 0.6 kJ/mol below the asymptote represented by the reactants. At the same level of theory the $U^+ + C_2H_6$ reaction proceeds along the quartet U^+ ground state, and the reaction is slightly endothermic (8.6 kJ/mol). The transition barriers associated to the first and third transition states are quite high in energy, well above the $U^+ + C_2H_6$ reactant asymptotes. In both reactions, the direct bond breaking processes from the common intermediate $H{-}An^+{-}C_2H_5$ to obtain AnH^+ and $AnC_2H_5^+$ fragments are not energetically competitive. These results indicate, therefore, that the dehydrogenation of C_2H_6 by U^+ in the gas phase is thermodynamically unfavorable, which justifies the nondetection of dehydrogenation during FTICR-MS experiments.

According to B3LYP/SDD computations, the overall methane elimination reaction is predicted to be exothermic by 100 kJ/mol for the activation by Th^+ and endothermic by almost 13 kJ/mol in the case of U^+. Even when the C−C insertion $CH_3{-}An^+{-}CH_3$ product is a very stable intermediate, the associated TS barrier is quite large and exceeds the energy of the ground state reactants by 72.1 (Th^+) and 105.3 kJ/mol (U^+), preventing the observation of these species under thermal conditions.

Alternative fragmentation pathways produced by direct bond cleavage appear to become competitive only at significantly higher kinetic energies.

Acknowledgment. Financial support from the Università degli Studi della Calabria and MIUR is gratefully acknowledged.

Supporting Information Available: Optimized geometries of all the intermediates and transition states reported in Figures 1−6 and reaction pathways 1−6 computed considering the GS reaction products as asymptotes to calculate the relative energies. This material is available free of charge via the Internet at http://pubs.acs.org.

References and Notes

(1) (a) Gibson, J. K. *Int. J. Mass Spectrom.* **2002**, *214*, 1. (b) Gibson, J. K.; Marçalo, J. *Coord. Chem. Rev.* **2006**, *250*, 776.

(2) (a) Heinemann, C.; Cornehl, H. H.; Schwarz, H. *J. Organomet. Chem.* **1995**, *501*, 201. (b) Cornehl, H. H.; Heinemann, C.; Marçalo, J.; Pires de Matos, A.; Schwarz, H. *Angew. Chem., Int. Ed. Engl.* **1996**, *35*, 891. (c) Cornehl, H. H.; Wesendrup, R.; Diefenbach, M.; Schwarz, H. *Chem.*−*Eur. J.* **1997**, *3*, 1083. (d) Santos, M.; Marçalo, J.; Pires de Matos, A.; Gibson, J. K.; Haire, R. G. *J. Phys. Chem. A* **2002**, *106*, 7190. (e) Santos, M.; Marçalo, J.; Leal, J. P.; Pires de Matos, A.; Gibson, J. K.; Haire, R. G. *Int. J. Mass Spectrom.* **2003**, *228*, 457. (f) Gibson, J. K.; Haire, R. G.; Santos, M.; Marçalo, J.; Pires de Matos, A. *J. Phys. Chem. A* **2005**, *109*, 2768.

(3) (a) Marçalo, J.; Leal, J. P.; Pires de Matos, A. *Int. J. Mass Spectrom. Ion Processes* **1996**, *157/158*, 265. (b) Gibson, J. K.; Haire, R. G.; Marçalo, J.; Santos, M.; Pires de Matos, A.; Mrozik, M. K.; Pitzer, R. M.; Bursten, B. E. *Organometallics* **2007**, *26*, 3947.

(4) (a) Michelini, M. C.; Russo, N.; Sicilia, E. *Angew. Chem., Int. Ed.* **2006**, *45*, 1095. (b) Michelini, M. C.; Russo, N.; Sicilia, E. *J. Am. Chem. Soc.* **2007**, *129*, 4229. (c) Mazzone, G.; Michelini, M. C.; Russo, N.; Sicilia, E. *Inorg. Chem.* **2008**, *47*, 2083. (d) Alikhani, M. E.; Michelini, M. C.; Russo, N.; Silvi, B. *J. Phys. Chem. A* **2008**, *112*, 12966. (e) Di Santo, E.; Michelini, M. C.; Russo, N. *Organometallics* **2009**, *28*, 3716.

(5) (a) Arakawa, H.; Aresta, M.; Armor, J. N.; Barteau, M. A.; Beckman, E. J.; Bell, A. T.; Bercaw, J. E.; Creutz, C.; Dinjus, E.; Dixon, D. A.; Domen, K.; DuBois, D. L.; Eckert, J.; Fujita, E.; Gibson, D. H.; Goddard, W. A.; Goodman, D. W.; Keller, J.; Kubas, G. J.; Kung, H. H.; Lyons, J. E.; Manzer, L. E.; Marks, T. J.; Morokuma, K.; Nicholas, K. M.; Periana, R.; Que, L.; Rostrup-Nielson, J.; Sachtler, W. M. H.; Schmidt, L. D.; Sen, A.; Somorjai, G. A.; Stair, P. C.; Stults, B. R.; Tumas, W. *Chem. Rev.* **2001**, *101*, 953. (b) Crabtree, R. H. *J. Chem. Soc., Dalton Trans.*

2001, 2437. (c) Labinger, J. A.; Bercaw, J. E. *Nature* **2002**, *417*, 507. (d) Bergman, R. G. *Nature* **2007**, *446*, 391. (e) Schwarz, H. *Int. J. Mass Spectrom.* **2004**, *237*, 75. (f) Schröder, D.; Schwarz, H. *Proc. Natl. Acad. Sci. U.S.A.* **2008**, *105*, 18114.

(6) See for instance: (a) Tolbert, M. A.; Beauchamp, J. L. B. *J. Am. Chem. Soc.* **1984**, *106*, 8117. (b) Armentrout, P. B.; Beauchamp, J. L. *Acc. Chem. Res.* **1989**, *22*, 315. (c) Armentrout, P. B. *Sience* **1991**, *251*, 175. (d) Weisshaar, J. C. *Acc. Chem. Res.* **1993**, *26*, 213. (e) Liu, F.; Zhang, X.-G.; Armentrout, P. B. *Phys. Chem. Chem. Phys.* **2005**, *7*, 1054.

(7) See for instance: (a) Russo, N.; Sicilia, E. *J. Am. Chem. Soc.* **2001**, *123*, 2588. (b) Sicilia, E.; Russo, N. *J. Am. Chem. Soc.* **2002**, *124*, 1471. (c) Michelini, M. C.; Russo, N.; Sicilia, E. *J. Phys. Chem. A* **2002**, *106*, 8937. (d) Michelini, M. C.; Sicilia, E.; Russo, N.; Alikhani, M. E.; Silvi, B. *J. Phys. Chem. A* **2003**, *107*, 4862. (e) Chiodo, S.; Kondakova, O.; Michelini, M. C.; Russo, N.; Sicilia, E. *J. Phys. Chem. A* **2004**, *108*, 1069.

(8) (a) Irikura, K. K.; Beauchamp, J. L. *J. Am. Chem. Soc.* **1989**, *111*, 75. (b) Irikura, K. K.; Beauchamp, J. L. *J. Am. Chem. Soc.* **1991**, *113*, 2769. (c) Irikura, K. K.; Beauchamp, J. L. *J. Phys. Chem.* **1991**, *95*, 8344. (d) Irikura, K. K.; Goddard, W. A., III. *J. Am. Chem. Soc.* **1994**, *116*, 8733.

(9) (a) Buckner, S. W.; MacMahon, T. J.; Byrd, G. D. B. S. *Inorg. Chem.* **1989**, *28*, 3511. (b) Ranasinghe, Y. A.; MacMahon, T. J.; Freiser, B. S. *J. Phys. Chem.* **1991**, *95*, 7721. (c) Blomberg, M. R. A.; Siegbahn, P. E. M.; Svensson, M. *J. Phys. Chem.* **1994**, *98*, 2062. (d) Perry, J. K.; Ohanessian, G.; Goddard, W. A., III. *Organometallics* **1994**, *13*, 1870. (e) Wesendrup, R.; Schröeder, D.; Schwarz, H. *Angew. Chem., Int. Ed.* **1994**, *33*, 1174. (f) Irikura, K. K.; Goddard, W. A., III. *J. Am. Chem. Soc.* **1994**, *116*, 8733. (g) Heinemann, C.; Hertwig, R. H.; Wesendrup, R.; Koch, W.; Schwarz, H. *J. Am. Chem. Soc.* **1995**, *117*, 495. (h) Pavlov, M.; Blomberg, M. R. A.; Siegbahn, P. E. M. *J. Phys. Chem. A* **1997**, *101*, 1567. (i) Heinemann, C.; Schwarz, H.; Koch, W.; Dyall, K. *Chem. Phys.* **1996**, *104*, 4642. (j) Heinemann, C.; Wesendrup, R.; Schwarz, H. *Chem. Phys. Lett.* **1995**, *239*, 75. (k) Achatz, U.; Beyer, M.; Joos, S.; Fox, B. S.; Niedner-Schatteburg, G.; Bondybey, V. E. *J. Phys. Chem. A* **1999**, *103*, 8200. (l) Heinemann, C.; Koch, W.; Schwarz, H. *Chem. Phys. Lett.* **1995**, *245*, 509. (m) Holthausen, M. C.; Heinemann, C.; Cornehl, H. H.; Koch, W.; Schwarz, H. *J. Chem. Phys.* **1995**, *102*, 4931.

(10) (a) Zhang, X.-G.; Liyanage, R.; Armentrout, P. B. *J. Am. Chem. Soc.* **2001**, *123*, 5563. (b) Armentrout, M. M.; Li, F.-X.; Armentrout, P. B. *J. Phys. Chem. A* **2004**, *108*, 9660. (c) Parke, L. G.; Hinton, C. S.; Armentrout, P. B. *Int. J. Mass Spectrom.* **2006**, *254*, 168. (d) Li, F.-X.; Armentrout, P. B. *J. Chem. Phys.* **2006**, *125*, 133114. (e) Armentrout, P. B.; Shin, S.; Liyanage, R. *J. Phys. Chem. A* **2006**, *110*, 1242. (f) Li, F.-X.; Zhang, X.-G.; Armentrout, P. B. *Int. J. Mass Spectrom.* **2006**, *255−256*, 279. (g) Parke, L. G.; Hinton, C. S.; Armentrout, P. B. *J. Phys. Chem. C* **2007**, *111*, 17773.

(11) De Almeida, K. J.; Duarte, H. A. *Organometallics* **2009**, *28*, 3203.

(12) (a) Sanders, L.; Hanton, S. D.; Weisshaar, J. C. *J. Phys. Chem.* **1987**, *91*, 5145. (b) Sanders, L.; Hanton, S. D.; Weisshaar, J. C. *J. Chem. Phys.* **1990**, *92*, 3498. (c) Holthausen, M. C.; Fiedler, A.; Koch, W.; Schwarz, H. *Angew. Chem., Int. Ed. Engl.* **1995**, *34*, 2282. (d) Holthausen, M. C.; Koch, W. *J. Am. Chem. Soc.* **1996**, *118*, 9932. (e) Holthausen, M. C.; Fiedler, A.; Koch, W.; Schwarz, H. *J. Phys. Chem.* **1996**, *100*, 6236. (f) Sievers, M. R.; Chen, Y.-M.; Haynes, C. L.; Armentrout, P. B. *Int. J. Mass Spectrom.* **2000**, *195/196*, 149. (g) Zhang, D.; Liu, C.; Bi, S.; Yuan, S. *Chem.−Eur. J.* **2003**, *9*, 484. (h) Zhang, D.; Liu, C.; Wensheng, B. *J. Mol. Struct.: THEOCHEM* **2003**, *635*, 239.

(13) (a) Chen, Y.-M.; Armentrout, P. B. *J. Phys. Chem.* **1995**, *99*, 11424. (b) Chen, Y.-M.; Armentrout, P. B. *J. Am. Chem. Soc.* **1995**, *117*, 9291. (c) Armentrout, P. B.; Chen, Y.-M. *J. Am. Soc. Mass Spectrom.* **1999**, *10*, 821. (d) Armentrout, P. B. *Organometallics* **2007**, *26*, 5486. (e) Michelini, M. C.; Rivalta, I.; Sicilia, E. *Theor. Chem. Acc.* **2008**, *120*, 395.

(14) (a) Armentrout, P. B. *Annu. Rev. Phys. Chem.* **1990**, *41*, 313. (b) Eller, K.; Schwarz, H. *Chem. Rev.* **1991**, *91*, 1121.

(15) See for instance: (a) Schröder, D.; Shaik, S.; Schwarz, H. *Acc. Chem. Res.* **2000**, *33*, 139. (b) Poli, R.; Harvey, J. N. *Chem. Soc. Rev.* **2003**, *32*, 1.

(16) (a) Becke, A. D. *J. Chem. Phys.* **1993**, *98*, 5648. (b) Lee, C.; Yang, W.; Parr, R. G. *Phys. Rev. B* **1988**, *37*, 785.

(17) (a) http://www.theochem.unistuttgart.de/pseudopotentiale/. (b) Küchle, W.; Dolg, M.; Stoll, H.; Preuss, H. *J. Chem. Phys.* **1994**, *100*, 7535.

(18) (a) Krishnan, R.; Binkley, J. S.; Seeger, R.; Pople, J. A. *J. Chem. Phys.* **1980**, *72*, 650. (b) Blaudeau, J.-P.; McGrath, M. P.; Curtiss, L. A.; Radom, L. *J. Chem. Phys.* **1997**, *107*, 5016. (c) Clark, T.; Chandrasekhar, J.; Schleyer, P. V. R. *J. Chem. Phys.* **1983**, *74*, 294.

(19) Frisch, M. J.; et al. *Gaussian 03*. See Supporting Information for full citation.

(20) (a) te Velde, G.; Bickelhaupt, F. M.; van Gisbergen, S. J. A.; Fonseca Guerra, C.; Baerends, E. J.; Snijders, J. G.; Ziegler, T. *J. Comput. Chem.* **2001**, *22*, 931. (b) Fonseca Guerra, C.; Snijders, J. G.; te Velde, G.; Baerends, E. J. *Theor. Chem. Acc.* **1998**, *99*, 391. (c) ADF2004.01, SCM, Theoretical Chemistry, Vrije Universiteit, Amsterdam, The Netherlands, http://www.scm.com.

(21) (a) Burke, K.; Perdew, J. P.; WangY. In *Electronic Density Functional Theory: Recent Progress and New Directions*; Dobson, J. F., Vignale, G., Das, M. P., Eds.; Plenum: New York, 1998. (b) Perdew, J. P. In *Electronic Structure of Solid'91*, Ziesche, P., Eschrig, H., Eds.; Akademie Verlag: Berlin, 1991; p 11. (c) Perdew, J. P.; Burke, K.; Wang, Y. *Phys. Rev. B* **1996**, *54*, 16533. (d) Perdew, J. P.; Chevary, J. A.; Vosko, S. A.; Jackson, K. A.; Pederson, M. R.; Singh, D. J.; Fiolhais, C. *Phys. Rev. B* **1992**, *46*, 6671. (e) Perdew, J. P.; Chevary, J. A.; Vosko, S. H.; Jackson, K. A.; Pederson, M. R.; Singh, D. J.; Fiolhais, C. *Phys. Rev. B* **1993**, *48*, 4978.

(22) Blaise, J.; Wyart, J.-F. Tables of Constants and Numerical Data. *International Tables of Selected Constants, Energy Levels and Atomic Spectra of Actinides*; 1992; Vol. 20, taken from http://www.lac.u-psud.fr/Database/Contents.html.

(23) Vallet, V.; Schimmelpfennig, B.; Maron, L.; Teichteil, C.; Leininger, T.; Gropen, O.; Grenthe, I.; Wahlgren, U. *Chem. Phys.* **1999**, *244*, 185.

JP9048154

Supporting Information

Activation of Ethane C-H and C-C Bonds by Gas–Phase Th^+ and U^+: A theoretical Study.

E. Di Santo, M.C. Michelini, and N. Russo

Dipartimento di Chimica and Centro di Calcolo ad Alte Prestazioni per Elaborazioni Parallele e Distribuite-Centro d'Eccellenza MURST, Università della Calabria, I-87030 Arcavacata di Rende, Italy

Table of Contents

Figure S5. B3LYP/SDD (PW91/ZORA) optimized geometries of calculated minima and transition states (lowest energy spin-state) for the ethane C-C bond activation by Th^+. Bond lengths are in angstrom and angles in degrees.

Figure S6. B3LYP/SDD (PW91/ZORA) optimized geometries of calculated minima and transition states (lowest energy spin-state) for the ethane C-C bond activation by U^+. Bond lengths are in angstrom and angles in degrees.

Figure S7. B3LYP/SDD (PW91/ZORA) quartet and doublet PESs for first dehydrogenation of C_2H_6 by Th^+. Energies are in kJ/mol and relative to the ground-state products.

Figure S8. B3LYP/SDD (PW91/ZORA) quartet, sextet and doublet PESs for the first dehydrogenation of C_2H_6 by U^+. Energies are in kJ/mol and relative to the ground-state products.

Figure S9. B3LYP/SDD (PW91/ZORA) quartet and doublet PESs for the second dehydrogenation of C_2H_6 by Th^+. Energies are in kJ/mol and relative to the ground-state products.

Figure S10. B3LYP/SDD (PW91/ZORA) quartet, sextet and doublet PESs for the second dehydrogenation of C_2H_6 by U^+. Energies are in kJ/mol and relative to the ground-state products.

Figure S11. B3LYP/SDD (PW91/ZORA) quartet and doublet PESs for the C-C activation branch of the reaction of Th^+ bare cation with C_2H_6. Energies are in kJ/mol and relative to the ground-state products.

Figure S12. B3LYP/SDD (PW91/ZORA) quartet, sextet and doublet PESs for the C-C activation branch of the reaction of U^+ bare cation with C_2H_6. Energies are in kJ/mol and relative to the ground-state products.

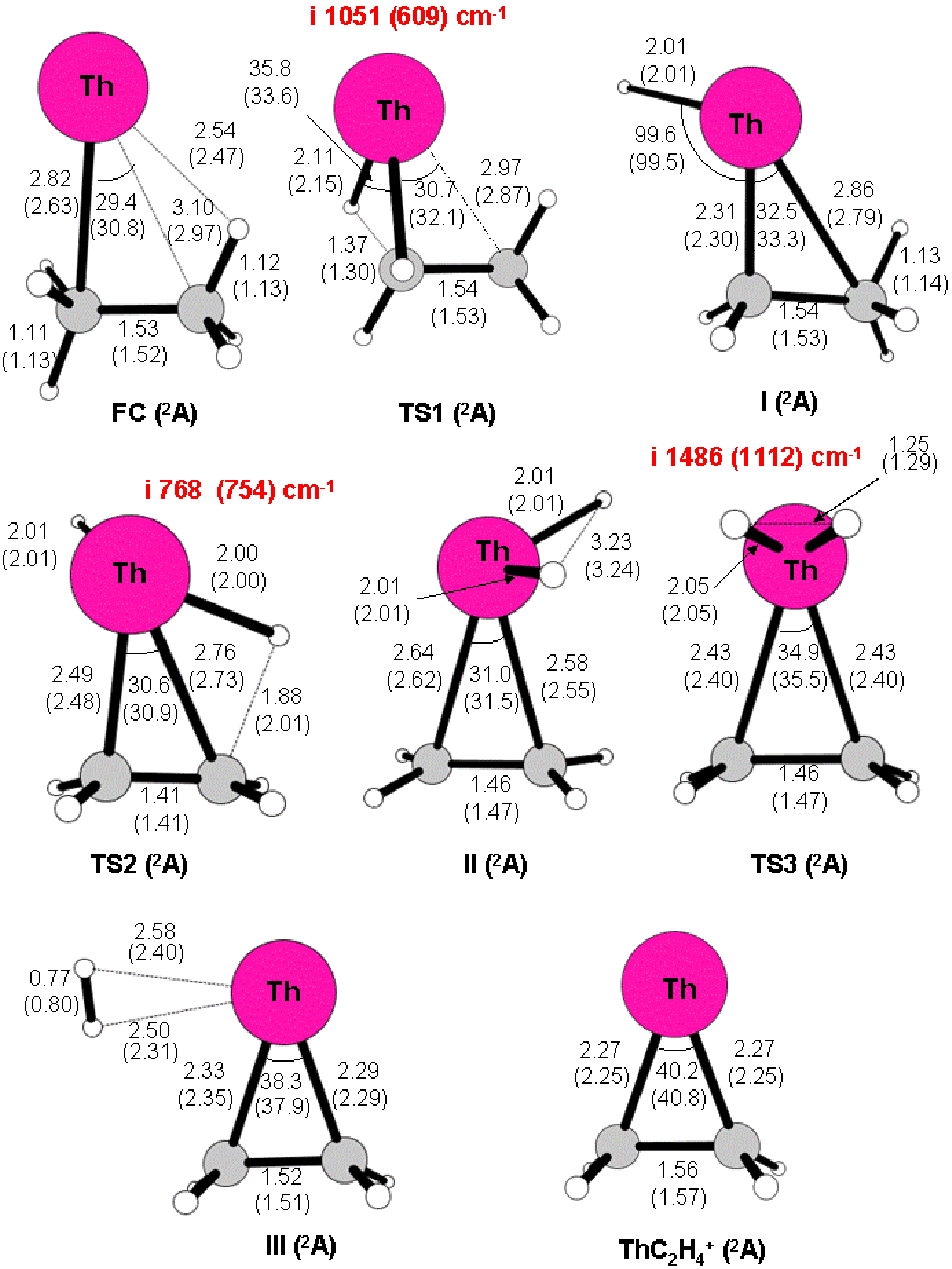
Th
2.82 (2.63)
29.4 (30.8)
2.54 (2.47)
3.10 (2.97)
1.12 (1.13)
1.11 (1.13)
1.53 (1.52)
FC (²A)
i 1051 (609) cm⁻¹
35.8 (33.6)
2.11 (2.15)
30.7 (32.1)
2.97 (2.87)
1.37 (1.30)
1.54 (1.53)
TS1 (²A)
2.01 (2.01)
99.6 (99.5)
2.31 (2.30)
32.5 (33.3)
2.86 (2.79)
1.13 (1.14)
1.54 (1.53)
I (²A)
i 768 (754) cm⁻¹
2.01 (2.01)
2.00 (2.00)
2.49 (2.48)
30.6 (30.9)
2.76 (2.73)
1.88 (2.01)
1.41 (1.41)
TS2 (²A)
2.01 (2.01)
3.23 (3.24)
2.01 (2.01)
2.64 (2.62)
31.0 (31.5)
2.58 (2.55)
1.46 (1.47)
II (²A)
i 1486 (1112) cm⁻¹
1.25 (1.29)
2.05 (2.05)
2.43 (2.40)
34.9 (35.5)
2.43 (2.40)
1.46 (1.47)
TS3 (²A)
2.58 (2.40)
0.77 (0.80)
2.50 (2.31)
2.33 (2.35)
38.3 (37.9)
2.29 (2.29)
1.52 (1.51)
III (²A)
2.27 (2.25)
40.2 (40.8)
2.27 (2.25)
1.56 (1.57)
ThC₂H₄⁺ (²A)

Figure S1

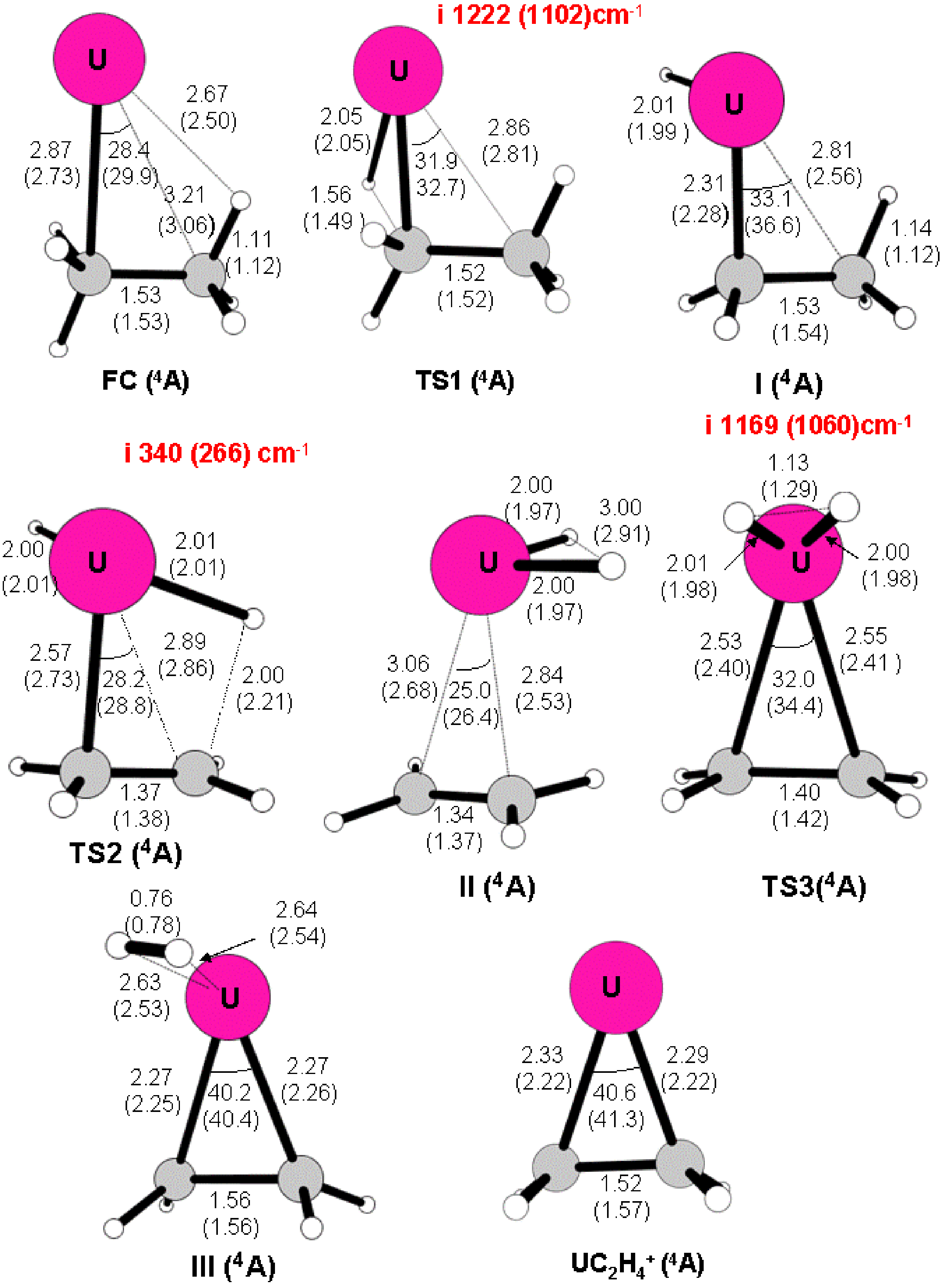
i 1222 (1102)cm-1
U
2.67 (2.50)
2.87 (2.73)
28.4 (29.9)
3.21 (3.06)
1.11 (1.12)
1.53 (1.53)
FC (4A)
2.05 (2.05)
31.9 32.7)
2.86 (2.81)
1.56 (1.49)
1.52 (1.52)
TS1 (4A)
2.01 (1.99)
2.31 (2.28)
33.1 (36.6)
2.81 (2.56)
1.14 (1.12)
1.53 (1.54)
I (4A)
i 1169 (1060)cm-1
i 340 (266) cm-1
2.00 (2.01)
2.01 (2.01)
2.57 (2.73)
28.2 (28.8)
2.89 (2.86)
2.00 (2.21)
1.37 (1.38)
TS2 (4A)
2.00 (1.97)
3.00 (2.91)
2.00 (1.97)
3.06 (2.68)
25.0 (26.4)
2.84 (2.53)
1.34 (1.37)
II (4A)
1.13 (1.29)
2.01 (1.98)
2.00 (1.98)
2.53 (2.40)
32.0 (34.4)
2.55 (2.41)
1.40 (1.42)
TS3(4A)
0.76 (0.78)
2.64 (2.54)
2.63 (2.53)
2.27 (2.25)
40.2 (40.4)
2.27 (2.26)
1.56 (1.56)
III (4A)
2.33 (2.22)
40.6 (41.3)
2.29 (2.22)
1.52 (1.57)
UC2H4+ (4A)

Figure S2

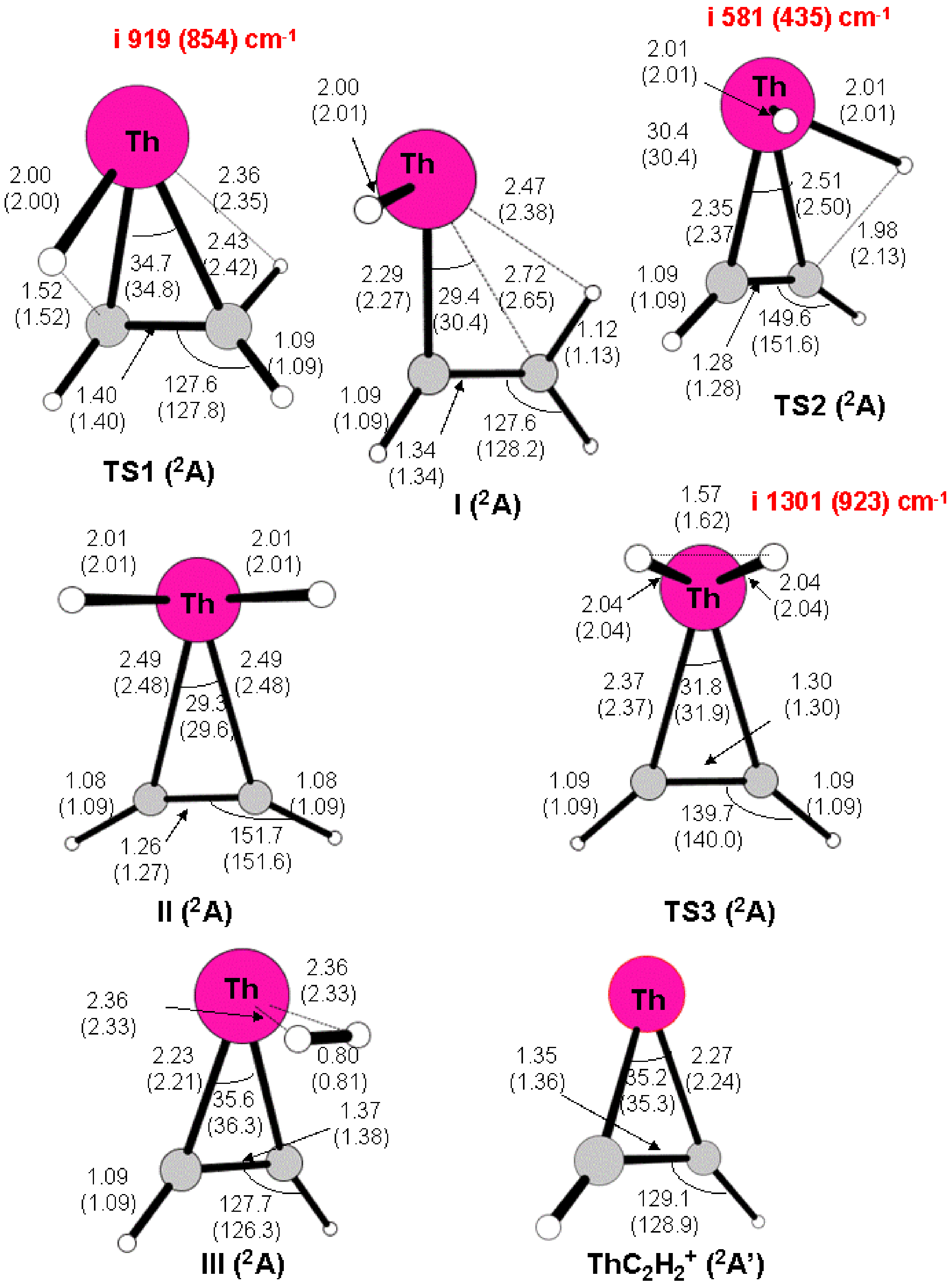
i 919 (854) cm-1
Th
2.00 (2.00)
2.36 (2.35)
2.43 (2.42)
34.7 (34.8)
1.52 (1.52)
1.09 (1.09)
1.40 (1.40)
127.6 (127.8)
TS1 (²A)
2.00 (2.01)
Th
2.47 (2.38)
2.29 (2.27)
29.4 (30.4)
2.72 (2.65)
1.12 (1.13)
1.09 (1.09)
1.34 (1.34)
127.6 (128.2)
I (²A)
i 581 (435) cm-1
2.01 (2.01)
Th
2.01 (2.01)
30.4 (30.4)
2.51 (2.50)
2.35 (2.37)
1.98 (2.13)
1.09 (1.09)
149.6 (151.6)
1.28 (1.28)
TS2 (²A)
2.01 (2.01)
2.01 (2.01)
Th
2.49 (2.48)
2.49 (2.48)
29.3 (29.6)
1.08 (1.09)
1.08 (1.09)
1.26 (1.27)
151.7 (151.6)
II (²A)
1.57 (1.62)
i 1301 (923) cm-1
Th
2.04 (2.04)
2.04 (2.04)
2.37 (2.37)
31.8 (31.9)
1.30 (1.30)
1.09 (1.09)
1.09 (1.09)
139.7 (140.0)
TS3 (²A)
Th
2.36 (2.33)
2.36 (2.33)
0.80 (0.81)
2.23 (2.21)
35.6 (36.3)
1.37 (1.38)
1.09 (1.09)
127.7 (126.3)
III (²A)
Th
1.35 (1.36)
2.27 (2.24)
35.2 (35.3)
129.1 (128.9)
ThC2H2+ (²A')

Figure S3

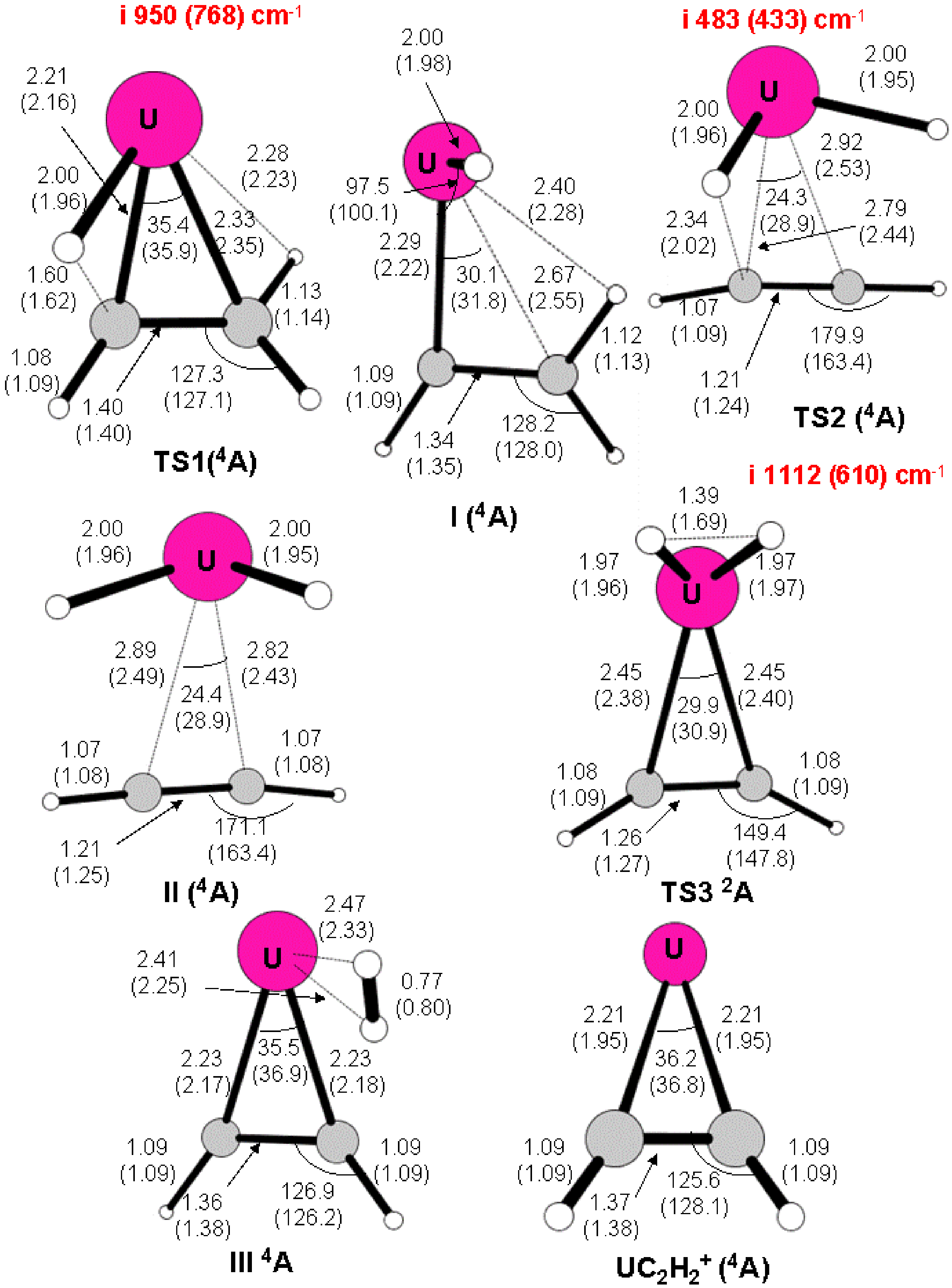
i 950 (768) cm-1
U
2.21 (2.16)
2.00 (1.96)
2.28 (2.23)
35.4 (35.9)
2.33 (2.35)
1.60 (1.62)
1.13 (1.14)
1.08 (1.09)
1.40 (1.40)
127.3 (127.1)
TS1(4A)
2.00 (1.98)
U
97.5 (100.1)
2.40 (2.28)
2.29 (2.22)
30.1 (31.8)
2.67 (2.55)
1.12 (1.13)
1.09 (1.09)
1.34 (1.35)
128.2 (128.0)
I (4A)
i 483 (433) cm-1
U
2.00 (1.95)
2.00 (1.96)
2.92 (2.53)
24.3 (28.9)
2.34 (2.02)
2.79 (2.44)
1.07 (1.09)
179.9 (163.4)
1.21 (1.24)
TS2 (4A)
U
2.00 (1.96)
2.00 (1.95)
2.89 (2.49)
2.82 (2.43)
24.4 (28.9)
1.07 (1.08)
1.07 (1.08)
171.1 (163.4)
1.21 (1.25)
II (4A)
i 1112 (610) cm-1
1.39 (1.69)
1.97 (1.96)
U
1.97 (1.97)
2.45 (2.38)
2.45 (2.40)
29.9 (30.9)
1.08 (1.09)
1.08 (1.09)
1.26 (1.27)
149.4 (147.8)
TS3 2A
U
2.47 (2.33)
2.41 (2.25)
0.77 (0.80)
35.5 (36.9)
2.23 (2.17)
2.23 (2.18)
1.09 (1.09)
1.09 (1.09)
1.36 (1.38)
126.9 (126.2)
III 4A
U
2.21 (1.95)
2.21 (1.95)
36.2 (36.8)
1.09 (1.09)
1.09 (1.09)
1.37 (1.38)
125.6 (128.1)
UC2H2+ (4A)

Figure S4

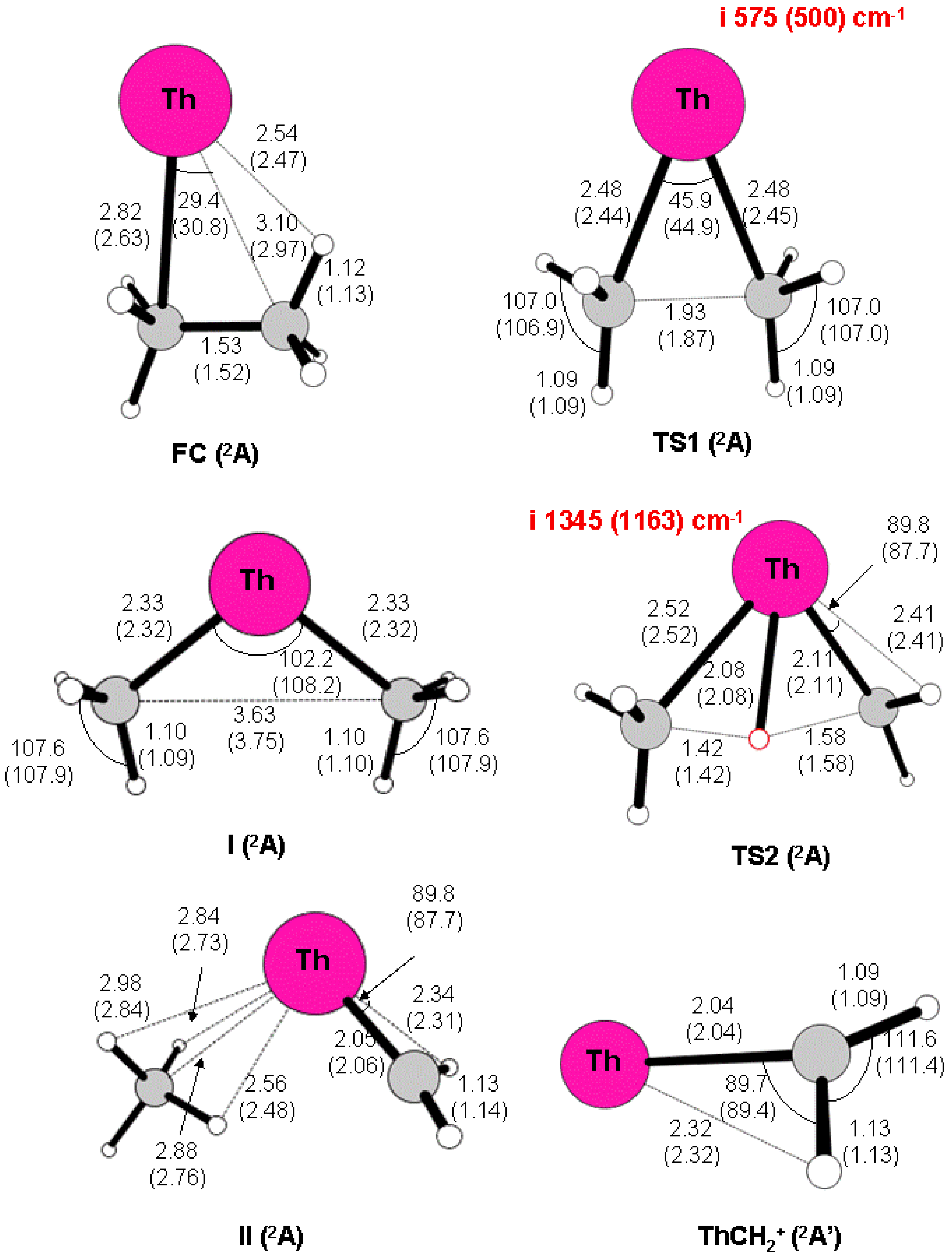

FC (^{2}A)

TS1 (^{2}A)

I (^{2}A)

TS2 (^{2}A)

II (^{2}A)

ThCH$_2^+$ (^{2}A')

Figure S5

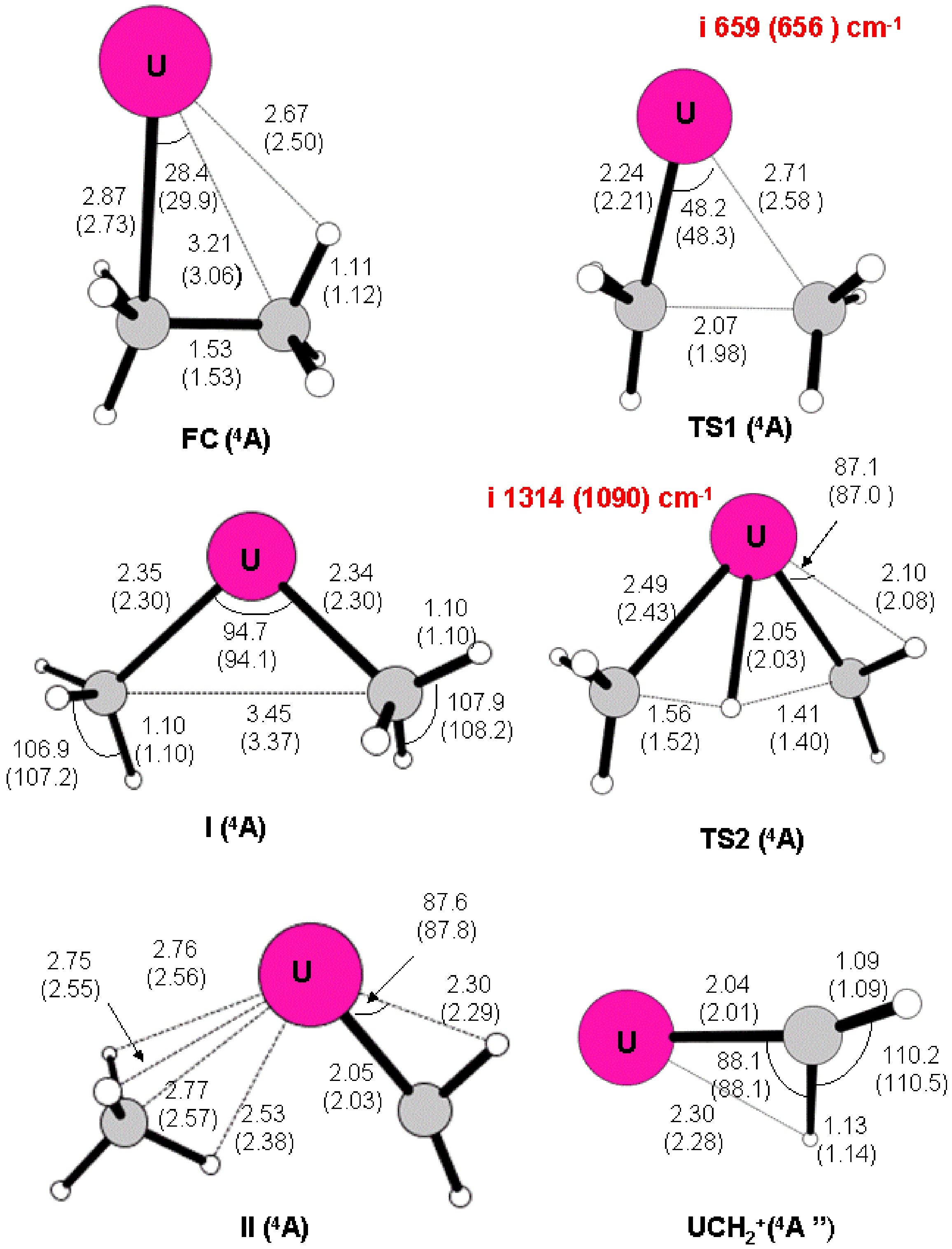

FC (^{4}A)

TS1 (^{4}A)

I (^{4}A)

TS2 (^{4}A)

II (^{4}A)

UCH$_2^+$(^{4}A ”)

Figure S6

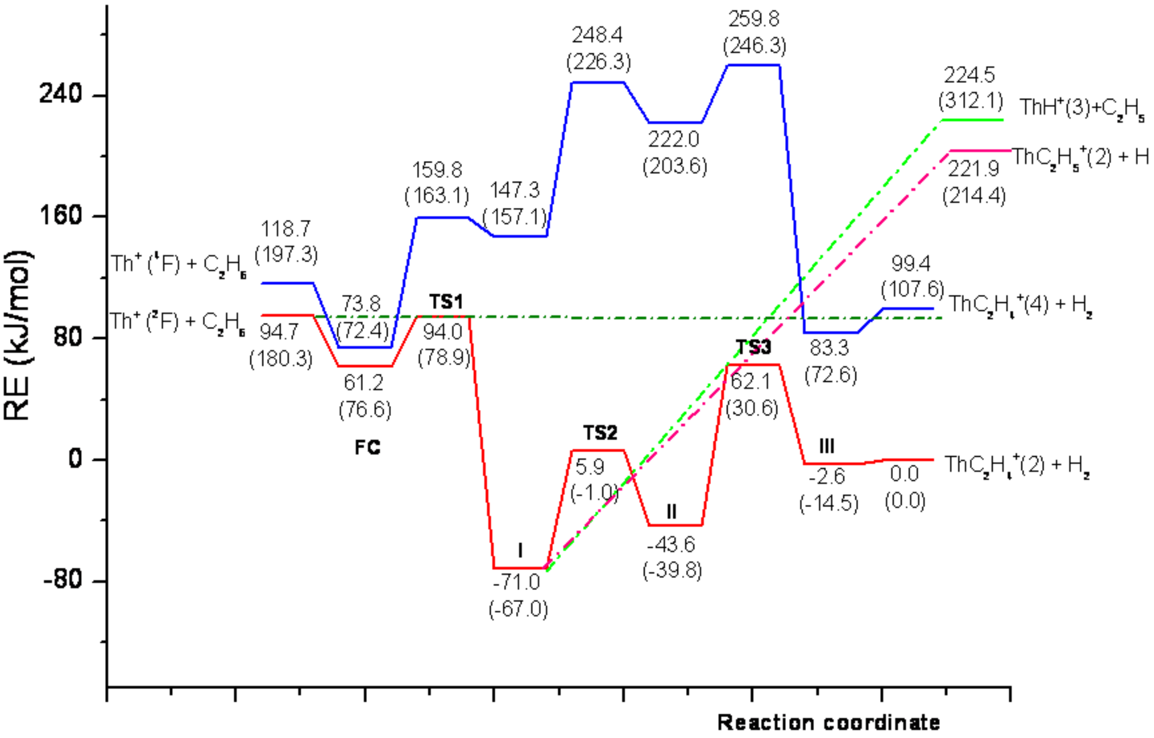
RE (kJ/mol)
240
160
80
0
-80
Reaction coordinate
Th+ (4F) + C2H6
Th+ (2F) + C2H6
118.7
(197.3)
94.7
(180.3)
73.8
(72.4)
61.2
(76.6)
FC
159.8
(163.1)
TS1
94.0
(78.9)
147.3
(157.1)
I
-71.0
(-67.0)
248.4
(226.3)
TS2
5.9
(-1.0)
222.0
(203.6)
II
-43.6
(-39.8)
259.8
(246.3)
TS3
62.1
(30.6)
83.3
(72.6)
III
-2.6
(-14.5)
99.4
(107.6)
0.0
(0.0)
224.5
(312.1)
ThH+(3)+C2H5
221.9
(214.4)
ThC2H5+(2) + H
ThC2H4+(4) + H2
ThC2H4+(2) + H2

Figure S7

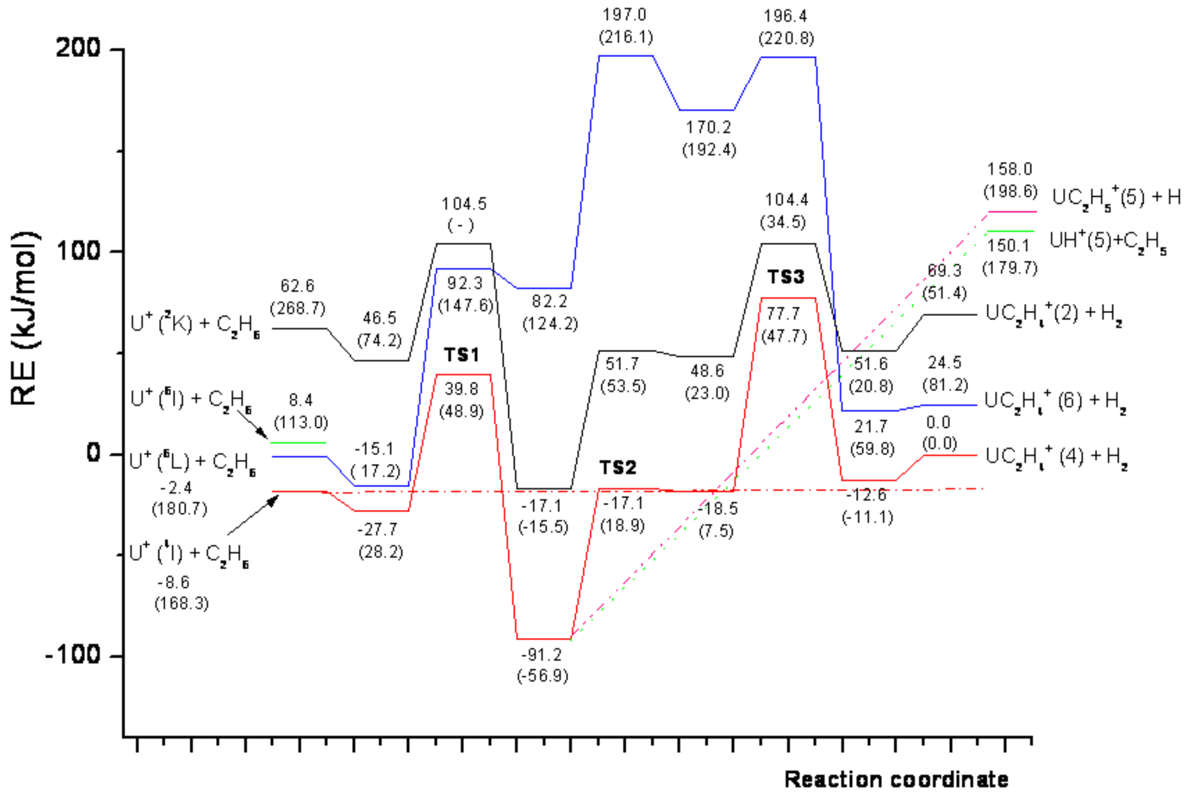
RE (kJ/mol)
200
100
0
-100
Reaction coordinate
U^+ (^2K) + C_2H_6
62.6
(268.7)
U^+ (^6I) + C_2H_6
8.4
(113.0)
U^+ (^6L) + C_2H_6
-2.4
(180.7)
U^+ (^4I) + C_2H_6
-8.6
(168.3)
46.5
(74.2)
-15.1
(17.2)
-27.7
(28.2)
104.5
(-)
92.3
(147.6)
TS1
39.8
(48.9)
82.2
(124.2)
-17.1
(-15.5)
-91.2
(-56.9)
197.0
(216.1)
51.7
(53.5)
TS2
-17.1
(18.9)
170.2
(192.4)
48.6
(23.0)
-18.5
(7.5)
196.4
(220.8)
104.4
(34.5)
TS3
77.7
(47.7)
51.6
(20.8)
21.7
(59.8)
-12.6
(-11.1)
69.3
(51.4)
24.5
(81.2)
0.0
(0.0)
158.0
(198.6)
150.1
(179.7)
$UC_2H_5^+$(5) + H
UH^+(5)+C_2H_5
$UC_2H_4^+$(2) + H_2
$UC_2H_4^+$ (6) + H_2
$UC_2H_4^+$ (4) + H_2

Figure S8

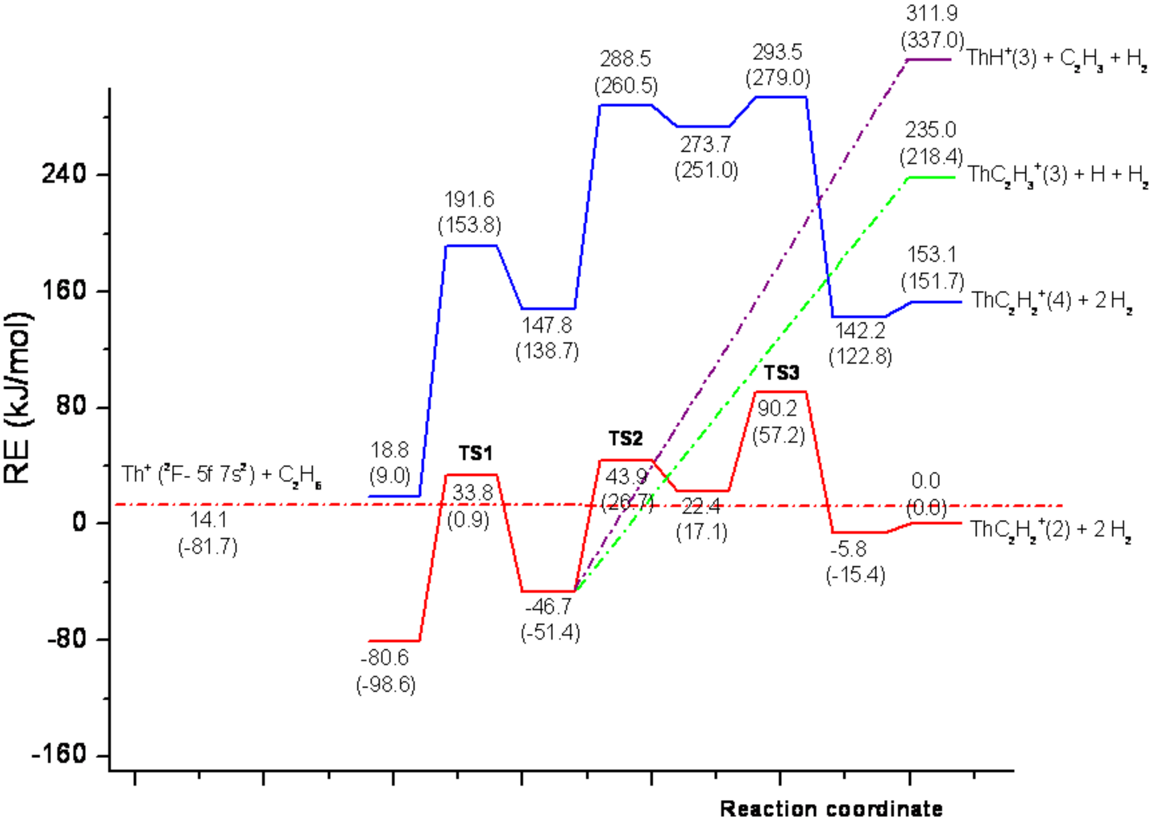
RE (kJ/mol)
240
160
80
0
-80
-160
Reaction coordinate
Th+ (2F- 5f 7s2) + C2H6
14.1
(-81.7)
18.8
(9.0)
-80.6
(-98.6)
191.6
(153.8)
TS1
33.8
(0.9)
147.8
(138.7)
-46.7
(-51.4)
288.5
(260.5)
TS2
43.9
(26.7)
273.7
(251.0)
22.4
(17.1)
293.5
(279.0)
TS3
90.2
(57.2)
142.2
(122.8)
-5.8
(-15.4)
311.9
(337.0)
ThH+(3) + C2H3 + H2
235.0
(218.4)
ThC2H3+(3) + H + H2
153.1
(151.7)
ThC2H2+(4) + 2 H2
0.0
(0.0)
ThC2H2+(2) + 2 H2

Figure S9

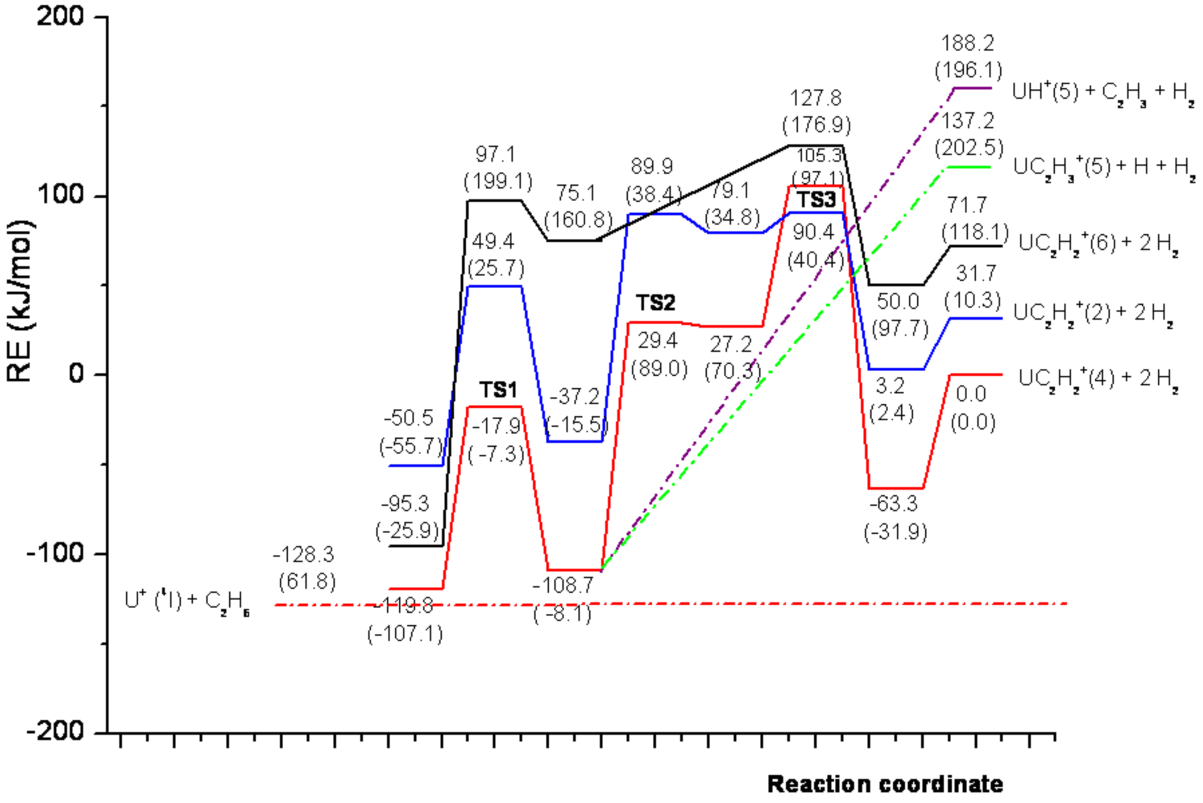
RE (kJ/mol)
200
100
0
-100
-200
Reaction coordinate
U^+ (^{4}I) + C_2H_6
-128.3
(61.8)
-119.8
(-107.1)
-95.3
(-25.9)
-50.5
(-55.7)
TS1
-17.9
(-7.3)
49.4
(25.7)
97.1
(199.1)
-108.7
(-8.1)
-37.2
(-15.5)
75.1
(160.8)
TS2
29.4
(89.0)
89.9
(38.4)
27.2
(70.3)
79.1
(34.8)
TS3
105.3
(97.1)
90.4
(40.4)
127.8
(176.9)
-63.3
(-31.9)
3.2
(2.4)
50.0
(97.7)
188.2
(196.1)
UH^+(5) + C_2H_3 + H_2
137.2
(202.5)
$UC_2H_3^+$(5) + H + H_2
71.7
(118.1)
$UC_2H_2^+$(6) + 2 H_2
31.7
(10.3)
$UC_2H_2^+$(2) + 2 H_2
0.0
(0.0)
$UC_2H_2^+$(4) + 2 H_2

Figure S10

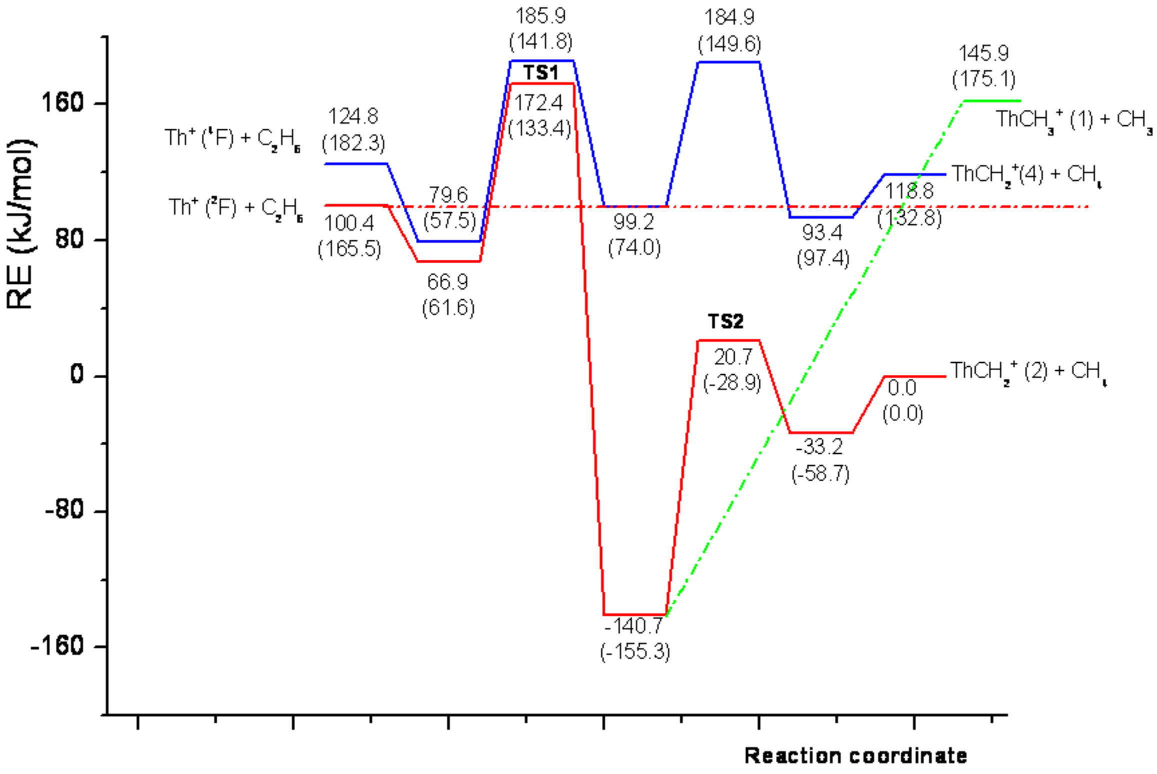
RE (kJ/mol)
160
80
0
-80
-160
Reaction coordinate
Th$^+$ (^{4}F) + C$_2$H$_6$
Th$^+$ (^{2}F) + C$_2$H$_6$
124.8
(182.3)
100.4
(165.5)
79.6
(57.5)
66.9
(61.6)
185.9
(141.8)
TS1
172.4
(133.4)
99.2
(74.0)
-140.7
(-155.3)
184.9
(149.6)
TS2
20.7
(-28.9)
93.4
(97.4)
-33.2
(-58.7)
118.8
(132.8)
0.0
(0.0)
145.9
(175.1)
ThCH$_3^+$ (1) + CH$_3$
ThCH$_2^+$(4) + CH$_4$
ThCH$_2^+$ (2) + CH$_4$

Figure S11

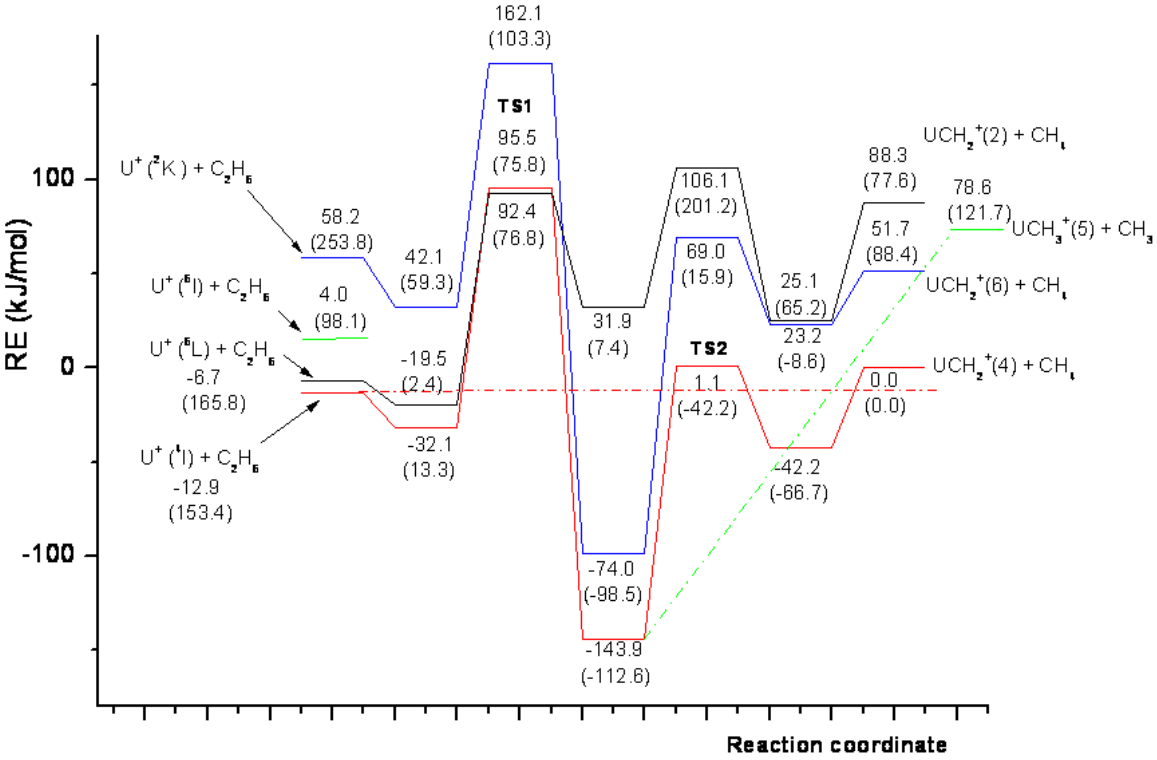
RE (kJ/mol)
100
0
-100
Reaction coordinate
U+ (2K) + C2H6
58.2
(253.8)
U+ (6I) + C2H6
4.0
(98.1)
U+ (6L) + C2H6
-6.7
(165.8)
U+ (4I) + C2H6
-12.9
(153.4)
42.1
(59.3)
-19.5
(2.4)
-32.1
(13.3)
162.1
(103.3)
TS1
95.5
(75.8)
92.4
(76.8)
31.9
(7.4)
-74.0
(-98.5)
-143.9
(-112.6)
106.1
(201.2)
69.0
(15.9)
TS2
1.1
(-42.2)
25.1
(65.2)
23.2
(-8.6)
-42.2
(-66.7)
88.3
(77.6)
51.7
(88.4)
0.0
(0.0)
78.6
(121.7)
UCH2+(2) + CH4
UCH3+(5) + CH3
UCH2+(6) + CH4
UCH2+(4) + CH4

Figure S12

Pubblicazione III

Gas phase reactions of the bare Th^{2+} *and* U^{2+} *ions with small alkanes,* CH_4, C_2H_6, *and* C_3H_8*: an experimental and theoretical study of elementary organoactinide chemistry.*

Emanuela Di Santo, Marta Santos, Maria del Carmen Michelini, Joaquim Marçalo, Nino Russo, John K. Gibson, 2010.
Submitted.

Gas-phase reactions of the bare Th^{2+} and U^{2+} ions with small alkanes, CH_4, C_2H_6 and C_3H_8: An experimental and theoretical study of elementary organoactinide chemistry.

Emanuela Di Santo[a], Marta Santos[b], Maria C. Michelini[a,*],
Joaquim Marçalo[b], Nino Russo[a], John K. Gibson[c,*]

[a]Dipartimento di Chimica, Università della Calabria, Via P. Bucci, Cubo 14 C, 87030
Arcavacata di Rende, Italy

[b] Unidade de Ciências Químicas e Radiofarmacêuticas, Instituto Tecnológico e
Nuclear, 2686-953 Sacavém, Portugal

[c] Chemical Sciences Division, Lawrence Berkeley National Laboratory, Berkeley, CA
94720, USA

*Corresponding authors: mc.michelini@unical.it (M.C.M.); jkgibson@lbl.gov (J.K.G.)

Abstract

The gas-phase reactions of two dipositive actinide ions, Th^{2+} and U^{2+}, with CH_4, C_2H_6 and C_3H_8 were studied by both experiment and theory. Fourier transform ion cyclotron resonance mass spectrometry was employed to study the bimolecular ion-molecule reactions; the potential energy profiles (PEPs) for the reactions, both observed and non-observed, were computed by density functional theory (DFT). The experiments revealed that Th^{2+} reacts with all three alkanes, including CH_4 to produce $ThCH_2^{2+}$, whereas U^{2+} reacts with C_2H_6 and C_3H_8, with different product distributions than for Th^{2+}. The comparative reactivities of Th^{2+} and U^{2+} towards CH_4 are well explained by the computed PEPs. The PEPs for the reactions with C_2H_6 effectively rationalize the observed reaction products, $ThC_2H_2^{2+}$ and $UC_2H_4^{2+}$. For C_3H_8 several reaction products were experimentally observed—these and additional potential reaction pathways were computed. The DFT results for the reactions with C_3H_8 are consistent with the observed reactions and the different products observed for Th^{2+} and

U^{2+}; however, several exothermic products which emerge from energetically favorable PEPs were not experimentally observed. The comparison between experiment and theory reveals that DFT can effectively exclude unfavorable reaction pathways, due to energetic barriers and/or endothermic products, and can predict energetic differences in similar reaction pathways for different ions. However, and not surprisingly, a simple evaluation of the PEP features is insufficient to reliably exclude energetically favorable pathways. The computed PEPs, which all proceed by insertion, were used to evaluate the relationship between the energetics of the bare Th^{2+} and U^{2+} ions and the energies for C-H and C-C activation. It was found that the computed energetics for insertion are entirely consistent with the empirical model which relates insertion efficiency to the energy needed to promote the An^{2+} ion from its ground state to a prepared divalent state with two non-5f valence electrons ($6d^2$) suitable for bond formation in C-An^{2+}-H and C-An^{2+}-C activated intermediates. The necessity for promotion reveals that the 5f electrons of U^{2+} are not suitable for organometallic bond formation.

Introduction

We have been engaged in studies of the gas-phase ion chemistry of the early actinides, An = Th, Pa, U, Np, Pu, Am, and Cm [1-6], using Fourier transform ion cyclotron resonance mass spectrometry (FTICR/MS) [7]. As was assessed in recent reviews [8-10], prior to these studies, gas-phase ion chemistry experiments with highly radioactive members of the actinide series, Pa, Np, Pu, Am, Cm, Bk, Cf, and Es, had been based on the use of the Laser Ablation with Prompt Reaction and Detection (LAPRD) technique, while FTICR/MS studies of An ions had been limited to Th and U. As FTICR/MS is well suited to extract kinetic and thermodynamic information from gas-phase reactivity studies, we have obtained new kinetic and thermochemical data for systems involving Pa [5], Np [1, 3, 4], Pu [1, 3], Am [2, 3], and Cm [6] by examining reactions of singly and doubly charged cations with oxidants. In addition to these recent studies of the reactivity of An^{2+} ions with oxidants [3,5,6], previous gas-phase experiments with An^{2+} ions have comprised reactions of U^{2+} with oxidants examined by FTICR/MS [11] and by quadrupole ion trap mass spectrometry (QIT-MS) [12], and reactions of Th^{2+} and U^{2+} with arenes studied by FTICR/MS [13].

As in actinide chemistry in general, one of the questions raised by gas-phase reactivity studies is the possible participation of the 5f electrons of the early actinides in the observed chemistry. A potential way to probe the role of the 5f (and other valence electrons) is to study the gas-phase reactivity of An^{2+} ions with hydrocarbons: An^{2+} ions exhibit electronic configurations and energetics that can reveal the chemical activity of 5f electrons [14]. Alkanes and alkenes are suitable reaction substrates to establish correlations of the electronic configurations of the ions with reaction products and mechanisms, as demonstrated in the last two decades for (mainly singly charged) d-block and f-block metal cations [15-19]. The reactivity of singly charged actinide cations with alkanes and alkenes has been investigated previously by FTICR/MS (Th, U) and by time-of-flight mass spectrometry (TOF/MS) in a LAPRD setup (Th to Es) [8-10]. Recently, we have used FTICR/MS to reinvestigate the reactivity of An^{+} ions (An = Th to Cm) with alkanes and alkenes for a systematic comparison with the reactivity of AnO^{+} ions (An = Th to Cm) with the same substrates [20]; particularly notable was the indication that the 5f electrons of Pa in PaO^{+} are chemically active.

The gas-phase reactivity of doubly charged d-block metal cations with alkanes was examined with some detail by Freiser and co-workers 10-20 years ago [21-31], following the seminal work by Tonkyn and Weisshaar [32,33] demonstrating that doubly charged d-transition metal cations were not limited to electron transfer in their reactions with hydrocarbons; formation of doubly charged bond activation products, as well as H^{-} or CH_3^{-} transfer reactions, were observed along with electron transfer. A simple one-dimensional potential energy curve-crossing model, derived from a Landau-Zener type of model, as first described by Spears et al. [34], was successfully used by the groups of Weisshaar [32,33] and Freiser [21-31] to explain the observed reactivity patterns. In brief, at long range, the reactants, M^{2+} + RH, follow attractive ion-induced dipole potential energy curves, whereas the charged products of electron transfer, M^{+} + RH^{+}, hydride transfer, MH^{+} + R^{+}, or methide transfer, MCH_3^{+} + $(RH-CH_3)^{+}$, follow repulsive Coulombic potential energy curves. The exothermicities of these reactions determine the curve crossing points and the products observed: if the reaction is not sufficiently exothermic and, consequently, the curve crossing distance is large, the transfer of an electron, a hydride, or a methide may not be feasible, and the M^{2+} ions can survive the crossing points to adequately short distances from the neutral to result in the formation of doubly charged products. This simplified model has been applied to varied systems involving doubly or, in general, multiply charged ions [35-41].

Freiser and co-workers studied the gas-phase reactivity of alkanes with transition metal dipositive ions with d^1 (Sc^{2+} [31], Y^{2+} [31], La^{2+} [28]), d^2 (Zr^{2+} [27]), and d^3 (Nb^{2+} [21,23], Ta^{2+} [27]) ground state electronic configurations (the core electrons are implicit), and a broad range of second ionization energies (11.1 - 16.2 eV). With these experiments, it was demonstrated that the d^1 metal ions had distinct reactivities relative to the d^2 and d^3 metal ions in terms of the formation of doubly charged products, and these differences were related to the occurrence of distinct reaction mechanisms [31]. Of particular interest is the proposed mechanism for alkane bond activation by M^{2+} ions with a d^1 configuration. As classical alkane activation by insertion—i.e. via generalized $H-M^{2+}-C$ or $C-M^{2+}-C$ types of intermediates—requires two valence bonding electrons at the metal center, activation by d^1 ions was rationalized by a generalized radical mechanism which proceeds by H-atom abstraction rather than formal insertion [28]. The reactivities of doubly charged lanthanide cations, Ln^{2+} (Ln = La, Ce, Pr, Nd, Sm, Eu, Gd, Tb, Dy, Ho, Er, Tm, Yb, Lu; that is, all Ln except Pm), were subsequently studied with the same hydrocarbons, as well as with alkenes [42]. These Ln^{2+} ions possess “inert” 4f electrons, different accessibilities of d^1 electronic configurations, and a range of ionization energies [43], such that these results provided a good basis for a refined comparison with the previous studies. The results for Ln^{2+} ion reactivity were essentially consistent with the model postulated by Freiser and co-workers, including the radical mechanism for activation of alkanes by d^1 M^{2+} ions [42].

In a recent review of activation of alkanes by gas-phase metal ions [41], Roithová and Schröder report on the plethora of theoretical studies of reactions of alkanes with monopositive metal ions, and the corresponding dearth of such studies of reactions of alkanes with dipositive metal ions. We have been recently involved in the study of elementary gas-phase reactions of Th and U ions using density functional theory (DFT). These studies have examined the reactions of U^+ and U^{2+} [44], UO^+ and UO^{2+} [45], and Th^+ and Th^{2+} [46] with H_2O, of U^+ and U^{2+} with N_2O [47], and of Th^+ and U^+ with CH_4 [48], and C_2H_6 [49]. Also recently, de Almeida and Duarte have reported

DFT studies of the reactions of CH_4 with An^+ (An = Ac-Pu) [50] and with Th, Th^+, and Th^{2+} [51].

In the present work, the gas-phase reactions of two dipositive actinide ions, Th^{2+} and U^{2+}, with small alkanes, CH_4, C_2H_6 and C_3H_8, were studied both experimentally and theoretically. These two actinides were chosen as the chemistry of thorium is essentially characteristic of a group 4 d-block transition element, whereas that of uranium is characteristic of an early 5f-block actinide element, with the possibility of chemically active 5f electrons. A central goal of this work is to determine if DFT can reliably model the reaction mechanisms of dipositive actinide ions with alkanes. As the applicability of DFT to reactions of alkanes with dipositive metal ions has received scant attention, the results provide a basis to evaluate both the general applicability of DFT to such reactions, as well as to the special and particularly challenging actinides, where relativistic and other complicating many-electron effects come into play [52].

Experimental Methods

The experiments were performed in a Finnigan FT/MS 2001-DT FTICR mass spectrometer, equipped with a 3 Tesla superconducting magnet, interfaced with a Spectra-Physics Quanta-Ray GCR-11 Nd:YAG laser operated at the fundamental wavelength (1064 nm), and controlled by a Finnigan Venus Odyssey data system.

The actinide samples were binary alloys of the actinide metal in a Pt matrix. These alloys were prepared by arc melting the An metal and Pt in water-cooled copper crucibles under Ti-gettered high purity argon. The alloy compositions were ~ 20 wt. % natural Th (~100% Th-232) and depleted U (99.8 % U-238). The hydrocarbons, obtained from Air Liquide (>99.9% purity), were introduced into the spectrometer as supplied, through a leak valve, to pressures in the range of $3x10^{-8}$ to $2x10^{-7}$ Torr, and were checked in situ for their purity through electron ionization mass spectra. The neutral reagent pressures were measured with a Bayard-Alpert type ionization gauge and calibrated using standard reactions of methane [53] and acetone [54] ions. The gauge readings were corrected for the relative sensitivities of the different reagents according to the approach of Bartmess and Georgiadis [55].

Doubly charged actinide metal cations were produced by laser desorption/ionization (LDI) of the samples mounted on the solids probe of the spectrometer. Isolation of the An^{2+} ions was achieved using single frequency, frequency sweep, or SWIFT excitation [56]. All ion manipulations and analyses were performed in the source cell of the dual cell instrument.

The reactant ions were thermalized by collisions with argon, which was introduced into the spectrometer through pulsed valves to pressures of $\sim 10^{-5}$ Torr, or through a leak valve to a constant pressure in the range of (1-5) x 10^{-6} Torr. The reproducibility of the reaction kinetics and the linearity of the semilog plots of normalized reactant ion intensities versus time indicated thermalization of the reactant ions. When there was more than one product ion, reproducible product distributions for different collisional cooling periods or collision gas pressures also indicated that effective thermalization had been achieved. It is well known that laser-ablated metal ions are produced with excess kinetic energies and can also be formed in electronically excited states [57,58]. For the actinides, the occurrence of strong spin-orbit coupling makes electronic relaxation less demanding than for d-transition metals [8], and, therefore, collisional cooling of electronic excited states eventually formed in LDI is presumed to be a straightforward process. Collisional cooling as performed in the present study is also usually sufficient to remove any excess translational energy on the ions formed by LDI. In previous studies of the reactivity of singly charged [1,2, 4, 5,6,,13,20] and doubly charged [3, 5,6,11,13] An ions, performed under similar experimental conditions , no evidence was found for the involvement of excited states in the observed chemistry.

Rate constants, k, were determined from the pseudo-first-order decay of the relative signals of the reactant ions as a function of time at constant neutral pressures. The decays were followed until the relative intensity of the reacting dipositive ion had reached less than 10% of its initial intensity. For comparative purposes, reaction efficiencies are also reported as k/k_{COL}, where the k_{COL} is the collisional rate constant derived from the modified variational transition-state/classical trajectory theory developed by Su and Chesnavich [59]. Collisional rate constants were calculated using experimental molecular polarizabilities of the hydrocarbons [60]. Due to uncertainties in the pressure measurements, we estimate errors up to ±50% in the absolute rate constants; however, relative errors are estimated to be ±20%.

In the reactions in which two singly charged products were generated, the product distributions were determined using the relative abundances of the metal-containing ions. The low-mass ions formed in these charge-separation reactions showed rather low and variable intensities, most probably due to the high kinetic energies that they acquire [29], which results in their loss from the ion trap. Conversely, the intensities of the high-mass metal-containing ions formed were observed to be reproducible, reflecting that these massive ions have relatively low kinetic energies [29].

Care was taken to minimize the interference of reactions with residual water and oxygen present in the background of the mass spectrometer. This was accomplished by using long pumping periods after the solids probe was inserted into the high-vacuum chamber of the instrument but before introducing the reagents. Base pressures in the turbomolecular-pumped spectrometer were typically ~10^{-8} Torr. All the reactions were compared with reactions that occurred under background conditions. When the reactions with residual gases were significant, the measured reaction rates and product distributions were corrected for the presence of oxygenated products forming directly from the reactant metal ions.

Computational Details

Density functional theory in its three-parameter hybrid B3LYP [61,62] formulation was used together with the Stuttgart–Dresden basis set for the uranium atom (25s 16p 15d 7f)/[7s 6p 5d 3f] in combination with the 60 core electrons [63] relativistic effective core potential (RECP). This small–core RECP, so–called SDD pseudopotential, replaces the 60 electrons in the inner shells 1 through 4, leaving the explicit treatment of the $n = 5$ shell (5s 5p 5d and 5f), and also the 6s, 6p, 6d and 7s valence electrons. The 6-311++G(d,p) basis set of Pople and co-workers was employed for the rest of the atoms [64-66] (we refer to these results as B3LYP/SDD, hereafter). These computations were carried out with GAUSSIAN 2003 package. [67] Ultrafine grids were employed in all cases. This computational approach was chosen based on the performance observed in our previous studies of bare actinide cations reactivities. [44, 46-49]

Singlet and triplet spin states were considered in all of the reactions involving Th^{2+}, and quintet and triplet spin states in the case of U^{2+} reactions. Singlet spin state optimizations were done within the restricted Kohn-Sham formalism, whereas the open shell structures were studied using spin-unrestricted methods. We have checked the $<S^2>$ values to evaluate whether spin contamination can influence the quality of the results. In all cases we have found that the calculated values differ from S(S+1) by less than 5%.

No symmetry restrictions were imposed during the geometry optimizations, and we have employed several initial geometries for each of the studied species. The nature of the calculated stationary points was characterized by a vibrational analysis performed within the harmonic approximation. For all of the studied reactions we report Potential Energy Profiles (PEPs) calculated as relative energies of the species involved in the reactions pathways with respect to the ground state reactant asymptotes at 0 K. The zero-point vibrational energy (ZPVE) corrections were included in all of the relative energies.

We have ensured that every transition state has only one imaginary frequency, and that the vibrational mode associated to the imaginary frequency corresponds to the correct movement of the involved atoms. All the minima connected by a given transition state were confirmed performing IRC (Intrinsic Reaction Coordinate) computations, as implemented in Gaussian03 program. [68,69]

The bonding properties of some key structures were studied using natural bond orbital analysis (NBO). [70,71]

Results and Discussion

The experimental results for the bimolecular reactions of Th^{2+} and U^{2+} with methane, ethane and propane are summarized in Table 1 as measured reaction rate constants, reaction efficiencies expressed as observed rate constants relative to collisional rate constants, and product distributions. With the exception of U^{2+}/CH_4, for which no reaction is observed, the other five An^{2+}/C_mH_n reactions each proceed with moderate efficiencies, in the range of $k/k_{COL} = 0.11 – 0.22$. The observed product distributions were quite disparate between Th^{2+} and U^{2+} and a focus of the following discussion is on evaluating the observed reactivity differences based on the computed PEPs.

As $IE[C_2H_6] = 11.0$ eV and $IE[C_3H_8] = 11.5$ eV [72] are both below $IE[Th^+] \approx 11.65$ eV and $IE[U^+] \approx 11.7$ eV [73], electron transfer from these neutrals to the An^{2+} is exothermic. The non-observation of these electron transfer channels can be attributed to the kinetic barrier discussed in the Introduction—a difference in IEs of at least 1 eV is generally required for electron transfer from a neutral to a dipositive ion [29,42]. As $IE[CH_4] = 12.5$ eV [72] exceeds $IE[Th^+]$ and $IE[U^+]$, electron transfer from CH_4 is endothermic and should not occur regardless of kinetic effects.

The general reaction pathways which were observed correspond to single- and double-dehydrogenation, methide-transfer, and hydride-transfer, as given by Eqns. (1) – (4).

$$An^{2+} + C_mH_n \rightarrow AnC_mH_{n-2}^{2+} + H_2 \quad (1)$$
$$An^{2+} + C_mH_n \rightarrow AnC_mH_{n-4}^{2+} + 2H_2 \quad (2)$$
$$An^{2+} + C_mH_n \rightarrow AnCH_3^{+} + C_{m-1}H_{n-5}^{+} + H_2 \quad (3)$$
$$An^{2+} + C_mH_n \rightarrow AnH^{+} + C_mH_{n-1}^{+} \quad (4)$$

The PEPs most pertinent to the observed reaction pathways are shown in Figures 1-12; additional PEPs, as well as geometrical parameters, are provided in the Supporting Information.

Reactions with CH_4

As indicated in Table 1, methane is activated by Th^{2+} to produce the carbene, $ThCH_2^{2+}$, via elimination of H_2. In contrast, U^{2+} is inert towards methane to within the experimental detection limit. The computed PEPs for the Th^{2+}/CH_4 and U^{2+}/CH_4 reactions are shown in Figures 1 and 2. The geometrical parameters of all the species involved in these pathways are included as Supporting Information (Figures S1 and S2, respectively).

The reaction mechanism for the activation of CH_4 is similar to that reported for Th^+ and U^+ [48]. The reaction starts with the insertion of the metal cation into the C-H bond of methane to form a hydrido-methyl intermediate, $H\text{-}An^{2+}\text{-}CH_3$ (Intermediate **I,** An = Th, U). From that intermediate the H_2 elimination evolves through the formation of a four-centered transition state (**TS2**), which yields a second insertion intermediate $(H_2)An^{2+}\text{-}CH_2$ (**II**), in which the H_2 molecule is already formed. The last step of the reaction, formation of the dehydrogenation products, takes place directly from the intermediate **II**, without an energy barrier. Other possible reaction products have been considered. In particular, the formation of AnH^+ and CH_3^+ products can be obtained by simple breaking of the An-C bond breaking in the $H\text{-}An^{2+}\text{-}CH_3$ intermediate, after the surpassing of the associated activation barrier (**TS3**).

For Th^{2+}/CH_4, the two reactions given by Equations (5) and (6) are comparably exothermic, as indicated by the computed reaction enthalpies (Fig. 1).

$$Th^{2+} + CH_4 \rightarrow ThCH_2^{2+} + H_2 \quad \Delta H = -66\ \text{kJ mol}^{-1} \qquad (5)$$
$$Th^{2+} + CH_4 \rightarrow ThH^+ + CH_3^+ \quad \Delta H = -72\ \text{kJ mol}^{-1} \qquad (6)$$

Although the CH_3^+-elimination reaction is computed to be energetically competitive, only H_2-elimination is observed. Referring to the PEPs for Equation (6) in Figure 1, it is apparent that the CH_3-elimination pathway is inhibited by transition states (**TS**s) which lie above the reactant energies, and cannot be surmounted under the thermal conditions of the experiments (298 K ≈ 2.5 kJ mol^{-1}). The very high **TS** energy barriers computed for this exothermic charge-separation reaction is seen for other charge separation reactions studied in this work. As discussed above, the general observation of inefficient charge-separation is consistent with the description of such reactions according to Landau-Zener theory, in which Coulombic repulsion of the two monopositive products presents an inherent barrier to such processes [34]. Referring to the PEP for Th^{2+}/CH_4, the very high-energy **TS3** which inhibits the exothermic formation of $ThH^+ + CH_3^+$ directly corresponds to the dissociation of $\{H\text{-}Th\text{-}CH_3\}^{2+}$ to the two monopositive products; the PEP computed by DFT evidently incorporates, at least qualitatively, the large barrier to the charge separation process.

For the Th^{2+}/CH_4 reaction, the H_2-elimination reaction proceeds with a moderate but significant efficiency, $k/k_{COL} = 0.11$. The computed PEP for this exothermic reaction (Fig. 1) lies below the entrance energy, consistent with its observation. It is notable that the pathway for this reaction requires a spin-crossing, from the triplet state reactants to the singlet products. As is typical for actinide ion reactions, such spin-crossing does not present a substantial barrier, presumably due to the enhanced spin-orbit coupling for these heavy atoms, which relaxes spin conservation restrictions. Several other spin-crossing PEPs were computed for other observed reactions, as discussed below.

The computed PEP for the Th^{2+}/CH_4 reaction is in good agreement with the results recently obtained by de Almeida and Duarte for the same reaction, using a similar computational approach [51].

As shown in Figure 2, for U^{2+}/CH_4 the dehydrogenation reaction corresponding to Eqn. 1 is computed to be substantially endothermic, in accord with the experimental observation that it does not occur. The CH_3^+-elimination channel corresponding to Eqn. 2 is computed to be slightly exothermic; however, substantial barriers are encountered on the PEP and this reaction is not expected to occur. The DFT results are in accord with the observed inert nature of U^{2+} towards CH_4.

Comparison of Figs. 1 and 2 reveals that the association energies between the two An^{2+} and CH_4—i.e., the energy of the first complex, **FC**, are comparable: 120 kJ mol^{-1} for Th^{2+}-CH_4 and 103 kJ mol^{-1} for U^{2+}-CH_4; as this is primarily an electrostatic interaction, such agreement is expected. A key difference between the two PEPs is the much higher energy of **TS1** and intermediate **I** for U^{2+}/CH_4 as compared with Th^{2+}/CH_4. This difference corresponds to a greater barrier to C-H bond insertion for U^{2+} and is in accord with empirical models which have related atomic energetics of metal ions with C-H (and C-C) bond activation efficiencies [74]. The correspondence between DFT and empirical models, evident for the An^{2+}/CH_4 reactions, also appears for other studied reactions, as elaborated below.

Reactions with C_2H_6

In contrast to CH_4, where U^{2+} is unreactive, with C_2H_6 both Th^{2+} and U^{2+} are reactive, with comparable efficiencies, 0.15 and 0.18, respectively. For Th^{2+} the sole product corresponds to double dehydrogenation, Eqn. (7), whereas for U^{2+} only single dehydrogenation is observed, Eqn. (8).

$Th^{2+} + C_2H_6 \rightarrow ThC_2H_2^{2+} + 2H_2$ (7)
$U^{2+} + C_2H_6 \rightarrow UC_2H_4^{2+} + H_2$ (8)

The PEP for the Th^{2+}/C_2H_6 dehydrogenation reaction is shown in Fig. 3; the geometrical parameters of all the minima and transition states involved in the reaction are presented in Fig. S3. The reaction mechanism is similar to that described for the activation of CH_4. The double dehydrogenation process involves the formation of four different insertion intermediates, H-Th^{2+}-C_2H_5 (**I**), (H_2)-Th^{2+}-C_2H_4 (**II**), H-Th^{2+}-C_2H_3 (**III**),and $(H_2)Th^{2+}$-C_2H_2 (**IV**); and the surmounting of the reaction barriers associated to each step (**TS1** to **TS4**). The pathway for the first H_2-elimination involves a spin-crossing from the triplet to singlet states to exothermically produce {$ThC_2H_4^{2+}$ + H_2}. This reaction is sufficiently exothermic that the pathway to the second dehydrogenation lies below the entrance energy asymptote. The sequential elimination of two H_2 molecules to give {$ThC_2H_2^{2+}$ + $2H_2$} is predicted by the PEP and is the only observed reaction.

The possibility of C-C activation of C_2H_6 by Th^{2+} was also considered, as shown in Fig. 4. According to the PEP, the insertion of Th^{2+} into the C-C bond to give the very stable intermediate is accessible; the reaction pathway then proceeds to {$ThCH_2^{2+}$ + CH_4}. The computed energy for this reaction channel indicates that it is substantially more exothermic than the observed double dehydrogenation channel. Comparison of the PEPs in Figs. 3 and 4 suggests why the more exothermic C-C activation pathway is not observed. The initial association complex, **FC**, is identical for C-H and C-C activation, at -160 kJ mol^{-1}. However, the subsequent barrier for C-H insertion, **TS1** at

-109 kJ mol^{-1}, is substantially lower than that for C-C insertion, **TS1** at -60 kJ mol^{-1}. The reaction evidently proceeds from the initial association complex exclusively via the lower **TS1**, resulting solely in the observed double dehydrogenation.

The PEP for the U^{2+}/C_2H_6 dehydrogenation reaction is shown in Fig. 5 and the corresponding optimized structures in Fig. S5. Assuming that the reaction proceeds along the lowest energy pathway, there is a crossing from the quintet reactants to the triplet pathway and then back to the quintet pathway, to the $\{UC_2H_4 + H_2\}^{2+}$ single-dehydrogenation product, which is exothermic, albeit substantially less so than for Th^{2+}/C_2H_6. As the computed energy for **TS1** in Fig. 5, 4 kJ mol^{-1}, is slightly above the entrance energy, the PEP predicts that this reaction should not proceed. However, because completely thermalized reactants in the room temperature FTICR/MS experiments are at 2.5 kJ mol^{-1} above zero, the computed barrier above the actual entrance energy is <2 kJ mol^{-1}, which is certainly well within the computational uncertainties. In contrast to the Th^{2+}/C_2H_6 reaction, the second dehydrogenation by U^{2+} is substantially endothermic, in accord with its non-observation. The computed PEP for C-C activation of C_2H_6 by U^{2+} (Fig. S8) reveals that the reaction is endothermic and should not be observed. The DFT results are entirely consistent with the distinctly exclusive double- and single-dehydrogenation products seen for Th^{2+} and U^{2+}, respectively, via a classical C-H insertion mechanism.

A notable aspect of the $UC_2H_4^{2+}$ product is that the quintet spin state suggests that there are four non-bonding electrons at the uranium metal center, which would indicate that two covalent U-C bonds are not formed; triplet $UC_2H_4^{2+}$ lies 8 kJ mol^{-1} above the entrance energy, rendering it slightly endothermic. The computed geometry of quintet $UC_2H_4^{2+}$ (Fig. S6) is in concurrence with the qualitative bonding interpretation, particularly when compared with the geometry of singlet $ThC_2H_4^{2+}$ (Fig. S3). In the case of $UC_2H_4^{2+}$ (^5A) the U-C distance is 2.66 Å and the C-C distance is 1.37 Å. In contrast, for $ThC_2H_4^{2+}$ (^1A), the Th-C distance is 2.20 Å and the C-C distance is 1.60 Å. Whereas $ThC_2H_4^{2+}$ exhibits a structure indicative of a metallacycle with covalent Th-C bonds, the structure of $UC_2H_4^{2+}$ suggests that a much weaker electrostatic interaction of the U^{2+} with the π-electron system of $H_2C{=}CH_2$ is occurring. To evaluate in greater detail the bonding in these species, NBO analyses were performed.

Our calculations indicate that in the case of $ThC_2H_4^{2+}$, the Th-C □-bonds are formed from Th hybrid orbitals that have 50 % of d-, 28 % of f- and 17 % of s-character. The main contribution to these molecular orbitals is due to the C atoms (approximately sp^3 hybrids) with a polarization coefficient (0.89) that indicates that the Th-C bond can be described as a highly polarized covalent bond. NBO analysis describes the C-C bond as a single bond formed from sp^3 C hybrids. A similar analysis performed on the quintet $UC_2H_4^{2+}$moiety indicates that there are no covalent bonds between the metal and the C atoms, and there is a double bond between the C-C atoms. As expected, the □- C-C bond is formed from sp^2 hybrids of C atoms, whereas the□ -bond is formed from pure p C atomic orbitals.

The singlet $ThC_2H_2^{2+}$ ground state geometry (Fig. S4) is characterized by a Th-C bond distance of 2.19 Å , a C-C bond distance of 1.36 Å and an H-C-C angle of 129.8 degrees. Accordingly, the NBO analysis predicts that a□ -bond is formed between the metal and each of the C atoms. These□ -bonds are formed from s-d-f metal hybrids (54% d, 25 % f and 20% s) with a very small contribution (2%) of p-orbitals, and sp^2 C hybrids. Again, the polarization coefficients (0.82 for C and 0.43 for Th) indicate that the covalent bonds are very polarized. In concurrence with the geometrical parameters, NBO indicates a double C-C bond.

In the case of the quintet ground state $UC_2H_2^{2+}$ structure the U-C bond distance (2.46 Å) is intermediate between that of $UC_2H_4^{2+}$ (2.66 Å) and the metal carbon distance in $ThC_2H_4^{2+}$ or $ThC_2H_2^{2+}$ (2.20 Å). The C-C bond (1.25 Å) is slightly shorter than that of $ThC_2H_2^{2+}$ (1.36 Å), whereas the H-C-C bond angle is slightly larger, 154.1 degrees compared to the 129.8 of $ThC_2H_2^{2+}$. As suggested by the geometrical analysis, bond analysis indicates that there is some covalent bond formation between U and the C atoms in $UC_2H_2^{2+}$. However, these cannot be described as two full covalent bonds, similar to those formed in $ThC_2H_2^{2+}$. This structure is better described as a superposition of two Lewis structures in which the spin density is partially delocalized onto the C atoms (see scheme 1 in the Supporting Information).

As is evident in Figs. 3, 4, 5 and S8, the charge-separation reactions for Th^{2+} and U^{2+} with C_2H_6 to produce the corresponding $\{AnH^+ + C_2H_5^+\}$ or $\{AnCH_3^+ + CH_3^+\}$ are all substantially exothermic. However, for each of these reactions there is a high **TS** barrier which corresponds to the charge-separation process and can be attributed to Coulombic repulsion between the nascent product ions, as discussed above. The case of the non-formation of $\{ThH^+ + C_2H_5^+\}$ is particularly illustrative as this reaction is substantially more exothermic than the observed double-dehydrogenation reaction and does not exhibit a **TS** which exceeds the entrance energy. As seen in Fig. 3, the charge-separation and dehydrogenation pathways diverge on the PEP after the insertion intermediate **I**: charge-separation proceeds directly to the products via **TS5** which lies at -14 kJ mol^{-1} whereas dehydrogenation proceeds by hydrogen-atom abstraction via **TS2** at -151 kJ mol^{-1}. The absence of the charge-separation channel is attributed to the much higher **TS5** versus **TS2** such that the reaction proceeds exclusively via the lower **TS2** at this stage of the mechanism, which guides the reaction to the thermodynamically less stable products, $ThC_2H_2^{2+} + 2H_2$.

As with CH_4, the initial association complex energy wells, **FC**, are roughly comparable for Th^{2+} and U^{2+}, at -160 and -131 kJ mol^{-1}, respectively. These association energies are somewhat greater for the more polarizable C_2H_6 molecule as compared with CH_4, as expected for a primarily electrostatic interaction.

Reactions with C_3H_8

The reactions of the An^+ ions with C_3H_8 are considerably more complex than with C_2H_6, from both the experimental and theoretical perspectives. As seen in Table 1, three products are observed with Th^{2+} and four with U^{2+}, as opposed to only one for C_2H_6 with both An^{2+} ions. To evaluate the experimental observations, many reaction pathways were evaluated by theory. For clarity, the discussion of the relationship between the experimental and theoretical results is focused on key points which establish that the computed PEPs are consistent with the observed reaction pathways. The seven experimentally observed reactions, reported in Table 1, are given by Eqns. (9) – (15).

$$Th^{2+} + C_3H_8 \rightarrow ThC_3H_4^{2+} + 2H_2 \qquad (9)$$

$$Th^{2+} + C_3H_8 \rightarrow ThC_2H_2^{2+} + CH_4 + H_2 \qquad (10)$$

$Th^{2+} + C_3H_8 \rightarrow ThCH_3^+ + C_2H_5^+$ (11)
$U^{2+} + C_3H_8 \rightarrow UC_3H_6^{2+} + H_2$ (12)
$U^{2+} + C_3H_8 \rightarrow UC_2H_4^{2+} + CH_4$ (13)
$U^{2+} + C_3H_8 \rightarrow UCH_3^+ + C_2H_5^+$ (14)
$U^{2+} + C_3H_8 \rightarrow UH^+ + C_3H_7^+$ (15)

The only reaction pathway common to both Th^{2+} and U^{2+} is the formation of $\{AnCH_3^+ + C_2H_5^+\}$, Eqns. (11) and (14). The overall reaction efficiency of U^{2+}, $k/k_{COL} = 0.22$ is somewhat greater than that of Th^{2+}, $k/k_{COL} = 0.13$.

Figs. 6 and 9 show the computed PEPs for dehydrogenation of C_3H_8 by Th^{2+} and U^{2+}, respectively. It is evident that the mechanisms are essentially identical—the primary difference is that the PEP for U^{2+} is shifted to higher energies after the first association complex, **FC**. This shift appears for the first intermediate complex, **I**, and is evidently related to the greater barrier for the initial insertion of U^{2+} into the C-H bond. The PEP for Th^{2+} proceeds to the highly exothermic single-dehydrogenation product, $ThC_3H_6^{2+}$, at -253 kJ mol^{-1}. In analogy with the Th^{2+}/C_2H_6 reaction, the Th^{2+} PEP continues on to the double-dehydrogenation product, with all of the transition state energies lying well below the entrance energy. The result is the considerably exothermic double-dehydrogenation to give the product corresponding to Eqn. (9). As seen in Fig. 9, the corresponding PEP for U^{2+} proceeds below the entrance energy to the exothermic formation of $UC_3H_6^{2+}$, the observed dehydrogenation product. As with C_2H_6, the PEP then continues to endothermic double-dehydrogenation, with transition states which lie well above the entrance energy. The computed PEPs are consistent with the observed double- and single-dehydrogenation reactions, Eqns. (9) and (12), for Th^{2+} and U^{2+}, respectively. Alternative PEPs for dehydrogenation of C_3H_8 by Th^{2+} and U^{2+} are shown in Figs. S13 and S27—these alternative pathways are consistent with the observed double- and single-dehydrogenations. These alternative PEPs differ from the dehydrogenation mechanism previously described in that the initial C-H bond activation occurs on a secondary C atom. Both dehydrogenation mechanisms are energetically very close. The first dehydrogenation products are slightly less exothermic in the case of Th^{2+} (-224 kJ/mol) and more exothermic in the case of U^{2+} (-100 kJ/mol). The double dehydrogenation products are the same in both reaction mechanisms.

Figs. 7 and 11 show the computed PEPs for the activation of a C-C bond leading to CH_4-elimination, followed by H_2-elimination, for Th^{2+} and U^{2+} respectively. As for the case of C-H activation and double-dehydrogenation, the two mechanisms are essentially the same. Again, the main difference is that the PEP for U^{2+} is shifted to substantially higher energies after the first association complex, **FC**, such that the insertion intermediate, **I**, lies at -315 kJ mol^{-1} for Th^{2+}, but at only -83 kJ mol^{-1} for U^{2+}. After the triplet to singlet spin-crossing, the Th^{2+} PEP proceeds well below the entrance energy to the CH_4-elimination product, at -231 kJ mol. This is followed by intramolecular C-H activation and ultimately exothermic H_2-elimination along a PEP which lies below the entrance energy. The predicted and observed overall reaction is as given by Eqn. (10). In the corresponding case of U^{2+} (Fig. 11), the C-C activation PEP proceeds to the observed exothermic CH_4-elimination product along a PEP which lies below the entrance energy. As for the U^{2+}/C_2H_6 PEP (Fig. 5), there is double spin-crossing, from quintet to triplet back to quintet, such that the product is $UC_2H_4^{2+}$ (^5A) discussed above, rather than $UC_2H_4^+$ (3) in which two of the four uranium valence electrons would be engaged in U-C covalent bonds. From the CH_4-elimination product, $UC_2H_4^{2+}$ (5), the U^{2+}/C_3H_8 reaction proceeds to intramolecular C-H activation and endothermic H_2-elimination along a PEP which lies above the entrance energy. It is evident from the computed PEPs why only CH_4-elimination is observed for U^{2+} (Eq. (13)) whereas $\{CH_4 + H_2\}$-elimination is observed for Th^{2+} (Eq. (10)). Alternative PEPs for $\{CH_4 + H_2\}$ elimination by Th^{2+} are shown in Figs. S15 and S17—these alternative pathways are consistent with Eqn. (10); the high TS3 for H_2-elimination followed by CH_4-elimination (Fig. S15) suggests initial CH_4-elimination by one or both of the favorable pathway shown in Fig. 7 and S17. Alternative PEPs for $\{CH_4 + H_2\}$ elimination by U^{2+} are shown in Figs. S29 and S31—these alternative pathways are consistent with Eqn. (13), the observation of CH_4-elimination without H_2-elimination.

The only reaction channel common to both Th^{2+} and U^{2+} is the methide-abstraction charge separation, to produce $\{AnCH_3^+ + C_2H_5^+\}$, Eqns. (11) and (14); the respective PEPs are shown in Figs. 8 and 10, respectively. For these reactions, the first association complexes, **FC’**, between the An^{2+} and C_3H_8 do not engage all three carbon atoms and lie at slightly higher energies than the association complexes involved in the CH_4-elimination PEPs in Figs. 7 and 11—e.g., compare **FC** in Fig. 7 and **FC’** in Fig. 8. Again, the PEPs for Th^{2+} and U^{2+} are similar, the primary difference being the typical shift of the PEP for U^{2+} to higher energies beginning at the first insertion intermediate, **I**. Both PEPs proceed below the entrance energy to the highly exothermic $\{AnCH_3^+ + C_2H_5^+\}$ products. The less exothermic $\{AnC_2H_5^+ + CH_3^+\}$ products are not experimentally observed.

The reaction of U^{2+} with C_3H_8 also proceeds to hydride abstraction, Eqn. (15), as a minor channel. The PEP for this reaction (Fig. 12) reveals that it is highly exothermic and proceeds below the entrance energy. As would be predicted by analogy with other reactions, the corresponding reaction for Th^{2+} should proceed along a similar PEP with a lower barrier to insertion and a more stable $\{H\text{-}Th\text{-}C_3H_7\}^{2+}$ insertion complex which can dissociate to the exothermic products $\{ThH^+ + C_3H_7^+\}$—the computed PEP for Th^{2+} (Fig. S21) indicates just this scenario. This is an example where it is evident that a computed PEP is consistent with an observed reaction, Eq. (15), whereas the corresponding computed PEP for another metal ion, here Th^{2+}, would be consistent with the occurrence of the analogous reaction which is not observed. The experimental results suggest that the **FC’** between U^{2+} and C_3H_8 (Figs. 10 and 12) are roughly three times more likely to proceed to C-C activation (Fig. 10) rather than C-H activation (Fig. 12), a result which would not be clearly predictable from the PEPs, specifically from the comparative **TS1** barriers, which lie at -48 kJ mol^{-1} for C-C activation and a -68 kJ mol^{-1} for the less abundant C-H activation channel. It is evident that the computed PEPs are effective at rationalizing and predicting allowable reaction pathways and products, but cannot alone be employed to predict which allowable reaction pathways will predominate. These results illustrate the capabilities and limitations of considering the features of PEPs alone, such as well depths and barrier heights, for predicting and modeling reaction mechanisms. A deeper insight into the reaction mechanisms could be only obtained studying the actual motion of the atoms on the PES, by means of molecular dynamics methodologies [75].

Other computed PEPs are shown in Figs. S19, S33, S35 and S37. The only other potentially favorable computed reaction pathway was C_2H_6 elimination by Th^{2+}, to exothermically produce $ThCH_2^{2+}$. However, the PEP for this reaction (Fig. S19) exhibits a high **TS1,** only 16 kJ mol^{-1} below the entrance energy, and it is not surprising that this pathway is not experimentally observed.

Correlations between computed mechanisms and atomic energetics

In early studies of hydrocarbon activation by lanthanide cations it was found that there was a good correlation between the energy needed to excite the bare Ln^+ ions from their ground states to the lowest-lying excited state with two non-4f valence electrons [74]. This observation indicated that the quasi-valence 4f electrons were ineffective at covalent bond formation, as is required in C-Ln^+-H and C-Ln^+-C activated intermediates. An analogous relationship was subsequently identified for the actinide ions, whereby the efficiencies of hydrocarbon activation processes parallels the energy needed to promote the An^+ from their ground electronic configuration to the lowest-lying configuration with two non-5f valence electrons [8]. This latter observation indicated that for the actinide ions the 5f electrons are generally ineffective at covalent bond formation in hydrocarbon activation.

For the dipositive lanthanide ions, the promotion energies to electronic configurations with two non-4f electrons are much higher than for the monopositive ions and the observed reactivities towards small hydrocarbons have been attributed to the accessibility of the d^1 configurations and a radical reaction mechanism which does not involve direct insertion into a C-H or C-C bond [42]. The only Ln^{2+} ion which was found to (inefficiently) activate C_2H_6 and induce H_2-elimination was Gd^{2+}. The promotion energy for Gd^{2+} from its ground state, $4f^75d^1$, to the lowest-lying configuration with two non-4f valence electrons, $4f^65d^2$, has been estimated as 930±90 kJ mol^{-1} [76]; this energy is prohibitively large to be accessible in an insertion reaction mechanism. Instead, the reactivity of Gd^{2+} was attributed to the ground state d^1 configuration and the radical reaction mechanism postulated for d^1 transition metal ions by Freiser and co-workers [28,31].

A systematic study of reactions of the early monopositive actinide ions, Th^+ through

Cm^+, with small alkanes was previously performed [20]. It was found that only Th^+ activated CH_4 and C_2H_6; as other An^+, including U^+, with ground or low-lying electronic states with two non-5f electrons were unreactive, it is apparent that the monopositive An^+ ions are inherently less reactive towards alkanes as compared with the dipositive An^{2+} ions. It is instructive to compare our previous computational results for reactions of monopositive Th^+ and U^+ with CH_4 [48] and C_2H_6 [49] with the present results for the corresponding dipositive ions at the same level of theory, B3LYP/SDD. Of particular interest are the comparative depths of the energy wells for the initial **FC** association complexes, $An^{+/2+}$-C_xH_y (in kJ mol^{-1}): Th^+-CH_4/-31; U^+-CH_4/-22; Th^+-C_2H_6/-33; U^+-C_2H_6/-19; Th^{2+}-CH_4/-120; U^{2+}-CH_4/-103; Th^{2+}-C_2H_6/-160; U^{2+}-C_2H_6/-131; Th^{2+}-C_3H_8/-215; U^{2+}-C_3H_8/-177. As expected, the association energy is substantially greater for the dipositive ions; these energies increase as the size and polarizability of the alkane increases. It would be expected that the additional energy provided to the reaction system for the dipositive ions could enable reaction mechanisms, such as insertion, which might not be feasible for a monopositive ion with otherwise similar electronic characteristics.

The first intermediate **I** for all of the computed reaction PEPs in this work corresponds to insertion of an An^{2+} ion into a C-H or a C-C bond to produce an activated intermediate. The reliability of empirical correlations of the efficiencies of such insertion mechanisms with the energy needed to promote the inserting actinide ion from its ground state to an excited state with two non-5f valence electrons suggests that the relative energies of the insertion complexes for Th^{2+} and U^{2+} should correlate with the promotion energies to a prepared divalent state suitable for insertion for these two ions. The energetics of the low-lying electronic configurations Th^{2+} and U^{2+} are known [14]. For both ions the lowest-lying configuration with two non-5f electrons is $5f^{n-2}6d^2$ ($n = 2$ for Th^{2+}; $n = 4$ for U^{2+}). In the case of Th^{2+}, the ground state is $5f^16d^1$ and the $6d^2$ configuration is nearly degenerate, at 1 kJ mol^{-1}; with U^{2+}, the ground state is $5f^4$, the $5f^36d^1$ configuration is 3 kJ mol^{-1} higher, and the $5f^26d^2$ configuration is at 232 kJ mol^{-1} above ground [14]. The $6d^17s^1$ configurations of Th^{2+} and U^{2+} are substantially higher in energy [14,76]; it is the $6d^2$ configuration which is considered important for effective insertion. According to the empirical promotion energy model, which presumes that a $6d^2$ configuration is necessary for insertion, it is predicted that the energy of the insertion should be approximately 230 kJ mol^{-1} less favorable for U^{2+} as compared with Th^{2+}. This proposed correlation can be evaluated from the computed PEPs for C-H and C-C activation—the results are compiled in Table 2. The computed insertion energies, ΔE_i, correspond to the difference in energy between the first association complex, **FC**, and the first insertion intermediate, **I**; the two C-C insertion energies given for C_3H_8 correspond to the two different first association complexes, **FC** and **FC'**, and insertion intermediates, **I**, which have very slightly different geometries. All of the insertion processes, **FC** → **I**, are substantially exothermic for Th^{2+}, from -75 kJ mol^{-1} for C-H activation in CH_4 down to -167 kJ mol^{-1} for C-C activation in C_3H_8. In contrast, all of the corresponding insertions are endothermic for U^{2+}, from +150 kJ mol for C-H activation in CH_4 down to +39 kJ mol^{-1} for C-C activation in C_3H_8. The differences between the ΔE_i for Th^{2+} and U^{2+}, given in Table 2, are in the range of 184 - 261 kJ mol^{-1}. Although these differences are not unerringly at the predicted value of 230 kJ mol^{-1}, the results are clearly consistent with the correlation between promotion energies and insertion energies; as the electronic structure of the bare ions are perturbed by association and subsequent insertion, the consistent albeit non-exact agreement with the promotion energy model is quite remarkable. This evaluation of the PEPs demonstrates a direct relationship between electronic promotion energies of the bare Th^{2+} and U^{2+} ions with the computed DFT insertion energies, and effectively validates the empirical promotion energy model which has been extensively and effectively employed to understand and predict the reactivities of bare lanthanide and actinide ions in the gas phase.

The resulting shifts to higher energy of the entire PEPs for U^{2+} as compared with Th^{2+} due to the relative energies of the first insertion intermediates determines whether a reaction proceeds, as in the case of non-activation of CH_4 by U^{2+}, and the product distributions for reactions which do proceed, as in the case of H_2-elimination from C_2H_6 by U^{2+} rather than $2H_2$-elimination by Th^{2+}. A key implication of the evident necessity for promotion of ground state U^{2+} from its $5f^4$ ground state configuration to the $5f^26d^2$ configuration is that the quasi-valence 5f electrons of uranium are not effective in covalent bond formation in C-H or C-C bond activation.

In a previous study of the reactivities of the dipositive lanthanide ions, Ln^{2+}, with alkanes and alkenes, the reactivity patterns indicated reactivity mechanisms associated with $5d^1$ electronic configurations [42]. These radical ion reactions were considered to proceed by H-atom abstraction, rather than activation by insertion; the radical mechanism was first proposed by Freiser and co-workers [28,31]. The promotion energies for the Ln^{2+} from their ground states to the $5d^2$ configuration are much higher than the value of 232 kJ mol^{-1} for U^{2+}. Brewer has estimated that the lowest Ln^{2+} $5d^2$ configuration occurs for Ce^{2+}, which is known to lie 484 kJ mol^{-1} above the ground state [76]. It was previously found that Ce^{2+} is unreactive with C_2H_6, and only very inefficiently ($k/k_{COL} = 0.007$) dehydrogenates C_3H_8; in contrast, Gd^{2+}, which has a $5d^1$ ground state (but a very high promotion energy to the $5d^2$ configuration) dehydrogenates C_2H_6 and larger alkanes [42]. It is evident that the 484 kJ mol^{-1} promotion energy for Ce^{2+} is prohibitively large for alkane activation by insertion whereas the 232 kJ mol^{-1} promotion energy for U^{2+} is adequately low that activation by insertion proceeds for alkanes larger than CH_4. A promotion energy of 232 kJ mol^{-1} would render a monopositive f-block ion inert towards activation of small alkanes—the deeper energy well introduced by the interaction of the dipositive uranium ion with C_2H_6 and C_3H_8 surmounts the barrier to insertion. As the promotion energies to $6d^2$ for the dipositive transuranium actinide ions increase rapidly beyond U^{2+} [76], it is anticipated that activation by insertion will not proceed and that d^1 radical-type reactivity reminiscent of the Ln^{2+} ions will be observed.

Conclusions

A primary focus of this work was evaluating the ability of DFT to reliably model very elementary gas-phase organometallic reaction mechanisms. The dipositive actinide ions, Th^{2+} and U^{2+}, were of particular interest to test the efficacy of DFT for many-electron actinides, as well as for dipositive ions. The PEPs computed by DFT for the smallest alkanes were entirely consistent with the observations. The DFT results predict that Th^{2+} should active CH_4 whereas U^{2+} should not, just as observed. For C_2H_4, DFT predicts that Th^{2+} should induce double-dehydrogenation whereas U^{2+} should induce only single-dehydrogenation, again as observed. The complexity increases drastically for the reactions with even the rather small alkane, C_3H_8. The DFT results accurately predict several key aspects of the observed reaction pathways with C_3H_8: 1) double-dehydrogenation for Th^{2+} and single-dehydrogenation for U^{2+}; 2) $\{CH_4 + H_2\}$-elimination for Th^{2+} but only CH_4-elimination for U^{2+}; 3) $\{AnCH_3^+ + C_2H_5^+\}$ for both An = Th and U; and 4) the favorable $\{UH^+ + C_3H_7^+\}$ reaction channel. However, the computed PEPs do not obviously predict certain features of the observed reaction pathways, such as why the favorable $\{ThH^+ + C_3H_7^+\}$ reaction channel is not observed. The ability of DFT to effectively model these reaction mechanisms has been clearly demonstrated—the non-observation of pathways which are computed to be allowable is not whatsoever unexpected as these are not dynamic computations. The key result is that DFT effectively predicts allowable reaction pathways and that the experimental results—notably the significant differences between the products seen for Th^{2+} and U^{2+}—are entirely consistent with the computed PEPs.

All of the studied reactions were computed to proceed by initial insertion of the dipositive metal ion into either a C-H or a C-C bond. Evaluation of the DFT results in the context of elementary models used to understand such activation by f-element ions revealed a close correspondence. Specifically, the energy required for the insertion of U^{2+} was consistently found to be greater than that for insertion of Th^{2+}, with insertion energy differences in the range of 185 - 261 kJ mol^{-1}. According to a hypothesis widely applied to reactions of monopositive lanthanide and actinide ions, if the quasi-valence f-electrons are ineffective at covalent bond formation, and thus C-H or C-C bond activation, then promotion of the ion to a prepared divalent state with two non-f electrons is required for insertion. The non-5f divalent $6d^2$ configuration of Th^{2+} is nearly degenerate with the ground state, whereas the $6d^2$ configuration of U^{2+} lies 232 kJ mol^{-1} above its $5f^4$ ground state configuration. The energy analysis of the computed PEPs thus indicates that the promotion model is valid, and that promotion of U^{2+} is required for insertion. This latter conclusion implies that the 5f electrons of U^{2+} are ineffective at bond formation during activation of small alkanes. Finally, it is evident that the observed reactivity of U^{2+} would not be observed for a monopositive ion with a comparable electronic configuration and promotion energy: the enhanced reactivity for the dipositive U^{2+} ion is attributed primarily to the greater energy of association of a dipositive ion with an alkane, as compared with the association energy for a monopositive ion.

Acknowledgements

This work was supported by the Università degli Studi della Calabria and by FP7 project HYPOMAP (project n. 233482); by Fundação para a Ciência e a Tecnologia (FCT) under Contract No. PPCDT/QUI/58222/2004; and by the Director, Office of Science, Office of Basic Energy Sciences, Division of Chemical Sciences, Geosciences and Biosciences of the U.S. Department of Energy at LBNL, under Contract No. DE-AC02-05CH11231. The CINECA supercomputing centre (Casalecchio di Reno, Italy) is gratefully acknowledged for providing computational resources. M.C.M. is grateful for the opportunity to be a Guest Scientist in the Chemical Sciences Division at LBNL. M.S. is grateful to FCT for a Ph.D. grant. The authors are grateful to Drs. António Pires de Matos and Richard G. Haire for their invaluable support in this project.

Supporting Information

Full citation for reference 67. Geometrical parameters for all of the minima and transition states in the reaction paths presented in Figures 1 -12. Alternative PEPs and associated geometrical parameters for observed reactions, and PEPs and associated geometrical parameters for non-observed reactions.

References

1. Santos, M.; Marçalo, J.; Pires de Matos, A.; Gibson, J. K.; Haire, R. G. *J. Phys. Chem. A* **2002**, *106*, 7190-7194.

2. Santos, M.; Marçalo, J.; Leal, J. P.; Pires de Matos, A.; Gibson, J. K.; Haire, R. G. *Int. J. Mass Spectrom.* **2003**, *228*, 457-465.

3. Gibson, J. K.; Haire, R. G.; Santos, M.; Marçalo, J.; Pires de Matos, A. *J. Phys. Chem. A* **2005**, *109*, 2768-2781.

4. Gibson, J. K.; Haire, R. G.; Marçalo, J.; Santos, M.; Pires de Matos, A.; Leal, J. P. *J. Nucl. Mater.* **2005**, *344*, 24-29.

5. Santos, M.; Pires de Matos, A.; Marçalo, J.; Gibson, J. K.; Haire, R. G.; Tyagi, R.;

Pitzer, R. M. *J. Phys. Chem. A* **2006**, *110*, 5751-5759.

6. Gibson, J. K.; Haire, R. G.; Santos, M.; Pires de Matos, A.; Marçalo, J. *J. Phys. Chem. A* **2008**, *112,* 11373–11381.

7. Marshall, A. G.; Hendrickson, C. L.; Jackson, G. S. *Mass Spectrom. Rev.* **1998**, *17*, 1-35.

8. Gibson, J. K. *Int. J. Mass Spectrom.* **2002**, *214*, 1-21.

9. Gibson, J. K.; Marçalo, J. *Coord. Chem. Rev.* **2006**, *250*, 776-783.

10. Heaven, M. C.; Gibson, J. K.; Marçalo, J. In *The Chemistry of the Actinide and Transactinide Elements,* 3rd Edition; Morss, L. R.; Edelstein N. M.; Fuger, J., Eds.; Springer: Dordrecht, 2010; Vol. 6, Ch. 38, in press.

11. Cornehl, H. H.; Heinemann, C.; Marçalo, J.; Pires de Matos, A.; Schwarz, H. *Angew. Chem. Int. Ed. Engl.* **1996**, *35*, 891-894.

12. Jackson, G. P.; King, F. L.; Goeringer, D. E.; Duckworth, D. C. *J. Phys. Chem. A* **2002**, *106*, 7788-7794.

13. Marçalo, J.; Leal, J. P.; Pires de Matos, A.; Marshall, A. G. *Organometallics* **1997**, *16*, 4581-4588.

14. Blaise, J.; Wyart, J.-F. *Energy Levels and Atomic Spectra of Actinides*, Tables Internationales de Constantes: Paris, 1992.

15. Eller, K.; Schwarz, H. *Chem. Rev.* **1991**, *91*, 1121-1177.

16. Armentrout, P. B. *Int. J. Mass Spectrom.* **2003**, *227*, 289-302.

17. Operti, L.; Rabezzana, R. *Mass Spectrom. Rev.* **2006**, *25*, 483-513.

18. Bohme, D. K. In *The Encyclopedia of Mass Spectrometry, Vol. 4*; Gross, M. L., Caprioli, R., Eds.; Elsevier: New York, 2004, pp. 638-648.

19. Roithová, J.; Schröder, D. *Chem. Rev.* **2010**, *110*, 1170-1211.

20. Gibson, J. K.; Haire, R. G.; Marçalo, J.; Santos, M.; Pires de Matos, A.; Mrozik, M.

K.; Pitzer, R. M.; Bursten, B. E. *Organometallics*, **2007**, *26*, 3947-3956.

21. Buckner, S. W.; Freiser, B. S. *J. Am. Chem. Soc.* **1987**, *109*, 1247-1248.

22. Huang, Y.; Freiser, B. S. *J. Am. Chem. Soc.* **1988**, *110*, 4434-4435.

23. Gord, J. R.; Freiser, B. S.; Buckner, S. W. *J. Chem. Phys.* **1989**, *91*, 7530-7536.

24. Gord, J. R.; Freiser, B. S.; Buckner, S. W. *J. Chem. Phys.* **1991**, *94*, 4282-4290.

25. Gord, J. R.; Freiser, B. S.; Buckner, S. W. *J. Phys. Chem.* **1991**, *95*, 8274-8279.

26. Hill, Y. D.; Freiser, B. S.; Bauschlicher, C. W., Jr. *J. Am. Chem. Soc.* **1991**, *113*, 1507-1510.

27. Ranasinghe, Y. A.; MacMahon, T.J.; Freiser, B. S. *J. Phys. Chem.* **1991**, *95*, 7721-7726.

28. Ranasinghe, Y. A.; MacMahon, T.J.; Freiser, B. S. *J. Am. Chem. Soc.* **1992**, *114*, 9112-9118.

29. Roth, L. M.; Freiser, B. S. *Mass Spectrom. Rev.* **1991**, *10*, 303-328.

30. Freiser, B. S. *Acc. Chem. Res.* **1994**, *27*, 353-360.

31. Hill, Y. D.; Huang, Y.; Ast, T.; Freiser, B. S. *Rapid Commun. Mass Spectrom.* **1997**, *11*, 149-154.

32. Tonkyn, R.; Weisshaar, J. C. *J. Am. Chem. Soc.* **1986**, *108*, 7128-7130.

33. Weisshaar, J. C. *Acc. Chem. Res.* **1993**, *26*, 213-219.

34. Spears, K. G.; Fehsenfeld, G. C.; McFarland, M.; Ferguson, E. E. *J. Chem. Phys.* **1972**, *56*, 2562-2566.

35. Bohme, D. K. *Int. Rev. Phys. Chem.* **1994**, *13*, 163-185.

36. Herman, Z. *Int. Rev. Phys. Chem.* **1996**, *15*, 299-324.

37. Schröder, D.; Schwarz, H. *J. Phys. Chem. A* **1999**, *103*, 7385-7394.

38. Stace, A. J. *J. Phys. Chem. A* **2002**, *106*, 7993-8005.

39. Price, S. D. *Phys. Chem. Chem. Phys.* **2003**, *5*, 1717-1729.

40. Price, S. D. *Int. J. Mass Spectrom.* **2007**, *260*, 1-19.

41. Roithová, J.; Schröder, D. *Phys. Chem. Chem. Phys.* **2007**, *9*, 2341-2349.

42. Marçalo, J.; Santos, M.; Pires de Matos, A.; Gibson, J.K.; Haire, R.G. *J. Phys. Chem. A* **2008**, *112*, 12647-12656.

43. Martin, W. C.; Zalubas, R.; Hagan, L. *Atomic Energy Levels - The Rare-Earth Elements*; U.S. National Bureau of Standards (NIST): Washington, DC, 1978.

44. Michelini, M. C.; Russo, N.; Sicilia, E. *Angew. Chem., Int. Ed.* **2006**, *45*, 1095-1099.

45. Michelini, M. C.; Russo, N.; Sicilia, E. *J. Am. Chem. Soc.* **2007**, *129*, 4229-4239.

46. Mazzone, G.; Michelini, M. C.; Russo, N.; Sicilia, E. *Inorg. Chem.* **2008**, *47*, 2083-2088.

47. Alikhani, M. E.; Michelini, M. C.; Russo, N.; Silvi, B. *J. Phys. Chem. A* **2008**, *112*, 12966-12974.

48. Di Santo, E.; Michelini, M. C.; Russo, N. *Organometallics* **2009**, *28*, 3716-3726.

49. Di Santo, E.; Michelini, M. C.; Russo, N. *J. Phys. Chem. A* **2009**, *113*, 14699-14705.

50. de Almeida, K. J.; Duarte, H. A. *Organometallics* **2009**, *28*, 3203-3211.

51. de Almeida, K. J.; Duarte, H. A. *Organometallics* **2010**, *29*, 3735–3745.

52. Pepper, M.; Bursten, B.E. *Chem. Rev* **1991**, *91*, 719-741.

53. Bruce, J. E.; Eyler, J. R. *J. Am. Soc. Mass Spectrom.* **1992**, *3*, 727-733.

54. Lin, Y.; Ridge, D. P.; Munson, B. *Org. Mass Spectrom.* **1991**, *26*, 550-558.

55. Bartmess, J. E.; Georgiadis, R. M. *Vacuum* **1983**, *33*, 149-153.

56. Guan, S.; Marshall, A. G. *Int. J. Mass Spectrom. Ion Proc.* **1996**, *157/158*, 5-37.

57. Kang, H.; Beauchamp, J. L. *J. Phys. Chem.* **1985**, *89*, 3364-3367.

58. Ibrahim, Y.; Alsharaeh, E.; Mabrouki, R.; Momoh, P.; Xie, E.; El-Shall, M. S. *J. Phys. Chem. A* **2008**, *112*, 1112–1124.

59. Su, T.; Chesnavich, W. J. *J. Chem. Phys.* **1982**, *76*, 5183-5185.

60. Lide, D. R., Ed.; *CRC Handbook of Chemistry and Physics, 88th ed.*; CRC Press: Boca Raton, FL, 2007.

61. Becke, A. D. *J. Chem. Phys.* **1993**, *98*, 5648-5652.

62. Lee, C.; Yang, W.; Parr, R. G. *Phys. Rev. B* **1988**, *37*, 785-789.

63. (a) http://www.theochem.unistuttgart.de/pseudopotentiale/. (b) Küchle, W.; Dolg, M.; Stoll, H.; Preuss, H. *J. Chem. Phys.* **1994**, *100*, 7535-7542.

64. Krishnan, R.; Binkley, J. S.; Seeger, R.; Pople, J. A. *J. Chem. Phys.* **1980**, *72*, 650-654.

65. Blaudeau, J. -P. ; McGrath, M. P.; Curtiss, L. A.; Radom L. *J. Chem. Phys.* **1997**, *107*, 5016-5021.

66. Clark, T.; Chandrasekhar, J.; Schleyer, P. v. R. *J. Comp. Chem.* **1983**, *4*, 294-301.

67. Frisch, M. J.; et. al. *Gaussian 03*. See Supporting Information for full citation.

68. Gonzales, C.; Shlegel, H. B. *J. Chem. Phys.* **1989**, *90*, 2154-2161.

69. Gonzales, C.; Shlegel, H. B. *J. Phys. Chem A.*, **1990**, *94*, 5523-5527.

70. Reed, A. E.; Weinhold, F. *J. Chem. Phys,* **1985**, *83*, 1736-1740.

71. Reed, A. E.; Curtiss, L. A.; Weinhold, F. *Chem. Rev.* **1988**, *88*, 899-926.

72. Lias, S. G.; Bartmess, J. E.; Liebman, J. F.; Holmes, J. L.; Levin, R. D.; Mallard, W. G. *Gas-Phase Ion and Neutral Thermochemistry*; American Chemical

Society: Washington, DC, 1988.

73. Marçalo, J.; Gibson, J. K. *J. Phys. Chem. A* **2009**, *113*, 12599-12606.

74. Cornehl, H. H.; Heinemann, C.; Schröder, D.; Schwarz, H. *Organometallics* **1995**, *14*, 992-999.

75. Zhou, J.; Schlegel, H. B. *J. Phys. Chem. A* **2010**, *114*, 8613-8617.

76. L. Brewer *J. Opt. Soc. Am.* **1971**, *61*, 1666-1682.

Table 1. Product distributions, rate constants (*k*), and reaction efficiencies (k/k_{COL}) for the reactions of Th^{2+} and U^{2+} with CH_4, C_2H_6, and C_3H_8. [a]

An^{2+}	**CH_4**			**C_2H_6**			**C_3H_8**		
	Products	***k***	**k/k_{COL}**	**Products**	***k***	**k/k_{COL}**	**Products**	***k***	**k/k_{COL}**
Th^{2+}	$ThCH_2^{2+}$ (100)	0.22	0.11	$ThC_2H_2^{2+}$ (100)	0.28	0.15	$ThC_3H_4^{2+}$ (55) $ThC_2H_2^{2+}$ (35) $ThCH_3^{+}$ (10)	0.26	0.13
U^{2+}	No Reaction	<0.001	<0.001	$UC_2H_4^{2+}$ (100)	0.34	0.18	$UC_3H_6^{2+}$ (40) $UC_2H_4^{2+}$ (15) UH^{+} (10) UCH_3^{+} (35)	0.42	0.22

[a] Product distributions in parentheses as %; *k* in units of 10^{-9} cm^3 $molecule^{-1}$ s^{-1}.

Table 2. Computed An^{2+} insertion energies for C-H and C-C bond activation.[a]

C_mH_n	**$\Delta E_i[Th^{2+}]$**	**$\Delta E_i[U^{2+}]$**	**$\Delta E_i[U^{2+}] - \Delta E_i[Th^{2+}]$**
CH_4			
C-H[b]	-75	150	225
C_2H_6			
C-H[c]	-92	110	202
C-C[d]	-156	50	206
C_3H_8			
C-H[e]	-100	94	194
C-C[f]	-145	39	184
C-C[g]	-167	94	261

[a] $\Delta E_i[An^{2+}]$ is the energy difference, in kJ mol^{-1}, between the first association complex, **FC**, and the insertion intermediate, **I**.

[b] From Figs. 1 and 2.

[c] From Figs. 3 and 5.

[d] From Figs. 4 and S8.

[e] From Figs. 6 and 9.

[f] From Figs. 8 and 10.

[g] From Figs. S17 and S31.

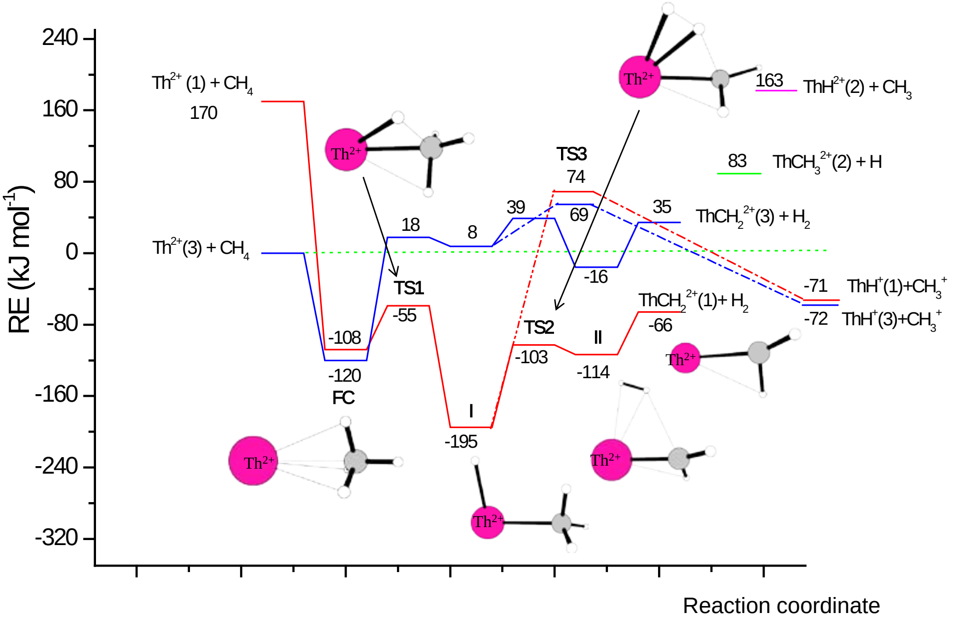

Figure 1 : PEP for the reaction of Th^{2+} + CH_4 (triplet and singlet spin states) at B3LYP/SDD level of theory. The labelling between the reactants and products identifies the first association complex (**FC**), the transition states (**TS1**, **TS2** and **TS3**), and the intermediates (**I** and **II**). Spin states are given between parentheses. The geometrical parameters are in Fig. S1.

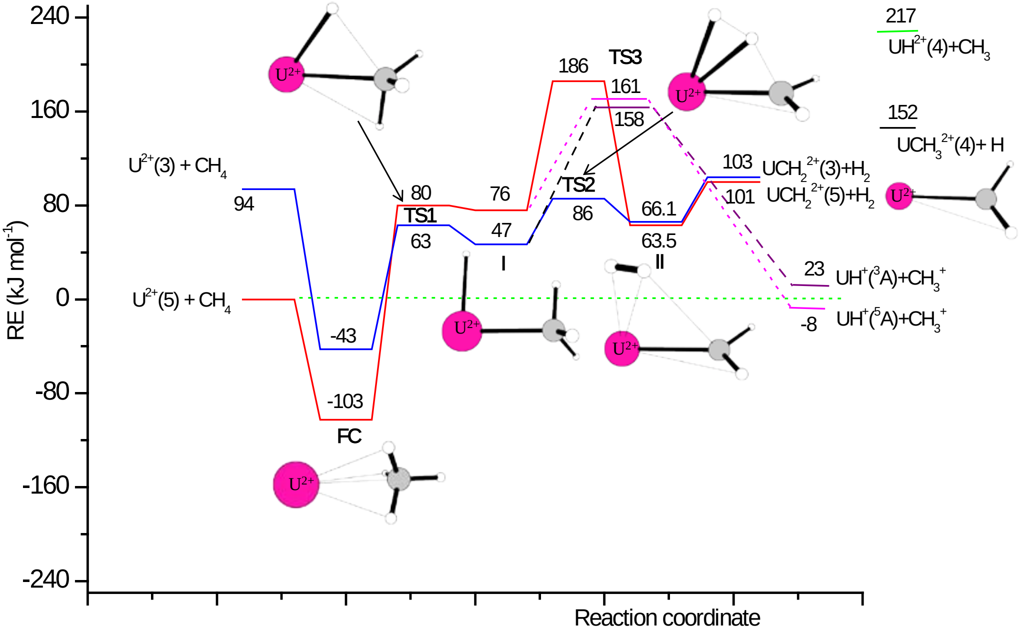

Figure 2 : PEP for the reaction of U^{2+} + CH_4 (quintet and triplet spin states) at B3LYP/SDD level of theory. The labelling between the reactants and products identifies the first association complex (**FC**), the transition states (**TS1**, **TS2** and **TS3**), and the intermediates (**I** and **II**). Spin states are given between parentheses. The geometrical parameters are in Fig. S2.

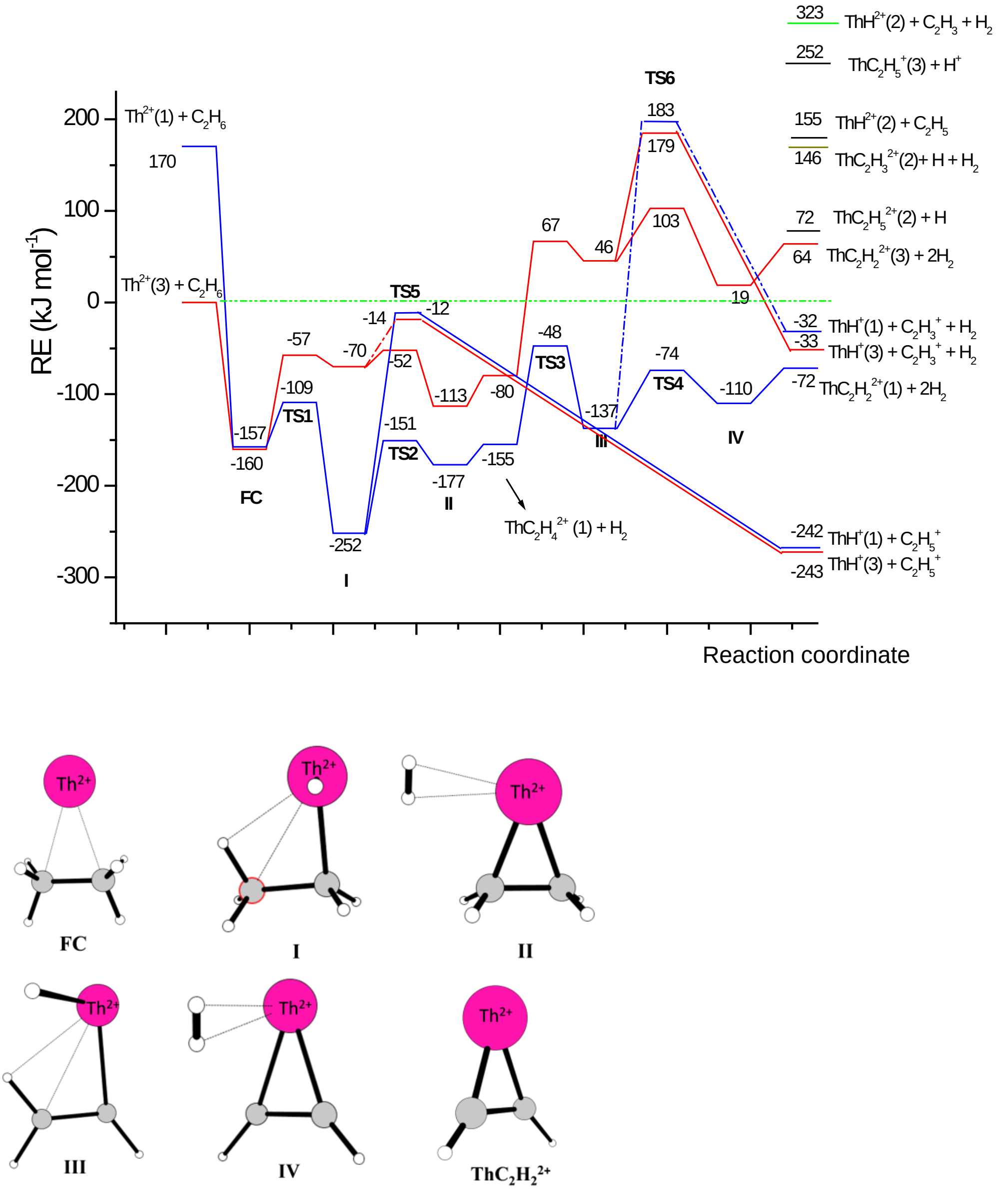

Figure 3 : PEP for the first and second dehydrogenation of C_2H_6 by Th^{2+} (triplet and singlet spin states) at B3LYP/SDD level of theory. The labelling between the reactants and products identifies the first association complex (**FC**), the transition states (**TS1-TS6**), and the intermediates (**I** to **IV**). Spin states are given between parentheses. The geometrical parameters for dehydrogenation are in Figs. S3 and S4.

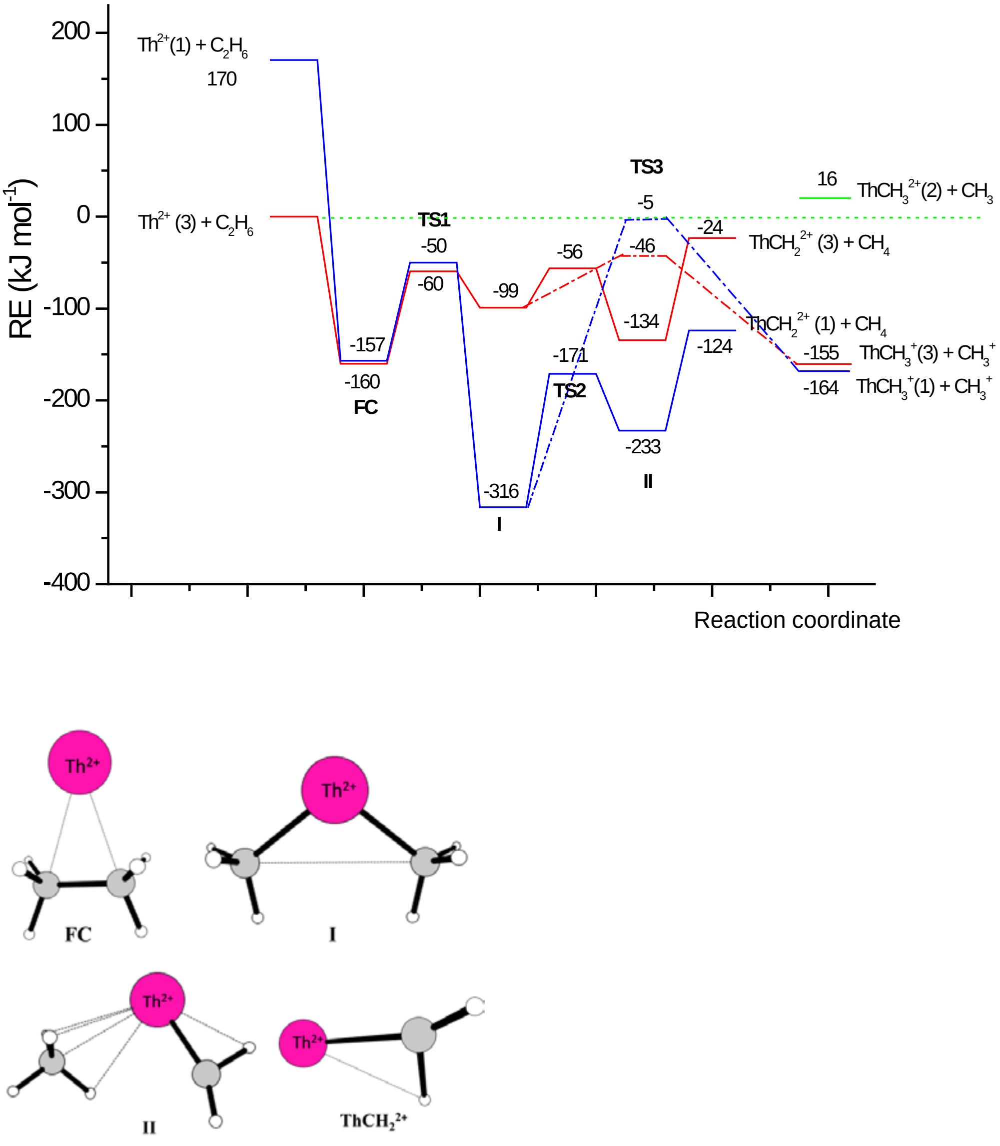

Figure 4 : PEP for the C-C bond activation of C_2H_6 by Th^{2+} (triplet and singlet spin states) at B3LYP/SDD level of theory. The labelling between the reactants and products identifies the first association complex (**FC**), the transition states (**TS1**, **TS2** and **TS3**), and the intermediates (**I** and **II**). Spin states are given between parentheses. The geometrical parameters are in Fig. S5.

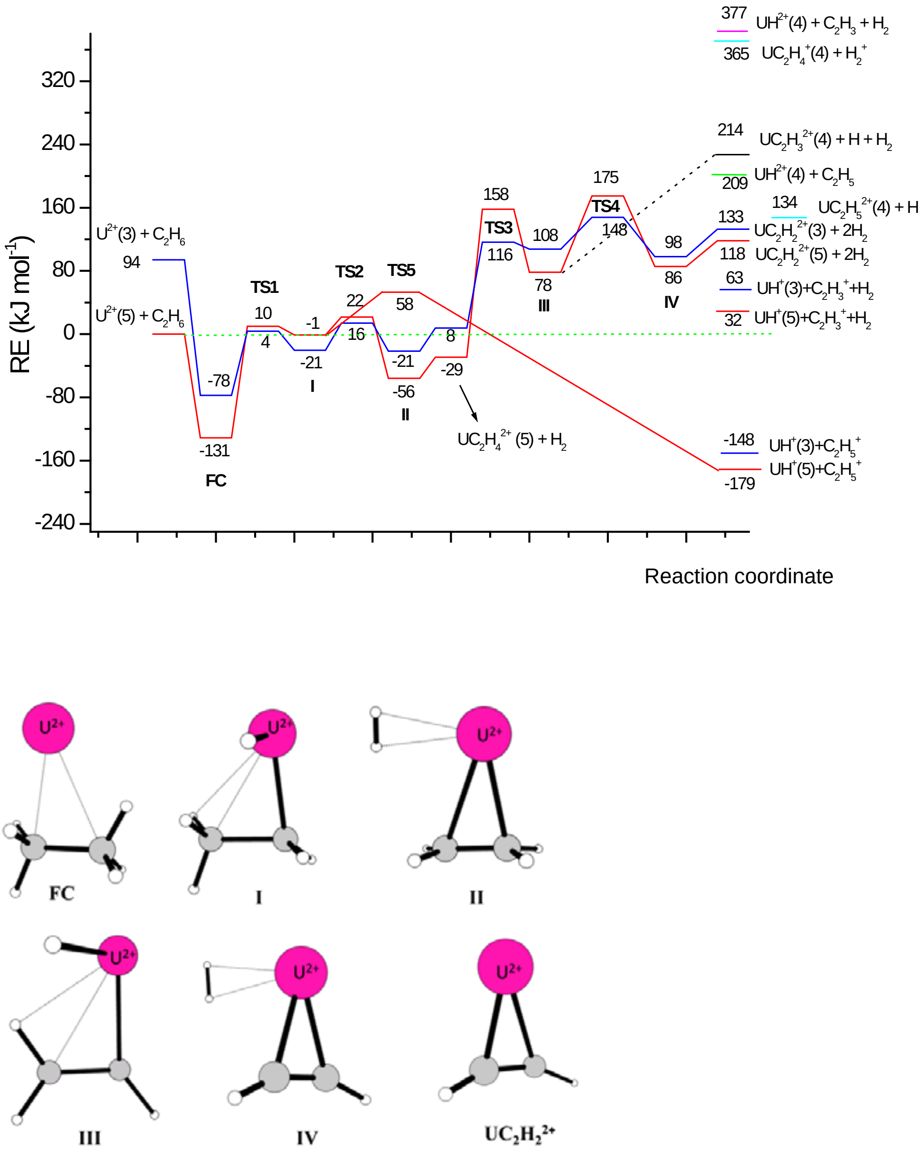

Figure 5 : PEP for the first and second dehydrogenation of C_2H_6 by U^{2+} (quintet and triplet spin states) at B3LYP/SDD level of theory. The labelling between the reactants and products identifies the first association complex (**FC**), the transition states (**TS1-TS5**), and the intermediates (**I** to **IV**). Spin states are given between parentheses. The geometrical parameters for dehydrogenation are in Figs. S6 and S7.

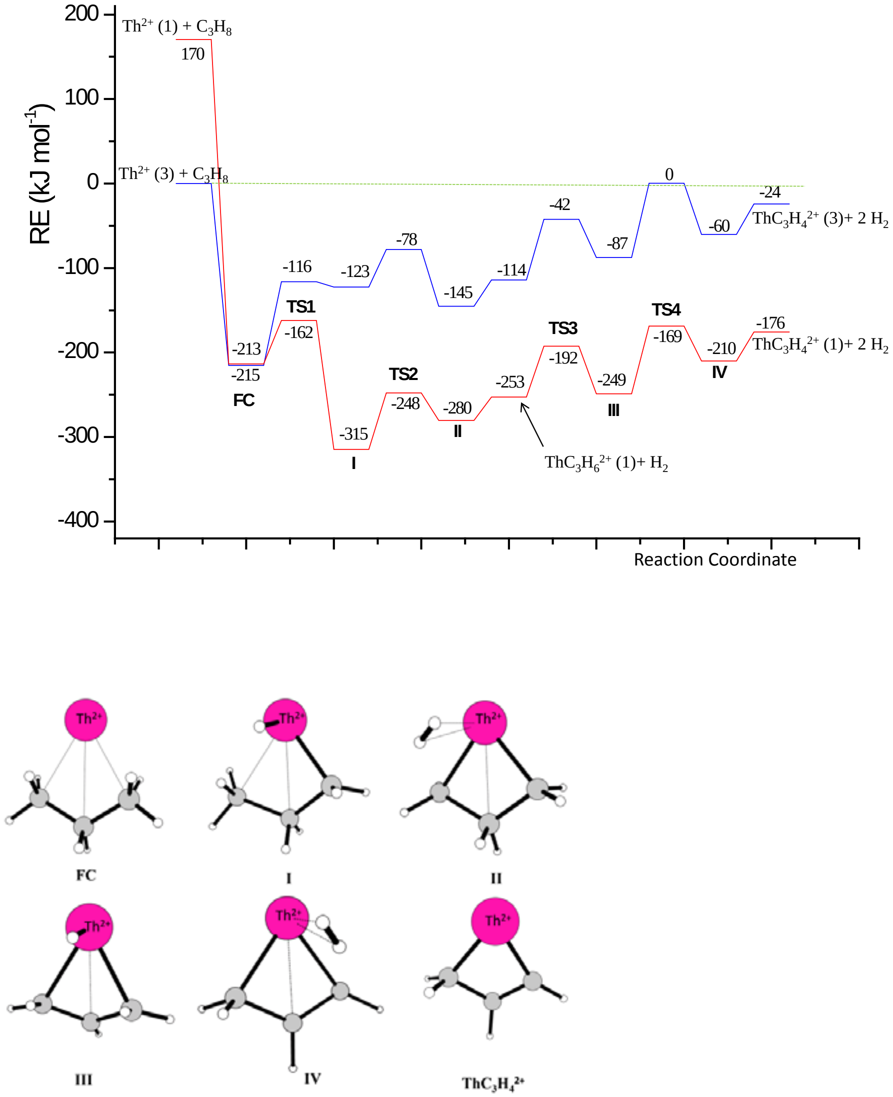

Figure 6 : PEP for the first and second dehydrogenation of C_3H_8 by Th^{2+} (triplet and singlet spin states) at B3LYP/SDD level of theory. The labelling between the reactants and products identifies the first association complex (**FC**), the transition states (**TS1-TS4**), and the intermediates (**I** to **IV**). Spin states are given between parentheses. The geometrical parameters are in Fig. S10.

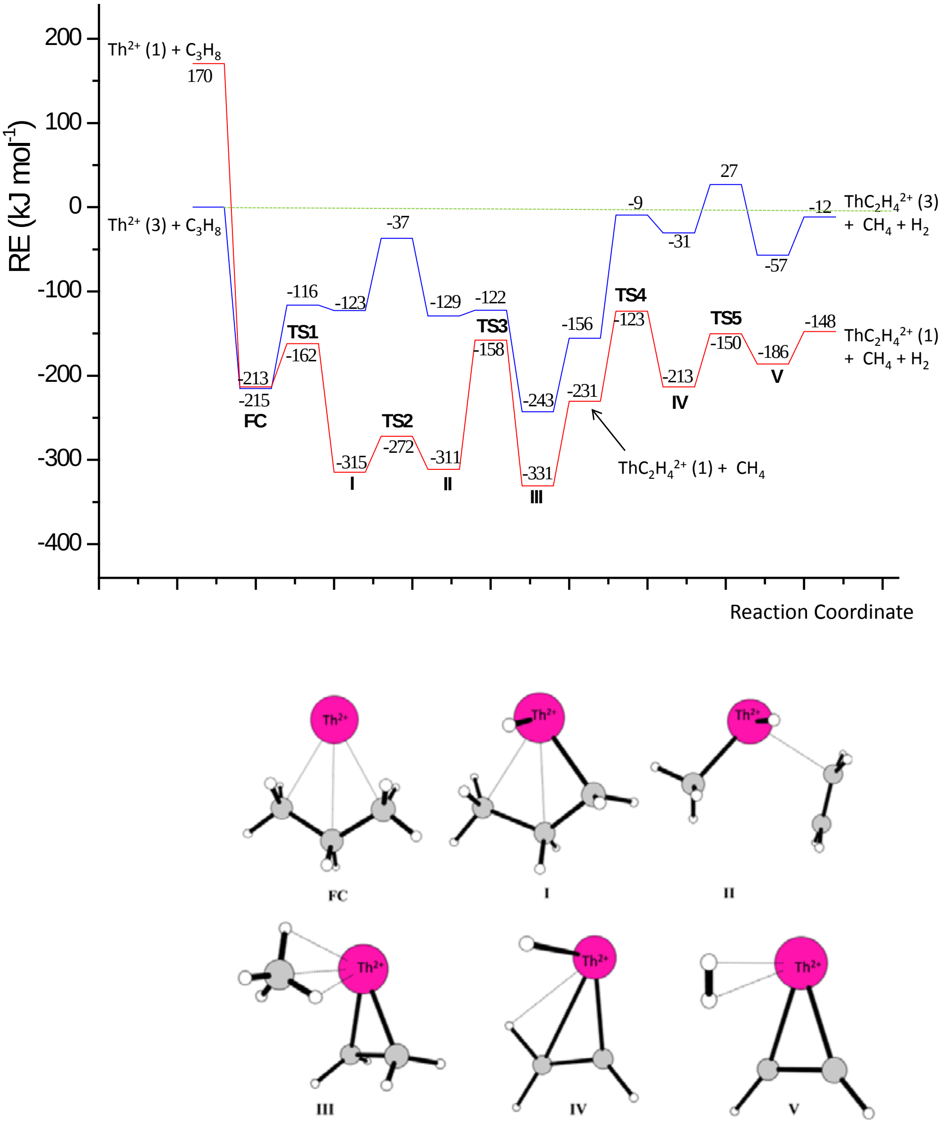

Figure 7: PEP for the elimination of CH_4 and H_2 from C_3H_8 by Th^{2+} (triplet and singlet spin states) at B3LYP/SDD level of theory. The labelling between the reactants and products identifies the first association complex (**FC**), the transition states (**TS1-TS5**), and the intermediates (**I** to **V**). Spin states are given between parentheses. The geometrical parameters are in Fig. S11.

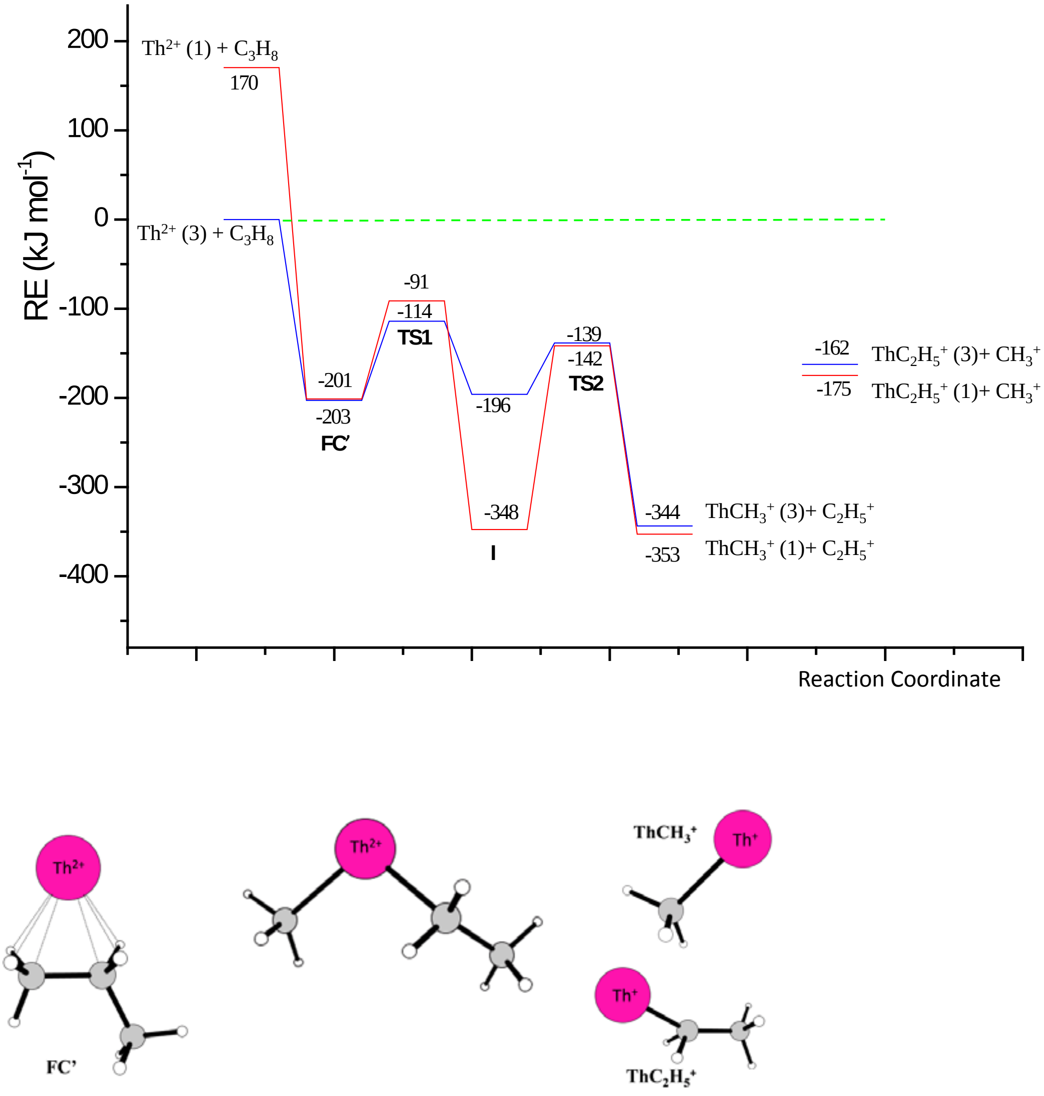

Figure 8 : PEP for the elimination of $C_2H_5^+$ from C_3H_8 by Th^{2+} (triplet and singlet spin states) at B3LYP/SDD level of theory. The labelling between the reactants and products identifies the first association complex (**FC'**), the transition states (**TS1-TS2**), and the intermediate (**I**). Spin states are given between parentheses. The geometrical parameters are Fig. S12.

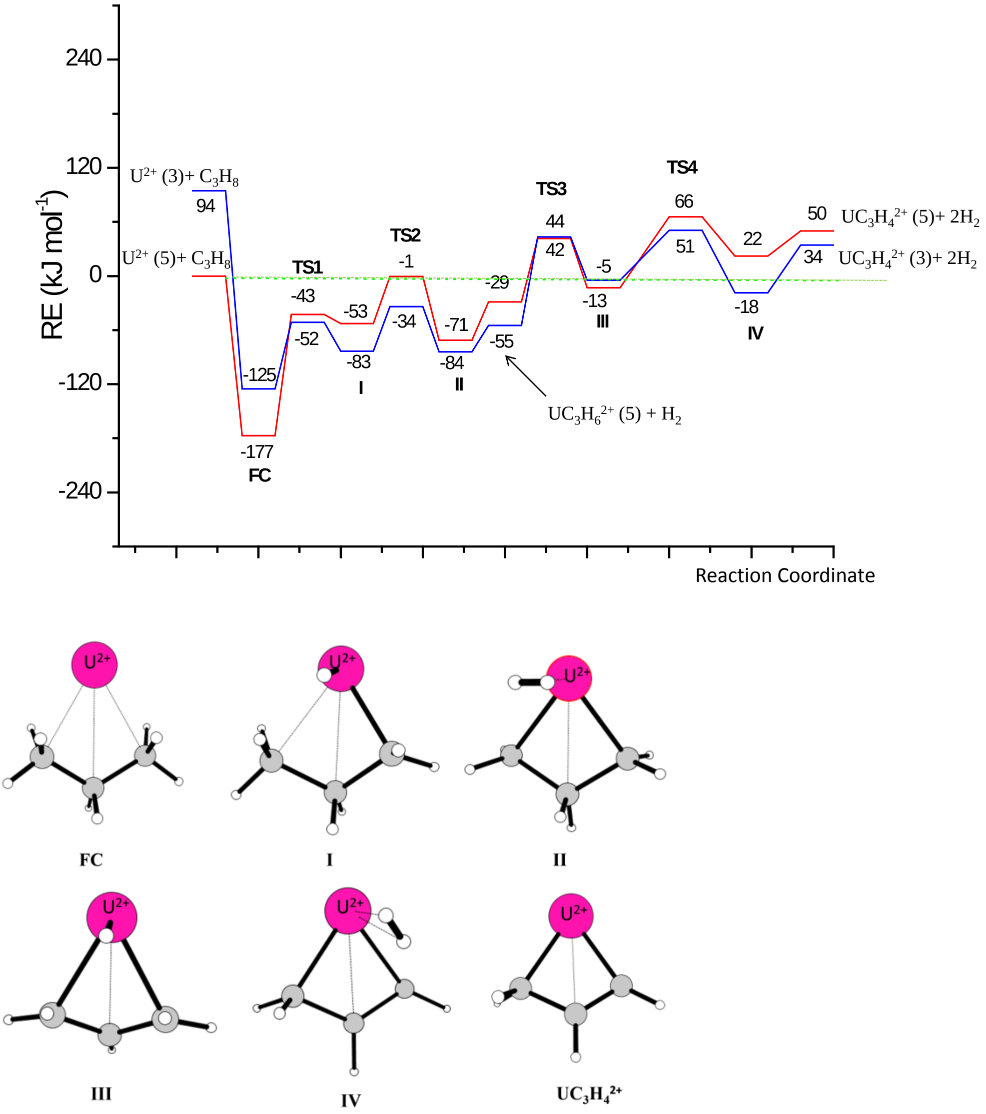

Figure 9 : PEP for the first and second dehydrogenation of C_3H_8 by U^{2+} (quintet and triplet spin states) at B3LYP/SDD level of theory. The labelling between the reactants and products identifies the first association complex (**FC**), the transition states (**TS1-TS4**), and the intermediates (**I** to **IV**). Spin states are given between parentheses. The geometrical parameters are in Fig. S23.

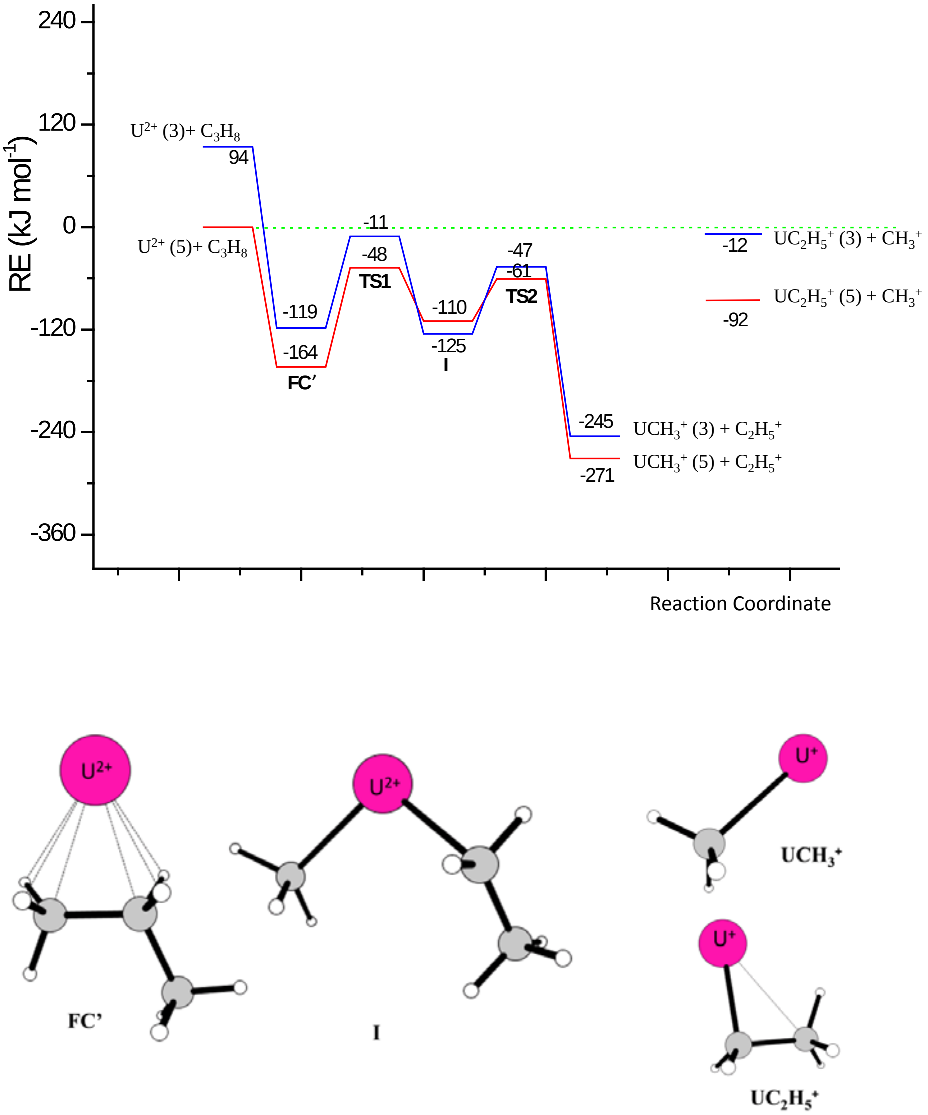

Figure 10 : PEP for the elimination of $C_2H_5^+$ from C_3H_8 by U^{2+} (quintet and triplet spin states) at B3LYP/SDD level of theory. The labelling between the reactants and products identifies the first association complex (**FC'**), the transition states (**TS1-TS2**), and the intermediate (**I**). Spin states are given between parentheses. The geometrical parameters are in Fig. S24.

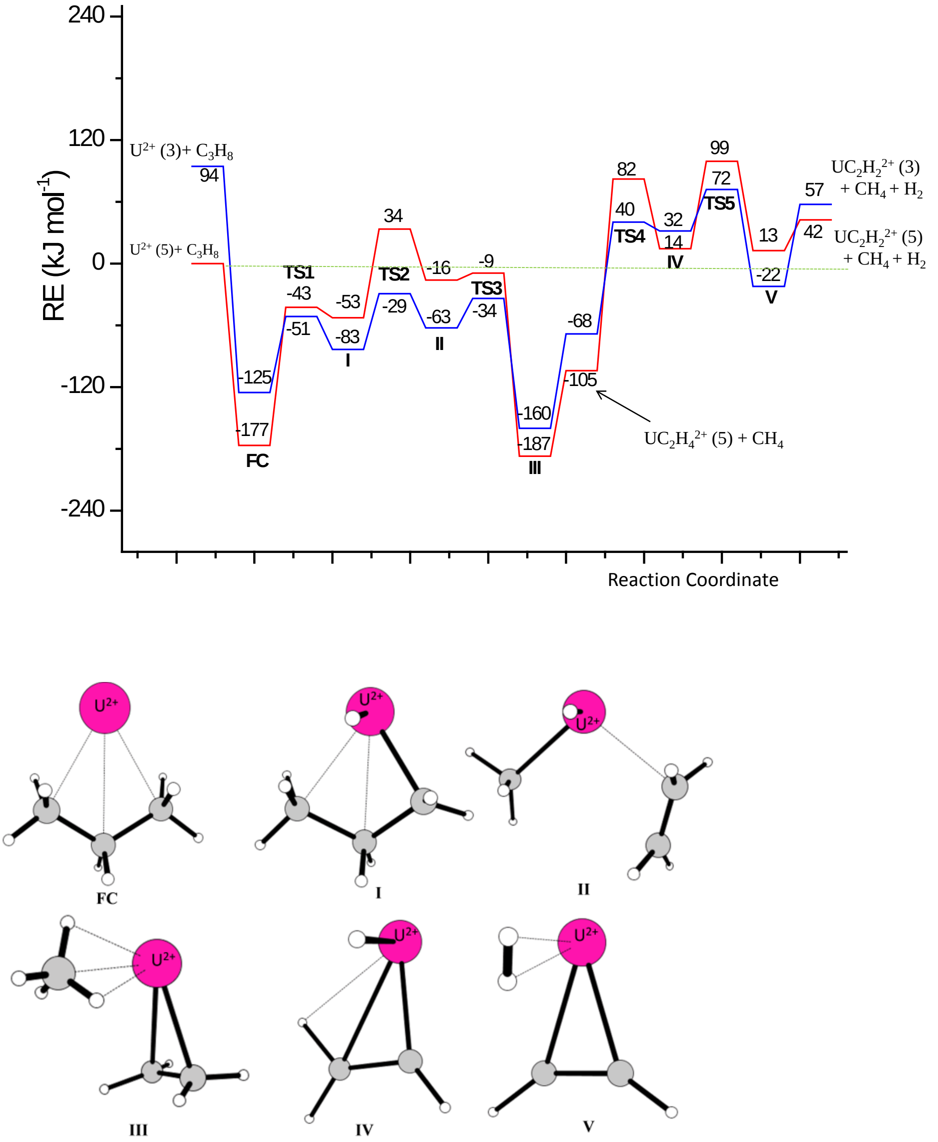

Figure 11 : PEP for the elimination of CH_4 from C_3H_8 by U^{2+} (quintet and triplet spin states) at B3LYP/SDD level of theory. The labelling between the reactants and products identifies the first association complex (**FC**), the transition states (**TS1-TS5**), and the intermediates (**I** to **V**). Spin states are given between parentheses. The geometrical parameters are in Fig. S25.

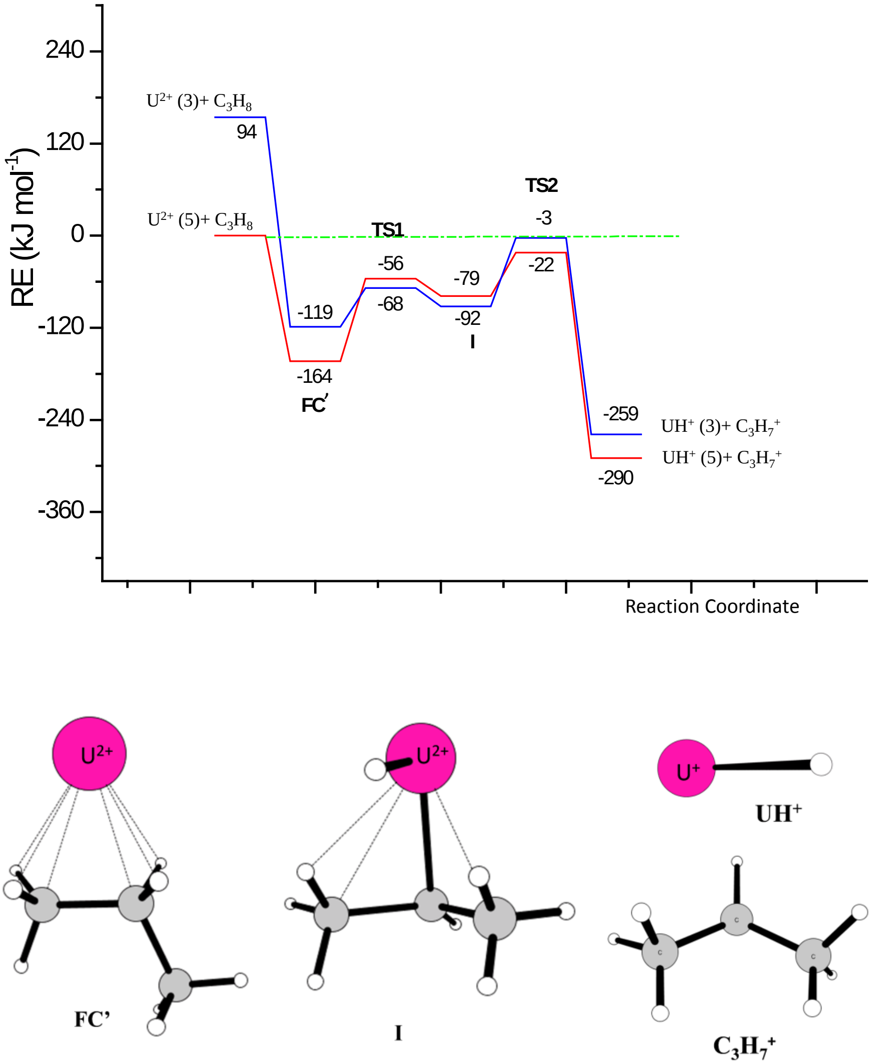

Figure 12 : PEP for the elimination of $C_3H_7^+$ from C_3H_8 by U^{2+} (quintet and triplet spin states) at B3LYP/SDD level of theory. The labelling between the reactants and products identifies the first association complex (**FC'**), the transition states (**TS1-TS2**), and the intermediates (**I**). Spin states are given between parentheses. The geometrical parameters are in Fig. S26.

Supporting Information

Gas-phase reactions of the bare Th^{2+} and U^{2+} ions with small alkanes, CH_4, C_2H_6 and C_3H_8: An experimental and theoretical study of elementary organoactinide chemistry.

Emanuela Di Santo[a], Marta Santos[b], Maria C. Michelini[a,]*,
Joaquim Marçalo[b], Nino Russo[a], John K. Gibson[c,]*

[a]Dipartimento di Chimica, Università della Calabria, Via P. Bucci, Cubo 14 C, 87030
Arcavacata di Rende, Italy

[b] Unidade de Ciências Químicas e Radiofarmacêuticas, Instituto Tecnológico e
Nuclear, 2686-953 Sacavém, Portugal

[c] Chemical Sciences Division, Lawrence Berkeley National Laboratory, Berkeley, CA
94720, USA

*Corresponding authors: mc.michelini@unical.it (M.C.M.); jkgibson@lbl.gov (J.K.G.)

Table of Contents

Complete citation for reference 67.

Figure S1: Geometrical parameters of all of the minima and transition states involved in the reaction of Th^{2+} + CH_4 (ground spin state structures). Bond lengths are in angstrom and angles are in degrees.

Figure S2: Geometrical parameters of all of the minima and transition states involved in the reaction of U^{2+} + CH_4 (ground spin state structures). Bond lengths are in angstrom and angles are in degrees.

Figure S3: Geometrical parameters of all of the minima and transition states involved in the first dehydrogenation reaction of Th^{2+} + C_2H_6 (ground spin state structures). Bond lengths are in angstrom and angles are in degrees.

Figure S4: Geometrical parameters of all of the minima and transition states involved in the second dehydrogenation reaction of Th^{2+} + C_2H_6 (ground spin state structures). Bond lengths are in angstrom and angles are in degrees.

Figure S5 : Geometrical parameters of all of the minima and transition states involved in the C-C bond activation reaction of Th^{2+} + C_2H_6 (ground spin state structures). Bond lengths are in angstrom and angles are in degrees

Figure S6: Geometrical parameters of all of the minima and transition states involved in the first dehydrogenation reaction of U^{2+} + C_2H_6 (ground spin state structures). Bond lengths are in angstrom and angles are in degrees.

Figure S7: Geometrical parameters of all of the minima and transition states involved in the second dehydrogenation reaction of U^{2+} + C_2H_6 (ground spin state structures). Bond lengths are in angstrom and angles are in degrees.

Figure S8 : PEP for the C-C bond activation of C_2H_6 by U^{2+} (quintet and triplet spin states).

Figure S9 : Geometrical parameters of all of the minima and transition states involved in the C-C bond activation reaction of U^{2+} + C_2H_6 (ground spin state structures). Bond lengths are in angstrom and angles are in degrees.

Figure S10 (a and b) : Geometrical parameters of all of the minima and transition states involved in the reaction path presented in **Figure 6** (double dehydrogenation of C_3H_8 by Th^{2+}). Bond lengths are in angstrom and angles are in degrees.

Figure S11 (a and b) : Geometrical parameters of all of the minima and transition states involved in the reaction path presented in **Figure 7** (elimination of CH_4 and H_2 from C_3H_8 by Th^{2+}). Bond lengths are in angstrom and angles are in degrees.

Figure S12 : Geometrical parameters of all of the minima and transition states involved in the reaction path presented in **Figure 8** (elimination of $C_2H_5^+$ from C_3H_8 by Th^{2+}). Bond lengths are in angstrom and angles are in degrees.

Figure S13 : Alternative PEP for the double dehydrogenation of C_3H_8 by Th^{2+} (triplet and singlet spin states).The labelling between the reactants and products identifies the first association complex (**FC**), the transition states (**TS1-TS4**), and the intermediates (**I** to **IV**). Spin states are given between parentheses.

Figure S14 (a and b) : Geometrical parameters of all of the minima and transition states involved in the first and second dehydrogenation of C_3H_8 by Th^{2+} presented in **Figure S13**. (ground spin state structures). Bond lengths are in angstrom and angles are in degrees.

Figure S15 : Alternative PEP for the elimination of H_2 and CH_4 from C_3H_8 by Th^{2+} (triplet and singlet spin states). The labelling between the reactants and products identifies the first association complex (**FC**), the transition states (**TS1-TS5**), and the intermediates (**I** to **V**). Spin states are given between parentheses.

Figure S16 (a and b) : Geometrical parameters of all of the minima and transition states involved in the elimination of H_2 and CH_4 from C_3H_8 by Th^{2+} presented in **Figure S15**. (ground spin state structures). Bond lengths are in angstrom and angles are in degrees.

Figure S17 : Second alternative PEP for the elimination of CH_4 and H_2 from C_3H_8 by Th^{2+} (triplet and singlet spin states). The labelling between the reactants and products identifies the first association complex (**FC**), the transition states (**TS1-TS4**), and the intermediates (**I** to **IV**). Spin states are given between parentheses.

Figure S18 (a and b) : Geometrical parameters of all of the minima and transition states involved in elimination of CH_4 and H_2 from C_3H_8 by Th^{2+} presented in **Figure S17**. (ground spin state structures). Bond lengths are in angstrom and angles are in degrees.

Figure S19 : PEP for the elimination of C_2H_6 from C_3H_8 by Th^{2+} (triplet and singlet spin states). The labelling between the reactants and products identifies the first association complex (**FC**), the transition state (**TS1**), and the intermediates (**I**). Spin states are given between parentheses.

Figure S20 (a and b) : Geometrical parameters of all of the minima and transition states involved in the elimination of C_2H_6 from C_3H_8 by Th^{2+} presented in **Figure S19** (ground spin state structures). Bond lengths are in angstrom and angles are in degrees.

Figure S21 : PEP for the elimination of $C_3H_7^+$ from C_3H_8 by Th^{2+} (triplet and singlet spin states). The labelling between the reactants and products identifies the first association complex (**FC**), the transition states (**TS1-TS2**), and the intermediates (**I**). Spin states are given between parentheses.

Figure S22 : Geometrical parameters of all of the minima and transition states involved in the elimination of $C_3H_7^+$ from C_3H_8 by Th^{2+} presented in **Figure S21** (ground spin state structures). Bond lengths are in angstrom and angles are in degrees.

Figure S23 (a and b) : Geometrical parameters of all of the minima and transition states involved in the double dehydrogenation of C_3H_8 by U^{2+} presented in **Figure 9** (ground spin state structures). Bond lengths are in angstrom and angles are in degrees.

Figure S24 : Geometrical parameters of all of the minima and transition states involved in the elimination of $C_2H_5^+$ from C_3H_8 by U^{2+} presented in **Figure 10** (ground spin state structures). Bond lengths are in angstrom and angles are in degrees.

Figure S25 (a and b) : Geometrical parameters of all of the minima and transition states involved in the elimination of CH_4 and H_2 from C_3H_8 by U^{2+} presented in **Figure 11** (ground spin state structures). Bond lengths are in angstrom and angles are in degrees.

Figure S26 : Geometrical parameters of all of the minima and transition states involved in the elimination of $C_3H_7^+$ from C_3H_8 by U^{2+} presented in **Figure 12** (ground spin state structures). Bond lengths are in angstrom and angles are in degrees.

Figure S27 : Alternative PEP for the first and second dehydrogenation of C_3H_8 by U^{2+} (quintet and triplet spin states). The labelling between the reactants and products identifies the first association complex (**FC**), the transition states (**TS1-TS4**), and the intermediates (**I** to **IV**). Spin states are given between parentheses.

Figure S28 : Geometrical parameters of all of the minima and transition states involved in the first and second dehydrogenation of C_3H_8 by U^{2+} presented in **Figure S27**. (ground spin state structures). Bond lengths are in angstrom and angles are in degrees.

Figure S29 : Alternative PEP for the elimination of CH_4 and H_2 from C_3H_8 by U^{2+} (quintet and triplet spin states). The labelling between the reactants and products identifies the first association complex (**FC**), the transition states (**TS1-TS3**), and the intermediates (**I** to **III**). Spin states are given between parentheses.

Figure S30 (a and b) : Geometrical parameters of all of the minima and transition states involved in the first and second dehydrogenation of C_3H_8 by U^{2+} presented in **Figure S29**. (ground spin state structures). Bond lengths are in angstrom and angles are in degrees.

Figure S31 : Alternative PEP for the elimination of CH_4 and H_2 from C_3H_8 by U^{2+} (triplet and singlet spin states). The labelling between the reactants and products identifies the first association complex (**FC**), the transition states (**TS1-TS5**), and the intermediates (**I** to **V**). Spin states are given between parentheses.

Figure S32 (a and b) : Geometrical parameters of all of the minima and transition states involved in elimination of CH_4 and H_2 from C_3H_8 by U^{2+} presented in **Figure S31**. (ground spin state structures). Bond lengths are in angstrom and angles are in degrees.

Figure S33 : PEP for the C-C bond activation of C_3H_8 by Th^{2+} (triplet and singlet spin states).

Figure S34 : Geometrical parameters of all of the minima and transition states involved in the C-C bond activation of C_3H_8 by Th^{2+} presented in **Figure S33** (ground spin state structures). Bond lengths are in angstrom and angles are in degrees.

Figure S35 : PEP for the C-C bond activation of C_3H_8 by U^{2+} (quintet and triplet spin states).

Figure S36 : Geometrical parameters of all of the minima and transition states involved in the C-C bond activation of C_3H_8 by U^{2+} presented in **Figure S33** (ground spin state structures). Bond lengths are in angstrom and angles are in degrees.

Figure S37 : PEP for the elimination of C_2H_6 from C_3H_8 by U^{2+} (quintet and triplet spin states). The labelling between the reactants and products identifies the first association complex (**FC**), the transition state (**TS1**), and the intermediates (**I**). Spin states are given between parentheses.

Figure S38: Geometrical parameters of all of the minima and transition states involved in the elimination of C_2H_6 from C_3H_8 by U^{2+} presented in **Figure S35** (ground spin state structures. Bond lengths are in angstrom and angles are in degrees.

Scheme 1 : Lewis resonance structures for $UC_2H_2^{2+}$.

Complete citation for reference 67.

Gaussian 03, Revision C.02, Frisch, M. J.; Trucks, G. W.; Schlegel, H. B.; Scuseria, G. E.; Robb, M. A.; Cheeseman, J. R.; Montgomery, Jr., J. A.; Vreven, T.; Kudin, K. N.; Burant, J. C.; Millam, J. M.; Iyengar, S. S.; Tomasi, J.; Barone, V.; Mennucci, B.; Cossi, M.; Scalmani, G.; Rega, N.; Petersson, G. A.; Nakatsuji, H.; Hada, M.; Ehara, M.; Toyota, K.; Fukuda, R.; Hasegawa, J.; Ishida, M.; Nakajima, T.; Honda, Y.; Kitao, O.; Nakai, H.; Klene, M.; Li, X.; Knox, J. E.; Hratchian, H. P.; Cross, J. B.; Bakken, V.; Adamo, C.; Jaramillo, J.; Gomperts, R.; Stratmann, R. E.; Yazyev, O.; Austin, A. J.; Cammi, R.; Pomelli, C.; Ochterski, J. W.; Ayala, P. Y.; Morokuma, K.; Voth, G. A.; Salvador, P.; Dannenberg, J. J.; Zakrzewski, V. G.; Dapprich, S.; Daniels, A. D.; Strain, M. C.; Farkas, O.; Malick, D. K.; Rabuck, A. D.; Raghavachari, K.; Foresman, J. B.; Ortiz, J. V.; Cui, Q.; Baboul, A. G.; Clifford, S.; Cioslowski, J.; Stefanov, B. B.; Liu, G.; Liashenko, A.; Piskorz, P.; Komaromi, I.; Martin, R. L.; Fox, D. J.; Keith, T.; Al-Laham, M. A.; Peng, C. Y.; Nanayakkara, A.; Challacombe, M.; Gill, P. M. W.; Johnson, B.; Chen, W.; Wong, M. W.; Gonzalez, C.; and Pople, J. A.; Gaussian, Inc., Wallingford CT, 2004.

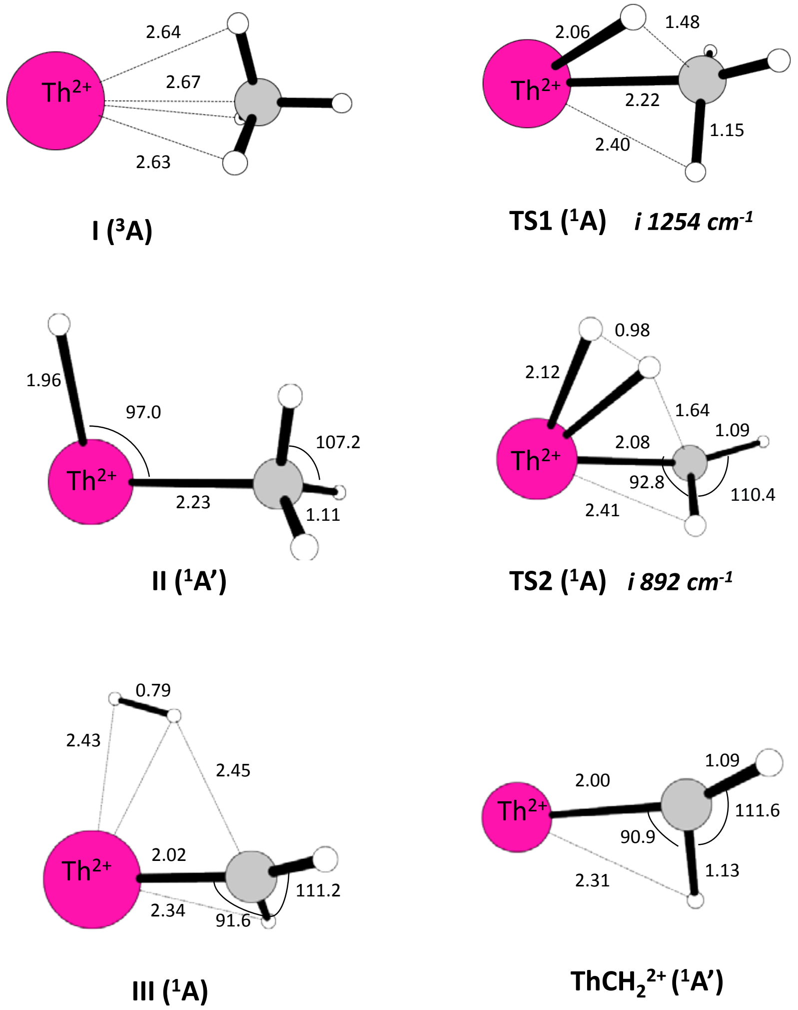

I (^{3}A)

TS1 (^{1}A) ***i 1254 cm^{-1}***

II (^{1}A')

TS2 (^{1}A) ***i 892 cm^{-1}***

III (^{1}A)

ThCH$_2^{2+}$ (^{1}A')

Figure S1

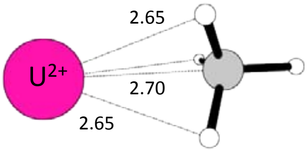

I (^{5}A)

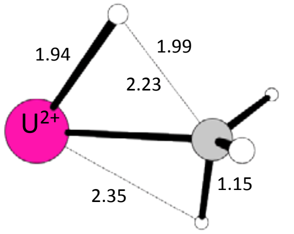

TS1 (^{3}A) ***i 715 cm^{-1}***

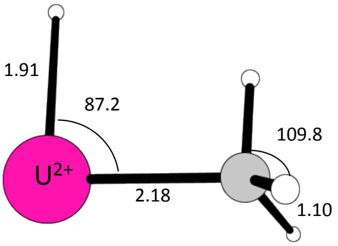

II (^{3}A')

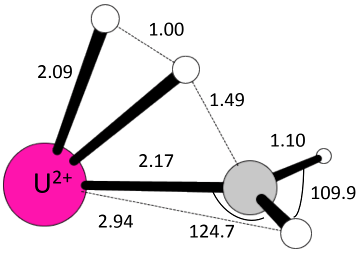

TS2 (^{3}A) ***i 1020 cm^{-1}***

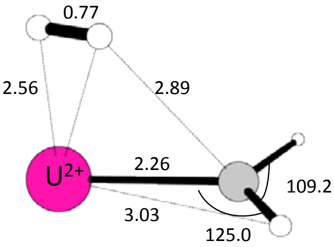

III (^{5}A)

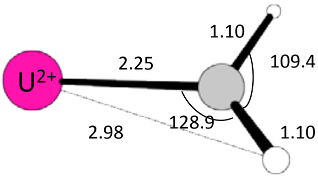

UCH$_2^{2+}$ (^{5}A)

Figure S2

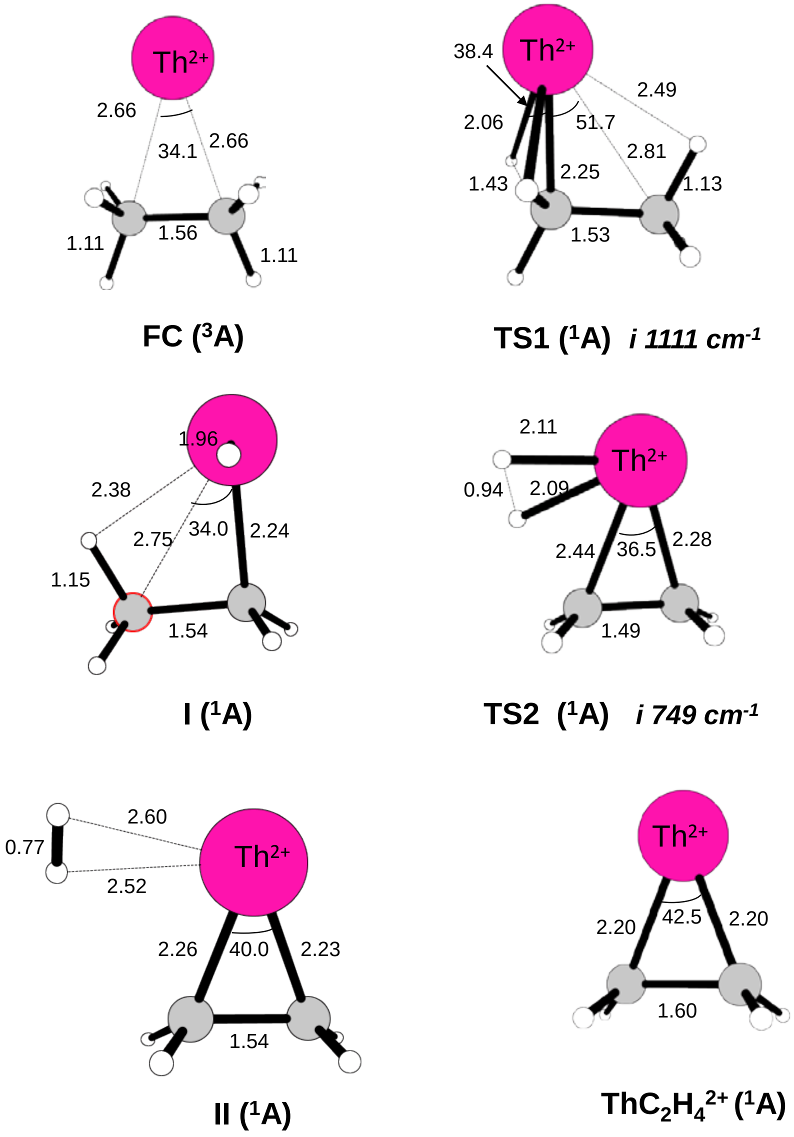

FC (^{3}A) **TS1 (^{1}A)** ***i 1111 cm^{-1}***

I (^{1}A) **TS2 (^{1}A)** ***i 749 cm^{-1}***

II (^{1}A) **$ThC_2H_4^{2+}$ (^{1}A)**

Figure S3

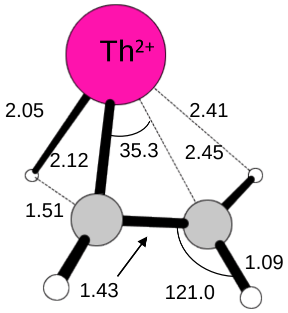

TS3 (^{1}A) ***i 992 cm^{-1}***

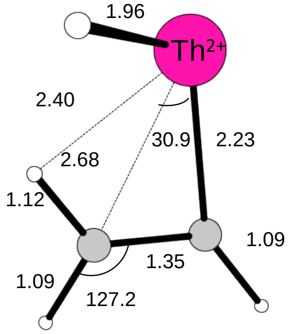

III (^{1}A)

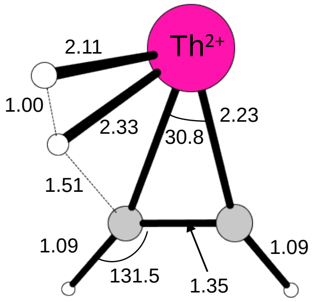

TS4 (^{1}A) ***i 1041 cm^{-1}***

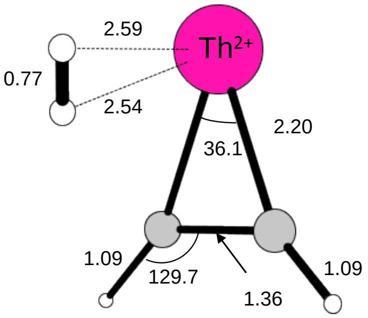

IV (^{1}A)

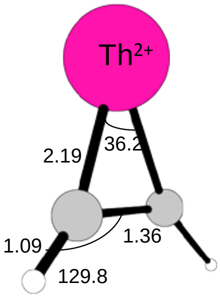

$ThC_2H_2^{2+}$ (^{1}A)

Figure S4

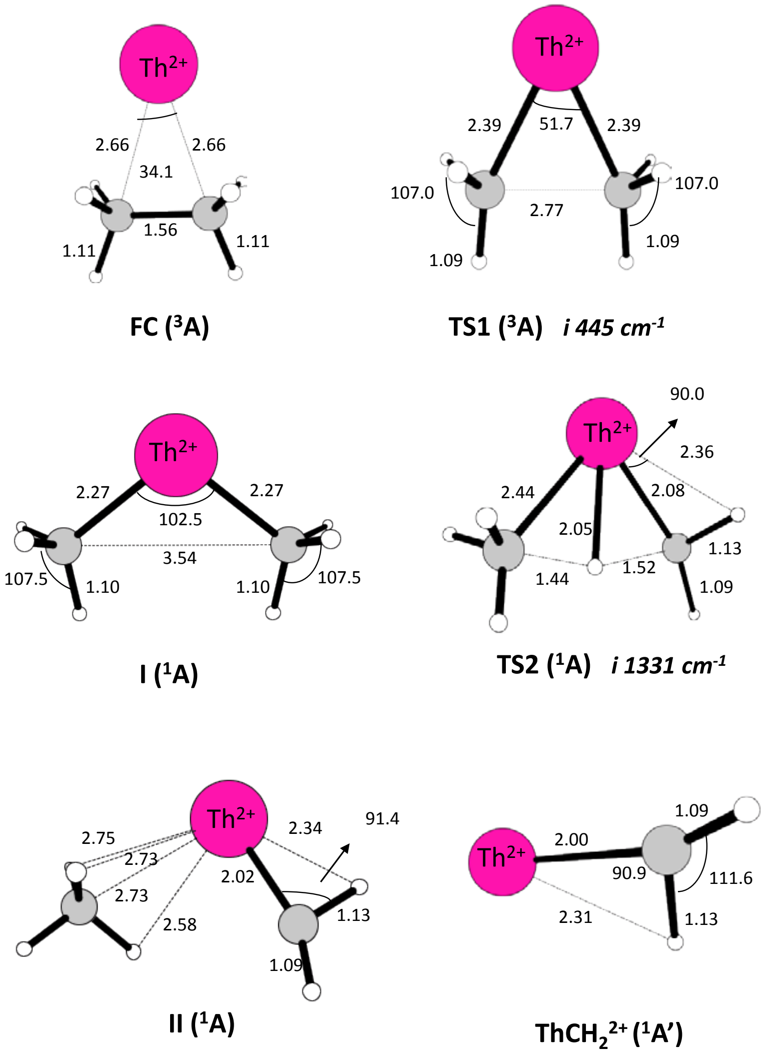

FC (^{3}A)

TS1 (^{3}A) ***i 445 cm^{-1}***

I (^{1}A)

TS2 (^{1}A) ***i 1331 cm^{-1}***

II (^{1}A)

$ThCH_2^{2+}$ (^{1}A’)

Figure S5

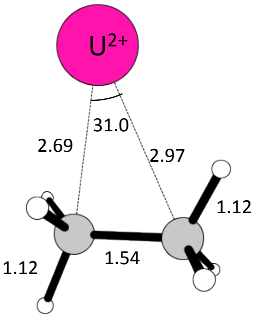

FC (^{5}A)

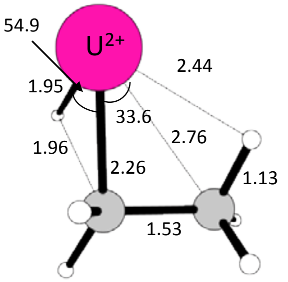

TS1 (^{3}A) ***i 276 cm^{-1}***

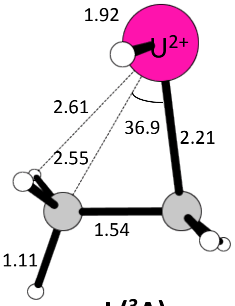

I (^{3}A)

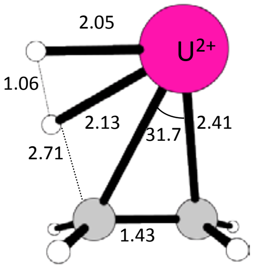

TS2 (^{3}A) ***i 1017 cm^{-1}***

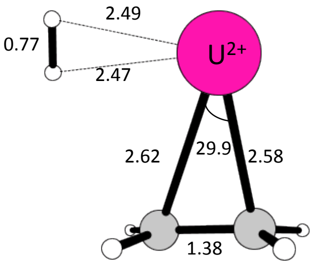

II (^{5}A)

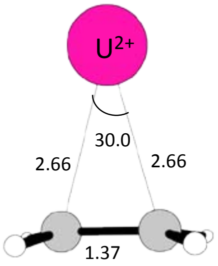

$UC_2H_4^{2+}$ (^{5}A)

Figure S6

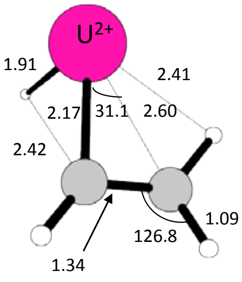

TS3 (^{3}A) *i 240 cm^{-1}*

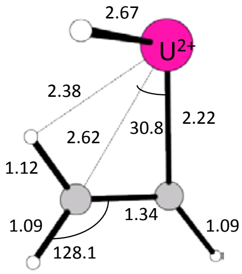

III (^{5}A)

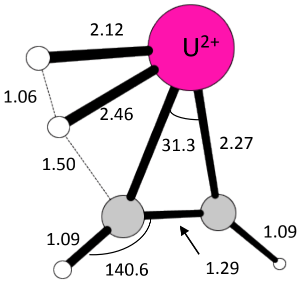

TS4 (^{3}A) *i 947 cm^{-1}*

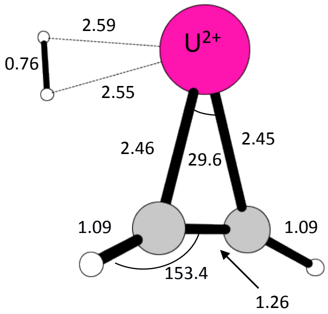

IV (^{5}A)

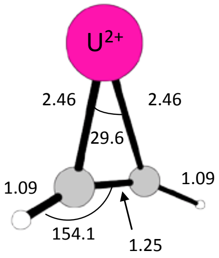

$UC_2H_2^{2+}$ (^{5}A)

Figure S7

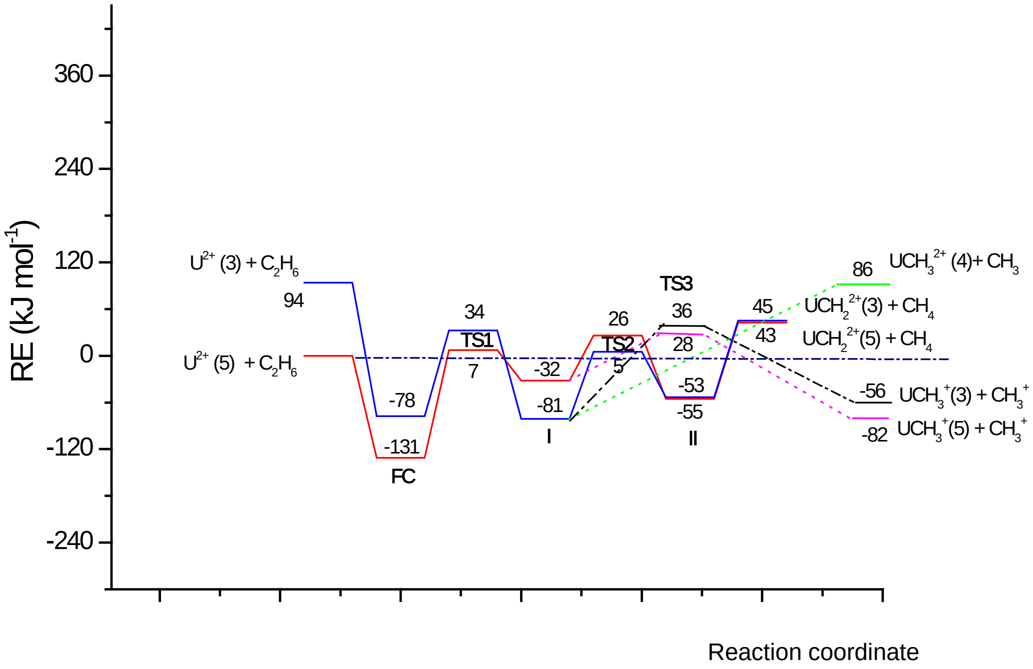
RE (kJ mol^{-1})
360
240
120
0
-120
-240
Reaction coordinate
U^{2+} (3) + C_2H_6
94
U^{2+} (5) + C_2H_6
-78
-131
FC
34
TS1
7
-32
-81
I
26
TS2
5
TS3
36
28
-53
-55
II
45
43
86
UCH_3^{2+} (4)+ CH_3
UCH_2^{2+}(3) + CH_4
UCH_2^{2+}(5) + CH_4
-56
UCH_3^+(3) + CH_3^+
-82
UCH_3^+(5) + CH_3^+

Figure S8

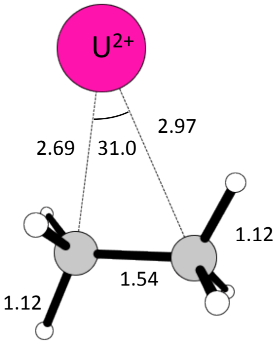

FC (^{5}A)

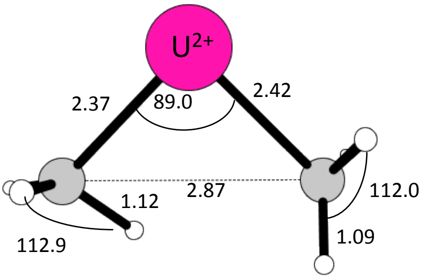

TS1 (^{5}A) ***i 696 cm^{-1}***

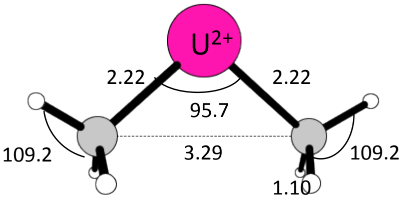

I (^{3}A)

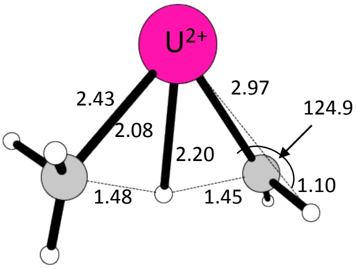

TS2 (^{3}A) ***i 1359 cm^{-1}***

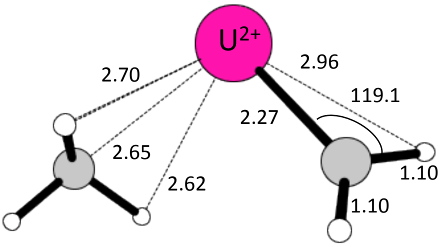

II (^{5}A)

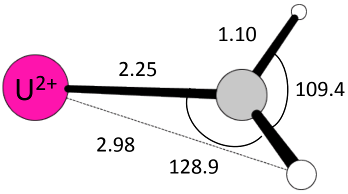

UCH$_2^{2+}$ (^{5}A)

Figure S9

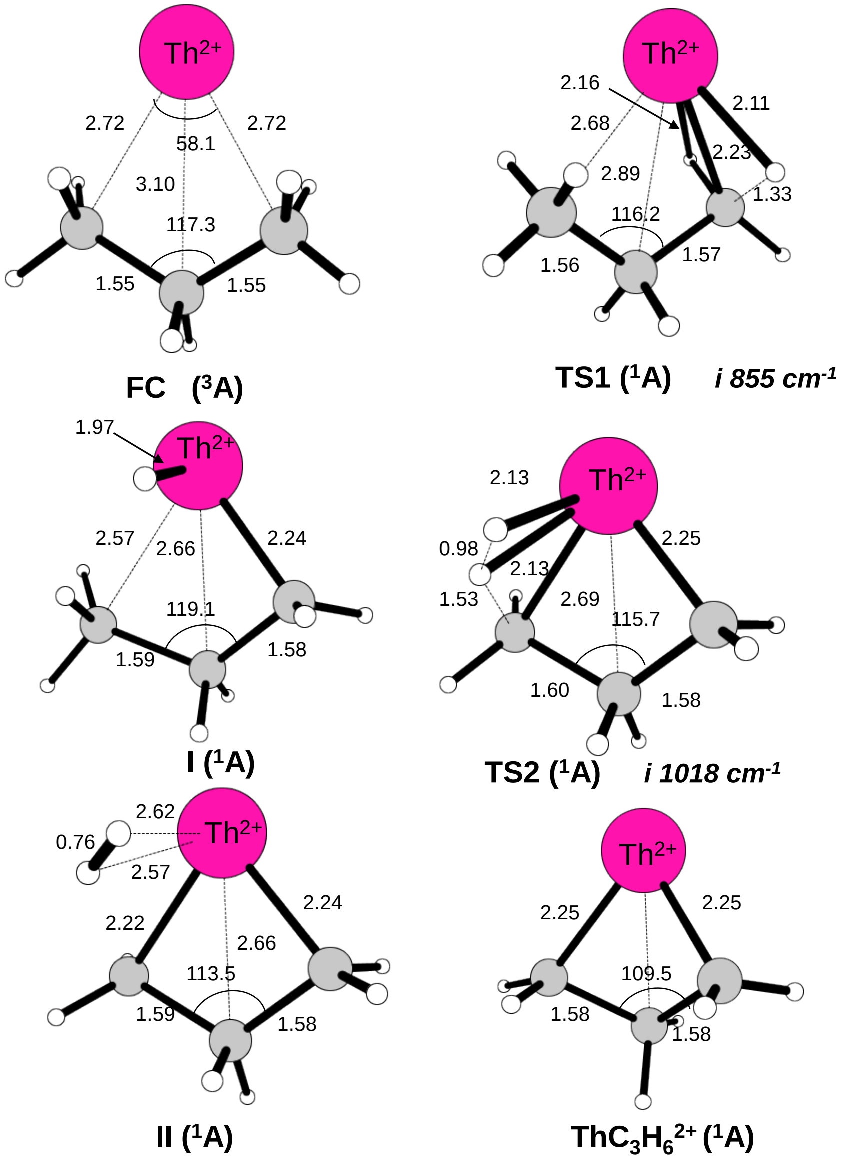

FC (^{3}A)

TS1 (^{1}A) ***i* 855 cm^{-1}**

I (^{1}A)

TS2 (^{1}A) ***i* 1018 cm^{-1}**

II (^{1}A)

ThC$_3$H$_6^{2+}$ (^{1}A)

Figure S10 (a)

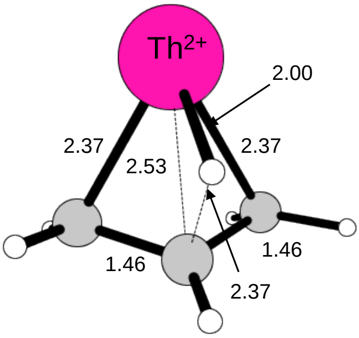

TS3 (^{1}A) ***i* 833 cm^{-1}**

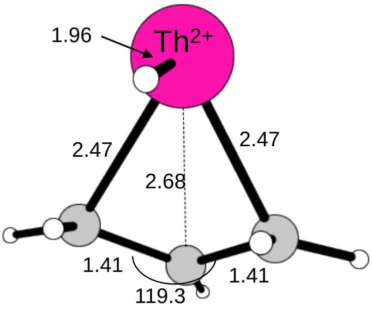

III (^{1}A)

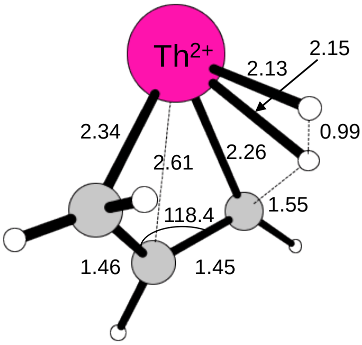

TS4 (^{1}A) ***i* 1075 cm^{-1}**

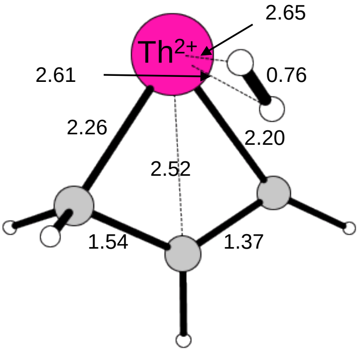

IV (^{1}A)

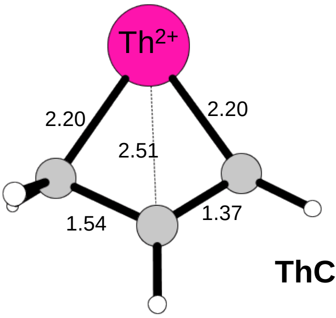

ThC$_3$H$_4$$^{2+}$ (^{1}A)

Figure S10 (b)

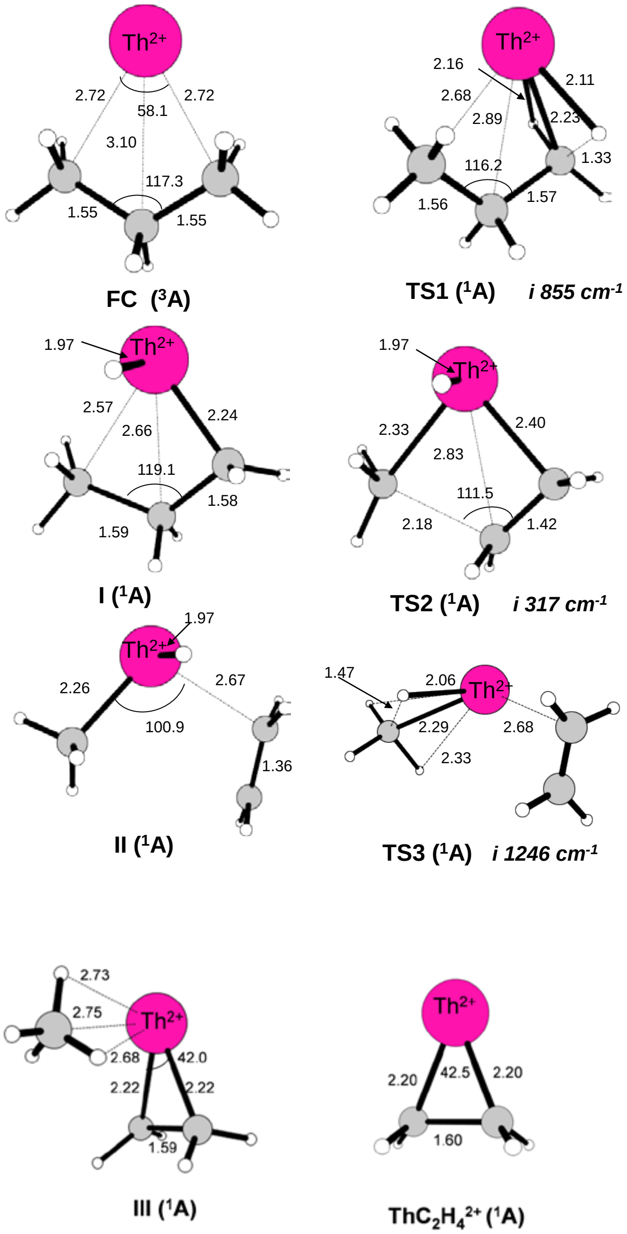
FC (^{3}A)

TS1 (^{1}A) *i 855 cm^{-1}*

I (^{1}A)

TS2 (^{1}A) *i 317 cm^{-1}*

II (^{1}A)

TS3 (^{1}A) *i 1246 cm^{-1}*

III (^{1}A)

$ThC_2H_4^{2+}$ (^{1}A)

Figure S11 (a)

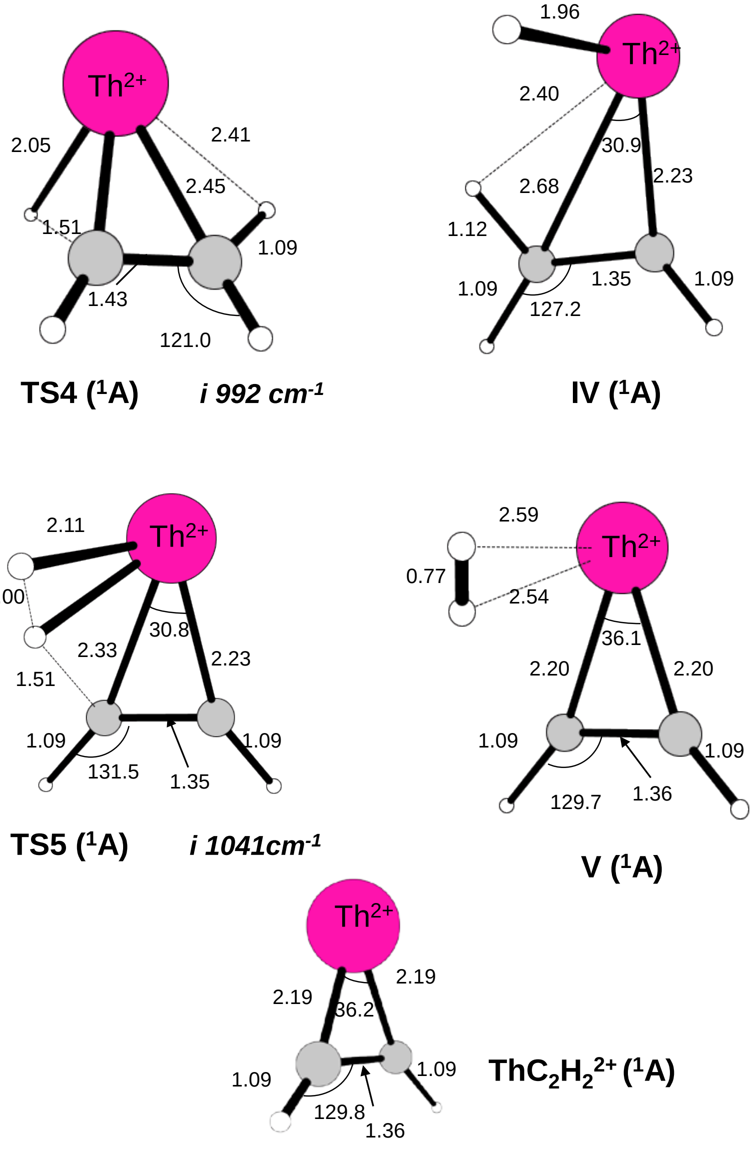

TS4 (^{1}A) ***i 992 cm^{-1}***

IV (^{1}A)

TS5 (^{1}A) ***i 1041cm^{-1}***

V (^{1}A)

$ThC_2H_2^{2+}$ (^{1}A)

Figure S11 (b)

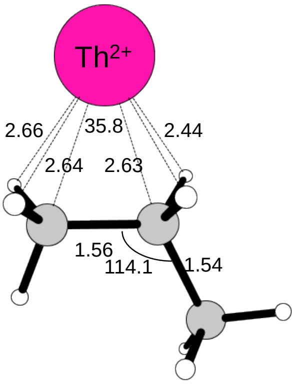

FC' (^{3}A)

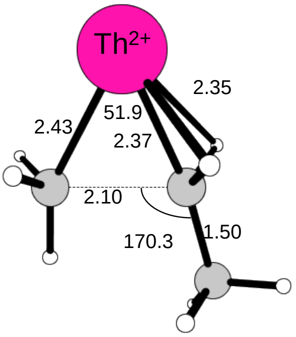

TS1 (^{3}A) ***i 450 cm^{-1}***

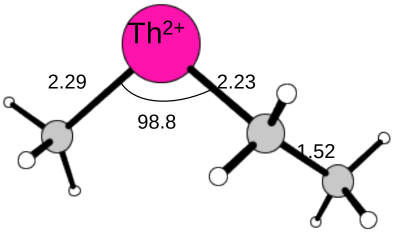

I (^{1}A)

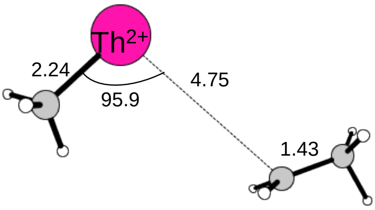

TS2 (^{1}A) ***i 52 cm^{-1}***

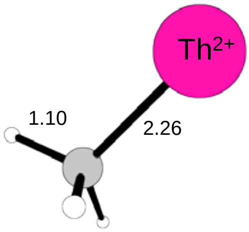

$ThCH_3^{2+}$ (^{1}A)

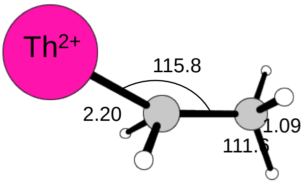

$ThC_2H_5^{2+}$ (^{1}A)

Figure S12

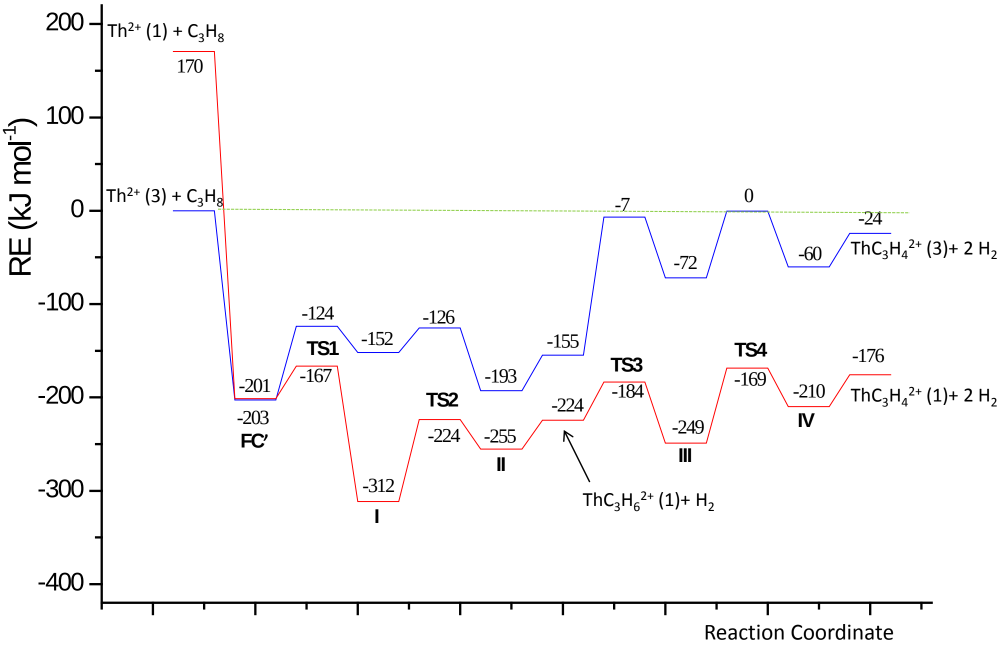
RE (kJ mol^{-1})
200
100
0
-100
-200
-300
-400
Reaction Coordinate
Th^{2+} (1) + C_3H_8
170
Th^{2+} (3) + C_3H_8
-201
-203
FC'
-124
TS1
-167
-152
-312
I
-126
TS2
-224
-193
-255
II
-155
-224
$ThC_3H_6^{2+}$ (1)+ H_2
-7
TS3
-184
-72
-249
III
0
TS4
-169
-60
-210
IV
-24
$ThC_3H_4^{2+}$ (3)+ 2 H_2
-176
$ThC_3H_4^{2+}$ (1)+ 2 H_2

Figure S13

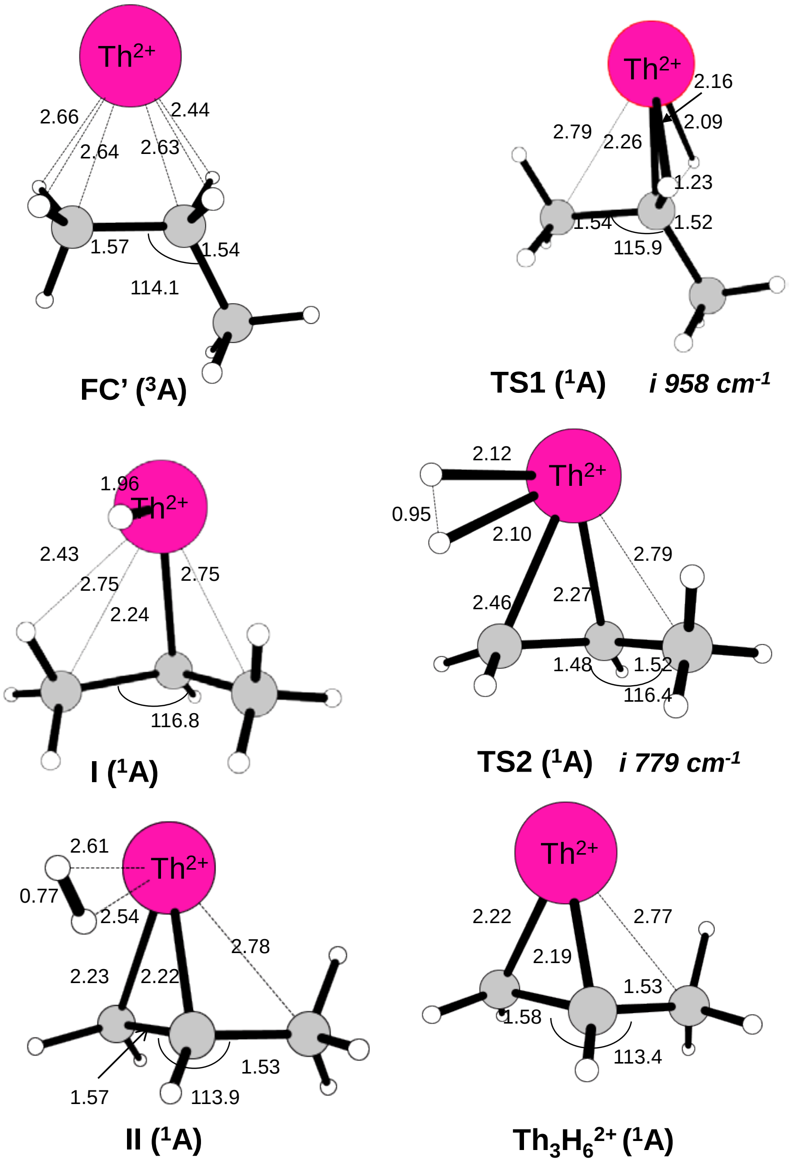

FC’ (^{3}A)

TS1 (^{1}A) ***i 958 cm^{-1}***

I (^{1}A)

TS2 (^{1}A) ***i 779 cm^{-1}***

II (^{1}A)

$Th_3H_6^{2+}$ (^{1}A)

Figure S14 (a)

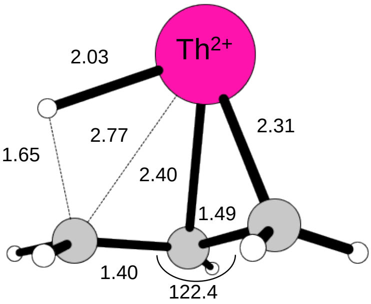

TS3 (^{1}A) ***i 743 cm^{-1}***

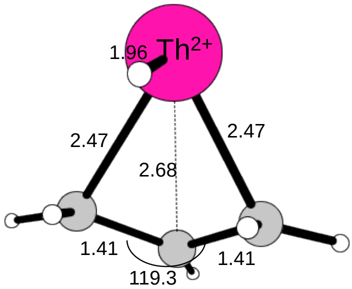

III (^{1}A)

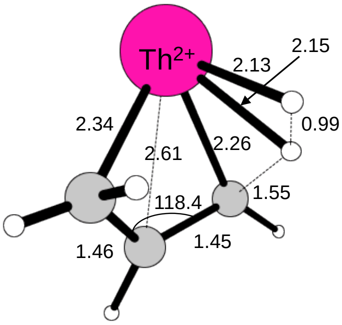

TS4 (^{1}A) ***i 1075 cm^{-1}***

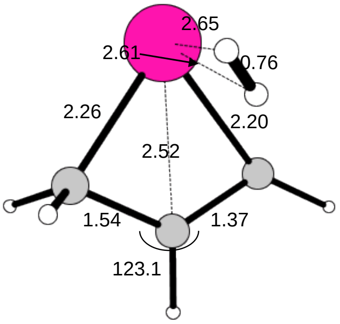

IV (^{1}A)

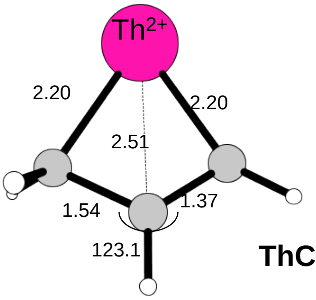

$ThC_3H_4^{2+}$ (^{1}A)

Figure S14 (b)

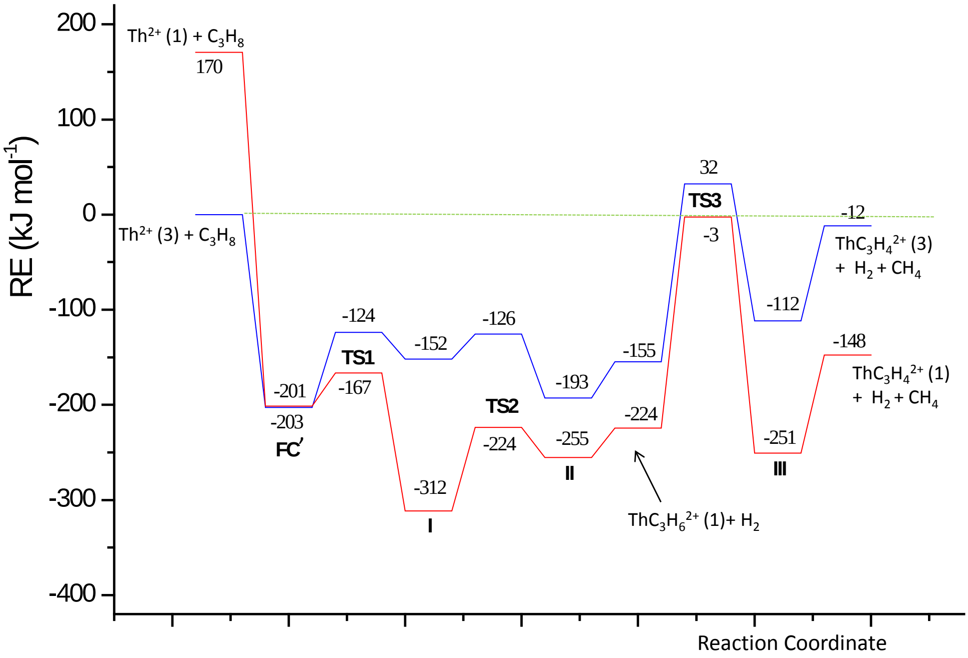
RE (kJ mol-1)
200
100
0
-100
-200
-300
-400
Reaction Coordinate
Th2+ (1) + C3H8
170
Th2+ (3) + C3H8
-201
-203
FC′
-124
TS1
-167
-152
-312
I
-126
TS2
-224
-193
-255
II
-155
-224
ThC3H62+ (1)+ H2
32
TS3
-3
-112
-251
III
-12
ThC3H42+ (3)
+ H2 + CH4
-148
ThC3H42+ (1)
+ H2 + CH4

Figure S15

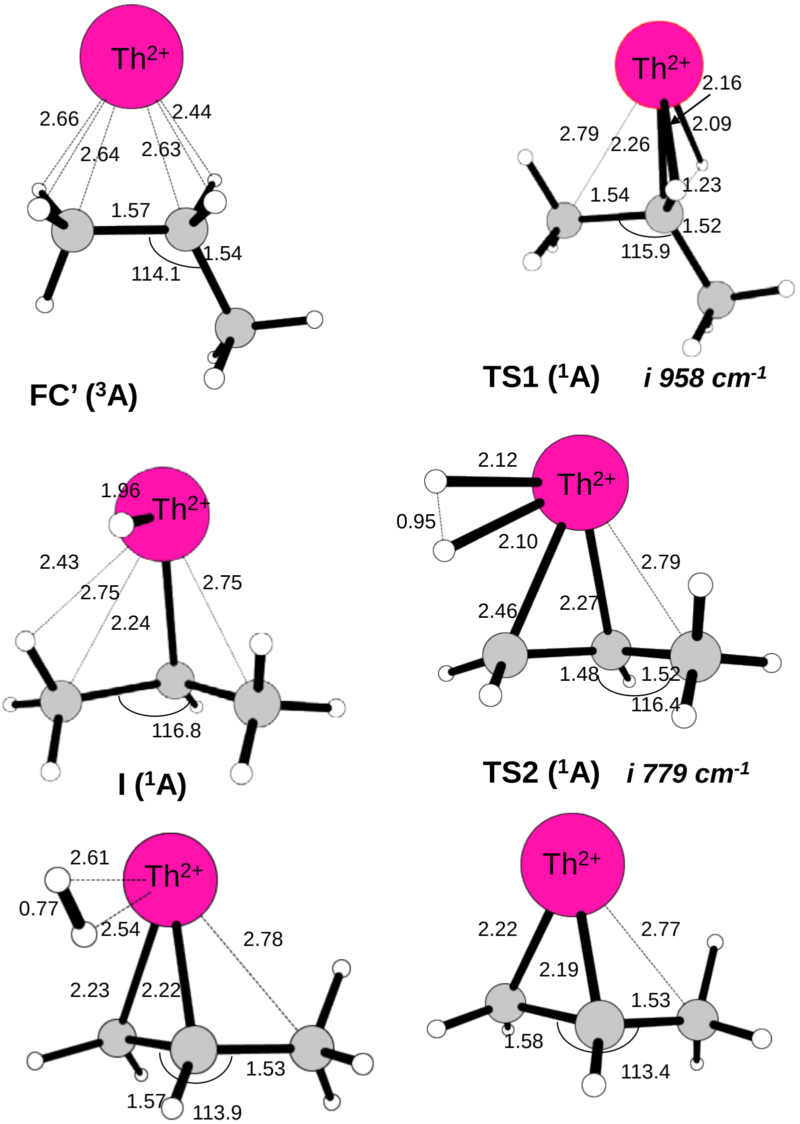

FC’ (^{3}A)

TS1 (^{1}A) ***i 958 cm^{-1}***

I (^{1}A)

TS2 (^{1}A) ***i 779 cm^{-1}***

II (^{1}A)

$ThC_3H_6^{2+}$ (^{1}A)

Figure S16 (a)

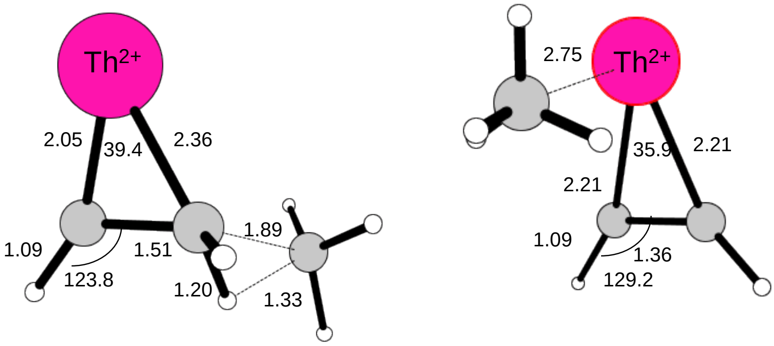

TS3 (^{1}A) ***i 726 cm^{-1}***

III (^{1}A)

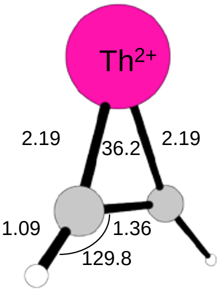

$ThC_2H_2^{2+}$ (^{1}A)

Figure S16 (b)

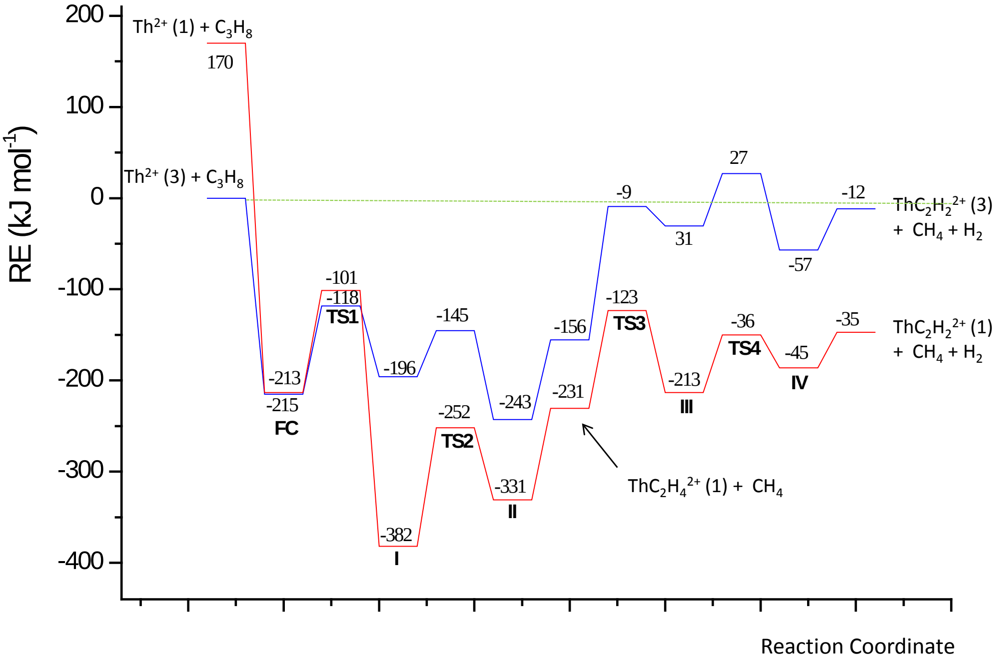
RE (kJ mol^{-1})
200
100
0
-100
-200
-300
-400
Reaction Coordinate
Th^{2+} (1) + C_3H_8
170
Th^{2+} (3) + C_3H_8
-213
-215
FC
-101
-118
TS1
-196
-145
-382
I
-252
TS2
-243
-331
II
-156
-231
-9
-123
TS3
31
-213
III
27
-36
TS4
-57
-45
IV
-12
-35
$ThC_2H_2^{2+}$ (3)
+ CH_4 + H_2
$ThC_2H_2^{2+}$ (1)
+ CH_4 + H_2
$ThC_2H_4^{2+}$ (1) + CH_4

Figure S17

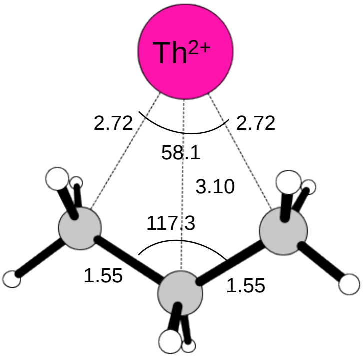

FC (³A)

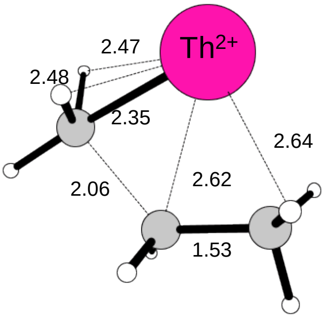

TS1 (³A) ***i 485 cm⁻¹***

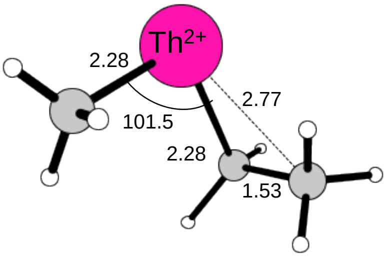

I (¹A)

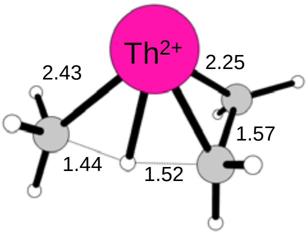

TS2 (¹A) ***i 1366 cm⁻¹***

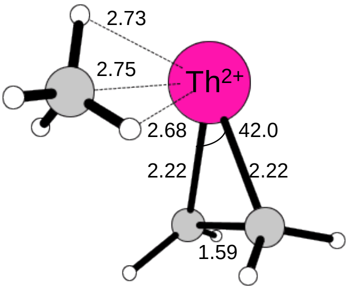

II (¹A)

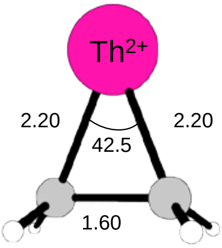

$ThC_2H_4^{2+}$ (¹A)

Figure S18 (a)

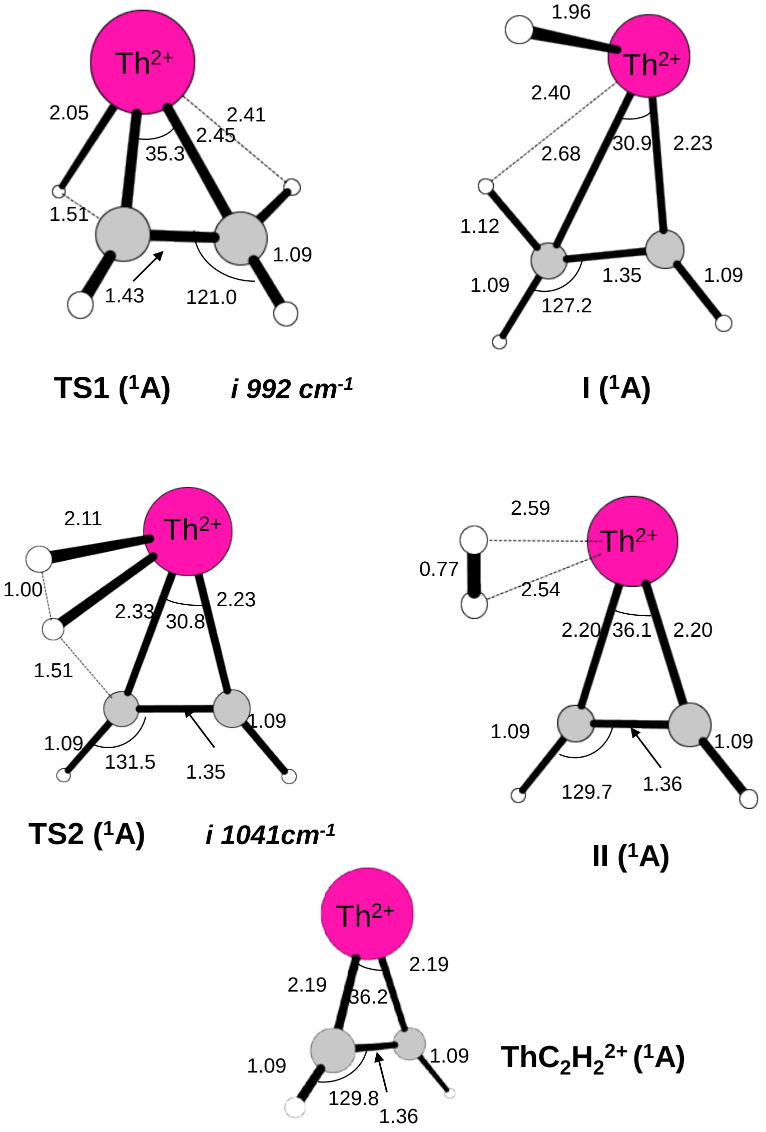
Th^{2+}
2.05
2.41
2.45
35.3
1.51
1.09
1.43
121.0
TS1 (^{1}A)
i 992 cm^{-1}
1.96
Th^{2+}
2.40
30.9
2.23
2.68
1.12
1.09
1.35
1.09
127.2
I (^{1}A)
2.11
Th^{2+}
1.00
2.33
30.8
2.23
1.51
1.09
1.09
131.5
1.35
TS2 (^{1}A)
i 1041cm^{-1}
2.59
Th^{2+}
0.77
2.54
2.20
36.1
2.20
1.09
1.09
129.7
1.36
II (^{1}A)
Th^{2+}
2.19
2.19
36.2
1.09
1.09
129.8
1.36
ThC$_2$H$_2$$^{2+}$ (^{1}A)

Figure S18 (b)

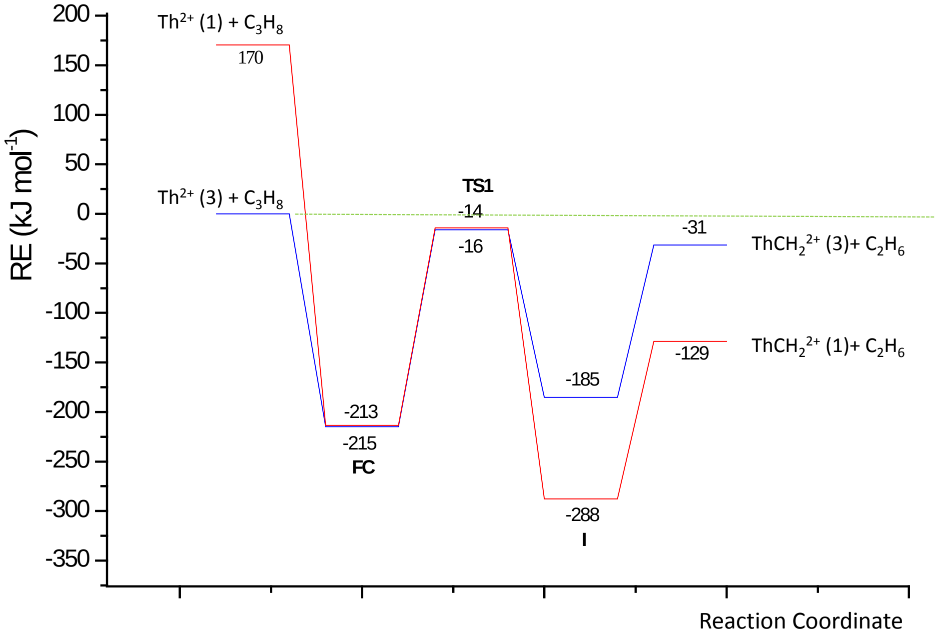

Th^{2+} (1) + C_3H_8
170
Th^{2+} (3) + C_3H_8
TS1
-14
-16
-31
ThCH$_2^{2+}$ (3)+ C_2H_6
-129
ThCH$_2^{2+}$ (1)+ C_2H_6
-185
-213
-215
FC
-288
I
RE (kJ mol^{-1})
200
150
100
50
0
-50
-100
-150
-200
-250
-300
-350
Reaction Coordinate

Figure S19

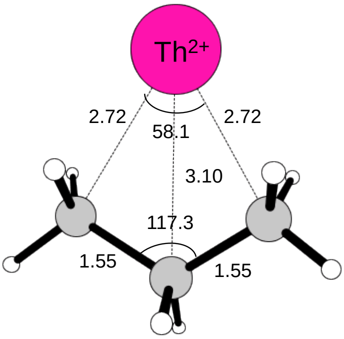

FC (^{3}A)

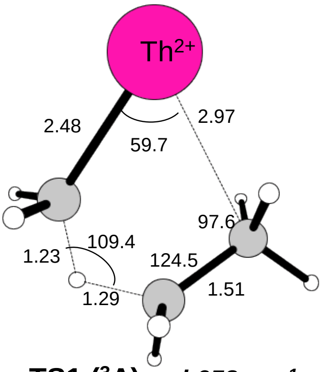

TS1 (^{3}A) ***i 653 cm^{-1}***

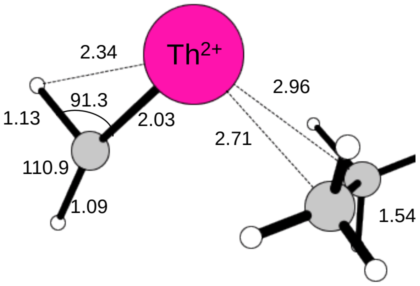

I (^{1}A)

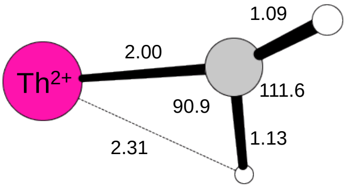

ThCH$_2^{2+}$ (^{1}A’)

Figure S20

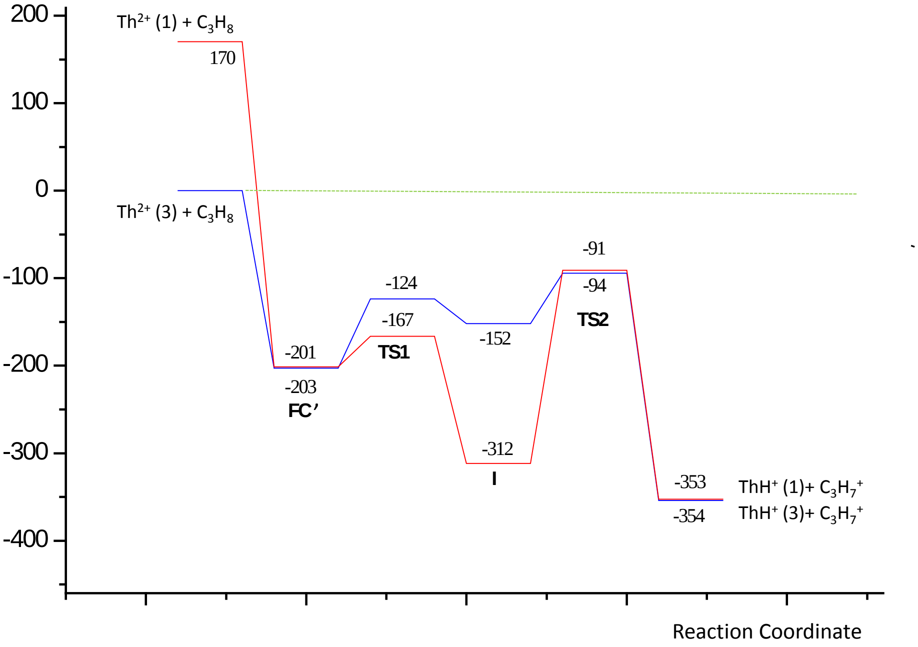
200
100
0
-100
-200
-300
-400
Th^{2+} (1) + C_3H_8
170
Th^{2+} (3) + C_3H_8
-201
-203
FC’
-124
-167
TS1
-152
-312
I
-91
-94
TS2
-353
-354
ThH^{+} (1)+ $C_3H_7^+$
ThH^{+} (3)+ $C_3H_7^+$
Reaction Coordinate

Figure S21

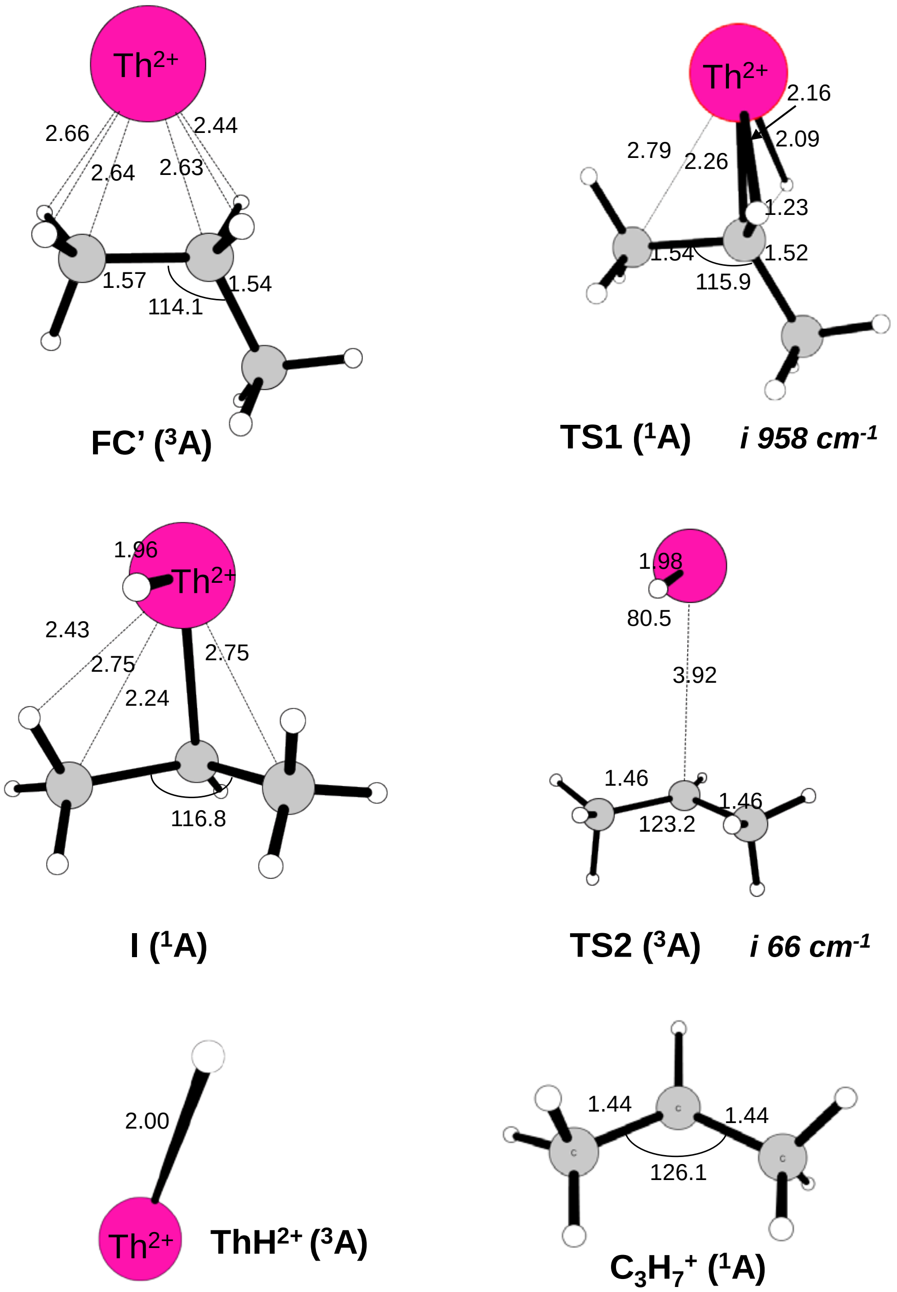

FC' (^{3}A)

TS1 (^{1}A) ***i 958 cm^{-1}***

I (^{1}A)

TS2 (^{3}A) ***i 66 cm^{-1}***

ThH^{2+} (^{3}A)

$C_3H_7^+$ (^{1}A)

Figure S22

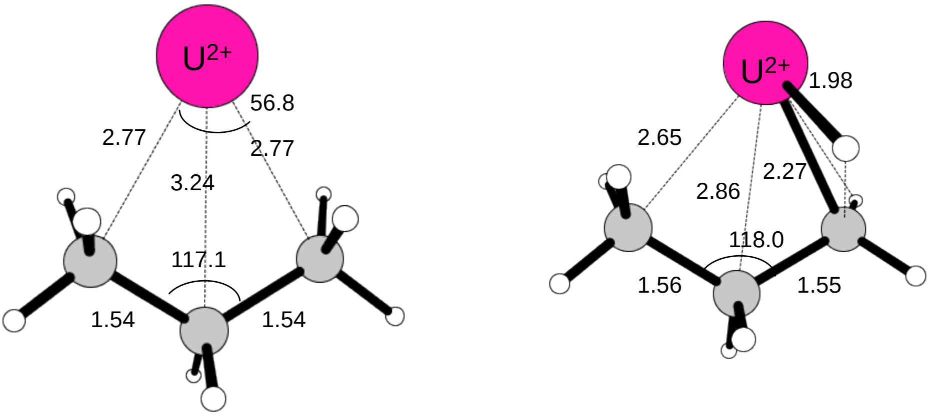

FC (^{5}A) **TS1 (^{3}A) *i 240 cm^{-1}***

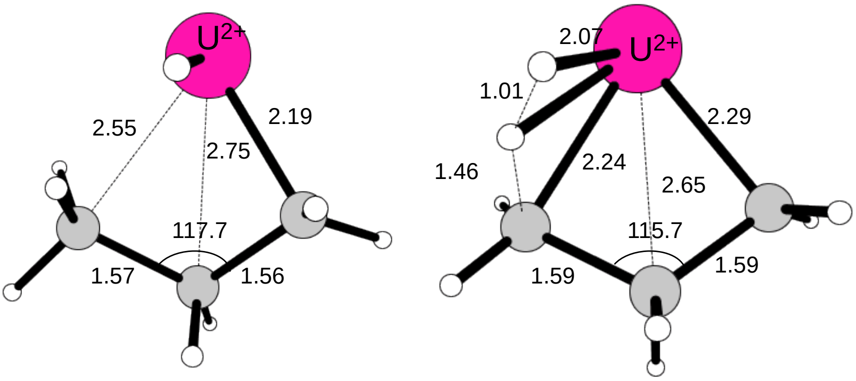

I (^{3}A) **TS2 (^{3}A) *i 1096 cm^{-1}***

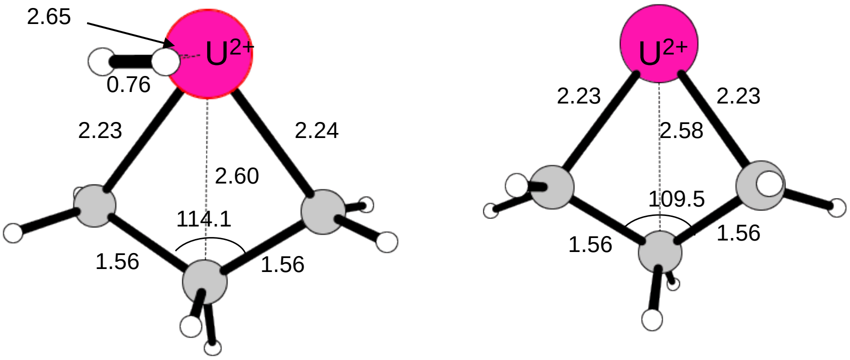

II (^{3}A) **$UC_3H_6^{2+}$ (^{3}A)**

Figure S23 (a)

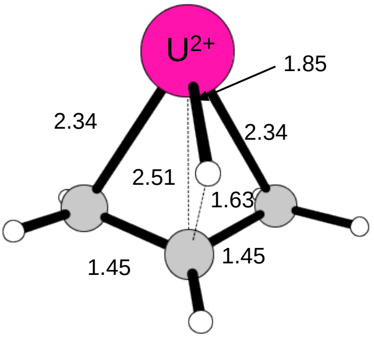

TS3 (^{5}A) ***i* 858 cm^{-1}**

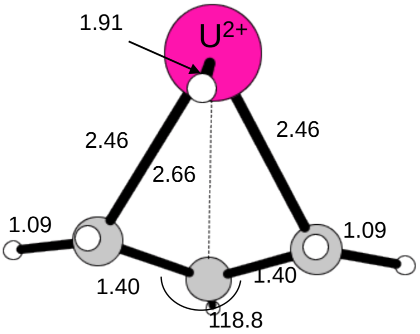

III (^{3}A)

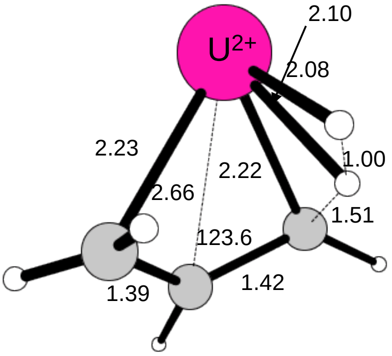

TS4 (^{3}A) ***i* 671 cm^{-1}**

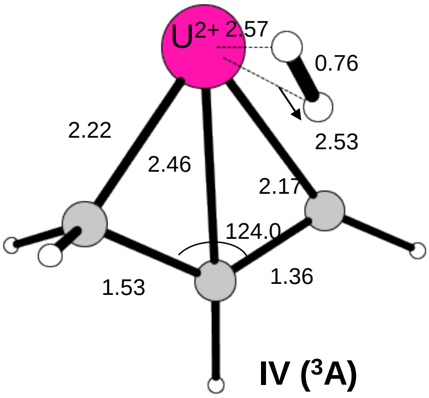

IV (^{3}A)

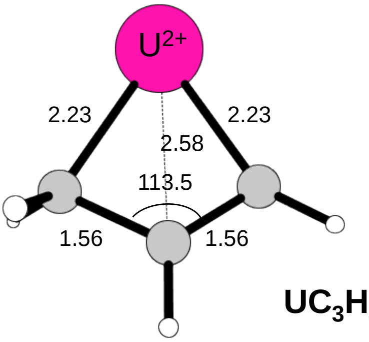

$UC_3H_4^{2+}$ (^{3}A)

Figure S23 (b)

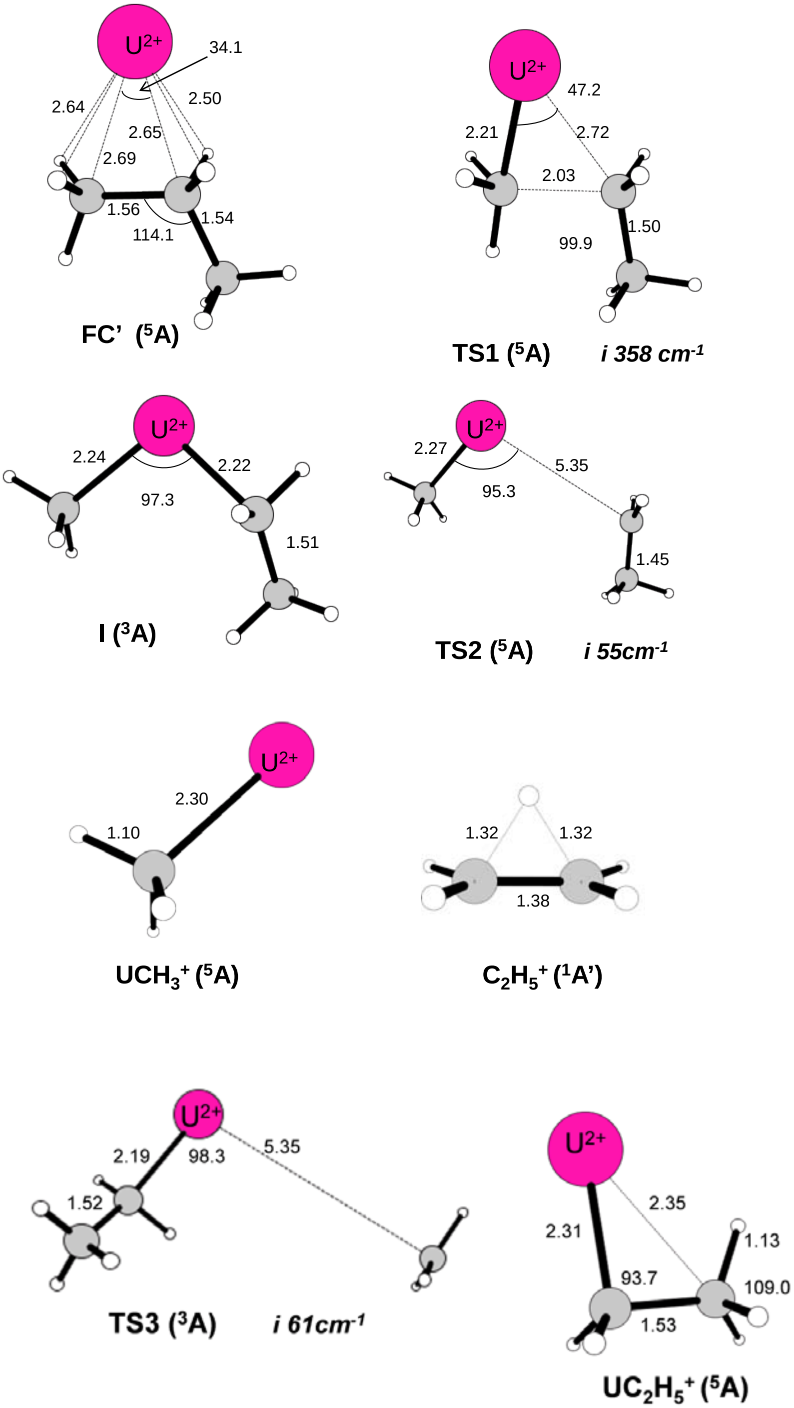

FC' (^{5}A)

TS1 (^{5}A) ***i 358 cm^{-1}***

I (^{3}A)

TS2 (^{5}A) ***i 55cm^{-1}***

UCH$_3^+$ (^{5}A)

C$_2$H$_5^+$ (^{1}A')

TS3 (^{3}A) ***i 61cm^{-1}***

UC$_2$H$_5^+$ (^{5}A)

Figure S24

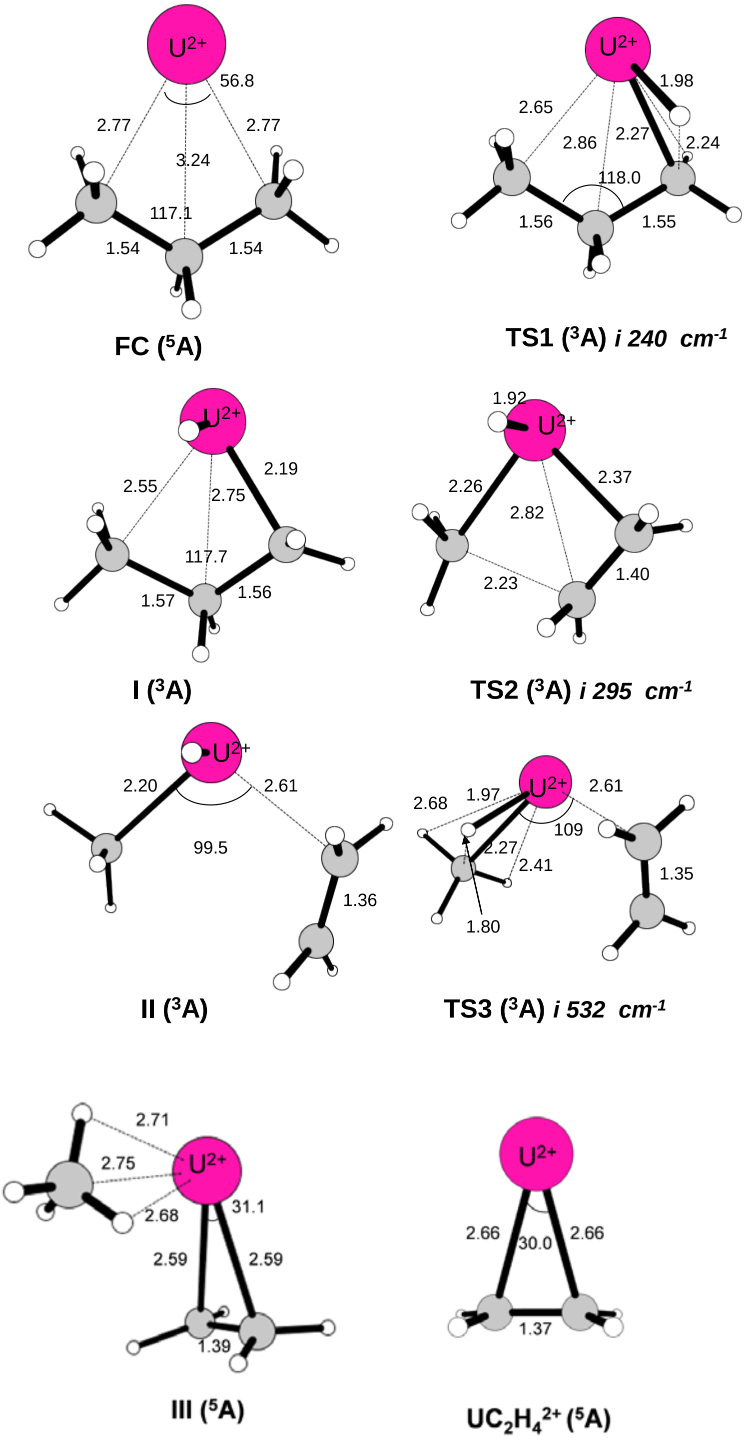

FC (^{5}A)

TS1 (^{3}A) *i 240 cm^{-1}*

I (^{3}A)

TS2 (^{3}A) *i 295 cm^{-1}*

II (^{3}A)

TS3 (^{3}A) *i 532 cm^{-1}*

III (^{5}A)

UC$_2$H$_4^{2+}$ (^{5}A)

Figure S25 (a)

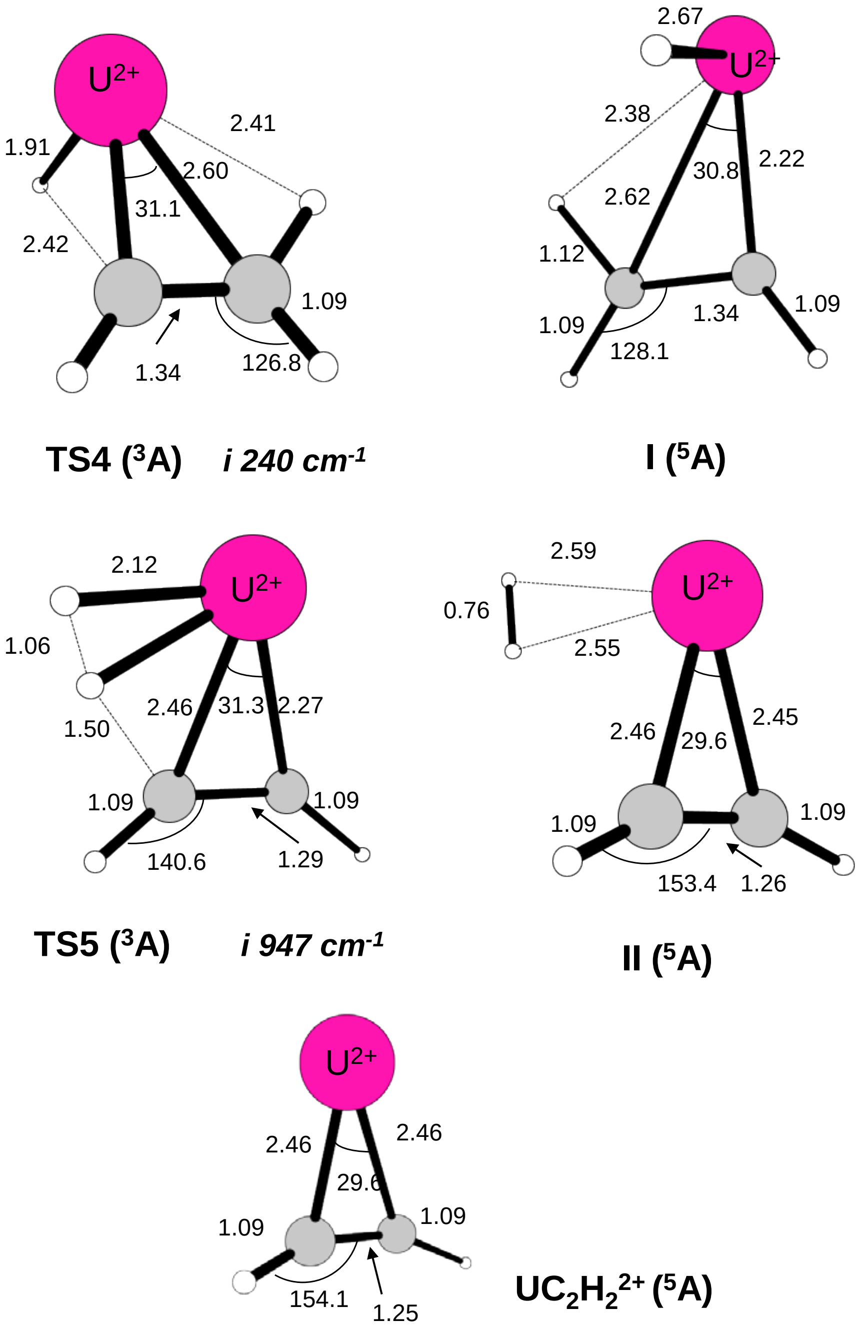

TS4 (^{3}A) ***i* 240 cm^{-1}**

I (^{5}A)

TS5 (^{3}A) ***i* 947 cm^{-1}**

II (^{5}A)

$UC_2H_2^{2+}$ (^{5}A)

Figure S25 (b)

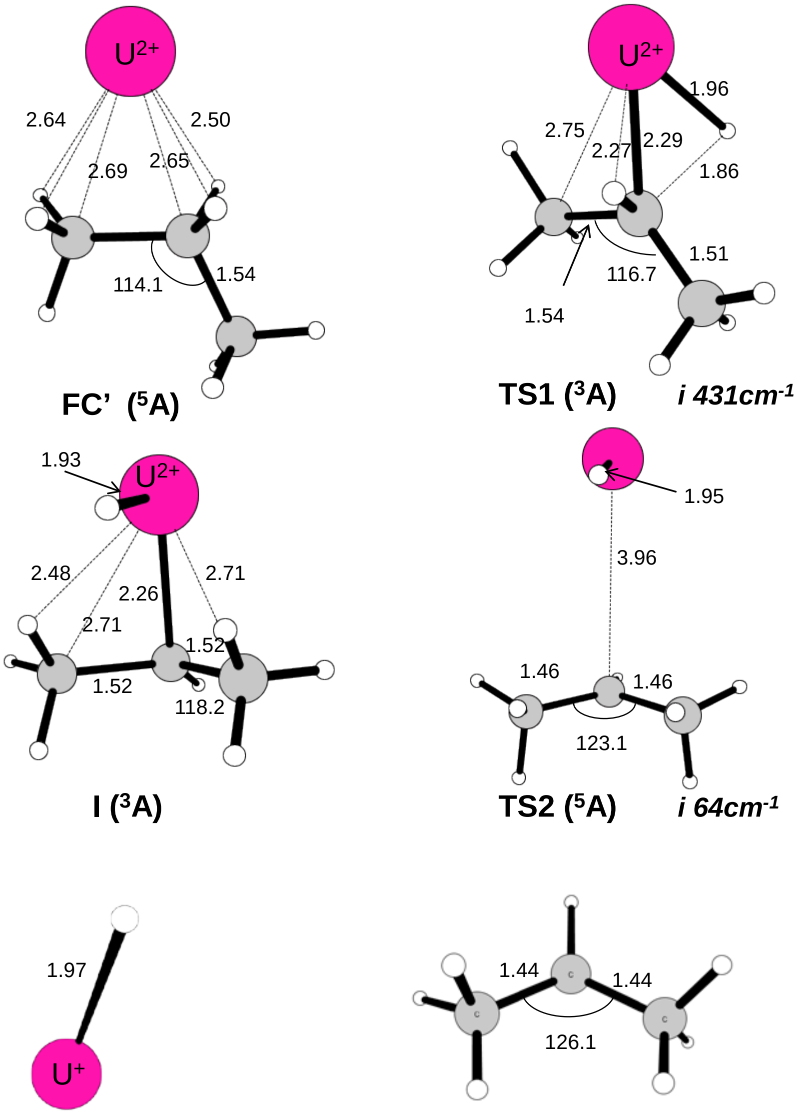

FC' (^5A)

TS1 (^3A) *i 431cm^{-1}*

I (^3A)

TS2 (^5A) *i 64cm^{-1}*

UH^+ (^5A)

$C_3H_7^+$ (^1A)

Figure S26

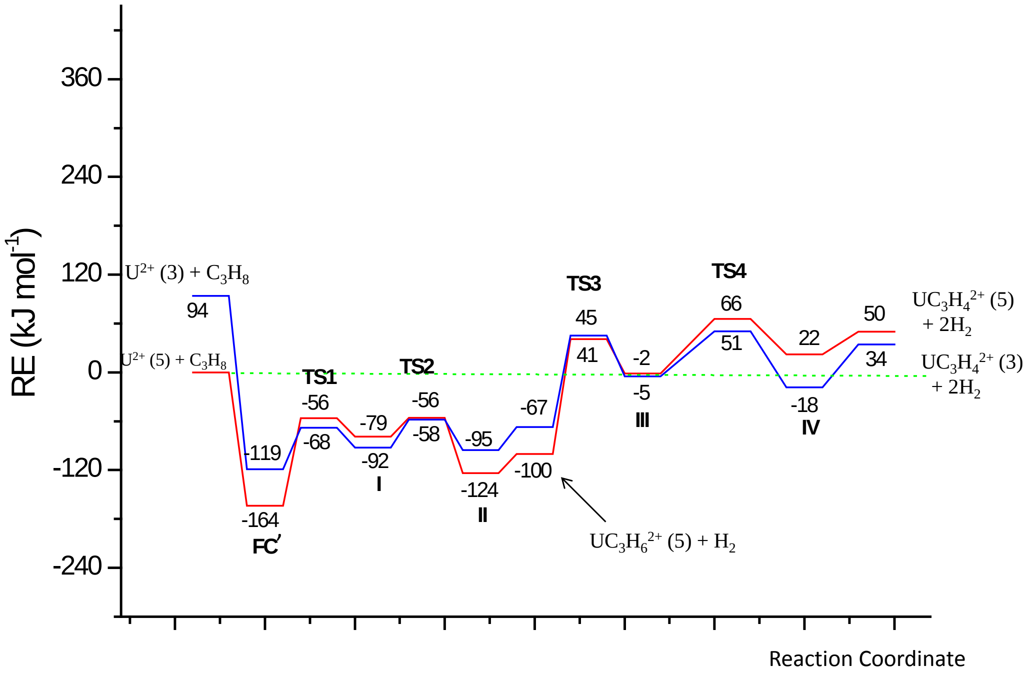
RE (kJ mol^{-1})
360
240
120
0
-120
-240
Reaction Coordinate
U^{2+} (3) + C_3H_8
U^{2+} (5) + C_3H_8
94
-119
-164
FC′
TS1
-56
-68
-79
-92
I
TS2
-56
-58
-95
-124
II
-67
-100
$UC_3H_6^{2+}$ (5) + H_2
TS3
45
41
-2
-5
III
TS4
66
51
22
-18
IV
50
34
$UC_3H_4^{2+}$ (5) + $2H_2$
$UC_3H_4^{2+}$ (3) + $2H_2$

Figure S27

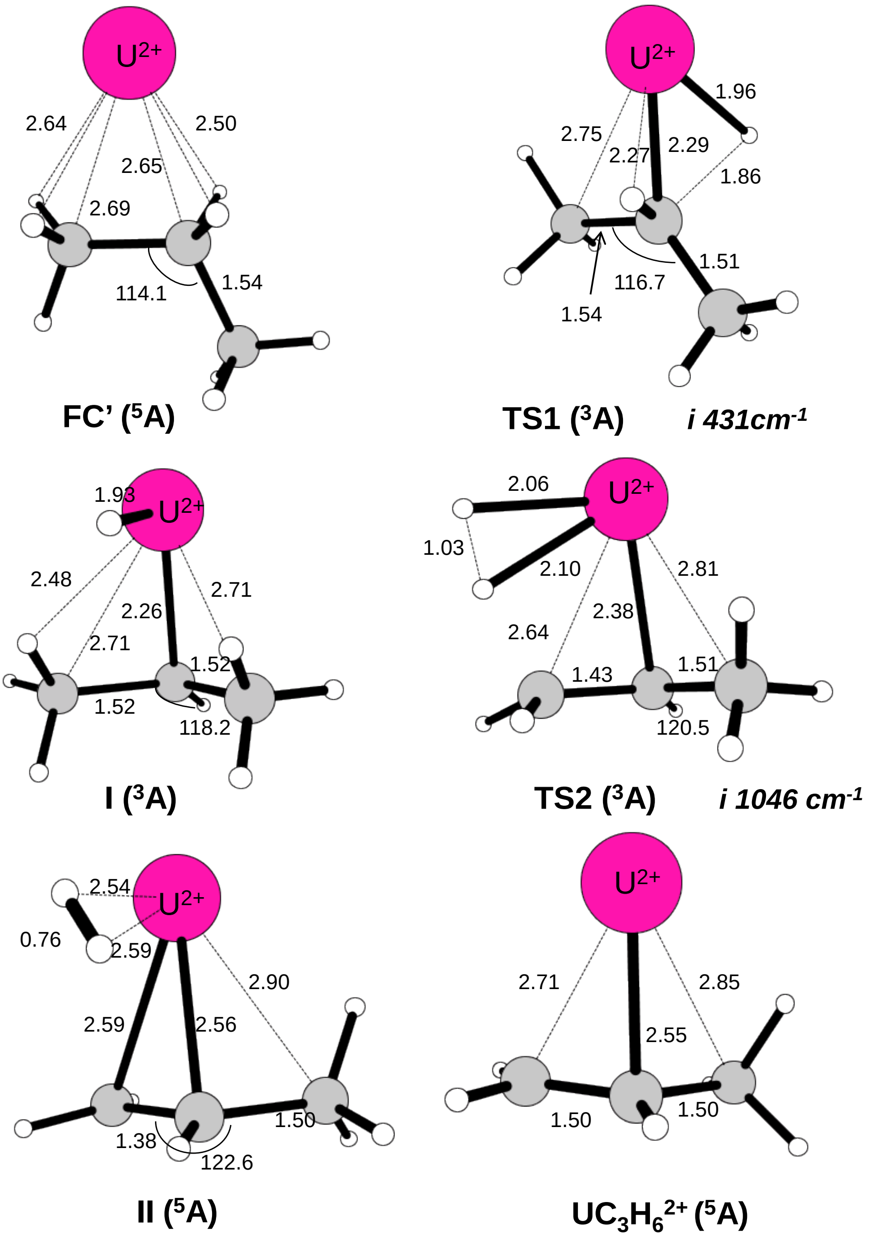

FC’ (^{5}A)

TS1 (^{3}A) ***i 431cm^{-1}***

I (^{3}A)

TS2 (^{3}A) ***i 1046 cm^{-1}***

II (^{5}A)

$UC_3H_6^{2+}$ (^{5}A)

Figure S28 (a)

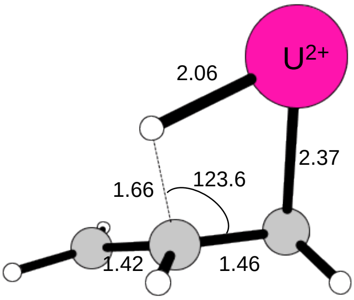

TS3 (^{5}A) *i 671 cm^{-1}*

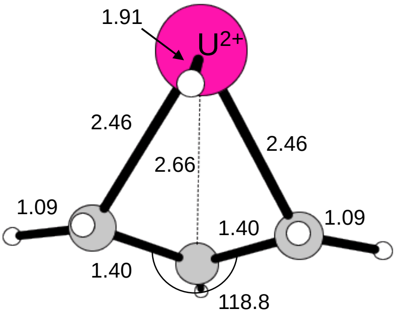

III (^{3}A)

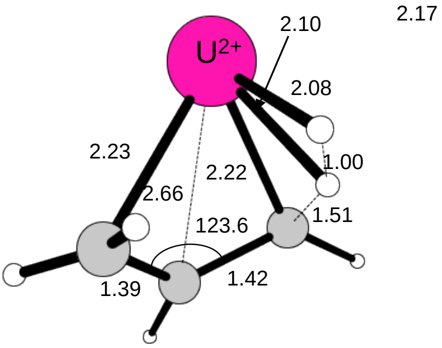

TS4 (^{3}A) *i 671 cm^{-1}*

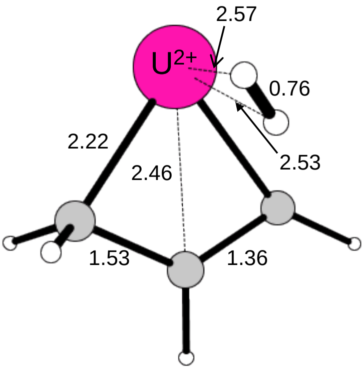

IV (^{3}A)

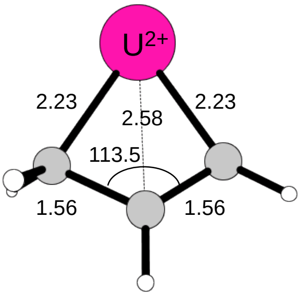

$UC_3H_4^{2+}$ (^{3}A)

Figure S28 (b)

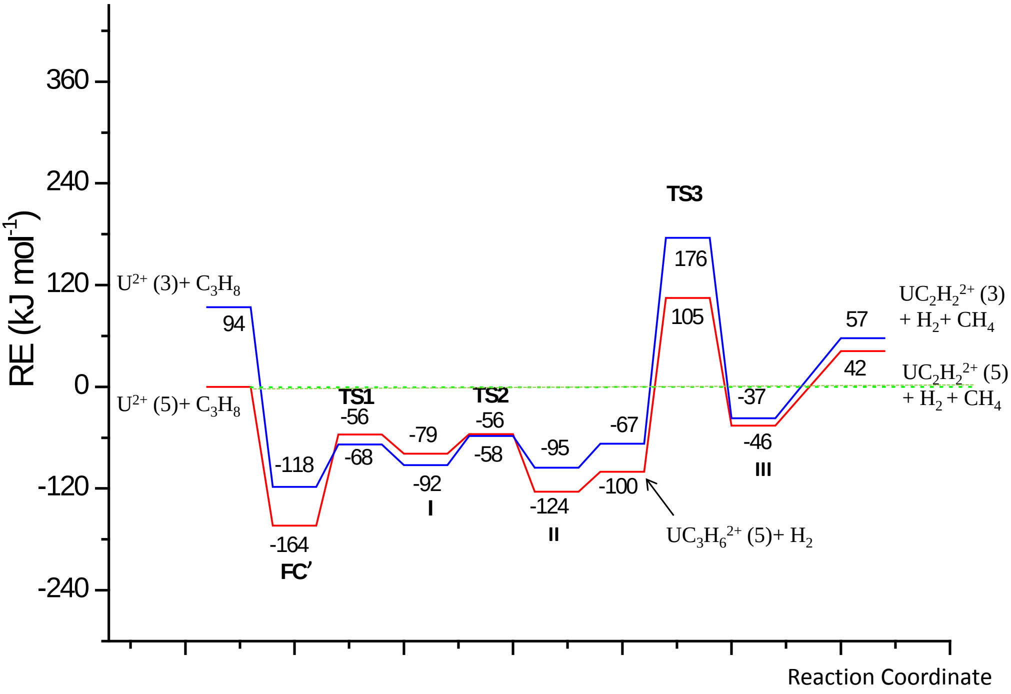
RE (kJ mol^{-1})
360
240
120
0
-120
-240
Reaction Coordinate
U^{2+} (3)+ C$_3$H$_8$
U^{2+} (5)+ C$_3$H$_8$
94
-118
-164
FC′
TS1
-56
-68
-79
-92
I
TS2
-56
-58
-95
-124
II
-67
-100
UC$_3$H$_6$$^{2+}$ (5)+ H$_2$
TS3
176
105
-37
-46
III
57
42
UC$_2$H$_2$$^{2+}$ (3)
+ H$_2$+ CH$_4$
UC$_2$H$_2$$^{2+}$ (5)
+ H$_2$ + CH$_4$

Figure S29

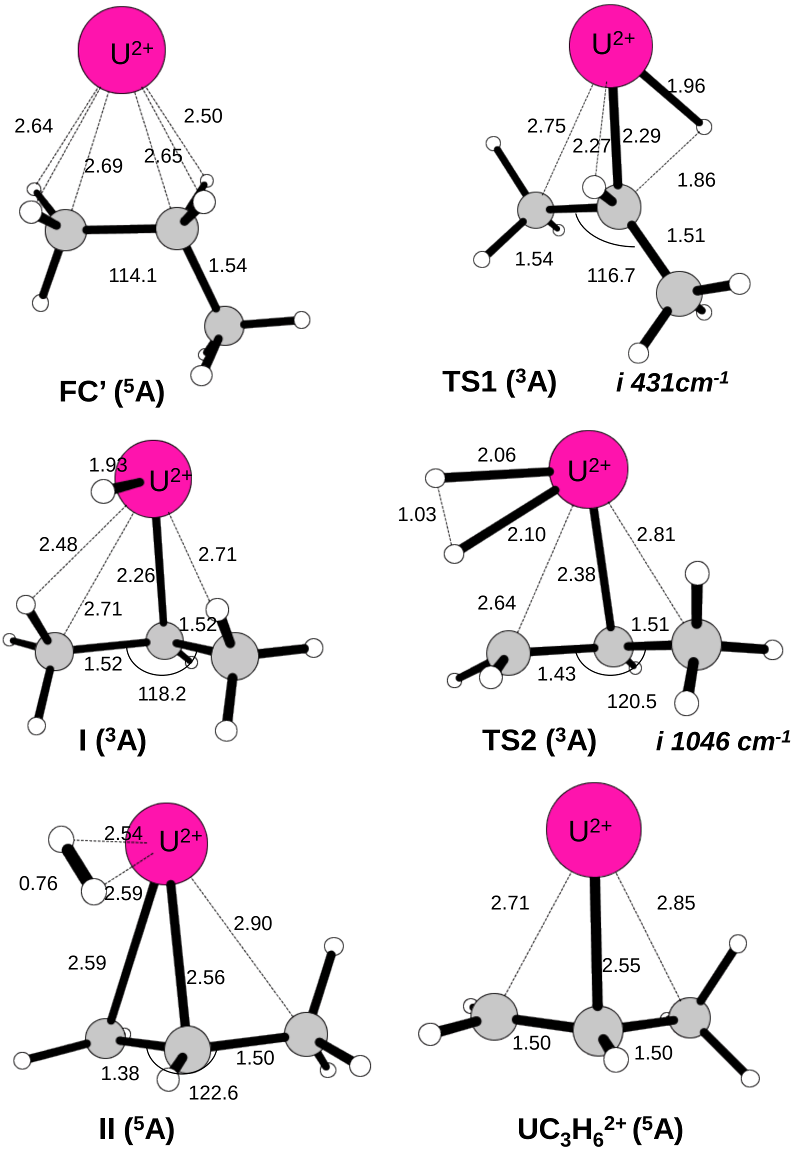

FC’ (^{5}A)

TS1 (^{3}A) ***i 431cm^{-1}***

I (^{3}A)

TS2 (^{3}A) ***i 1046 cm^{-1}***

II (^{5}A)

$UC_3H_6^{2+}$ (^{5}A)

Figure S30 (a)

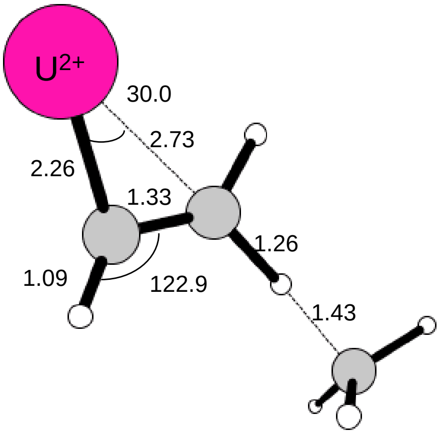

TS3 (^{5}A) ***i* 693 cm^{-1}**

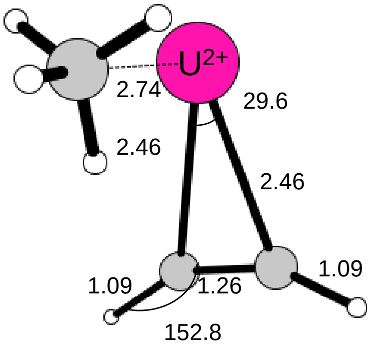

III (^{5}A)

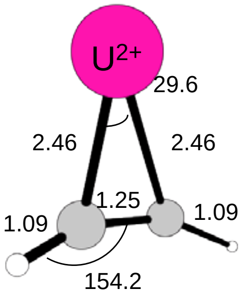

$UC_2H_2^{2+}$ (^{5}A)

Figure S30 (b)

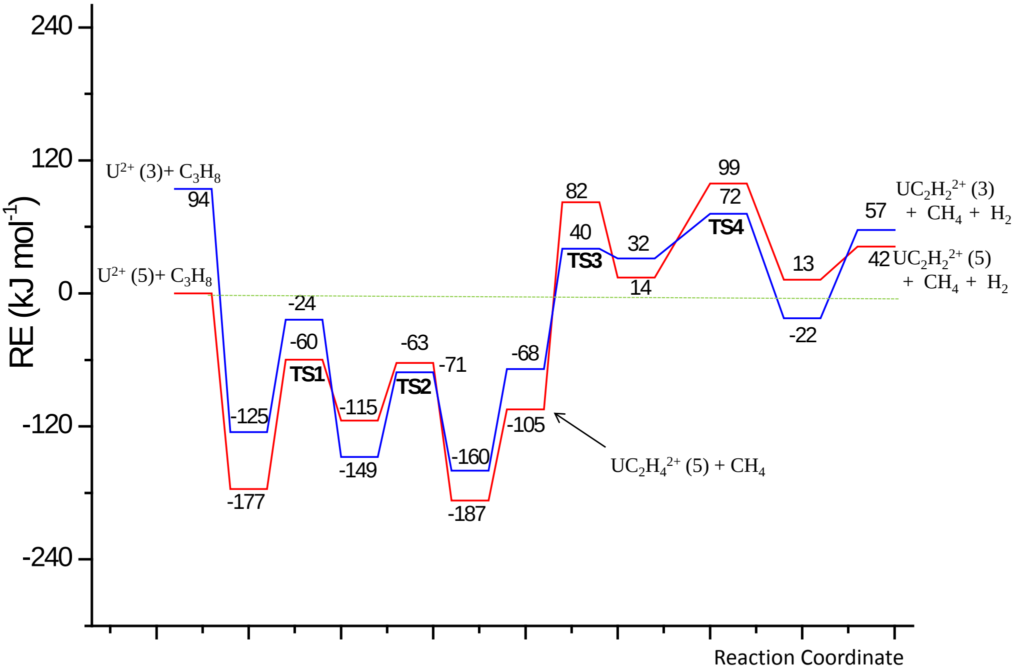
240
120
0
-120
-240
RE (kJ mol-1)
Reaction Coordinate
U2+ (3)+ C3H8
U2+ (5)+ C3H8
94
-125
-177
-24
-60
TS1
-115
-149
-63
-71
TS2
-160
-187
-68
-105
UC2H42+ (5) + CH4
82
40
TS3
32
14
99
72
TS4
13
-22
57
42
UC2H22+ (3) + CH4 + H2
UC2H22+ (5) + CH4 + H2

Figure S31

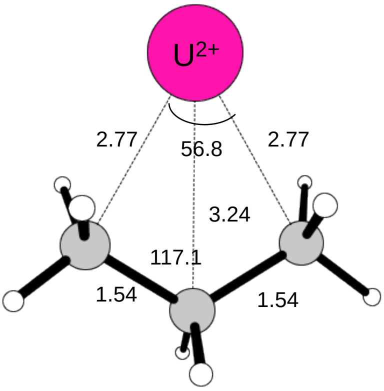

FC (^{5}A)

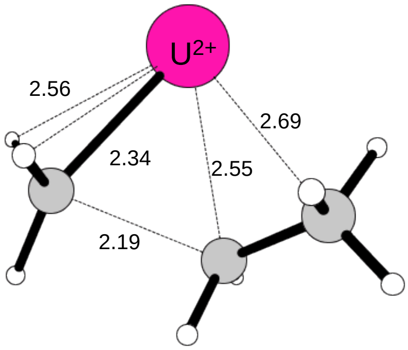

TS1 (^{5}A) *i 354 cm^{-1}*

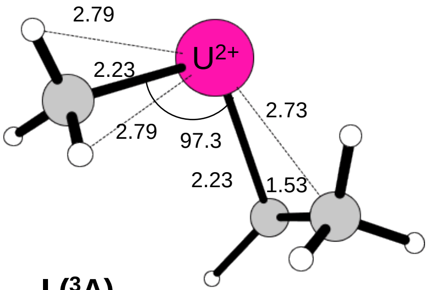

I (^{3}A)

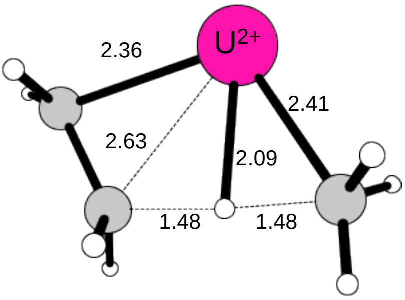

TS2 (^{3}A) *i 1275cm^{-1}*

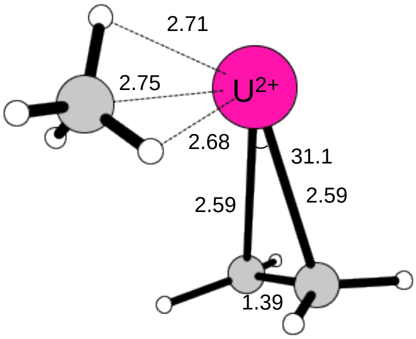

III (^{5}A)

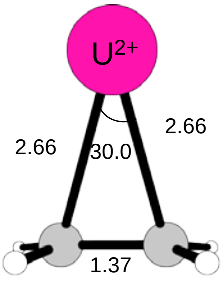

UC$_2$H$_4^{2+}$ (^{5}A)

Figure S32 (a)

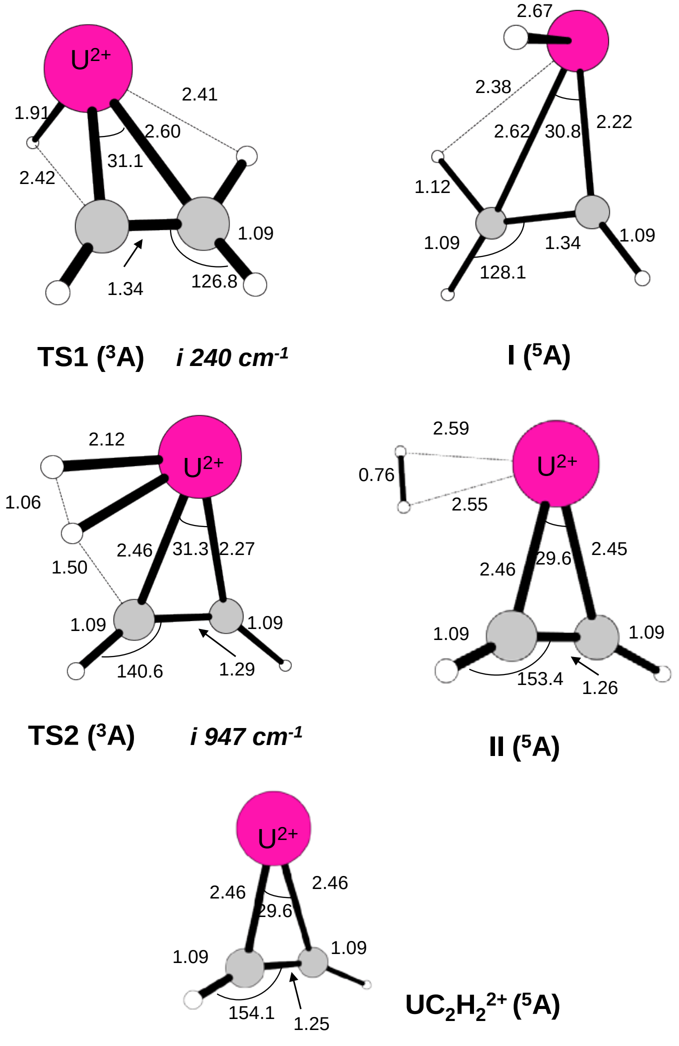

TS1 (^{3}A) ***i 240 cm^{-1}***

I (^{5}A)

TS2 (^{3}A) ***i 947 cm^{-1}***

II (^{5}A)

$UC_2H_2^{2+}$ (^{5}A)

Figure S32 (b)

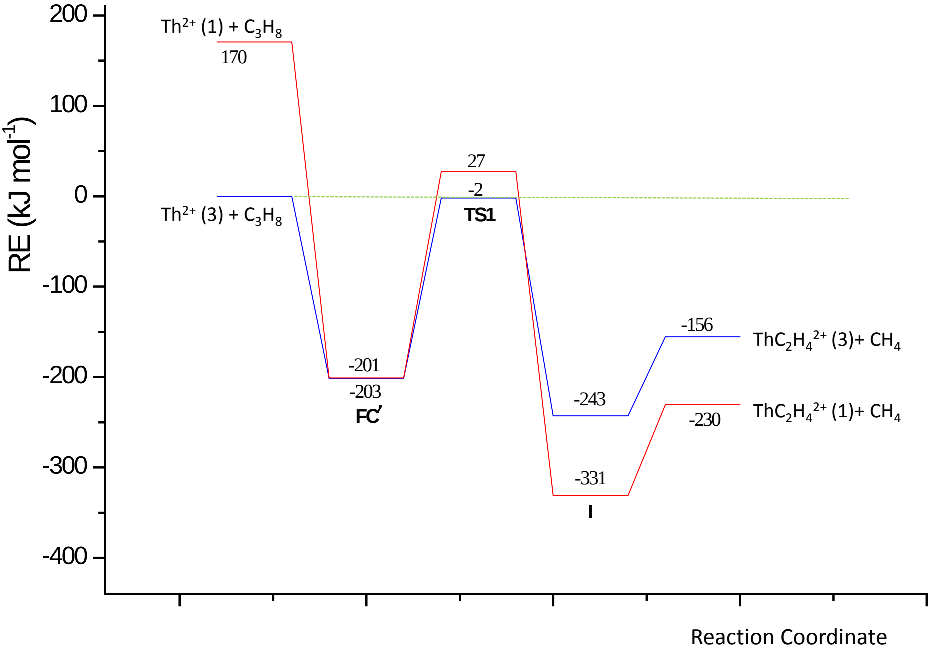
RE (kJ mol-1)
200
100
0
-100
-200
-300
-400
Reaction Coordinate
Th2+ (1) + C3H8
170
Th2+ (3) + C3H8
27
-2
TS1
-201
-203
FC′
-243
-331
I
-156
ThC2H42+ (3)+ CH4
-230
ThC2H42+ (1)+ CH4

Figure S33

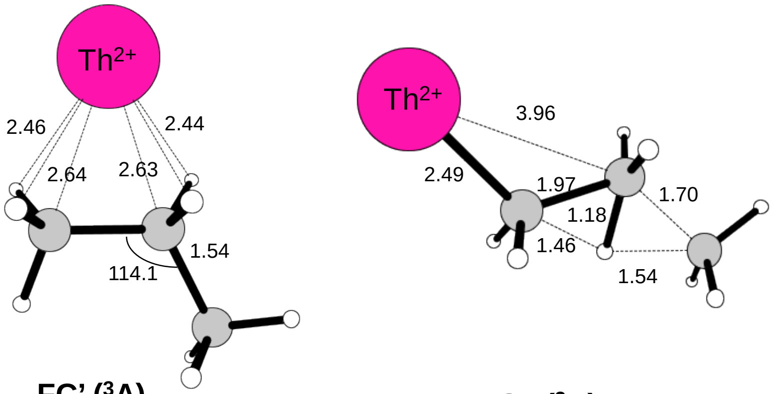

FC' (^{3}A)

TS1 (^{3}A) ***i 952 cm^{-1}***

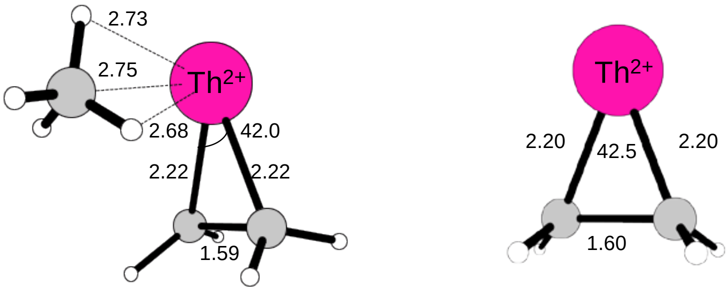

I (^{1}A)

ThC$_2$H$_4^{2+}$ (^{1}A)

Figure S34

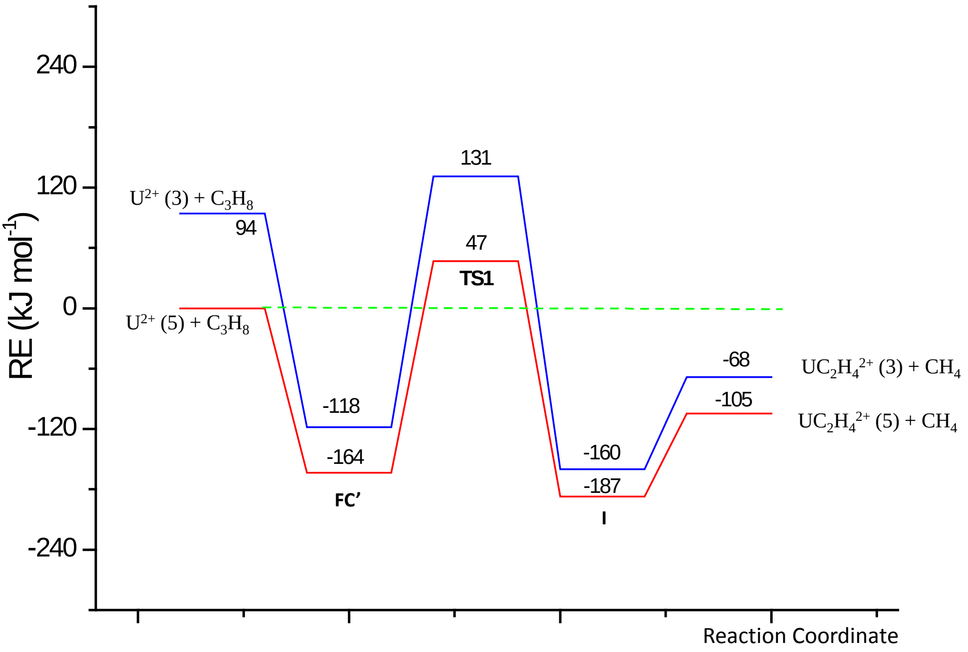
RE (kJ mol^{-1})
240
120
0
-120
-240
Reaction Coordinate
U^{2+} (3) + C$_3$H$_8$
94
U^{2+} (5) + C$_3$H$_8$
-118
-164
FC'
131
47
TS1
-160
-187
I
-68
-105
UC$_2$H$_4$$^{2+}$ (3) + CH$_4$
UC$_2$H$_4$$^{2+}$ (5) + CH$_4$

Figure S35

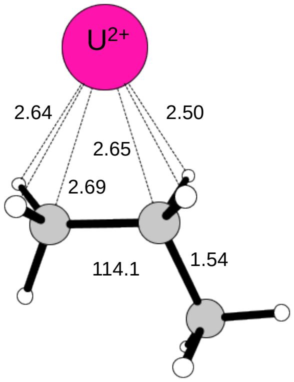

FC’ (^{5}A)

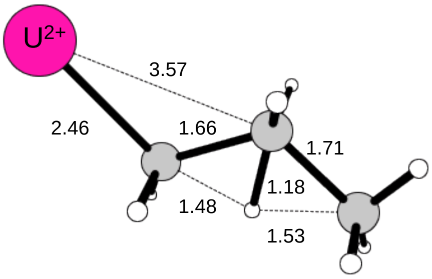

TS1 (^{5}A) ***i* *972cm^{-1}***

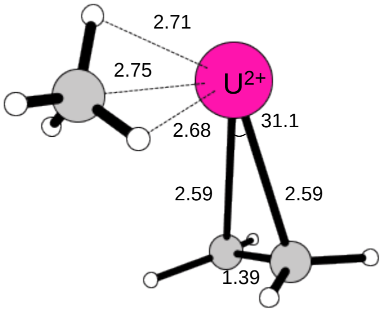

III (^{5}A)

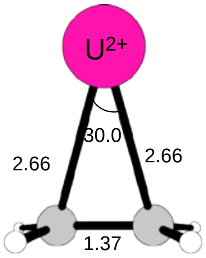

UC$_2$H$_4^{2+}$ (^{5}A)

Figure S36

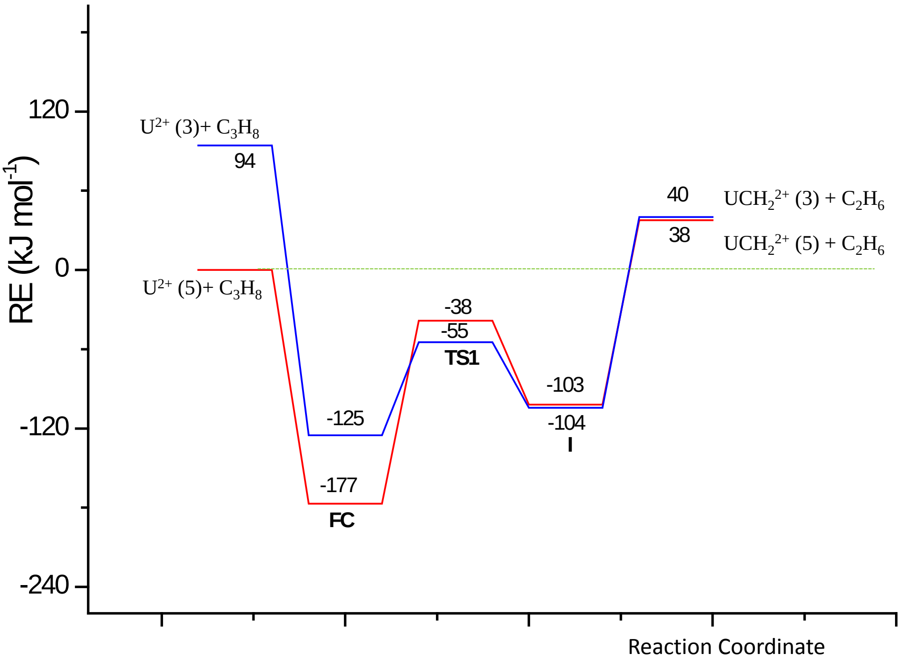
RE (kJ mol^{-1})
120
0
-120
-240
U^{2+} (3)+ C_3H_8
94
U^{2+} (5)+ C_3H_8
-125
-177
FC
-38
-55
TS1
-103
-104
I
40
38
UCH_2^{2+} (3) + C_2H_6
UCH_2^{2+} (5) + C_2H_6
Reaction Coordinate

Figure S37

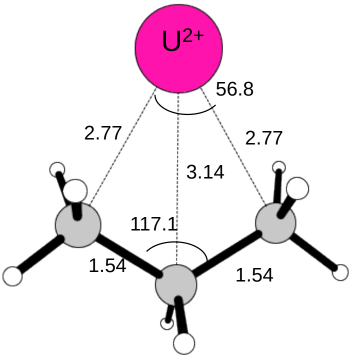

FC (^{5}A)

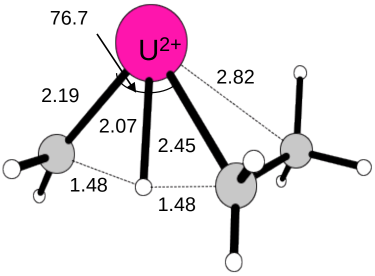

TS1 (^{3}A) *i 1378 cm^{-1}*

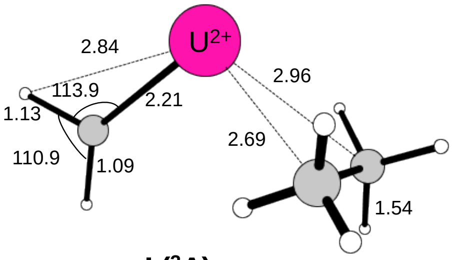

I (^{3}A)

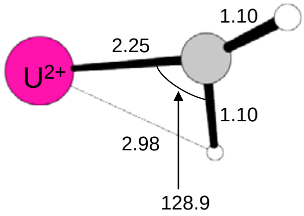

UCH$_2^{2+}$ (^{5}A)

Figure S38

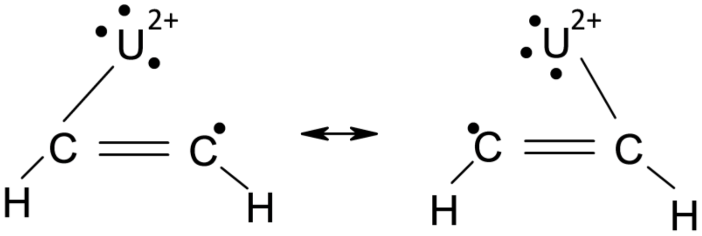

Scheme 1